Process-based modelling of storm impacts on gravel coasts

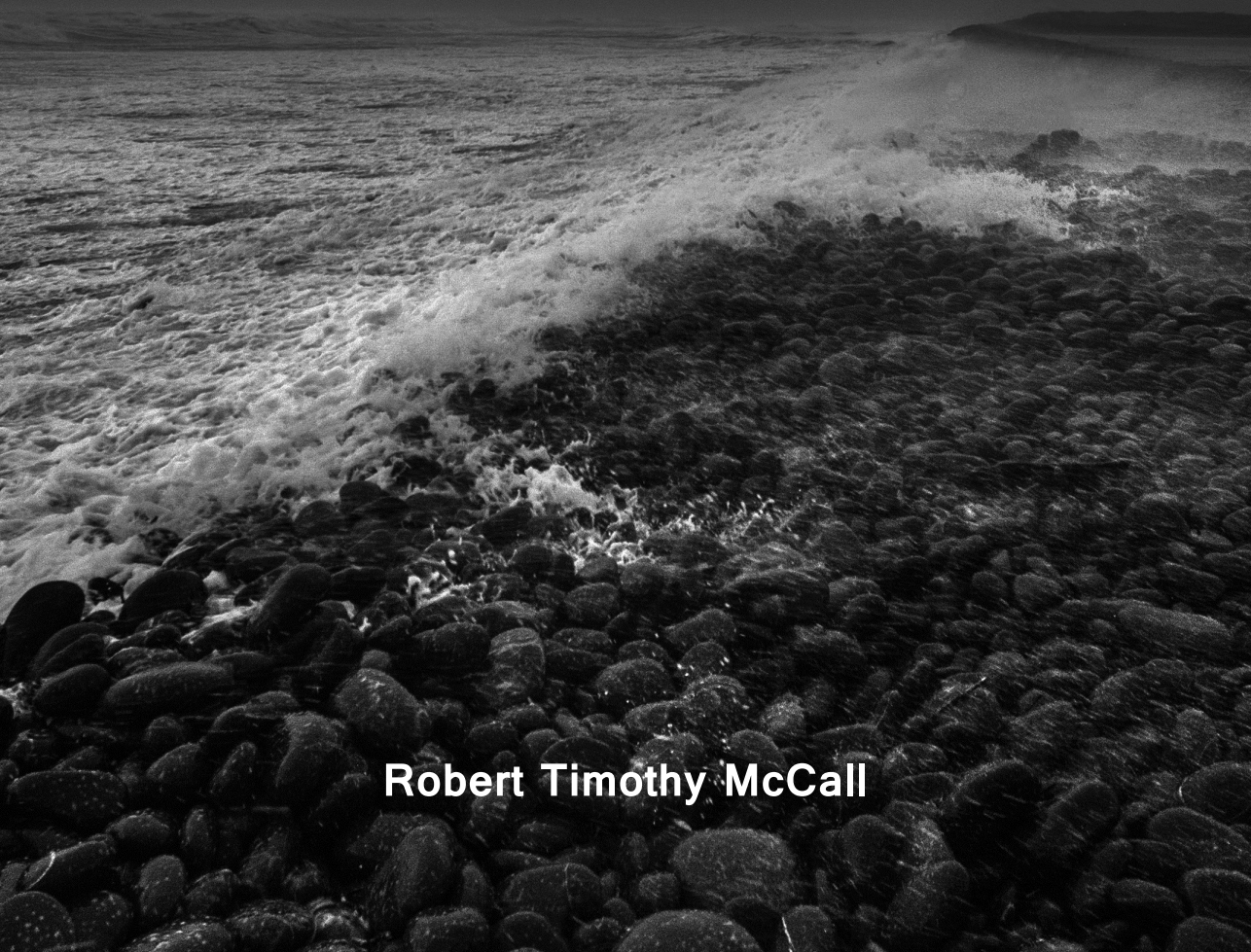

Robert Timothy McCall

Process-based modelling of storm impacts on gravel coasts

Robert Timothy McCall

School of Marine Science and Engineering

Faculty of Science and Engineering

Plymouth University

A thesis submitted to the Plymouth University in partial fulfillment of the requirements for the degree of:

Doctor of Philosophy

November 2015

Abstract

Process-based modelling of storm impacts on gravel coasts

Robert Timothy McCall

Gravel beaches and barriers occur on many high-latitude, wave-dominated coasts across the world. Due to their natural ability to dissipate large amounts of wave energy, gravel coasts are widely regarded as an effective and sustainable form of coastal defence. However, during extreme events waves may overtop, overwash, and even lower, the crest of the gravel beach, flooding the hinterland. In the evaluation of the safety of gravel coasts against flooding, coastal managers currently rely on models that have been shown in previous studies to be inaccurate. The research in this thesis attempts to improve the current predictive capacity of gravel beach storm response by developing a new process-based model to simulate storm impacts on gravel coasts.

The numerical model developed in this thesis, called XBeach-G, is a morphodynamic, depth-averaged, cross-shore profile model, based on the XBeach model for sandy coasts (Roelvink et al., 2009). The model simulates the morphological response of gravel beaches and barriers to storms by solving: (1) intra-wave flow and surface elevation variations using a non-hydrostatic extension of the non-linear shallow water equations; (2) groundwater processes, including infiltration and exfiltration, using a Darcy-Forchheimer-type model; and (3) bed load transport of gravel using a modification of the Van Rijn (2007a) bed load transport equation to include flow acceleration effects, which are shown to be significant on coarse-grained beaches. The model is extensively validated for hydrodynamics, groundwater dynamics and morphodynamics using detailed data collected in physical model experiments, as well as data collected in the field on four natural gravel beaches in the UK and one in France.

Validation results show that the model has high quantitative skill in simulating observed hydrodynamics on gravel beaches across a wide range of forcing conditions, in particular with regard to wave transformation, wave run-up and wave overtopping. Spatial and temporal variations in groundwater head are shown to be well represented in the model through comparison to data recorded in a physical model experiment. Validation of the morphodynamic component of XBeach-G shows that the model has high model skill (median BSS 0.75) in simulating storm impacts on five gravel beaches during ten storm events, with observed morphodynamic response ranging from berm-building to barrier rollover.

The model is used to investigate hydrodynamic processes on gravel beaches during storms, where it is found that incident-band variance is elemental in the generation of wave run-up on gravel beaches. Furthermore, simulations of wave run-up during high-energy wave events show a distinct disparity between run-up predicted by

empirical relations based on the Iribarren parameter and wave steepness, and run-up predicted by XBeach-G, where predictions by the empirical relations substantially underestimate observed wave run-up.

Groundwater processes are shown, by means of sensitivity simulations, to strongly affect the morphodynamic response of gravel beaches and barriers to storms. The research in this thesis supports the hypothesis that infiltration in the swash is a key driver for the berm-building response of gravel beaches and helps to reduce erosion of the upper beach during storms. Through model simulations on a schematic gravel barrier it is shown that groundwater processes effectively increases the capacity of gravel barriers to withstand storms with 1–3 m higher surge levels than if groundwater processes did not occur. Reducing the width of a barrier leads to a lowering of this capacity, thereby reducing the resilience of the barrier to extreme storm events. Despite its strong influence on gravel beach morphodynamics, it is found that infiltration plays a relatively small role on wave run-up levels on most natural gravel beaches (median $R_{2\%}$ run-up level reduction of 8%).

Application of the model in validation simulations and sensitivity simulations in this thesis, as well as in storm hindcast simulations discussed by McCall et al. (2013) shows the value of using the process-based XBeach-G model in coastal flooding analysis over the use of empirical tools. While no model can be considered entirely accurate, application of XBeach-G in all hindcast overwash simulations has lead to reasonable estimates of overtopping discharge and of morphological change, which is a significant improvement over the frequently substantial errors of the empirical tool designed for this purpose.

Contents

List of Figures

List of Tables

List of symbols

Symbol	Unit	Description
A	m^2	Cross sectional area of the barrier above SWL (cf., Bradbury, 2000)
As	-	Wave asymmetry
C	$m^{½}s$	Chézy bed friction coefficient
D	m	Characteristic grain size
D_{50}	m	Median grain size
D_{90}	m	Grain size that exceeds by size 90% of the sediment distribution
D_*	-	Dimensionless grain size
H	m	Wave height
H	m	Groundwater head
H_{bc}	m	Groundwater head imposed at the groundwater surface
H_{m0}	m	Spectral significant wave height, computed from the zero-order moment of the variance density spectrum
$H_{m0,0}$	m	Spectral significant deep water wave height, computed from the zero-order moment of the variance density spectrum and deshoaled to deep water using the peak wave period
I_b	-	Barrier inertia parameter (cf., Bradbury, 2000)
K	ms^{-1}	Effective hydraulic conductivity
K_{lam}	ms^{-1}	Hydraulic conductivity in case of laminar flow
P	$Jm^{-1}s^{-1}$	Wave energy flux per unit width
$P_{p,0}$	$Jm^{-1}s^{-1}$	Deep water wave energy flux per unit width computed with the significant wave height and group velocity at the peak frequency
Re	-	Reynolds number
Re_{crit}	-	Critical Reynolds number for the start of turbulent groundwater flow
S	ms^{-1}	Surface water-groundwater exchange flux

Symbol	Unit	Description
S_f	Jsm^{-2}	Frequency-wave energy density spectrum per unit of surface area
Sk	-	Wave skewness
T	s	Wave period
T_m	s	Mean wave period
$T_{m-1,0}$	s	Spectral wave period based on the first negative moment of the energy spectrum
$T_{m0,2}$	s	Spectral wave period based on the second positive moment of the energy spectrum
T_p	s	Spectral peak wave period
U	ms^{-1}	Combined velocity vector
W_{crest}	m	Width of the barrier crest
b_{CI}	-	Empirical bed boundary layer ventilation parameter, set at $b = 0.9$ in all simulations in this thesis, following Conley and Inman (1994)
c_a	-	Added mass coefficient
c_f	-	Dimensionless Chézy bed friction coefficient
c_g	ms^{-1}	Wave group velocity
$c_{g,p}$	ms^{-1}	Wave group velocity computed using the spectral peak wave period
c_i	-	Inertia parameter in bed shear stress, set at $c_i = 1.0$ in all simulations in this thesis
c_m	-	Coefficient of mass
c_n	-	Coefficient of grain density per unit of surface area
c_s	-	Smagorinsky constant, set at $c_s = 0.1$ in all simulations in this thesis
c_v	-	Volume shape factor
d_{toe}	m	Depth of the gravel barrier toe below SWL
f	s^{-1}	Wave frequency
f_p	s^{-1}	Spectral peak wave frequency
f_s	-	Friction factor when using the bed load transport equation of Nielsen (2002); Appendix D.

Symbol	Unit	Description
g	ms^{-2}	Gravitational constant, set at $g = 9.81$ ms^{-2} in all simulations in this thesis
h	m	Water depth
h_b	m	Closure depth relative to SWL in model of Powell (1990)
h_c	m	Beach crest elevation relative to SWL in model of Powell (1990)
h_{crest}	m	Barrier crest elevation above SWL
h_{gw}	m	Height of the groundwater level above the bottom of the aquifer
h_t	m	Elevation of the top of the gravel step relative to SWL in model of Powell (1990)
i	-	Cross-shore coordinate in the numerical solution grid
j	-	Longshore coordinate in the numerical solution grid
k	m	Characteristic roughness height
k	m^{-1}	Wave number, defined as $\frac{2\pi}{\lambda}$
m_0	Jm^{-2}	Zeroth order moment of the wave energy density spectrum
n	-	Temporal coordinate in the numerical solution grid
n_{EF}	-	Bed load transport probability coefficient when using the bed load transport equation of Engelund and Fredsøe (1976); Appendix D.
n_p	-	Porosity
p	$kgm^{-1}s^{-2}$	Pressure
p_b	m	Horizontal position of the closure depth relative to the SWL shoreline in model of Powell (1990)
p_c	m	Horizontal position of the beach crest relative to the SWL shoreline in model of Powell (1990)
p_t	m	Horizontal position of the top of the gravel step relative to the SWL shoreline in model of Powell (1990)
q	m^2s^{-2}	Dynamic pressure normalised by density
q	$m^3s^{-1}m^{-1}$	Cross-sectional discharge
q_b	$m^3s^{-1}m^{-1}$	Volumetric bed load transport rate, excluding pore space

Symbol	Unit	Description
$s_{m,0}$	-	Wave steepness based on the significant wave height and deep water length of the mean period wave
$s_{p,0}$	-	Wave steepness based on the significant wave height and deep water length of the peak period wave
t	s	Temporal coordinate
u	ms^{-1}	Depth-average cross-shore surface water velocity
u_{gw}	ms^{-1}	Depth-average cross-shore groundwater velocity
u_*	ms^{-1}	Friction velocity
v	ms^{-1}	Depth-average longshore velocity
w	ms^{-1}	Vertical velocity
x	m	Horizontal coordinate
z	m	Vertical coordinate
Δ	-	Relative submerged weight of sediment
Δ_i	-	Relative effective submerged weight of sediment, including the effect of through-bed flow
Δt	s	Numerical time step
Δx	m	Horizontal numerical grid size (in the cross-shore direction)
Δxy	m^2	Grid cell surface area
Δy	m	Horizontal numerical grid size (in the longshore direction)
Δz	m	Vertical numerical grid size
Λ_t	-	Fraction of time step (Δt) used for infiltration and exfiltration
Φ	-	Dimensionless ventilation parameter of Conley and Inman (1994)
α	-	Scaling parameter
α	-	Ratio between the surface seepage force and the seepage force in the bed, following Martin and Aral (1971)
β	-	Groundwater head parabolic curvature coefficient
β	-	Local bed slope, defined in degrees in this thesis
β_b	-	Slope of the beach

Symbol	Unit	Description
γ	-	Bed load transport calibration coefficient, set to $\gamma = 0.5$ (Chesil Beach, Loe Bar, Slapton Sands and Sillon de Talbert) and $\gamma = 1.0$ (BARDEX) in this thesis
δ_{wf}	m	Infiltration wetting front thickness
ε	m	Measure for numerical roundoff error, or instrument error
ζ	m	Free surface elevation
ζ_{gw}	m	Groundwater surface elevation
ζ_{lpf}	m	Low-pass filtered surface elevation
θ	-	Shields parameter
θ_{cr}	-	Critical Shields parameter for the initiation of transport
θ'	-	Effective Shields parameter including bed slope effects
κ	-	State indicating if groundwater and surface water are connected
λ	m	Wave length
λ_m	m	Wave length related to the spectral mean wave frequency
$\lambda_{m,0}$	m	Deep water wave length related to the spectral mean wave frequency
λ_p	m	Wave length related to the spectral peak wave frequency
$\lambda_{p,0}$	m	Deep water wave length related to the spectral peak wave frequency
ν	m^2s^{-1}	Kinematic viscosity of water, set at $\nu = 10^{-6}$ m^2s^{-1} in this thesis
ν_h	m^2s^{-1}	Modelled horizontal viscosity
ξ	m	Elevation of the bed
ξ_{gw}	m	Elevation of the bottom of the groundwater aquifer
$\xi_{p,0}$	-	Deep water Iribarren parameter based on the peak period wave length: $\xi_{p,0} = \frac{\tan\beta_b}{\sqrt{\frac{H_{m0}}{\lambda_{p,0}}}}$
ρ	kgm^{-3}	Density of water, assumed $\rho = 1000$ kgm^{-3} for fresh water and $\rho = 1025$ kgm^{-3} for salt water
ρ	-	Correlation coefficient

Symbol	Unit	Description
ρ_s	kgm^{-3}	Density of sediment, assumed $\rho_s = 2650\ kgm^{-3}$ in this thesis
σ	m	Vertical coordinate above the bottom of the aquifer
τ_b	$kgm^{-1}s^{-2}$	Bed shear stress
τ_{bd}	$kgm^{-1}s^{-2}$	Bed shear stress due to drag
τ_{bi}	$kgm^{-1}s^{-2}$	Bed shear stress due to inertia
ϕ	-	Angle of repose, defined in degrees and set at $\phi = 35^o$ in all simulations in this thesis
ϕ	-	Phi logarithmic scale for sediment size (Krumbein and Sloss, 1963).
φ	-	Phase lag angle when using the bed load transport equation of Nielsen (2002); Appendix D.

Glossary

Abbreviation	Description
1D	One-dimensional (in this thesis referring to the resolution of the cross-shore horizontal dimension and no vertical dimension)
2DH	Two-dimensional horizontal (resolution of two horizontal dimensions and no vertical dimension)
2DV	Two-dimensional vertical (resolution of one horizontal dimension and one vertical dimension)
3D	Three-dimensional (resolution of two horizontal dimensions and one vertical dimension)
BIM	Barrier Inertia Model (cf., Bradbury, 2000)
BLS	Bed level sensor
BSS	Brier Skill Score
CCO	Channel Coastal Observatory
MHWS	Mean high water spring
MSG	Mixed sand-gravel; referring to the gravel beach classification scheme of Jennings and Shulmeister (2002)
MSL	Mean sea level
NLSWE	Non-linear shallow water equations for free surface flow
ODN	Ordnance Datum Newlyn
OP	Overwash potential (cf., Matias et al., 2012)
PT	Pressure transducer
Q3D	Quasi-three-dimensional. Usually referring to resolution of two horizontal dimensions and partial resolution of the vertical dimension. See 2DH, 2DV and 3D.
RMS	Root mean square, defined as: $\mathrm{RMS}(x) = \sqrt{\frac{1}{n}\sum_{i=1}^{n} x_i^2}$
RMSE	Root mean square of the error
RPRF	Relative potential run-up freeboard
RTK-GPS	Real Time Kinematic Global Positioning System

Abbreviation	Description
SCI	Scatter index, defined as $\mathrm{SCI}(x) = \frac{\mathrm{RMSE}(x)}{\overline{x_{measured}}}$ (cf., Zambreskey, 1988; Ris et al., 1999; Roelvink et al., 2009)
SWL	Still water level
VOF	Volume of Fluid; referring to a free-surface numerical modelling approach
b_{rel}	Relative bias

Acknowledgements

First, I would like to thank the members of my supervisory team, Gerd Masselink, Paul Russell, Mark Davidson and Dano Roelvink, for their excellent support and advice. Gerd, thank you for showing a modeller the world of field research, for the many discussions on coastal processes, the seemingly unlimited time you make available for your students, and your constant support and enthusiasm for the research project. I couldn't have asked for a better Director of Studies. Thank you Paul and Mark for the very warm welcome you gave me when I arrived in Plymouth and your help in getting to grips with gravel beach dynamics. And Dano, thank you for being one of the most positive people I know and being an excellent brainstorming partner, always ready to think about how to capture complex coastal behaviour in our models (and for having been so ever since I joined the XBeach project).

I'd also like to thank Tim Poate for teaching me all about surveys and field data collection, putting up with fumbled surveys and dropped PTs with a brave face, and for being great company on all those stormy gravel beaches. The data you collected for the NUPSIG project has been absolutely pivotal in the development of this model. Thanks go to Pedro Almeida as well, not just for your support in the field and the provision of excellent laser scanner data of swash processes on gravel beaches, but also for your friendship and very Portuguese sense of humour!

The development of XBeach-G was made indefinitely easier by the work carried out prior to this research at Delft University of Technology on the non-hydrostatic extension to the non-linear shallow water equations in XBeach, which was later developed further in the SWASH model. I would like to take this opportunity to thank Marcel Zijlema, Guus Stelling, and in particular Pieter Smit for the improvements they made to the XBeach model and advice they gave me during this research.

I would like to thank Jaap van Thiel de Vries whose enthusiasm for coastal science planted a seed in my mind, Martin Austin for introducing me to the great research being done in Plymouth, and Ap van Dongeren for supporting the opportunity for this research, for being a mentor and for always being ready to discuss new ideas.

Thank you Joana, for packing everything up and moving with me to Plymouth and for being supportive every step of the way, even during long hours at the end of thesis writing. And thank you Evan for providing welcome, if sometimes forced, relief from that same writing.

Finally, I would like to acknowledge funding for this research from the Engineering and Physical Sciences Research Council (EP/H040056/1) and support given by Deltares (Event-driven Hydro- and Morphodynamics Strategic Research Programme Projects 1204516, 1202362 and 1209342). Data reported in this thesis from the BARDEX experiment were collected in the Delta Flume (Netherlands) as part of the EU-funded BARDEX project (HYDRALAB III Contract no. 022441 (RII3), Barrier Dynamics Experiment). Wave data at the Loe Bar, Chesil Beach and Slapton Sands

field sites, as well as bathymetric data at Chesil Beach and Slapton Sands are courtesy of the Channel Coast Observatory.

Authors declaration

At no time during the registration for the degree of Doctor of Philosophy has the author been registered for any other University award without prior agreement of the Graduate Committee. Work submitted for this research degree at the Plymouth University has not formed part of any other degree either at Plymouth University or at another establishment.

This study was financed with the aid of a studentship from the Engineering and Physical Sciences Research Council (EPSRC), relating to the EPSRC-funded research project NUPSIG (EP/H040056/1).

The author acknowledges the collaborative contribution of Dr T. Poate in the collection, analysis and processing of wave run-up and morphological change data recorded at Loe Bar, Slapton Sands, Chesil Beach and Seascale during the course of this research and used in Chapters 3–5, as well as wave run-up data measured on Loe Bar, Slapton Sands and Chesil Beach presented in Chapter 6. The auther would further like to acknowledge the contribution of Mr L.P. Almeida of Plymouth University in the collection of the data stated above, as well as the collection and analysis of the cross-shore laser scanner data at Loe Bar and Chesil Beach presented in Chapters 3 and 5, respectively.

The non-hydrostatic extension to XBeach discussed in Chapter 3, and applied in XBeach-G in Chapters 3–6, was primarily developed by Dr P. Smit, Dr M. Zijlema and Prof. Dr G. Stelling, with limited assistance from the author of this thesis relating to the implementation in the XBeach model code and the development of model boundary conditions. Chapter 3 of this thesis concerns the validation of the non-hydrostatic extension of XBeach for application on gravel beaches, which has solely been carried out by the author, and does not concern the development of the non-hydrostatic extension itself.

Relevant scientific seminars and conferences were regularly attended at which work was presented. Three first-author papers have been published in refereed journals, as well as two first-author conference proceedings. Furthermore the author co-authored six peer-reviewed journal articles and two conference proceedings.

Word count for the main body of this thesis: 46,363

First-author journal publications :

McCall, R.T., Masselink, G., Poate, T.G., Roelvink, J.A., and Almeida, L.P. Modelling the morphodynamics of gravel beaches during storms with XBeach-G. *Coastal Engineering* 2015, 103

McCall, R.T., Masselink, G., Poate, T.G., Roelvink, J.A., Almeida, L.P., Davidson, M., and Russell, P.E. Modelling storm hydrodynamics on gravel beaches with XBeach-G. *Coastal Engineering* 2014 , 91

McCall, R.T., Masselink, G., Poate, T.G., Bradbury, A.P., Russell, P.E., and Davidson, M.A Predicting overwash on gravel barriers. *Journal of Coastal Research* 2013 , 65

First-author conference proceedings :

McCall, R.T., Masselink, G., Poate, T.G., and Roelvink, J.A. Modeling gravel barrier resilience during storms with XBeach-G: The role of infiltration *Proceedings of Coastal Sediments* 2015

McCall, R.T., Masselink, G., Roelvink, J.A., Russell, P.E., Davidson, M. and Poate, T.G., Modeling overwash and infiltration on gravel barriers. *Proceedings of the 33rd International Conference on Coastal Engineering* 2012

Co-author journal publications :

Masselink, G., McCall, R.T., Poate, T.G., Van Geer, P. Modelling storm response on gravel beaches using XBeach-G. *Proceedings of the ICE - Maritime Engineering* 2014 , 167

Poate, T.G., Masselink, G., McCall, R.T., Russell, P.E., and Davidson, M. Storm-driven cusp behaviour on a high energy gravel beach *Journal of Coastal Research* 2014 , 70

Puleo, J., Blenkinsopp, C., Conley, D., Masselink, G., Turner, I., Russell, P., Buscombe, D., Howe, D., Lanckriet, T., McCall, R., and Poate, T. Comprehensive Field Study of Swash-Zone Processes. I: Experimental Design with Examples of Hydrodynamic and Sediment Transport Measurements *Journal of Waterway, Port, Coastal and Ocean Engineering* 2014 , 140

Almeida, L.P., Masselink, G., Russell, P.E., Davidson, M.A., Poate, T.G., McCall, R.T., Blenkinsopp, C.E., and Turner, I.L Observations of the swash zone on a gravel beach during a storm using a laser-scanner *Journal of Coastal Research* 2013 , 65

Austin, M.J., Masselink, G., McCall, R.T., and Poate, T.G. Groundwater dynamics in coastal gravel barriers backed by freshwater lagoons and the potential for saline intrusion: Two cases from the UK *Journal of Marine Systems* 2013 , 123-124

Poate, T.G., Masselink, G., Davidson, M.A., McCall, R.T., Russell, P.E., and Turner, I.L High frequency in-situ field measurements of morphological response on a fine gravel beach during energetic wave conditions *Marine Geology* 2013 , 342

Co-author conference proceedings :

Poate, T.G., McCall, R.T., Masselink, G., Russell, P.E., and Davidson, M. Contrasting storm impacts on gravel beaches - examples from South England. *Proceedings of the 33rd International Conference on Coastal Engineering* 2012

Puleo, J., Blenkinsopp, C., Conley, D., Masselink, G., Russell, P., Turner, I., Buscombe, D., Lanckriet, T., McCall, R., and Poate, T. Contrasting storm impacts on gravel beaches - examples from South England. *Proceedings of the 33rd International Conference on Coastal Engineering* 2012

Posters and conference presentations :

2014:

NCK days: the Netherlands Centre for Coastal Research Annual Symposium. Delft. *Oral presentation:* Increasing Coastal Flooding Preparedness in the UK: towards the development of a storm impact tool for gravel beaches.

EGU General Assembly. Vienna. *Session co-convener:* Monitoring and modelling research to guide coastal adaptation to climate change / extreme storms.

2013:

NCK days: the Netherlands Centre for Coastal Research Annual Symposium. Kijkduin. *Poster presentation:* Storm Impacts on Gravel Beaches.

Chapter 1

Introduction

1.1 Context

Gravel beaches and barriers occur on many former glacial and wave-dominated coasts around the world (e.g., Canada, USA, Northern Europe, Russia, Japan, Chile, Argentina, Australia and New Zealand), as well as on high-relief coasts where short, fast-flowing rivers provide abundant input of gravel into the coastal system (e.g., the Mediterranean and Black Sea coasts). In England and Wales gravel beaches and barriers constitute approximately one third of coastline (Fuller and Randall, 1988). Due to their natural ability to dissipate large amounts of wave energy, gravel coasts are widely regarded as an effective and sustainable form of coastal defence (e.g., Powell, 1990), and they are routinely managed to maintain and enhance their protective ability (e.g., Zenkovich and Schwartz, 1987; Nicholls, 1990; Moses and Williams, 2008).

As demonstrated by the 2013–2014 winter storm season in the UK however, gravel coasts may experience erosion, wave overtopping and even barrier breaching during extreme events, resulting in high societal costs in the form of damage to coastal properties and infrastructure, flooding of the hinterland and the potential loss of lives (Scott et al., in prep). It is therefore noteworthy that despite their societal importance, relatively little research has been directed towards understanding gravel beach behaviour in general (cf. Buscombe and Masselink, 2006), and their response to storms in particular (Poate et al., 2013).

Despite the general lack of knowledge of gravel beach processes, coastal managers currently rely on empirical models to make evaluations of coastal safety (DEFRA, 2008). While these models have the advantage of being easy to use and have often been well validated for the range of conditions they are designed for, their disadvantage is that the range of conditions for which they have valid empirical relations is often limited, and that they are generally designed only to predict certain storm impact parameters (e.g., erosion distance, overwash potential, etc.), rather than give the user a comprehensive overview of all potential hazards. The application of such models on managed coastlines (approximately 44% of the England and Wales coastline; DEFRA, 2010), which containing man-made flood defence and beach regulation structures (seawalls, dikes, groynes), is complicated by the fact that most empirical models have been developed for relatively uncomplicated natural coastlines. Therefore, in some cases it is not possible to apply empirical models on managed coastlines without extrapolating beyond the capacity of the model. Most importantly, application of such models outside their implicit range of validity can lead to significant

errors in the assessment of the storm impacts and the associated flood risk, as demonstrated by McCall et al. (2013). These limitations clearly indicate that current empirical models for gravel beaches are not appropriate tools with which coastal managers can evaluate current and future storm impacts.

Process-based models offer an improvement over empirical models in that if the important underlying physics are well understood and included in these models, they can be universally applied. In recent years advancements have been made in the development of process-based models for storm impact on sandy coasts (e.g., Tuan et al., 2006; Roelvink et al., 2009; Van Thiel de Vries, 2009; Van Rijn, 2009; Johnson and Grzegorzewski, 2011). In contrast, relatively few process-based models have been developed for gravel beaches. Due to the lack of measurement data collected under energetic and storm conditions on gravel beaches, existing process-based morphodynamic models for gravel coasts (discussed later in Chapter 2) have primarily been developed using data collected on natural or laboratory gravel beaches during low to moderate wave energy conditions, and therefore may not be representative of the physics and morphodynamics occurring during energetic storm events. Additionally, while the initial results of these process-based numerical models are promising, the validation of the models has thus far typically been limited to comparisons of morphological changes, rather than the hydrodynamic processes at the heart of the morphodynamic cycle.

To effectively assess and maintain coastal safety against storms, coastal managers must be able to predict where and under what conditions coastal flooding will occur, and to decide what measures can be taken to reduce the impact of storms. Despite the clear potential for process-based models to help in this assessment, it is clear from the descriptions above that no current model has demonstrated the capacity to provide this assistance.

The benefit of a validated process-based storm-impact model would be great; such a model could not only be used to provide early-warning of flooding events and assist emergency response coordination, but can also greatly improve the design of coastal defence structures and mitigation plans (e.g., Anthony, 2008). The latter being particularly important when considering the large investments required to combat the potential effects of climate change and sea level rise on flooding (Environment Agency, 2009). Furthermore, the use of the model as a tool in scientific research could increase understanding of the importance of physical process interactions, and could moreover be used to develop more simple, but accurate, tools that can be easily applied by coastal managers.

1.2 Objective, methodology and constraints

The objective of this research is to improve the current predictive capacity of gravel beach storm response by developing a process-based morphodynamic model to simulate storm impacts on gravel beaches and barriers using detailed data collected in physical model experiments, as well as data collected in the field on natural gravel beaches. In addition, secondary objectives of the research are to use the model to increase our understanding of gravel beach morphodynamics by quantifying the effect of key hydrodynamic processes (identified in Chapter 2) on gravel beach storm

response, and to highlight the potential for the development of new, more universal, empirical models through the combined use of observational data and synthetic model data.

Rather than develop an entirely new process-based numerical model from scratch, this research builds upon an existing open-source, process-based, depth-averaged morphodynamic model for the nearshore and coast called XBeach[1] (Roelvink et al., 2009). The XBeach model was originally developed to simulate hurricane impacts in the Gulf of Mexico, and has been shown to have high model skill in simulating dune erosion, overwash and breaching on dissipative sandy beaches (Roelvink et al., 2009; Van Dongeren et al., 2009; Van Thiel de Vries, 2009; McCall et al., 2010). More recently, two modified versions of XBeach were applied with reasonable success to model low wave-energy berm-building on a gravel beach (Milford-On-Sea; Jamal et al., 2014) and overwash on a gravel barrier (Slapton Sands; Williams et al., 2012b), which are discussed in greater detail in Section 2.3. More importantly, the XBeach model has recently (prior to this thesis) been extended with a non-hydrostatic pressure module (Smit et al., 2010) that allows the model to solve wave-by-wave flow and surface elevation variations due to short waves in intermediate and shallow water depths in a similar manner to the SWASH model (Zijlema et al., 2011b; Smit et al., 2013). This improvement is particularly important on steep gravel beaches, where the standard phase-averaged approach of XBeach to wave modelling may under-represent the variance in the swash (see Section 2.2).

Several further developments of the XBeach model have been shown to be necessary to allow the model to simulate the dominant physical processes on gravel beaches, in particular the inclusion of groundwater processes and gravel sediment transport processes (discussed in Chapter 2). During this research, these processes have been developed in the numerical code of the XBeach model to create a gravel beach storm impact model, which is hereafter named XBeach-G (as in, XBeach-Gravel).

The hydrodynamic and morphodynamic processes of the XBeach-G model have been validated in this thesis using data collected during the BARDEX physical model experiment (Williams et al., 2012a), as well as field data collected during storms on gravel beaches around the coast of the UK as part of the EPSRC-funded NUPSIG[2] project (e.g., Poate et al., 2012, 2013, 2014, 2015; Almeida et al., 2015). These field measurements represent the most extensive set of data collected on the hydrodynamics and morphological response of natural gravel beaches during storms, and are shown to be an integral part of the development and validation of XBeach-G. Similarly, the state-of-the-art measurements of surface water and groundwater processes during the BARDEX experiment, as well as the range of forcing conditions and morphological response stages (varying form berm-building to barrier rollover), make this dataset highly valuable to the development and validation of the model.

To limit the scope of the development of XBeach-G, the model has been designed with the spatial and temporal scales of processes related to storm impact in mind

[1] eXtreme Beach behaviour (`www.xbeach.org`)

[2] New Understanding and Prediction of Storm Impacts on Gravel beaches (`http://www.research.plymouth.ac.uk/coastal-processes/projects/nupsigsite/home.html`)

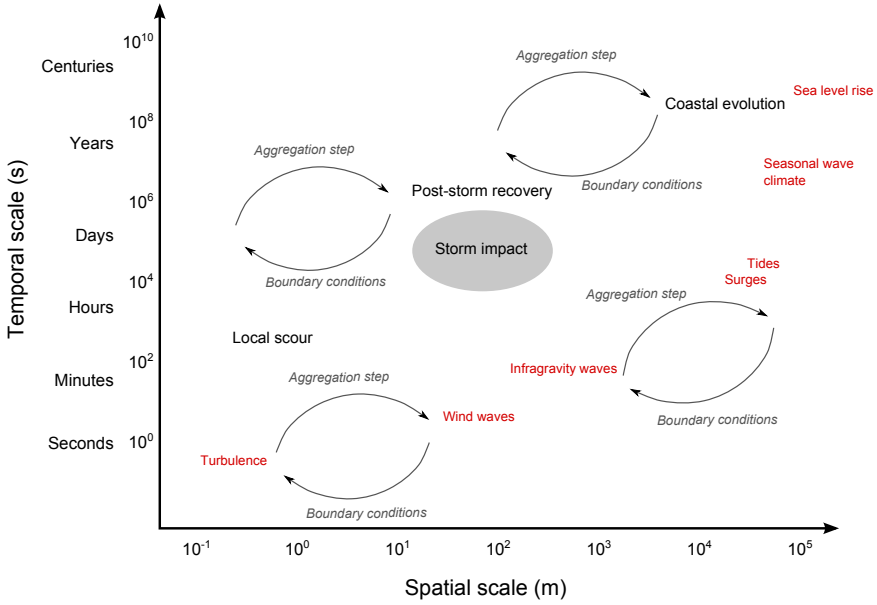

Figure 1.1: Scales of hydrodynamic processes (red) and coastal morphodynamics (black). Lower order (longer-term, larger scale) processes provide constraints and internal boundary conditions for higher (shorter-term, smaller scale) order processes, whereas the aggregation of higher order processes affects the behaviour of lower order processes (cf. De Vriend, 1991; Kraus et al., 1991; Cowell and Thom, 1994; De Vriend, 1998; Cowell et al., 2003). The focus of this thesis is at the scale of storm impact (grey shading).

(Figure 1.1). Therefore, the model does not address lower-order, or higher-order morphological processes (e.g., long-term coastal evolution and local scour, respectively), or attempt to solve other hydrodynamic processes than those directly relevant at the scale of storm-impact. While potentially feasible to simulate post-storm recovery at the same spatial and temporal scales as storm-impact, the dominant physical processes for recovery may differ to those during storms, and are therefore not the focus of this research.

The scope of research is further refined by primarily focussing on the development of a morphodynamic model for pure gravel beaches, as opposed to mixed sand-gravel (MSG) and composite gravel beaches (cf. Jennings and Shulmeister, 2002), although potential model developments to include all gravel beach types are discussed in Chapter 7. In the rest of this thesis, the terms GRAVEL BEACH and GRAVEL BARRIER refer only to pure gravel beaches and barriers in the classification scheme of Jennings and Shulmeister (2002), unless stated otherwise.

Finally, the development and validation of XBeach-G in this thesis is in the form

of a depth-averaged, one-dimensional (1D) cross-shore profile model. However, to account for further development of the model towards a depth-averaged two dimensional (2DH) area model, cross-shore process formulations will be developed that can be extended in the future to include longshore contributions.

1.3 Thesis outline

Chapter 2 gives a brief overview of our current understanding of the dominant physical processes controlling the morphodynamic response of gravel beaches and barriers. Chapter 2 also discusses existing conceptual, empirical and process-based models for gravel beaches with respect to their use as storm impact models and argues the need for a new process-based model, XBeach-G. The development and validation of XBeach-G is discussed in Chapters 3–5, where Chapter 3 addresses the validation of the surface water dynamics on gravel beaches using the existing non-hydrostatic pressure module of XBeach, Chapter 4 presents and validates a groundwater module for gravel beaches developed during this research, and Chapter 5 presents and validates a gravel sediment transport and morphology module developed during this research. The effect of key hydrodynamic processes identified in Chapter 2 on gravel beach storm impact is discussed throughout Chapters 3–5 by means of sensitivity simulations. The validated XBeach-G model is applied in Chapter 6 to investigate storm wave run-up on gravel beaches and the change from crest build-up to crest lowering on gravel barriers. Finally, Chapters 7 and 8 address the potential use of the XBeach-G model in research and engineering projects, the main model limitations and potential model developments to mitigate or overcome them, and final conclusions of the research.

Chapter 2

Gravel beach dynamics and models

This chapter reviews the current state of knowledge of physical processes on gravel beaches, as well as current morphodynamic models for gravel beaches. The reviews indicate the importance of swash hydrodynamics and groundwater interaction in the morphodynamic response of gravel beaches that is currently not well described by empiricial and process-based models. Furthermore, the review highlights that many current models have been developed and validated for relatively low-energy wave events and that there is a distinct lack of models for high-impact storm events.

2.1 Introduction

The development of a process-based storm impact model for gravel beaches requires understanding of the dominant physical processes leading to their morphodynamic response. In this chapter, a brief review is given of the current state of knowledge of physical processes on gravel beaches and their effect on beach morphodynamics. While relatively little research has been aimed at understanding the detailed processes at the heart of the morphodynamic response of gravel beaches to storms, a more detailed and general review of gravel beach processes than the one presented here is given by Buscombe and Masselink (2006). A review is presented of existing morphodynamic models for gravel beaches and their applicability to the simulation of storm impacts is discussed in the second part of this chapter.

2.2 Characteristic physical processes and morphology

Despite their wide-ranging use as cost-effective and sustainable forms of coastal defence (e.g., Johnson, 1987; Aminti et al., 2003), relatively little research has been directed at understanding detailed morphodynamic processes on gravel beaches in comparison to their sandy counterparts (Mason and Coates, 2001; Buscombe and Masselink, 2006), and in particular the processes that determine their morphodynamic response to storms (Poate et al., 2013). In general, however, gravel beaches are known to differ from sandy beaches in terms of dominant hydrodynamic processes, groundwater effects, sediment transport modes and morphodynamic response (Buscombe and Masselink, 2006).

Gravel beaches typically have a steep beach face, with a slope in the order of 1:20 – 1:5, and tend to fall in the reflective domain (Carter and Orford, 1984) of the morphological beach classification of Wright and Short (1984). As such, these beaches are characterised by an unsaturated and narrow surf zone with plunging waves breaking close to the shoreline and hence a high spatial concentration of wave energy dissipation on the beach face. Compared to dissipative sandy beaches, the surf zone of

a gravel beach has limited capacity for the generation of infragravity wave energy through the shoaling and release of bound long waves (Longuet-Higgins and Stewart, 1962, 1964; Battjes et al., 2004), or the time-varying breakpoint mechanism (Symonds et al., 1982), and its surf and swash zones are consequently dominated by incident-band motions (e.g., wind-wave or swell-wave band motions; cf., Wright et al., 1979; Miles and Russell, 2004), although zero-order subharmonic edge-waves may be generated at the shoreline under certain conditions (e.g., Huntley and Bowen, 1975; Guza and Inman, 1975). Furthermore, whereas the swash zone on sandy beaches is almost always saturated (i.e., increasing the incident wave height does not lead to increased swash variance; cf. Brocchini and Baldock, 2008), the swash zone on gravel beaches is unsaturated during long-period wave conditions on mild-sloping beaches and during most wave conditions on steep-sloping beaches (Figure 2.1), implying that the swash zone on gravel beaches cannot necessarily be assumed to be saturated during storm events. This observation is relevant to the dynamics of gravel beaches during storms, since the degree of swash saturation determines how much energy in the swash zone will increase, or stagnate with increased offshore wave forcing during storms, and the phasing of swash-swash interactions is thought to control the morphodynamic response of the swash and surf zone (e.g., Kemp, 1960; Kirk, 1970).

Due to their grain size and large interstitial pores, gravel beaches are relatively permeable compared to sandy beaches with hydraulic conductivity values typically in the range of $1 \cdot 10^{-3} - 1 \cdot 10^{0}$ ms^{-1} (e.g., Bear, 1972). Infiltration and exfiltration of surface water through the beach face has long been known to affect the morphodynamic response of permeable beaches through the first-order effect of reducing the backwash volume (e.g., Bagnold, 1940; Grant, 1948; Carter and Orford, 1993), as well as through second-order effects in the form of vertical pressure gradients, resulting in the modification of the effective weight and mobility of particles in the bed (e.g., Martin and Aral, 1971; Nielsen, 1992), and ventilation of the bed boundary layer, resulting in altered bed shear stresses (e.g., Martin, 1970; Oldenziel and Brink, 1974; Conley and Inman, 1994; Nielsen, 1997). Masselink and Li (2001) found through numerical model investigation that the first-order effect of infiltration (i.e., reduction of the backwash volume) only significantly altered the morphodynamic response of beaches with hydraulic conductivity greater than $1 \cdot 10^{-1}$ ms^{-1}, which they equated to a median grain diameter of 1.5 mm. Butt et al. (2001) investigated the second-order effects of groundwater exchange and found that the result of the two opposing processes (e.g., vertical pressure gradients and boundary layer ventilation) was net onshore-directed sediment transport for grain sizes greater than approximately 0.5 mm, and net offshore-directed sediment transport for smaller grain sizes. Field, laboratory and numerical investigations have confirmed the importance of groundwater processes on gravel beaches (e.g., Austin and Masselink, 2005; Horn and Li, 2006) and have further highlighted the importance of the thickness of the groundwater aquifer (e.g., Powell, 1990) and groundwater level fluctuations (e.g., Austin and Masselink, 2006a; Masselink and Turner, 2012) on the morphodynamics of gravel beaches.

The spatial concentration of incident wave breaking on the beach face of gravel beaches means that the critical threshold for sediment transport is almost always ex-

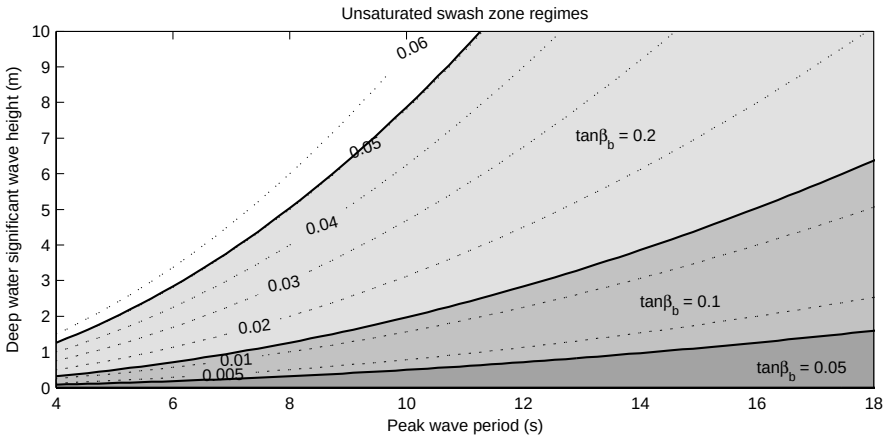

Figure 2.1: Approximate regimes in which gravel beach swash zones are unsaturated, based on the swash period relation of Brocchini and Baldock (2008), where swash saturation is estimated to occur when $\left(\frac{H}{gT^2(\tan\beta_b)^2}\right)^{\frac{1}{4}} \gtrsim 0.4$, and H is the offshore wave height, g is the gravitational constant, T is the offshore wave period and β_b is the angle of the beach slope. The dark, medium and light grey shaded areas correspond to unsaturated swash zone conditions on gravel beaches with a beach slope of 1:20, 1:10 and 1:5 respectively (note that these areas overlap in the lower-right area). The parameter space outside the shaded area corresponds to saturated swash conditions. Deep water peak wave steepness values are displayed as dotted contour lines for comparative purposes.

ceeded (cf. Buscombe and Masselink, 2006). However, in contrast to sandy beaches, sediment transport on gravel beaches is almost entirely composed of bed load and sheet flow transport and grain saltation (Carter and Orford, 1993; Isla and Bujalesky, 1993), and suspended transport is negligible[1] due to the high fall velocity of the particles. The variation in grain size on gravel beaches is generally several orders greater than that found on sandy beaches (Buscombe and Masselink, 2006), which allows the spatial and temporal variation in the uprush and downwash transport capacity to generate differentiated patterns of grain sizes on the beach face, where larger than average grains are found at the step and berm (e.g., Austin, 2005). These sedimentary patterns can become self-regulatory through positive feedback mechanisms related to particle interactions (e.g., particle acceptance and rejection; cf. Moss, 1962, 1963) and permeability (e.g., increased or decreased infiltration rates) and are a function not only of the grain size, but also of the shape of the grains (e.g., Bluck, 1967; Williams and Caldwell, 1988; Isla, 1993). The importance of such interactions is captured in the concept of morpho-sedimentary dynamics (cf. Carter and Orford, 1993; Buscombe and Masselink, 2006), where sediment heterogeneity is accepted as a fundamental and driving component of the morphodynamics of gravel beaches.

Gravel beaches are characterised by the presence of a step, a steep-faced, submerged feature at the base of the foreshore (e.g., Kirk, 1970). The morphology of the step is known to respond to the nearshore hydrodynamic forcing conditions by increasing in height under increased wave forcing (Hughes and Cowell, 1987) and by migrating across the cross-shore profile in step with the tide level (e.g., Masselink et al., 2010; Austin and Masselink, 2006a; Almeida et al., 2015). The step strongly controls the location of wave breaking by presenting an abrupt change in water depth (Hughes and Cowell, 1987) and strongly influences breaker-zone and swash-zone dynamics (Masselink et al., 2010; Poate et al., 2013; Almeida et al., 2015), and is therefore often described as the equivalent of a break-point bar on sandy beaches (cf. Austin and Masselink, 2006a; Austin and Buscombe, 2008). The step is thought to help maintain the reflective state of the beach by creating a sediment convergence point close to the shore and thereby limit the potential for the formation of a dissipative and mild beach slope (cf. Hughes and Cowell, 1987; Buscombe and Masselink, 2006; Austin and Buscombe, 2008).

In a similar manner to the step, the berm is considered one of the mechanisms through which gravel beaches present their reflective nature (e.g., Austin, 2005). A berm characterises a marked change in slope on the beach from a steep, seaward-facing slope, to a flat terrace at the start of the backshore. Berms are thought to be created by asymmetric swash sediment transport, leading to sediment convergence in the upper swash (cf. Bagnold, 1940; Grant, 1948; Duncan, 1964; Carter and Orford, 1993) and therefore their morphology is determined both by the still water level and the incident waves. Gravel beaches may display multiple berms at varying elevations, relating to tidal high water conditions and storm wave conditions (Jennings and Shulmeister,

[1] Note that visual observations made at Loe Bar and Chesil Beach during this research appear to suggest that some gravel may be entrained in the water column at the location of wave breaking during energetic conditions. However, to the author's knowledge, no measurements of such sediment concentrations have been attempted.

2002; Austin and Masselink, 2006a; Masselink et al., 2010). On gravel beaches the interaction between surface water and groundwater (i.e., infiltration) plays a particularly important role in the generation of berms (Austin and Masselink, 2005, 2006b).

Due to its limitation of being a 1D cross-shore profile model, the model to be developed in this research will not be able to simulate the three-dimensional cusp horns and bays common to many swash-aligned gravel beaches (e.g., Huntley and Bowen, 1975 , and many others). An analysis of the theories of the generation of cusps on gravel beaches is therefore omitted from this section.

2.3 Existing models for gravel beaches

Morphodynamic models for gravel beaches can be categorised by their complexity (cf. Masselink and Gehrels, 2014), where a near-continuous spectrum of models types can be described that ranges from simple conceptual models, to empirical and parametric models, and process-based models. In this classification, conceptual models are classed as models that attempt to qualitatively describe the observed behaviour of systems. Such models are particularly useful for discussing and identifying dominant processes in the behaviour of the system that can be included in more complex models, but have limited value in practical applications requiring quantitative predictions of system change (Masselink and Gehrels, 2014).

Empirical, or parametric models constitute an advancement over conceptual models in that they describe system response in a quantitative manner using correlative relationships found in data of observed system behaviour, without describing the underlying processes leading to the system response (Adams et al., 2013). Such models are commonly used in practical coastal engineering applications due to their limited computational requirement and ease of use, but are inherently limited to systems that are well described by the relationships in data underlying the model (cf., Thieler et al., 2000). While the terms *empirical model* and *parametric model* are both commonly used to describe such data-derived models, this thesis will henceforth address this type of models as empirical models. Behavioural models can be considered a special hybrid of conceptual and empirical modelling, in which qualitative concepts (e.g., equilibrium profile) are used to determine the overall direction of change in a system, and empirical models are used to describe the rate of change in the system (e.g., Kriebel and Dean, 1993).

Process-based models differ from empirical and conceptual models in that process-based models attempt to describe the behaviour of the system by understanding and quantifying the detailed physical processes and their interactions that lead to changes in the system (Adams et al., 2013). If the underlying physics of the system are well understood and captured in process-based models, these models can be applied in any given physical setting and are therefore more widely applicable than empirical models. However, due to the greater complexity of processes simulated by process-based models the computational requirements for process-based models is substantially greater than those for empirical models.

While there is theoretically a clear distinction between conceptual, empirical and process-based models, in practice most, if not all, empirical and process-based mod-

els are founded on conceptual descriptions of reality (Masselink and Gehrels, 2014). Similarly, all process-based models rely on empirical relations to resolve physical processes at scales smaller than the model resolution (e.g., molecular diffusion, subgrid turbulence) and most morphodynamic process-based models rely on empirical descriptions of sediment pick-up, rather than compute this explicitly from basic principles[2].

2.3.1 Conceptual models

A substantial proportion of research on storm impacts on gravel beaches and barriers has been directed at describing relatively large-scale processes (e.g., surge, wave run-up, overtopping) and their impact on the coast, in particular with respect to crest overtopping, overwash and barrier rollover (cf. Orford, 1977; Carter and Orford, 1993; Orford et al., 2003). In a qualitative sense, this knowledge is captured by a conceptual model for barrier overtopping and overwash (Crest build-up – Barrier rollover in Figure 2.2), in which the morphodynamic response of gravel barriers is related to the difference between wave run-up levels and the height of the barrier crest (Bradbury and Powell, 1992; Orford and Anthony, 2011). The transition between berm formation and beach erosion (top left panels in Figure 2.2) has generally not been the focus of conceptual storm impact models (e.g., Orford et al., 2003) and is not yet clearly understood. Principal mechanisms proposed for the transition between beach erosion and berm formation are the offshore wave steepness[3] (e.g., Hattori and Kawamata, 1980; Komar, 1998), that has to a certain degree been verified by measurements in flume experiments and in the field (e.g., Van Hijum, 1974; Powell, 1990; Sherman, 1991; Masselink et al., 2010; Poate et al., 2013), and the ratio between the wave period and the swash period (e.g., Kemp, 1960; Kirk, 1970; Holland and Puleo, 2001), which is related to the wave steepness, but has been less well investigated in field and laboratory studies.

[2]Recent work with Discrete Particle Models for sediment transport, e.g., Drake and Calantoni, 2001; Calantoni et al., 2004, has shown that true process-based modelling of sediment transport may become achievable in the future. However, at this stage such modelling requires prohibitive computational effort and itself still relies on empirical relations for drag and added mass of the sediment particles.

[3]Note that Orford (1977) also uses the concept of wave steepness (in terms of plunging and spilling breakers) in combination with tide and surge levels to explain the transition between beach erosion and crest build-up.

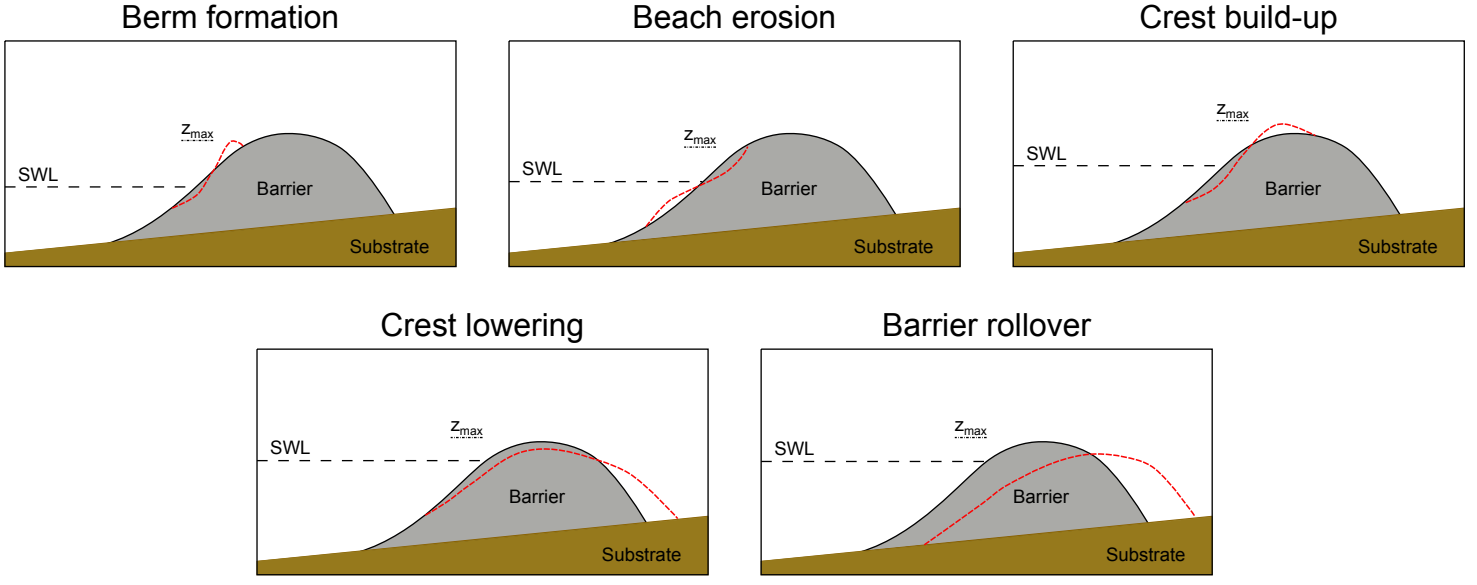

Figure 2.2: Conceptual model of the morphological response of a gravel barrier (– –) to varying wave forcing and water levels. From top-left to bottom-right the wave conditions become more energetic and the still water level higher, leading to higher maximum water levels on the barrier (z_{max}). Note that the distinction between berm formation and beach erosion is one based primarily on wave conditions, rather than water level (cf., Hattori and Kawamata, 1980; Komar, 1998) and barrier rollover can take place such that the post-storm crest is higher, or lower, than the pre-storm crest. Crest build-up – barrier rollover adapted from Orford et al. (1991) and Bradbury and Powell (1992).

2.3.2 Empirical models

Despite the similarity between the conceptual model of gravel barrier storm response shown in Figure 2.2 and the conceptual model underpinning the Storm Impact Scale for sandy barrier coasts (Sallenger, 2000), a generalised model to quantitatively describe thresholds between all stages of morphodynamic response has yet to be found. This, to a certain extent, may be due to the lack of observational data and empirical relations with which to specify changes in gravel barrier response. This section summarises existing empirical relations for hydrodynamic and morphodynamic processes on gravel beaches and their potential application in the prediction of storm impacts.

A focus of much storm impact research on both sandy and gravel coasts has focussed on wave run-up, leading to many Iribarren-type (Battjes, 1974) parametrisations of wave run-up of the form $\frac{R_{2\%}}{H} = a\xi_0^b + c$, where $R_{2\%}$ is the 2% wave run-up exceedence level, H is the wave height, $\xi_0 = \frac{\tan\beta_b}{\sqrt{H/\lambda_0}}$ is the deep water Iribarren parameter, β_b is the angle of the beach slope, λ_0 is the deep water wave length and a, b $\mathcal{O}(1)$ and c $\mathcal{O}(0.1)$ are fitting coefficients with varying values found at different field sites and in laboratory data (e.g., Hunt, 1959; Holman, 1986; Mase, 1989; Nielsen and Hanslow, 1991; Van der Meer and Stam, 1992; Van Gent, 2001). Although Iribarren-type run-up equations are found to correspond well to field observations on steep sandy beaches, wave run-up on flatter and dissipative beaches appears to be less dependent on the beach slope and to scale with the deep water significant wave height $H_{s,0}$ (Ruessink et al., 1998; Ruggiero et al., 2001), or $\sqrt{H_{s,0}/\lambda_0}$ (Nielsen and Hanslow, 1991), instead of the Iribarren parameter. In order to address this difference in a practical manner, Stockdon et al. (2006) developed an empirical run-up equation based on separate contributions of the incident-band and infragravity-band to wave run-up at the shore. The run-up equation was developed and validated using data from dissipative and reflective sandy beaches in the USA and the Netherlands, with separate optimal formulations for steep and mild sloping beaches:

$$R_{2\%} = 0.043\sqrt{H_{s,0}\lambda_{p,0}} \qquad \xi_{p,0} < 0.3 \tag{2.1a}$$

$$R_{2\%} = 0.73\beta_f\sqrt{H_{s,0}\lambda_{p,0}} \qquad \xi_{p,0} > 1.25 \tag{2.1b}$$

where β_f is the beach slope measured over the portion of the beach where run-up occurs, $\lambda_{p,0}$ is the deep water wave length of the peak period wave and $\xi_{p,0}$ is the deep water Iribarren parameter based on the significant wave height and the peak period wave length. Stockdon et al. also developed a general expression for application on all beaches:

$$R_{2\%} = 1.1\left(0.35\beta_f\sqrt{H_{s,0}L_{p,0}} + \frac{\sqrt{H_{s,0}L_{p,0}\left(0.563\beta_f^2 + 0.004\right)}}{2}\right) \tag{2.2}$$

where the first term inside the brackets relates to wave set-up and the second term relates to wave run-up. Equations 2.1b and 2.2 have been used with mixed results on gravel beaches, where the parametrisation was found to work well under laboratory conditions (Matias et al., 2012 discussed later in this section), but to underpredict observed wave run-up on steep gravel beaches in the field (Poate et al., 2012).

Powell (1990) derived wave run-up formulations specifically for gravel beaches as part of an empirical cross-shore profile response model, discussed later in this section, which is based on a series of physical model experiments. In this empirical formulation, wave run-up exceedence levels are related to the height of the gravel beach berm:

$$\frac{R_{2\%}}{H_s} = \frac{h_c}{H_s}\left(-\frac{\ln(0.02)}{4.2}\right)^{0.455} \tag{2.3}$$

where H_s is the offshore significant wave height, h_c is the height of the beach berm above still water level (SWL), discussed later in this section (Equation 2.5b), and the logarithmic numerator relates to the 2% exceedence level.

More recently, Polidoro et al. (2013) developed a wave run-up equation of similar structure to Equation 2.2 for MSG beaches, which incorporates the effect of bimodal wave spectra:

$$R_{2\%} = 1.04 H_{m0}\sqrt{\frac{T_{m-1,0}}{T_{m0,2}}}\sqrt{\xi_{m-1,0}}\sqrt{\exp(-Q_p)} + 0.095\sqrt{H_{m0}\lambda_{-1,0}} \tag{2.4}$$

where Q_p is the peakedness of a wave spectrum, defined as $Q_p = \frac{2}{m_0^2}\int f S_f^2 df$, S_f is the one-dimensional frequency-energy density spectrum, f is the frequency and the subscripts 0, -1 and 2 refer to spectral wave periods, wave height, Iribarren parameter and wave length based on the the zeroth, first negative and second positive order moments of the energy density spectrum, m_0, m_{-1} and m_2, respectively. While good results were found for mixed sand-gravel beaches, the wave run-up equation of Polidoro et al. (2013) has not yet been applied to, or validated for, steep, pure gravel beaches.

Some of the earliest empirical models to describe the cross-shore profile changes on gravel beaches under varying wave and surge forcing were developed in the Netherlands (Van Hijum, 1974, 1976; Van Hijum and Pilarczyk, 1982; Pilarczyk and Den Boer, 1983; Van der Meer and Pilarczyk, 1986; Van der Meer, 1988) and tested in the USA (Ahrens, 1990). However, work by Powell (1990) is regarded in the UK as the standard empirical model to compute cross-shore profile change on gravel beaches (DEFRA, 2008). This model (SHINGLE) describes the cross-shore profile between the horizontal position p_c and vertical position h_c of the beach crest and the SWL shoreline, the SWL shoreline and the horizontal position p_t and vertical position h_t of the top of the step, and the top of the step to the horizontal position p_b and vertical position h_b of the lower limit of profile deformations using three curves

(profile descriptors, Figure 2.3). The position of these curves with respect to the SWL shoreline is described using three non-dimensional parameters: ratio of wave height to sediment size, the ratio of wave power to sediment size, and the wave steepness:

$$\frac{p_c D_{50}}{H_s \lambda_m} = -0.23 \left(\frac{H_s T_m \sqrt{g}}{D_{50}^{1.5}} \right)^{-0.588} \qquad 0.01 \leq \frac{H_s}{\lambda_m} \leq 0.06 \tag{2.5a}$$

$$\frac{h_c}{H_s} = 2.86 - 62.69 \frac{H_s}{\lambda_m} + 443.29 \frac{H_s^2}{\lambda_m^2} \qquad 0.01 \leq \frac{H_s}{\lambda_m} \leq 0.06 \tag{2.5b}$$

$$\frac{p_t D_{50}}{H_s \lambda_m} = 1.73 \left(\frac{H_s T_m \sqrt{g}}{D_{50}^{1.5}} \right)^{-0.81} \qquad 0.01 \leq \frac{H_s}{\lambda_m} < 0.03 \tag{2.5c}$$

$$\frac{p_t}{D_{50}} = 55.26 + 41.24 \frac{H_s^2}{\lambda_m D_{50}} + 4.90 \left(\frac{H_s^2}{\lambda_m D_{50}} \right)^2 \qquad 0.03 \leq \frac{H_s}{\lambda_m} \leq 0.06 \tag{2.5d}$$

$$\frac{h_t}{H_s} = -1.12 + 0.65 \frac{H_s^2}{\lambda_m D_{50}} - 0.11 \left(\frac{H_s^2}{\lambda_m D_{50}} \right)^2 \qquad 0.01 \leq \frac{H_s}{\lambda_m} < 0.03 \tag{2.5e}$$

$$\frac{h_t}{D_{50}} = -10.41 - 0.025 \frac{H_s^2}{\sqrt{\lambda_m} D_{50}^{1.5}} - 7.5 \cdot 10^5 \left(\frac{H_s^2}{\sqrt{\lambda_m} D_{50}^{1.5}} \right)^2 \qquad 0.03 \leq \frac{H_s}{\lambda_m} \leq 0.06 \tag{2.5f}$$

$$\frac{p_b}{D_{50}} = 28.77 \left(\frac{H_s}{D_{50}} \right)^{0.92} \qquad 0.01 \leq \frac{H_s}{\lambda_m} \leq 0.06 \tag{2.5g}$$

$$\frac{h_b}{\lambda_m} = -0.87 \left(\frac{H_s}{\lambda_m} \right)^{0.64} \qquad 0.01 \leq \frac{H_s}{\lambda_m} \leq 0.06 \tag{2.5h}$$

where D_{50} is the median grain diameter, T_m is the mean wave period, g is the gravitational acceleration constant and λ_m is the mean wave length. Equations 2.5a–2.5h were derived from scaled physical model test and later verified using data collected at four natural gravel beaches. The application of this empirical model is limited to conditions that are similar in terms of composition and hydrodynamic forcing to those modelled in the laboratory experiments of Powell (1990), which includes normally incident wave conditions and situations with no longshore sediment transport gradient. Further research using the empirical model has shown that the relations are not appropriate for very coarse gravel beaches and conditions with long period swell (Obhrai et al., 2008), bimodal wave conditions (Bradbury et al., 2011), or conditions where overwash may occur (e.g., Bradbury and Powell, 1992; Van Rijn and

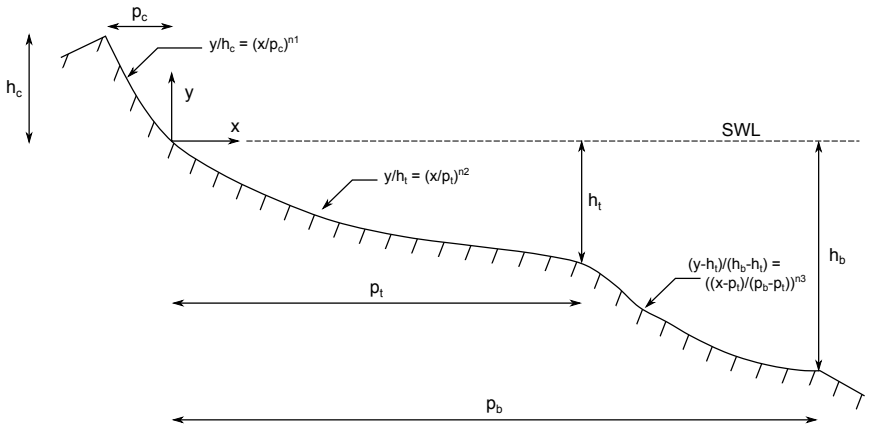

Figure 2.3: Schematised beach profile and profile descriptors in empirical model of Powell (1990)

Sutherland, 2011).

The transition from overtopping to overwash was studied by Matias et al. (2012) using data collected on one gravel barrier during the BARDEX physical model experiment (Williams et al., 2012a). In this work, potential wave run-up levels on the gravel barrier (e.g., in the case of a beach that extends sufficiently far to encompass all run-up motions) were computed using a large number of empirical run-up formulations and compared to measurements of wave overtopping. The result of this analysis showed good estimates for overtopping during the experiment using Equations 2.2 and 2.5b[4], with slightly better results for Equation 2.2. The authors subsequently found a threshold for overtopping and overwash, similar to the work of Sallenger (2000), based on the difference in potential wave run-up elevation and the elevation of the gravel barrier crest, defined as Overwash Potential (OP). While there is clear practical use for OP threshold relations, the results of Matias et al. are specific to the gravel barrier simulated in the BARDEX experiment and further research is currently required to generalise the results for application on other gravel barriers.

Bradbury (1998; 2000) developed an empirical threshold model for overwash on gravel barriers, called the Barrier Inertia Model (BIM). The BIM relates the potential for overwash on gravel beaches to the wave steepness of the incident waves $s_{m,0}$, and

[4]Note that this study approximated the maximum wave run-up level by the height of the beach crest, rather than the 2%-exceedence level in the empirical model of Powell (1990).

the dimensionless barrier inertia parameter I_b (cf. Orford et al., 1995), defined as:

$$s_{m,0} = \frac{H_s}{\lambda_{m,0}} \tag{2.6a}$$

$$I_b = \frac{h_{crest} A}{H_s^3} \tag{2.6b}$$

in which H_s is the significant wave height at the toe of the beach (m), which in the derivation of the BIM was measured in 6–8 m water depth (Bradbury, 2000), although also applied at 10–12 m water depth (Bradbury et al., 2005), $\lambda_{m,0} = \frac{gT_m^2}{2\pi}$ is the deep water wave length of the mean period wave measured at the toe of the beach (m), $h_{crest} = z_{crest} - \text{SWL}$ is the freeboard, or elevation of the barrier crest z_{crest} above SWL (m), and A is the cross sectional area of the barrier above SWL (m^2); see Figure 2.4 for schematic descriptions of these variables.

Through a series of physical model experiments based on conditions measured at Hurst Spit in the UK (Bradbury, 1998), as well as field data collected at Hurst Spit (Bradbury and Powell, 1992), Bradbury (2000) found that barrier overwash is unlikely to occur when:

$$I_b > 0.0006 s_{m,0}^{-2.54} \tag{2.7}$$

noting that lower values of I_b than this threshold value may not necessarily lead to overwash.

Although Bradbury (2000) validated the BIM using data collected at three other gravel beaches, the author stressed the importance of local calibration and limitations of the model. Later studies, including those by the original author of the model, have recognised that the BIM may under predict the potential for overwash under bimodal wave conditions (Bradbury et al., 2005, 2011), high wave steepness conditions (Obhrai et al., 2008) and on barriers that have a distinctly different geometry and shoreface to that of Hurst Spit (McCall et al., 2013). Despite these limitations, the BIM is commonly used in the UK and regarded as the most practical and advanced modelling tool available to coastal managers (Cope, 2005; DEFRA, 2008).

2.3.3 Process-based models

Whilst process-based models to compute the morphodynamics of sandy beaches have had a strong and diverse background in coastal research since the eighties of the last century (e.g., Stive and Battjes, 1984; Dally and Dean, 1986; Watanabe et al., 1986; Larson and Kraus, 1989), substantially fewer process-based models have been developed for gravel beaches, and almost none have been developed and validated for simulating the morphodynamic response of gravel beaches during storms. Those process-based models that are currently available can be divided into wave-resolving models, which tend to have a background in the study of man-made coastal engineering structures, and wave-averaged models, which are generally based on pre-existing

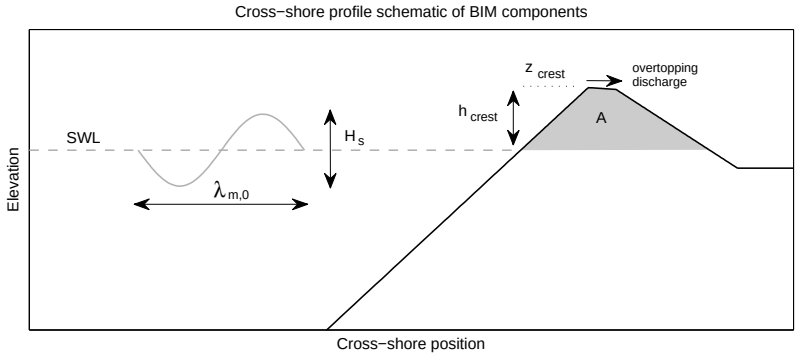

Figure 2.4: Schematic representation of the components of the BIM parametrisation of overwash.

morphodynamic models for sandy beaches.

Wave-resolving models based on the non-linear shallow water equations (NLSWE; e.g., Kobayashi et al., 1987; Wurjanto and Kobayashi, 1993 , and many others) and incompressible Navier-Stokes equations (e.g., Van der Meer et al., 1992; Petit et al., 1994 , and many others) have been primarily developed and applied for the study of hydraulic structures. Since such structures are generally designed not to deform under hydraulic loading, the focus of much of this work has been on computing hydrodynamics (wave run-up, penetration, reflection, overtopping, etc.), rather than morphodynamic response. However, due to the similarities between gravel beaches and hydraulic structures (e.g., steep and permeable slopes, relatively large grain size), as well as the prevalent use of gravel in scaled physical model experiments of coastal structures, there is evident appeal in using these models to simulate hydrodynamic processes on gravel beaches. It is unfortunate that very few (e.g., Clarke et al., 2004) have been validated for this task using data measured on natural gravel beaches.

Van Gent (1995a; 1995b; 1996) presented the first promising process-based model for the morphodynamic simulation of storm impacts on gravel beaches. This model computes the cross-shore, depth-averaged intra-wave flow of the surface water, as well as the groundwater inside the porous beach or hydraulic structure, using the NLSWE modified for porous media. The morphodynamics of the beach are computed in a simplified manner by displacing particles on the bed in an upslope or downslope direction when a critical threshold for motion is exceeded. While principally designed for rubble-mound berm breakwater-type structures, the model was validated using hydrodynamic and morphodynamic data from physical model experiments using gravel and the morphological response of one berm breakwater to storm conditions. The results of the validation showed that the model is capable of simulating varying types of cross-shore profile response, from berm building to crest lowering. Although the model showed great potential, its application and further development was not widespread, potentially due to the large (at that time) computational effort required and

the depth limitation of model due to the use of the NLSWE[5].

One decade after the work of Van Gent, Pedrozo-Acuña et al. (2006) and Pedrozo-Acuña et al. (2007) applied an existing Boussinesq wave model (COULWAVE; Lynett et al., 2002) to gravel beaches through incorporation of a modified version of the Meyer-Peter and Müller bed load transport equation (Meyer-Peter and Müller, 1948; Madsen et al., 1997; Calantoni et al., 2004) to compute morphological change. The model results were compared to cross-shore profile change (berm building) measured in a large-scale physical model experiment (López de San Román-Blanco et al., 2006) under mildly energetic forcing conditions. Although the model did not include groundwater processes, the model was found to reproduce the berm-building conditions observed in physical model experiment relatively well if the sediment friction factor in the uprush was increased with respect to that of the backwash. Groundwater processes, as well as the effects of acceleration in the swash and sediment fluidization under plunging breakers were hypothesized to cause the apparent difference in the sediment friction factor. The model was not applied to investigate more energetic morphological response stages (e.g., beach erosion – barrier rollover, Figure 2.2) and its validity as a storm-impact model is therefore unknown.

Horn and Li (2006) applied the BeachWin model (Li et al., 2002) to simulate observed morphological change over one tide at Slapton Sands (UK). The BeachWin model computes depth-average surface water motions by means of the NLSWE and groundwater flow using a two-dimensional cross-shore (2DV) model for groundwater pressure and Darcy's law (1856). Sediment transport is computed in the model using a modification of Bagnold's (1966) transport relation by Hardisty et al. (1984). While the model represented the growth of a beach berm relatively well and the model highlighted the importance of groundwater interactions on the morphological development of the berm (cf. Masselink and Li, 2001), the model was unable to reproduce the cross-shore profile change lower on the beach. The model was furthermore found to be very sensitive to the imposed friction factor, the imposed hydraulic conductivity and the ratio between the uprush and downwash sediment friction factor (cf. Pedrozo-Acuña et al., 2006) and further research on these processes and model parameters was recommended.

Other process-based models for gravel beaches have been based on wave-averaged approaches to modelling flow and sediment transport. Such types of model have frequently been used to simulate storm impact on dissipative sandy coasts (e.g., Larson and Kraus, 1989; Steetzel, 1990; Leont'yev, 1996; Roelvink et al., 2009; Van Rijn, 2009; Johnson and Grzegorzewski, 2011), where infragravity waves dominate the nearshore area and the incident-band wave motions can be parametrised without substantial loss of physical accuracy. The application of this type of model on gravel beaches, where the incident-band waves and their interactions remain dominant throughout the morphologically active zone is debatable and requires additional parametrisation of incident-band swash motions and sediment transport compared to

[5]The porous-flow model of Van Gent (1995b) was later coupled to a Boussinesq-type wave model to overcome the depth-limitation of the NLSWE in the original by Karambas (2003), but was never applied or developed further to simulate the morphodynamics of gravel beaches or berm breakwaters.

sandy-coast models.

One of the first attempts to model gravel beach morphodynamics using a wave-averaged approach was made by Hicks et al. (2010) through modification of the bed load sediment transport formulation in the CSHORE model (Kobayashi and Johnson, 1998; Kobayashi et al., 2007). The model did not address specific issues relating to swash-zone processes, or groundwater interactions, but did show reasonable similarity with the berm-building behaviour of the gravel beach in a scaled physical model experiment used to calibrate and validate the model. Subsequent work by Kobayashi et al. (2011) suggested that further research and more validation data would be required to develop the model for practical application.

Van Rijn and Sutherland (2011) applied the wave-averaged CROSMOR model (Van Rijn et al., 2007) to simulate berm-building observed during a gravel beach physical model experiment (Van der Meer, 1989) and hypothetical storms at Pevensey Bay, East Sussex, UK. The model does not include groundwater processes, or explicitly include the incident-band and infragravity-band wave run-up, which instead are incorporated through parametrization and extrapolation of the sediment transport rate at the shoreline. After calibration, the model appeared qualitatively to show more realistic cross-shore profile change compared to the empirical model of Powell (1990). Given the limited data used to calibrate and validate the model, as well as the sensitivity of the model to calibration parameters related to sediment transport in the swash zone, it is not yet clear to what extent the model is applicable in a predictive capacity.

Williams et al. (2012b) and Jamal et al. (2014) applied two modified versions of the wave-averaged XBeach model (Roelvink et al., 2009) to simulate the morphodynamic response of gravel beaches during overwash and berm-building conditions, respectively. Both studies used a so-called surf-beat model approach to simulate the wave energy in incident wave-groups (i.e., short-wave wave averaged, but modulating at the wave-group time-scale) and to explicitly model infragravity wave motions, which are generally considered less important on steep gravel beaches than on dissipative sandy beaches (Section 2.2). Both Williams et al. (2012b) and Jamal et al. (2014) incorporated the effect of infiltration in the swash through a one-dimensional groundwater model based on Darcy's law (1856; cf. McCall and Van Thiel de Vries 2010) , and a Packwood-type (1983) infiltration model, respectively, and found the permeability of the gravel beach to be important in the simulation of morphological change. While neither XBeach model explicitly computed the incident-band swash, Williams et al. (2012b) found through sensitivity analysis that the surf-beat type approach was sufficient to simulate overwash dynamics reasonably well, whereas Jamal et al. (2014) found that additional modification of the bed return flow was required to reduce the dominantly offshore-directed sediment transport in the surf-zone and swash. Both models were reasonable successful in reproducing observed cross-shore profile change observed in physical model experiments, and both models were applied to simulate the morphodynamic response of a natural gravel beach, where the results of Jamal et al. (2014) were compared to measurements, and the model of Williams et al. (2012b) was used to simulate hypothetical storms. Unfortunately, despite the fact that both models were based on XBeach, the implementation of groundwater, swash-zone and sediment transport processes differed between the studies. Furthermore, neither

model was applied to simulate any other morphological response stage (Figure 2.2) than it was calibrated for, thereby leaving the applicability of XBeach as a general storm impact model for gravel beaches open to discussion.

While clearly not a morphodynamic storm impact model in the sense of those discussed above, the STRAND model (Van Wellen, 1999; Van Wellen et al., 2000a) presents an interesting hybrid model to compute longshore sediment transport on gravel beaches, in which wave transformation between offshore and the start of the swash are modelled in a wave-averaged manner, and swash-zone dynamics are explicitly estimated using a ballistics-type approach. The longshore sediment transport rate predictions of the model were shown to correspond well with laboratory data (Kamphuis, 1991). The incorporation of such information in cross-shore profile models may be expected to substantially improve the predictions of profile change during storms in cases of large longshore sediment transport gradients.

2.4 Conclusions

The review of physical processes on gravel beaches and existing conceptual, empirical and process-based models for gravel beaches presented in this chapter shows that there is a clear gap between the knowledge of physical processes that may affect gravel beach morphology (e.g., interaction between surface water and groundwater, swash-swash interaction) and the use of this knowledge in process-based numerical models and universally applicable empirical models. Furthermore, the review of existing models has shown that most empirical (e.g., Van Hijum, 1974; Van Hijum and Pilarczyk, 1982; Van der Meer, 1988; Powell, 1990) and process-based (e.g., Pedrozo-Acuña et al., 2006, 2007; Hicks et al., 2010; Jamal et al., 2014) models have been developed and validated using data from physical model experiments in which the morphodynamic response was limited to change on the beach face (e.g., berm-building and beach erosion in Figure 2.2) and exhibited substantial deposition at the upper-swash limit. While the characterisation and description of this type of response is interesting from a scientific standpoint, it can be suggested that it is less relevant for storm-impact models from the point of view of flood-safety (cf., measured gravel beach response in Chapter 5 of this thesis). Furthermore, we may speculate that the use of these datasets alone for the development and validation of models is a source of model inaccuracies (e.g., the ever-present berm-building response in the empirical model of Powell, 1990) and moot model parametrisations (e.g., parametrisation of swash hydrodynamics in the models of Van Rijn and Sutherland, 2011, Williams et al., 2012b and Jamal et al., 2014). These considerations support the statement of Chapter 1 that there is a need for a universal process-based gravel beach storm impact model that is founded on physical principles and validated with a wide-ranging measurement data.

Chapter 3

Hydrodynamics of XBeach-G

This chapter discusses and validates the hydrodynamic component of XBeach-G for energetic and storm conditions on gravel beaches and barriers. The model makes use of a non-hydrostatic pressure correction term, previously developed for sandy beaches, that allows wave-by-wave modelling of the surface elevation and depth-averaged flow. Since the morphodynamic component of XBeach-G has not yet been developed, all simulations in this chapter are carried out without morphodynamic feedback. Modelled hydrodynamics are validated using data collected during a large-scale physical model experiment and detailed in-situ field data collected at Loe Bar, Cornwall, UK, as well as remote-sensed data collected at four gravel beach locations along the UK coast during the 2012–2013 and 2013–2014 storm seasons. Validation results show that the model has good skill in predicting wave transformation, run-up levels and initial wave overtopping, indicating that the model can be applied to estimate potential storm impact on gravel beaches. The inclusion of the non-hydrostatic pressure correction term to model intrawave motion is shown to be essential to predict wave run-up and overtopping events.

3.1 Introduction

The importance of the incident wave band over the infragravity band on swash dynamics on gravel beaches is acknowledged in Chapter 2. In this chapter, the effect of the incident band in modelling hydrodynamics on gravel beaches under energetic and storm conditions is investigated using the XBeach-G model. To this end, this chapter evaluates and validates a one-layer, depth-averaged, non-hydrostatic extension to the XBeach model that was developed prior to this thesis by Smit et al. (2010), which allows XBeach-G to solve wave-by-wave flow and surface elevation variations due to short waves in intermediate and shallow water depths. The non-hydrostatic extension of XBeach is similar to the SWASH model (Zijlema et al., 2011b; Smit et al., 2013), but has previously only been validated for use on dissipative sandy beaches (Smit et al., 2010) and has not previously been applied on, or validated for, steep, reflective beaches.

In this thesis, the non-hydrostatic extension of XBeach developed by Smit et al. (2010) is analysed for application on gravel beaches as part of the XBeach-G model. In particular, this chapter validates the hydrodynamics of XBeach-G, including the non-hydrostatic extension, using data collected during a large-scale physical model experiment (BARDEX; Williams et al., 2012a) and detailed in-situ field data collected at Loe Bar, Cornwall, UK (Poate et al., 2013, 2014), as well as remote-sensed data collected at three other gravel beach locations along the UK coast during the 2012–2013 and 2013–2014 storm seasons.

Sections of this chapter are based on work presented in McCall et al. (2014) and Masselink et al. (2014).

To correctly account for upper swash infiltration losses and exfiltration effects on lower swash hydrodynamics on gravel beaches the surface water model of XBeach-G is coupled to and exchanges water fluxes with a groundwater model, which is discussed and validated in Chapter 4. Since the morphodynamic component of XBeach-G has not yet been developed at this stage of the research, validation is carried out using a fixed bed.

This chapter will first address the central model equations of the XBeach-G surface water model (Section 3.2) and discuss the data used for model validation (Section 3.3). The model is validated for wave transformation, wave set-up, wave run-up and wave overtopping in Section 3.4 using the data described above. Finally, Section 3.6 discusses the importance of the incident band on wave run-up and overtopping predictions, as well as the consequences of the fixed bed approximation used in this chapter.

3.2 Model description

This section describes the central equations of the surface water model of XBeach-G. Although the surface water model can be applied in two-dimensional horizontal (2DH) simulations, in this thesis the description of the equations and application of the model is restricted to their one-dimensional cross-shore (1D) equivalent. Further details regarding the non-hydrostatic extension to XBeach which is used in XBeach-G is given by Smit et al. (2010).

3.2.1 Model coordinate system and grid

XBeach-G uses a coordinate system where the computational x-axis is orientated in the cross-shore direction, positive towards the coast, and a staggered grid system in which bed levels, surface water levels, groundwater levels, dynamic pressure, groundwater head and vertical fluxes are defined in cell centres, and horizontal fluxes are defined at cell interfaces. The computational grid can be rectilinear, non-equidistant in 1D applications, and curvilinear in 2DH applications (Roelvink et al., 2012). Since incident-band wave motions are resolved explicitly in the XBeach-G model, the grid resolution for an XBeach-G model is higher than for a regular XBeach model in which wave motions are computed on the wave group scale. In a 1D application of XBeach-G, this increase in model resolution leads to approximately 2–3 times greater computation times than a coarser resolution 1D XBeach model. The simulations presented in this thesis have a simulation to computation time ratio of approximately 1:1 – 5:1 on a standard desktop PC.

The surface water dynamics are computed using one layer in the vertical, and are therefore depth-averaged. However, in order to approximate the non-hydrostatic pressure distribution, a quasi-three-dimensional (Q3D) model is used to compute vertical velocities and pressures at the surface and bottom of the surface water layers. Surface water flow is solved using a limited MacCormack (1969) predictor-corrector scheme that is second-order accurate in areas where the solution is smooth, and first-order accurate near discontinuities (Smit et al., 2010). The scheme is mass and momentum conserving following Stelling and Duinmeijer (2003), allowing for the correct representation of drying and flooding, as well as supercritical flows and bore-like features.

3.2.2 Governing equations

Depth-averaged flow due to waves and currents are computed using the non-linear shallow water equations (NLSWE), including a non-hydrostatic pressure term and a source term for exchange with the groundwater:

$$\frac{\partial \zeta}{\partial t} + \frac{\partial hu}{\partial x} + S = 0 \tag{3.1}$$

$$\frac{\partial u}{\partial t} + u\frac{\partial u}{\partial x} - \frac{\partial}{\partial x}\left(\nu_h \frac{\partial u}{\partial x}\right) = -\frac{1}{\rho}\frac{\partial \left(\rho \bar{q} + \rho g \zeta\right)}{\partial x} - \frac{\tau_b}{\rho h} \tag{3.2}$$

where x and t are the horizontal spatial and temporal coordinates respectively, ζ is the free surface elevation above an arbitrary horizontal plane, u is the depth-average cross-shore velocity, h is the total water depth, S is the surface water-groundwater exchange flux (discussed in Chapter 4), ν_h is the horizontal viscosity, ρ is the density of water, $\bar{q}$ is the depth-averaged dynamic pressure normalized by the density, g is the gravitational constant and τ_b is the bed shear stress (discussed in Chapter 5). Note that the exchange of horizontal momentum between the surface water and groundwater layer is assumed negligible.

The horizontal viscosity (ν_h) is computed using the Smagorinsky (1963) model to account for the exchange of horizontal momentum at spatial scales smaller than the computational grid size, which under assumption of longshore uniformity in flow and absence of longshore current is given as:

$$\nu_h = 2\left(c_s \Delta x\right)^2 \sqrt{2\left(\frac{\delta u}{\delta x}\right)^2} \tag{3.3}$$

where c_S is the Smagorinsky constant, set at 0.1 in all model simulations and Δx is the computational grid size.

The depth-averaged normalized dynamic pressure ($\bar{q}$) is derived in a method similar to a one-layer version of the SWASH model (Zijlema et al., 2011b), in which the depth-averaged dynamic pressure is computed from the mean of the dynamic pressure at the surface and at the bed, assuming the dynamic pressure at the surface to be zero. In order to compute the normalized dynamic pressure at the bed, the contributions of advective and diffusive terms to the vertical momentum balance are assumed to be negligible:

$$\frac{\partial w}{\partial t} + \frac{\partial q}{\partial z} = 0 \tag{3.4}$$

where w is the vertical velocity and z is the vertical coordinate.

The vertical velocity at the bed is set by the kinematic boundary condition:

$$w_b = u\frac{\partial \xi}{\partial x} \tag{3.5}$$

where $\xi = \zeta - h$ is the elevation of the bed and the subscript b refers to the location at the bed.

Combining the Keller-box method (Lam and Simpson, 1976) as applied by Stelling and Zijlema (2003) for the description of the pressure gradient in the vertical, the dynamic pressure at the bed can be described by:

$$q_b = -\frac{h}{2}\left(\left.\frac{\partial q}{\partial z}\right|_s + \left.\frac{\partial q}{\partial z}\right|_b\right) \tag{3.6}$$

Substituting Equation 3.4 in Equation 3.6 allows the vertical momentum balance at the surface to be described by:

$$\frac{\partial w_s}{\partial t} = 2\frac{q_b}{h} - \frac{\partial w_b}{\partial t} \tag{3.7}$$

where the subscript s refers to the location at the surface. The dynamic pressure at the bed is subsequently solved by combining Equation 3.7 and the local continuity equation:

$$\frac{\partial u}{\partial x} + \frac{w_s - w_b}{h} = 0 \tag{3.8}$$

Smit et al. (2010) have shown that the inclusion of the dynamic pressure described above reduces the relative dispersion and celerity errors in the non-linear shallow water equations of XBeach to less than 5% for values of $kh \leq 2.5$, where k is the wave number, and allows for accurate modelling of wave transformation on dissipative beaches. In order to improve the computed location and magnitude of wave breaking, XBeach-G applies the hydrostatic front approximation (HFA) of Smit et al. (2013), in which the pressure distribution under breaking bores is assumed to be hydrostatic. Following the recommendations of Smit et al. (2013), waves are considered to be hydrostatic bores where $\frac{\partial \zeta}{\partial t} > 0.6$ and to reform if $\frac{\partial \zeta}{\partial t} < 0.3$. Although this method greatly oversimplifies the complex hydrodynamics of plunging waves on gravel beaches, validation in this chapter will show that the application of this model provides sufficient skill to describe dominant characteristics of the flow, without requiring computationally-expensive high-resolution discretisation of the vertical and surface tracking of overturning waves.

It should be noted that the manner of simulating wave breaking in the non-hydrostatic extension of the NLSWE described above does not introduce a separate roller model to evaluate the fate of surface rollers, as common in many Boussinesq-type wave models (e.g., Cienfuegos et al., 2010). Instead, Zijlema et al. (2011a; 2011b) argue that the effect of the surface rollers can be adequately incorporated in the

non-hydrostatic flow equations through strict adherence to the depth-averaged momentum equations. Simulation of wave breaking on dissipative beaches using the non-hydrostatic wave model SWASH (Smit et al., 2013, 2014) appears to support this conclusion. Although further discussion on the computation of surface rollers in non-hydrostatic wave models may lead to greater insights and new modelling approaches, it may be assumed that surface rollers are unlikely to play a large role in the narrow breaker zone of steep gravel beaches and are therefore less relevant to the modelling of storm impacts on gravel coasts.

3.3 Field and laboratory measurement data

The data used in this chapter to set-up and validate the surface water model of XBeach-G model have been collected during the BARDEX large-scale physical model experiment in the Deltaflume, The Netherlands, and at four gravel beach locations along the coast of the UK (Figures 3.1 and 3.2).

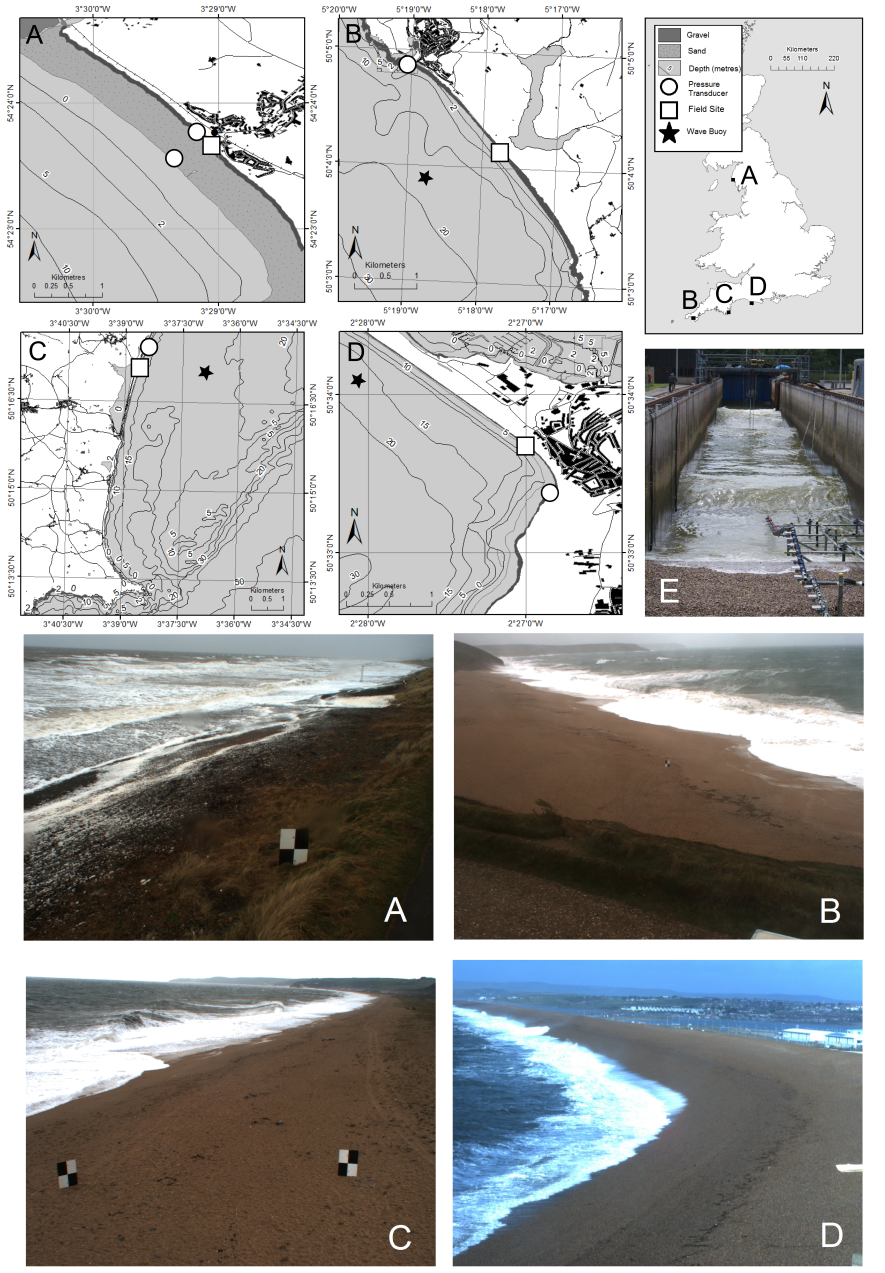

Figure 3.1: Location and overview photos of field data collection sites: (A) Seascale, (B) Loe Bar, (C) Slapton Sands and (D) Chesil Beach, and overview photo of the BARDEX-experiment in the Delta Flume, The Netherlands (E). Note that the location of the wave buoys at Chesil Beach and Seascale are beyond the extent of maps A and D. In the case of Chesil Beach, the wave buoy has been depicted at the correct water depth, closer to the field location.

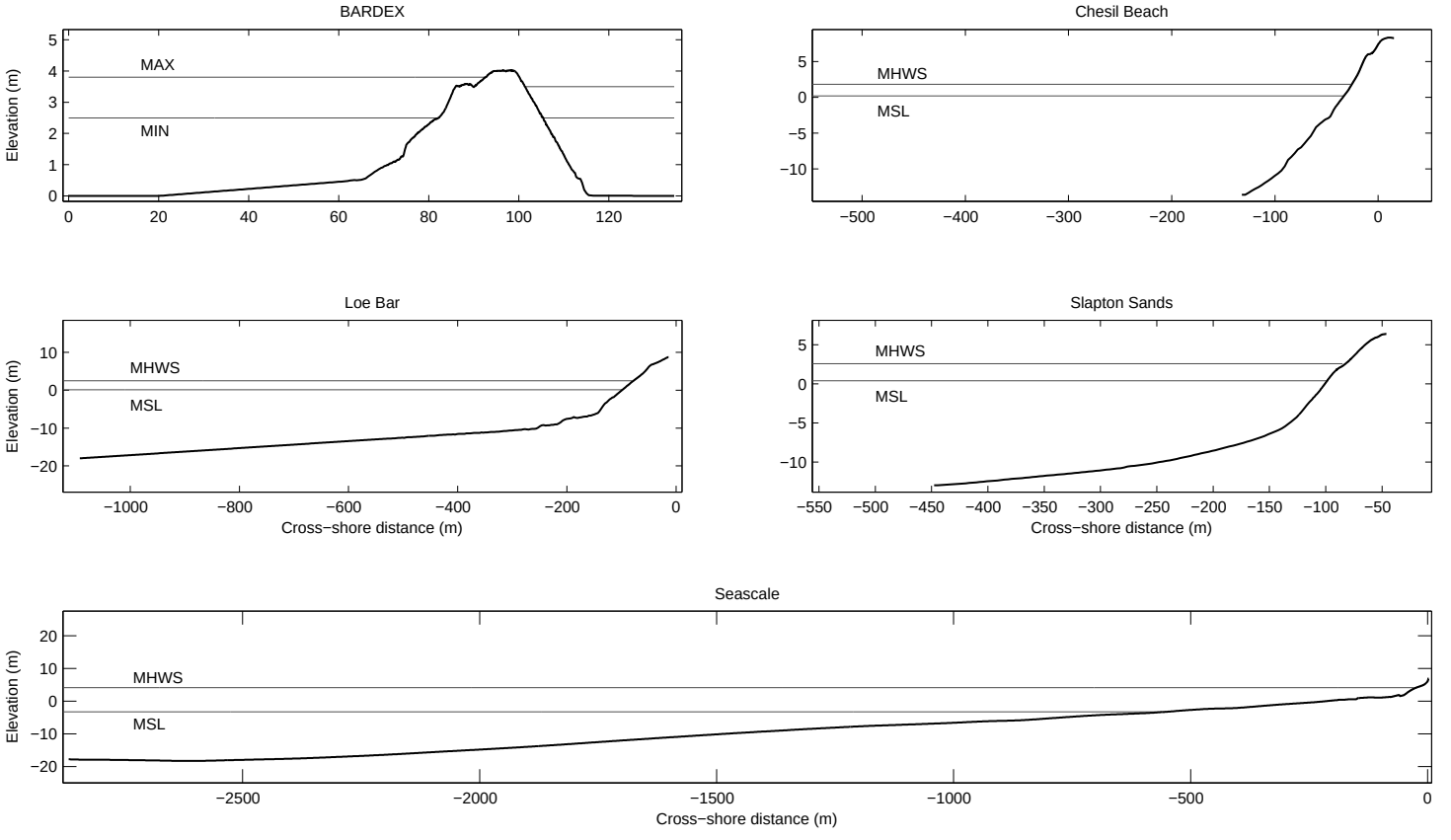

Figure 3.2: Representative cross-shore profiles (—) and water levels (—) at each of the validation sites. Note that although the cross-shore profiles of the models have different vertical and horizontal extents, the aspect ratio is the same in all plots.

During the BARDEX physical-model experiment, the hydrodynamics and morphodynamics of a 4 m high and 50 m wide gravel barrier were measured under varying hydraulic boundary conditions, ranging from wave run-up to wave overtopping and overwash (see Williams et al., 2012a for details). The morphodynamic response of the gravel barrier was measured by a mechanical roller and actuator following the bed profile from an overhead carriage before and after each 5–20-minute wave sequence. Wave transformation across the foreshore was measured using three wave gauges located c. 40 meters offshore of the beach and one nearshore pressure transducer (PT) near the toe of the gravel beach. Wave run-up and overtopping levels were measured using a cross-shore array of 45 acoustic bed level sensors (BLS; cf. Turner et al., 2008) that spanned the entire subaerial portion of the gravel barrier.

Poate et al. (2013) collected in-situ and remote-sensed hydrodynamic and morphodynamic data on a fine gravel barrier (Loe Bar, Cornwall, UK) over a period of four weeks. Two energetic events occurred during this period on 8 March 2012 (LB1) and 24 March 2012 (LB2) with offshore significant wave heights of 1.6–2.3 m. Offshore wave conditions were measured by a directional wave buoy in 15–20 m water depth maintained by the Channel Coastal Observatory (CCO). Tide and surge levels were measured by a PT located in Porthleven harbour, approximately 2 km from the field site (Figure 3.1, Site B). Wave transformation across the beach face was measured by a cross-shore array of five PTs, as shown in Figure 3.3. Wave run-up time series were extracted from water level and bed level data collected by a cross-shore array of 45 BLS that spanned the beach face from mean high water spring (MHWS) level to the barrier crest. Bed levels along the main instrument cross-shore transect were measured every low tide using Real Time Kinematic Global Positioning System (RTK-GPS). During wave event LB2, high-frequency (2 Hz) and horizontal resolution (0.05–0.20 m) bed level and water level data were collected continuously by a tower-mounted cross-shore laser scanner (cf. Almeida et al., 2013). Bathymetric data below the elevation of RTK-GPS surveys were collected by singlebeam echosounder survey in March 2012.

Wave run-up data were collected during storm conditions in the winter of 2012–2013 and 2013–2014 at three gravel beaches along the coast of the UK (Loe Bar, Slapton Sands and Chesil Beach) and one composite beach with a gravel upper beach fronted by a sandy low-tide terrace (Seascale). At Loe Bar and Slapton Sands, offshore wave data were provided by directional wave buoys maintained by CCO, located approximately 500 m from the study site in 15–20 m and 10–15 m water depth, respectively. At Chesil Beach offshore wave data were provided by a directional wave buoy maintained by CCO, located approximately 7 km from the study site in 12–15 m water depth. Wave data at Seascale were obtained from an offshore wave buoy maintained by the Centre for Environment, Fisheries & Aquaculture Science (CEFAS), located 50 km from the study site in 20 m water depth, supplemented by a nearshore PT in 0–4 m water depth (depending on tide), which is used to scale the offshore wave height to account for offshore wave refraction and sheltering. Tide and surge data at Chesil Beach, Loe Bar, Slapton Sands and Seascale in the 2012–2013 winter season, as well as tide and surge data for Slapton Sands in the 2013–2014 winter season were provided by PTs located approximately 500 m, 2 km, 1 km and 500 m from the main instrument transect lines, respectively (Figure 3.1). Tide and surge data for

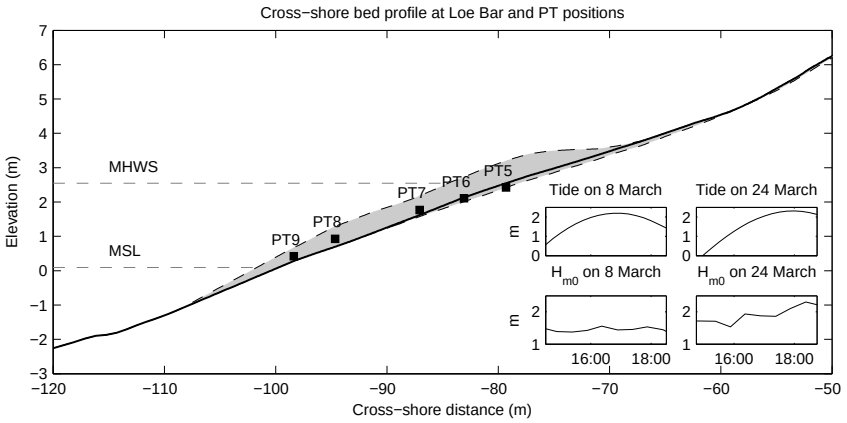

Figure 3.3: Overview of the location of five pressure transducers at Loe Bar relative to the cross-shore bed profile during the low tide prior to the LB2 wave event (—), the envelope of bed level change during LB2 derived from laser data ( ) and representative water levels for Loe Bar (– –). Data measured and modelled at PT5–PT9 are shown in Figures 3.5, 3.6, 3.7, 3.8, 3.9 and 3.15 and Table 3.2. Subplots in the lower right-hand corner show time series of the tidal water level and offshore wave height during LB1 (8 March) and LB2 (24 March).

Chesil Beach and Loe Bar for the 2013–2014 winter season were derived from tidal predictions, supplemented with measured surge time series at the nearest operational tide gauges at West Bay Harbour (30 km from Chesil Beach) and Newlyn (20 km from Loe Bar). The morphology of the four beaches was measured every low tide along cross-shore transects by RTK-GPS survey. Bathymetric data at Chesil Beach and Slapton sands below the elevation of the RTK-GPS surveys are derived from hydrographic multibeam survey data provided by CCO and collected in 2009 and 2007, respectively. At all four gravel beach field sites, shoreline position time series were extracted along 4–6 cross-shore transects from digital video camera pixel time stacks collected at 3.75Hz, following the method described by Poate et al. (2013). Pre- and post-event bed levels were measured using RTK-GPS at all four locations.

A summary of the measured, or estimated, median grain diameter D_{50}, hydraulic conductivity K and beach slope $\tan\beta_b$ at all four gravel beach field sites and the BARDEX experiment, as well as a summary of the instruments used to collect hydrodynamic and morphodynamic data presented in this chapter, is given in Table 3.1. The table furthermore lists the maximum hydrodynamic forcing conditions (offshore significant wave height H_{m0}, peak wave period T_p, relative freeboard (R_c/H_{m0}) and wave angle relative to shore normal θ_{rel}) during each of the storm events discussed in this chapter, and an overview of the use of the measurement data in the validation of the XBeach-G model.

Beach characteristics					Data collection		Storm simulation		Hydrodynamic forcing conditions				Model-data comparison			
Location	Sediment type	D_{50} (mm)	K (mms^{-1})	$\tan\beta_b$	Hydrodynamics	Morphology	Simulations	Date	H_{m0} (m)	T_p (s)	R_c/H_{m0}	θ_{rel} (°)	T	S	R	O
BARDEX[a,b]	Medium gravel	11	155	0.19	Surface PTs, BLS	Profiler	BAE10	29 Jul. 2008	0.8	7.7	0.7	0	x			x
							BAE9	28 Jul. 2008	0.8	7.7	0.8	0	x			x
							BAC2	30 Jun. 2008	0.7	4.3	2.0	0	x		x	
							BAC1	1 Jul. 2008	0.7	4.5	2.0	0	x		x	
							BABB1	27 Jun. 2008	0.7	4.3	2.0	0	x		x	
Loe Bar[c,d]	Very fine gravel	2	3[§]	0.12	Surface PTs, BLS, Video	RTK-GPS, laser	LB1	8 Mar. 2012	1.6	20.0	4.3	15	x	x	x	
							LB2	24 Mar. 2012	2.3	12.5	2.8	6	x	x	x	
							LB3	21–23 Nov. 2012	5.3	11.1	1.0	13			x	
							LB4	31 Jan. – 01 Feb. 2014	4.9	16.7	1.2	14			x	
Chesil Beach[e]	Very coarse gravel	20	400	0.20	Video	RTK-GPS	CB1	15–17 Dec. 2012	2.6	10.0	2.7	5			x	
							CB2	5–7 Feb. 2014	7.7	16.7	1.2	12			x	
Slapton Sands[f,g]	Fine gravel	6	75	0.15	Video	RTK-GPS	SS1	21 Feb. 2013	2.9	7.7	2.0	27			x	
							SS2	21 Oct. 2013	1.6	6.9	3.6	30			x	
Seascale	Mixed-sand-gravel	10[†]	50[†]	0.09[†]	Video	RTK-GPS	SE	27 Jun. 2008	2.3	8.3	1.5[‡]	10			x	

Table 3.1: Overview of beach characteristics and data collection instrumentation at each of the gravel beach sites and maximum hydrodynamic forcing conditions and model-data comparisons for each of the storm events. In model-data comparison, measurement data are used to validate wave transformation (T), set-up (S), run-up (R) and overtopping (O). Beach type is classified according to the Wentworth scale and gravel beach classification of Jennings and Shulmeister (2002). Literature referenced in this table are: a)Williams et al. (2012a), b) Turner and Masselink (2012), c) Poate et al. (2013), d) Poate et al. (2014), e) Heijne and West (1991), e) Austin et al. (2013), f) Austin (2005). In the case of Loe Bar [§]was determined for the beach face by in-situ falling head tests, and at Seascale, [†] is estimated for the gravel section of the beach and [‡]is relative to top of gravel beach.

3.4 Model setup and validation

This section describes the comparison of the model simulation data and data collected during the BARDEX experiment and the field measurements at the four UK gravel beaches. The model results are split into four categories: (1) wave transformation, (2) wave set-up, (3) wave run-up, and (4) wave overtopping. For comparison with the measurements, cross-shore transect models are set up in XBeach-G for all five gravel beaches (BARDEX, Loe Bar, Chesil Beach, Slapton Sands and Seascale). In each model, the bed level is set to the bed level measured along the main instrument array (for Loe Bar simulations LB1 and LB2, and BARDEX), or along the main cross-shore video image pixel time stack transect (for Loe Bar simulation LB3 and LB4, Slapton Sands, Chesil Beach and Seascale) for the low tide prior to the storm event. The models for Loe Bar, Chesil Beach, Slapton Sands and Seascale are forced using wave spectra measured at the nearest wave buoy, described in the previous section, and measured tide and surge levels. The XBeach-G model uses the input wave spectrum to generate a random time series of incident waves and bound low-frequency second order waves at the model boundary. In the BARDEX simulations, the incident wave elevation time series that was measured by the Delta Flume wave generator (cross-shore position 0 m) are used with linear wave theory and bound higher and lower harmonics to generate the time series of incident depth-averaged velocity. The total incident signal is scaled by up to 15% to ensure the modeled wave energy at the center wave gauge (cross-shore location 41 m) matches the measured wave energy at that location. The lagoon boundary is forced using measured water levels only. Wave-absorbing boundary conditions are imposed in all simulations at the offshore and bay-side boundary to minimize reflection of waves at the model boundaries. The hydraulic conductivity of the beach used by the groundwater component of the XBeach-G model and grain size properties are derived from in-situ measurements, literature or estimates (Table 3.1).

The cross-shore resolution of the models is set to vary gradually in the cross-shore direction, from $\frac{\lambda_m}{25} \approx$2–3 m at the offshore boundary of the model, where λ_m is the wave length related to the mean wave period, to $\sim$0.1 m near the waterline in order to correctly capture wave breaking and wave run-up in the model. In the case of the BARDEX simulations, the resolution has been increased to 0.25 m at the wave generator and 0.05 m at the beach.

Since not all types of measurement data are available at all five beaches, the validation of the model results will be restricted to certain datasets, as outlined in Table 3.1. Multiple simulations are carried out at all five gravel beaches, representing periods of different wave or tidal forcing.

In the comparison of measurement data to model results, four statistical measures are used to assess the accuracy of the model results: (1) the root-mean-square error (RMSE; defined in Equation 3.9); (2) the bias (Equation 3.10); (3) the relative bias (b_{rel}; Equation 3.11; and (4) the Scatter Index (SCI; Equation 3.12).

$$RMSE(x) = \sqrt{\frac{1}{n}\sum_{i=1}^{n}\left(x_{i,modelled} - x_{i,measured}\right)^2} \tag{3.9}$$

$$bias(x) = \frac{1}{n}\sum_{i=1}^{n}\left(x_{i,modelled} - x_{i,measured}\right) \tag{3.10}$$

$$b_{rel}(x) = \frac{1}{n}\sum_{i=1}^{n}\left(\frac{x_{i,modelled} - x_{i,measured}}{|x_{i,measured}|}\right) \tag{3.11}$$

$$SCI(x) = \frac{RMSE(x)}{max\left(\frac{1}{n}\sum_{i=1}^{n} x_{i,measured}, \sqrt{\frac{1}{n}\sum_{i=1}^{n} x_{i,measured}^2}\right)} \tag{3.12}$$

3.4.1 Wave transformation

Wave transformation from offshore to the gravel barrier toe and the lower swash is compared in the model to data collected during the BARDEX experiment and to data collected at Loe Bar. In the BARDEX experiment, surface water pressure was measured by a shallow water PT near the toe of the barrier (bottom panels in Figure 3.4). In this analysis, we convert the pressure measurements at the toe of the barrier to surface elevation time series using the local approximation method of Nielsen (1986). XBeach-G is used to simulate the wave transformation during five measurement series of the BARDEX experiment, categorised into two different characteristic wave periods (BABB1–BAC2 and BAE9–BAE10; Table 3.1). In these simulations, the model is forced at the offshore boundary using time series of the water surface elevation imposed at the wave-maker and an estimate of the incident intra-wave depth-average cross-shore velocity at the boundary based on linear wave theory.

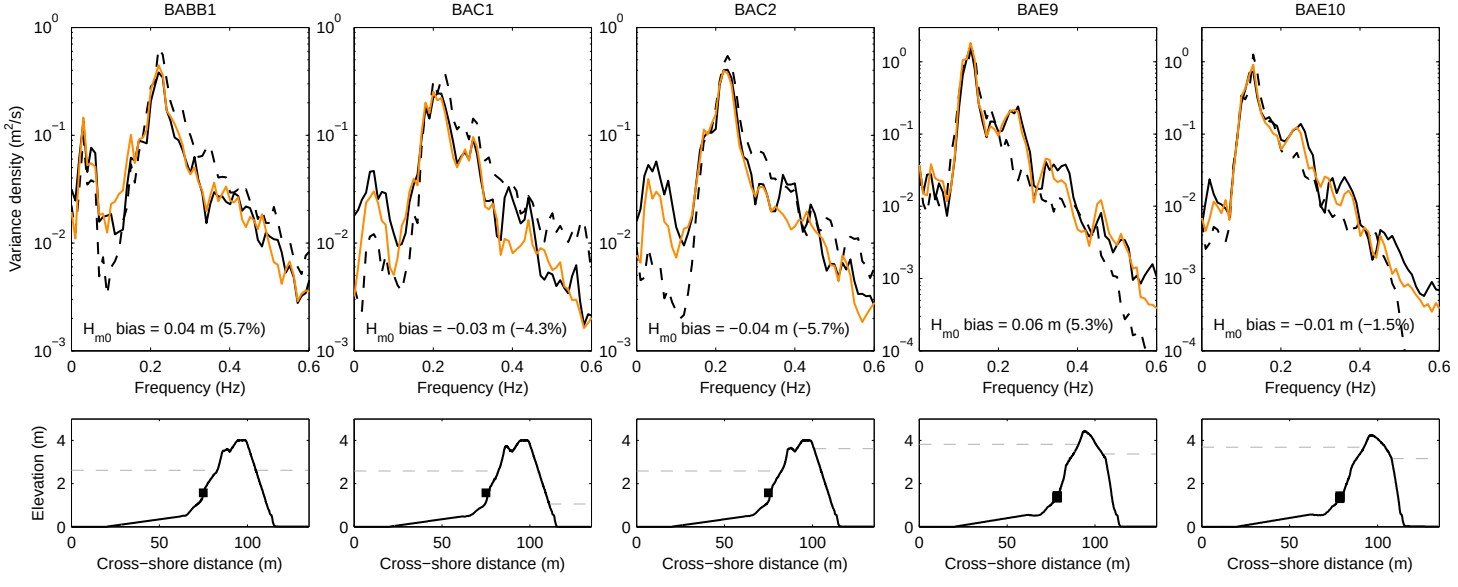

Figure 3.4: Top panels: Measured (—) and modelled (—) water surface elevation spectra at the location of the shallow water PT and at the offshore boundary of the model (– –) for BABB1, BAC1, BAC2, BAE9 and BAE10. Bottom panels: Cross-shore bed profile (—), still water levels (– –) and position of the shallow water pressure transducer (■). The offshore boundary of the model is at cross-shore distance 0 m.

To validate the transfer of the incident-band wave energy to higher and lower harmonics across the barrier foreshore, the wave spectrum at the model boundary is compared to the computed and measured wave spectrum at the location of the shallow water PT (Figure 3.4). The figure shows a transfer of wave energy from the peak of the wave spectrum (0.23 Hz) to lower frequencies (0.05 Hz) in BABB1–BAC2 (three left-most panels) and from the peak of the spectrum (0.13 Hz) to lower frequencies (0.02 Hz) as well as higher frequencies (0.25 Hz and 0.36 Hz) in BAE9 and BAE10 (two right-most panels), representing the transfer of energy to higher and lower harmonics of the peak frequency band. The results of the model simulations show that XBeach-G is capable of reproducing this transfer across the frequency band relatively well, although the energy in the upper and lower frequency bands appears to be under-predicted somewhat by the model in some cases. Since the measured water surface elevation at the toe of the gravel barrier contains both incident and reflected waves, this under-prediction may be both due to lower energy transfer rates in the incident wave components, as well as an incorrect representation of the amplitude or phase of the reflected wave components. Despite the under-prediction in the high and low frequency components, the overall spectral significant wave height at the shallow water PT is predicted well by the model with the maximum relative bias of 5.7%.

To determine whether the model is also capable of predicting wave transformation well on natural beaches, the XBeach-G model is used to simulate wave transformation at Loe Bar. During this field experiment, five PTs were mounted near bed level to a cross-shore scaffold instrument frame spanning the upper inter-tidal (see Figure 3.3 for an overview of the location of the PTs and Poate et al. (2013) for further details). As in the case of the BARDEX pressure data, water surface elevation time series were derived from the measured pressure data using the local approximation method of Nielsen (1986). An XBeach-G model was set up for two high-energy wave events on 8 March 2012 (LB1) and 24 March 2012 (LB2) with offshore significant wave heights 1.6–2.3 m, as discussed in Section 3.3. The XBeach-G model is forced using directional wave spectrum time series measured by the CCO nearshore wave buoy, which the XBeach-G model uses to generate a random time series of incident waves. Tidal and very low frequency water level modulations derived from the tide gauge record are imposed on the XBeach-G model as an additional water level boundary condition. The hydraulic conductivity of the Loe Bar barrier is set to 0.003 ms^{-1}, based on in-situ measurements.

A comparison of measured and modelled wave heights, split into high-, mid- and low-frequency components at the five cross-shore PTs at Loe Bar is shown in Figure 3.5 for LB1, and in Figure 3.6 for LB2. Figure 3.5 shows that for LB1, little wave height transformation takes place between the nearshore wave buoy and the most seaward pressure transducer (PT9), except for an increase in the low-frequency band. The wave height in the high-frequency band gradually decreases in the cross-shore direction between PT9 and PT6, whereas the wave height in the mid-frequency band shows relatively little decay compared to LB2, which is likely due to the slightly reflective state of the beach for the long-period waves of LB1 (Table 3.1). Note that water depths at PT5 during LB1 are too small to compute wave statistics during any part of the tide. Figure 3.6 shows a strong increase in the measured low-frequency wave height from the offshore boundary of the model to the most seaward pressure trans-

	LB1			LB2		
	RMSE (m)	SCI (-)	Bias (m)	RMSE (m)	SCI (-)	Bias (m)
PT9	0.08	0.05	-0.03	0.28	0.17	0.21
PT8	0.11	0.07	0.03	0.16	0.11	0.13
PT7	0.27	0.27	0.27	0.34	0.40	0.32
PT6	0.17	0.21	0.16	0.31	0.32	0.29
PT5	N/A	N/A	N/A	0.25	0.27	0.23
Combined	0.11	0.14	0.11	0.28	0.21	0.23

Table 3.2: RMSE, SCI and bias of the spectral significant wave height prediction in the XBeach-G model of LB1 and LB2. A positive bias indicates an over prediction of the wave height in the model. Note that PT5 did not record wave data during LB1. The locations of the five nearshore pressure transducers in the cross-shore are shown in Figure 3.3.

ducer (PT9) in LB2. During this event, wave heights in the mid- and high-frequency components of the wave spectrum are generally lower at PT9 than offshore. In the cross-shore direction, all measured wave heights are modulated by the tide level. Both figures show that wave heights in the low-, mid- and high-frequency bands are generally predicted well in the model. In contrast to the results of the BARDEX simulations, the high- and low-frequency components of the wave spectrum are slightly over-predicted during the LB1 and LB2 (positive bias), instead of under-predicted. During LB2, the accuracy of the model predictions of the wave height decreases over time at the most landward PTs (in particular PT5, PT6 and PT7), which may be due to the lack of morphological updating in the model. Notwithstanding these errors, the quantitative model skill in predicting wave height transformation across the foreshore and gravel beach is good, with RMSE in the high-, mid- and low-frequency band < 0.24 m for LB1 and< 0.30 m for LB2, which is approximately 15% and 13% of the total offshore wave height of the two wave events, respectively. The SCI of the model wave height prediction is low ($SCI < 0.26$) for all frequency bands at the two most offshore pressure transducers (PT8 and PT9), and reasonable ($SCI < 0.57$) at the three landward pressure transducers (PT5, PT6 and PT7). The overall RMSE for the integrated wave height is 0.11m during LB1 and 0.28m during LB2, corresponding to a SCI of 0.14 and 0.21, respectively (Table 3.2).

The evolution of the wave spectrum from offshore to the five cross-shore PTs is shown in Figure 3.7 at four stages of the tide during LB2. The figure shows a distinct drop in wave energy at the peak of the spectrum across the PT array, caused by depth-induced wave breaking, and transfer of wave energy to lower and higher harmonics of the peak frequency band. Both phenomena are represented well by the XBeach-G model, indicating that the model skill is not restricted to ensemble wave heights and the total wave energy, but can also be used to study wave spectrum transformation on

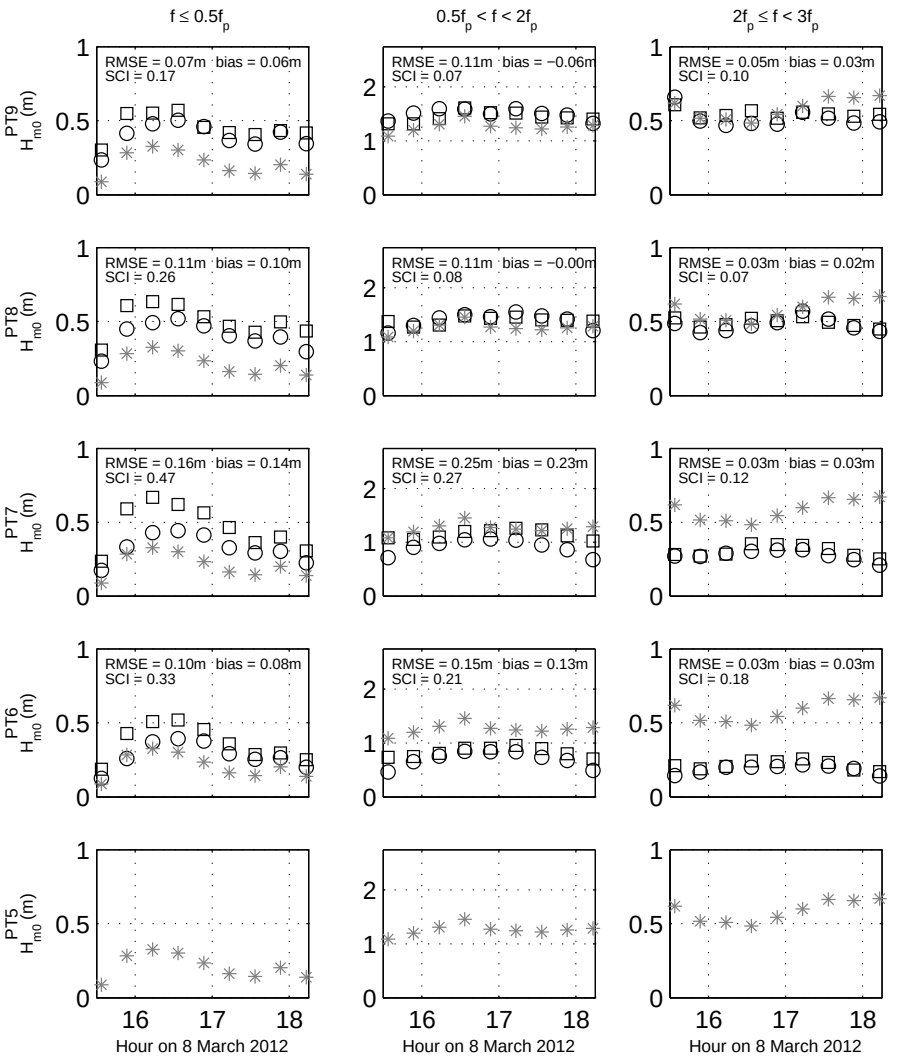

Figure 3.5: Offshore significant wave height time series $(*)$, significant wave height time series measured by five nearshore pressure transducers $(\bigcirc)$ and significant wave height time series modelled at the location of the nearshore pressure transducers$(\square)$ during LB1, separated into three frequency bands, where f_p represents the offshore spectral peak frequency. The locations of the five nearshore PTs in the cross-shore are shown in Figure 3.3.

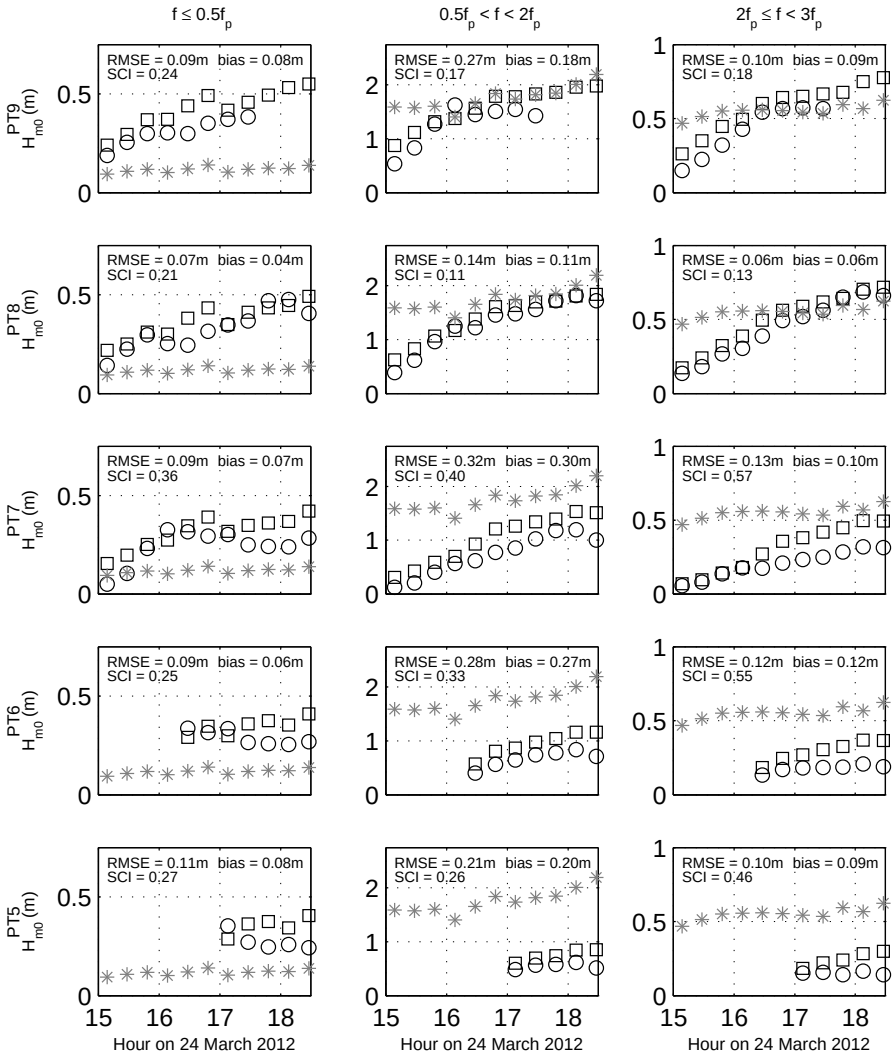

Figure 3.6: Offshore significant wave height time series ($*$), significant wave height time series measured by five nearshore pressure transducers ($\bigcirc$) and significant wave height time series modelled at the location of the nearshore pressure transducers($\square$) during LB2, separated into three frequency bands (cf. Figure 3.5).

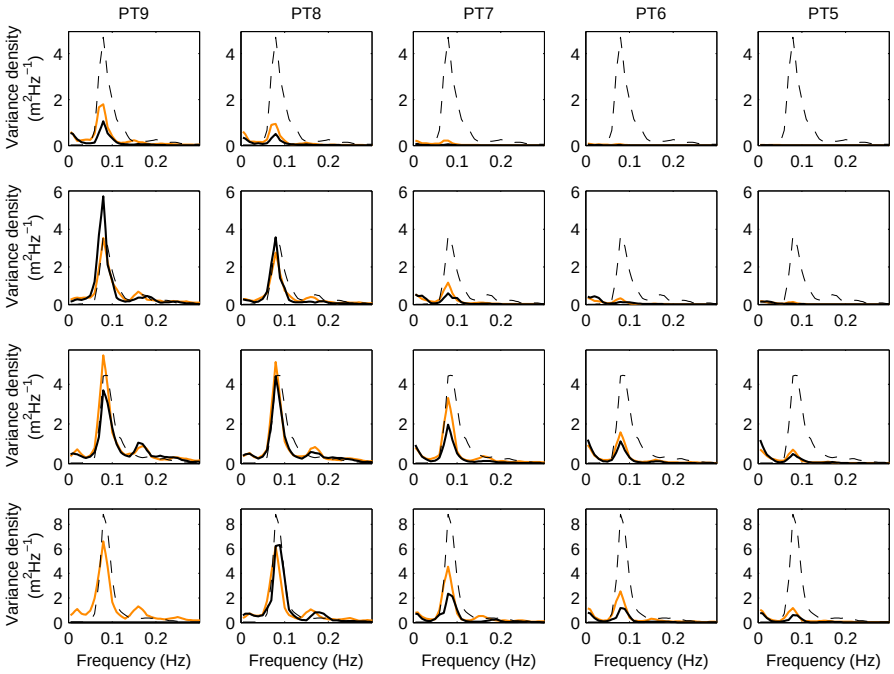

Figure 3.7: Offshore wave spectra (– –), wave spectra measured by five nearshore PTs (—) and wave spectra modelled at the location of the nearshore PTs (—) at 15:00 (first row), 16:00 (second row), 17:00 (third row) and 18:00 (fourth row) at Loe Bar during LB2. Note that PT9 did not record any data at 18:00.

gravel beaches.

Finally, the transformation of the wave shape is examined in terms of wave skewness Sk and wave asymmetry As. In this analysis, both parameters are computed from a low-pass ($f \leqq 5f_p$) filtered time series, where f_p represents the offshore spectral peak frequency, of the modelled water surface elevation and the water surface elevation derived from the measured pressure time series ζ_{lpf} as follows:

$$Sk\left(\zeta_{lpf}\right) = \frac{\frac{1}{n}\sum_{i=1}^{n}\left(\zeta_{lpf} - \overline{\zeta_{lpf}}\right)^3}{\left(\frac{1}{n}\sum_{i=1}^{n}\left(\zeta_{lpf} - \overline{\zeta_{lpf}}\right)^2\right)^{1.5}} \tag{3.13}$$

$$As\left(\zeta_{lpf}\right) = Sk\left(\frac{\delta\zeta_{lpf}}{\delta t}\right) \tag{3.14}$$

where overbars indicate time-averaged values.

Modelled and measured wave skewness and wave asymmetry at the five cross-shore PTs are shown in Figure 3.8. The figure shows that wave skewness and asymmetry are predicted relatively well by the model at the two most offshore pressure transducers (PT8 and PT9), but that in general wave asymmetry is slightly overpredicted by the model, particularly at the three most shoreward pressure transducers (PT5, PT6 and PT7). Error statistics for wave skewness (RMSE = 0.27) and asymmetry (RMSE = 0.33) for the computed wave shape at the location of the shallow water PT during BABB1, BAC1, BAC2, BAE9 and BAE10 (not shown), are similar to those at PT8 and PT9 during LB1 and LB2. The overprediction of the wave asymmetry in the model may be the result of the simplified method in which the model attempts to simulate the complex hydrodynamics of breaking waves using the hydrostatic front approximation (HFA), as also found to lesser extent in the SWASH-model under narrow-banded wave conditions (Smit et al., 2014). However, since wave skewness and asymmetry are sensitive to wave reflection and water depth, changes in the wave asymmetry due to errors in the imposed bed level may also contribute to the differences found between the model and measurements.

3.4.2 Wave set-up

Steady wave set-up at the five cross-shore PTs at Loe Bar is extracted from the measured pressure records for LB1 and LB2 by subtraction of the tide and surge level measured by the harbour tide gauge, from 15-minute averaged water levels measured at the PTs. Time series of the steady wave set-up for both wave events are shown in Figure 3.9. The figure shows little measured wave set-up at the most offshore cross-shore pressure transducer (PT9), where set-down dominates during LB1, and set-up is less than 0.5 m during LB2. For both events, wave set-up increases in shoreward direction across the PT-array, and reaches a minimum at all PTs at high tide (16:45 and 18:00 for LB1 and LB2, respectively). Wave set-up at all cross-shore PTs is predicted reasonably well, with RMSE < 0.10 m (approximately 6% of the tidal amplitude) for LB1 and < 0.25 m (approximately 13% of the tidal amplitude) for LB2. The larger error in the steady wave set-up during LB2 than LB1 is primarily due to an underestimation (negative bias) of the measured wave set-up at the most landward pressure transducers (PT5, 0.25 m; PT6, 0.20 m). This may partly be explained by the lack of morphological updating in the model, also noted in the discussion of the wave height transformation in Figure 3.6, and is addressed in Section 3.5. It should be noted that although the SCI is included in Figure 3.9 for reference, the value at the most seaward pressure transducers (PT8 and PT9) are poor in the case of LB1 due to the very low value of the denominator in the SCI calculation, rather than to particularly large errors in the predictions.

3.4.3 Wave run-up

Data on wave run-up levels were collected using a cross-shore array of bed-level sensors during the BARDEX experiment (Table 3.1; BABB1, BAC1 and BAC2) and at Loe Bar (LB1 and LB2), and using pixel time stacks derived from video data at Loe Bar (LB3 and LB4), Chesil Beach (CB), Slapton Sands (SS) and Seascale (SE). For the purpose of this study, the shoreline derived from the pixel time stacks is assumed to correspond to a water depth of 0.01 m, and this value is used as a depth criterion to

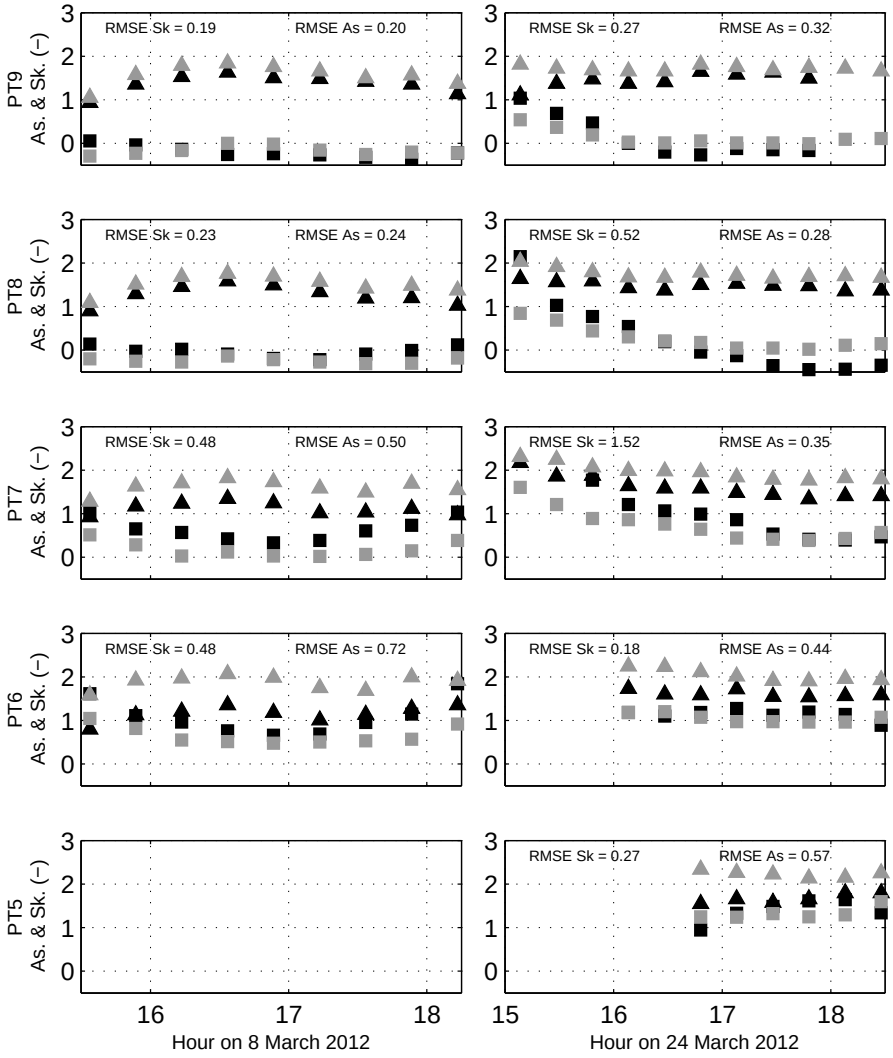

Figure 3.8: Measured (black) and modelled (grey) wave skewness(□) and wave asymmetry (△) at the location of the nearshore pressure transducers during LB1 (left column) and LB2 (right column). The locations of the five nearshore PTs in the cross-shore are shown in Figure 3.3.

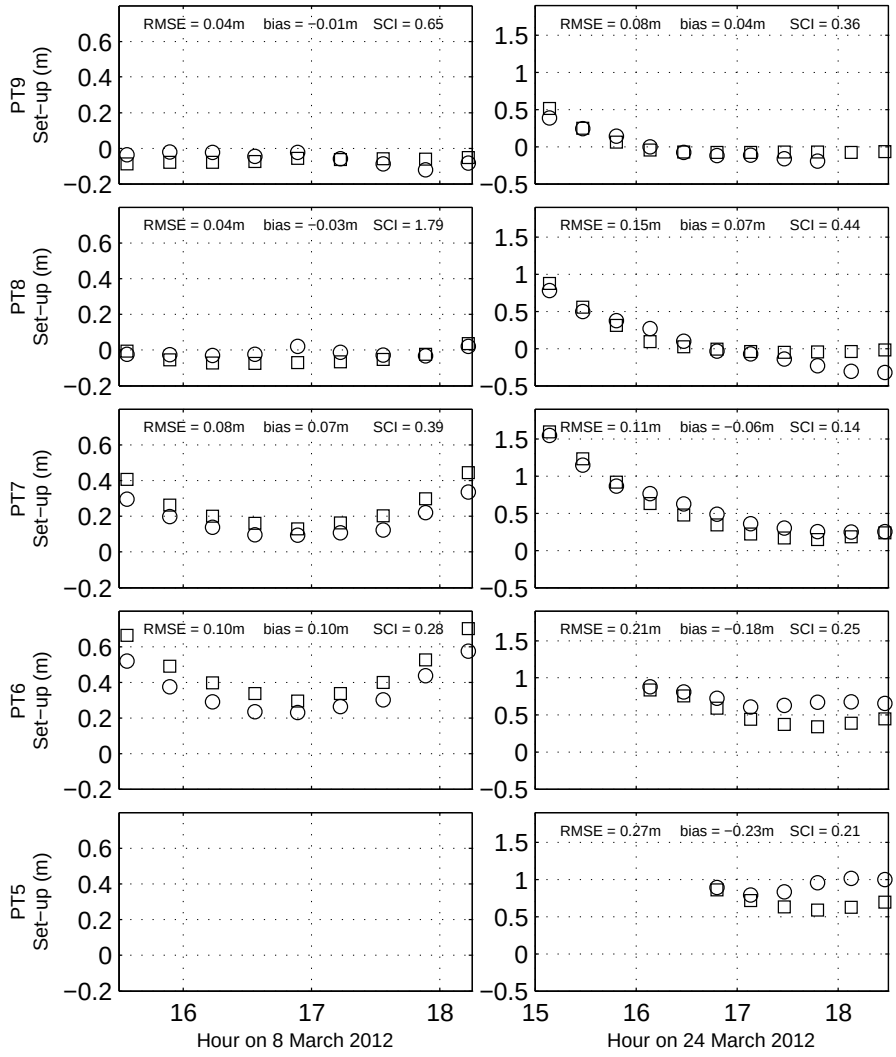

Figure 3.9: Wave setup time series measured by five nearshore pressure transducers (◯) and modelled at the same location(□) during LB1 (left column) and LB2 (right column). The locations of the five nearshore PTs in the cross-shore are shown in Figure 3.3.

determine the shoreline time series in the bed-level sensor data and XBeach-G model results. The 2%, 5%, 10% and 20% ($R_{2\%}$, $R_{5\%}$, $R_{10\%}$, $R_{20\%}$) run-up exceedence levels are computed from 15–20-minute sections of the shoreline time series above Still Water Level (SWL; cf. Stockdon et al., 2006).

To compare predicted and measured run-up levels, XBeach-G models are set up for the three measurement series of the BARDEX experiment and the nine storm events discussed above (cf., Table 3.1). Each BARDEX series simulation is run for one measured wave sequence of approximately 20 minutes. In the case of the storm events, one simulation is run for every 1–3 sequential daytime high-tides of the storm event. Each high-tide simulation is run for the duration of maximum tide levels and contiguous camera or bed-level sensor data, which was generally in the order of 0.5–1 hours. Run-up exceedence levels are computed from the modelled shoreline time series using identical methods and computation periods as used in the derivation of the measured run-up levels. To investigate the sensitivity of the modelled run-up levels to the selection of random wave components at the model boundary, each XBeach-G simulation is run ten times using a new random wave time series of the imposed offshore wave spectrum.

Mean measured and modelled run-up levels computed for every 15–20-minute section of shoreline time series data at all sites are shown in Figure 3.10. Vertical error bars in the figure represent variations in the modelled run-up levels due to variations in the random wave times series applied at the model boundary. Horizontal error bars represent the minimum and maximum measured run-up data across the multiple cross-shore camera pixel stacks, cf. Poate et al. (2014). Maximum variations in modelled and measured run-up levels due to variations in the imposed wave time series and cross-shore camera pixel stack locations exceed 1 m (20%) for run-up levels over 5 m. Note that data presented at BARDEX, Loe Bar, Chesil Beach and Slapton Sands represent multiple storm events, where differences are particularly visible for two clusters of run-up values at Chesil Beach, representing CB1 (measured $R_{2\%}$ approximately 3–4 m) and CB2 (measured $R_{2\%}$ approximately 8–10 m). The figure shows very good correspondence, low relative bias, and little scatter between measured and modelled run-up levels for all exceedence probabilities and at all five gravel beaches, given the number of data points and variety of forcing conditions and beach geometries.

The relative bias of the model run-up level prediction is shown in Figure 3.11 as a function of the measured run-up level. The figure shows the the model performs least well at Seascale, where three out of four $R_{2\%}$ run-up exceedence level predictions have a relative bias greater than 20% (approximately 30% under estimation of the run-up level). The $R_{2\%}$ run-up exceedence level prediction errors at the three other pure gravel beaches and in the BARDEX experiment are generally less than 20%, which is of the same order as the measured and modelled variability in run-up levels.

The model accuracy is further examined in Figure 3.12, which presents histograms of the absolute relative error in the mean run-up level prediction for all 15–20-minute sections of shoreline time series at all five gravel beaches. The figure shows that the majority of absolute relative run-up level prediction errors are in the order of 0–15% of the measured run-up. The empirical relative error exceedence function in the same

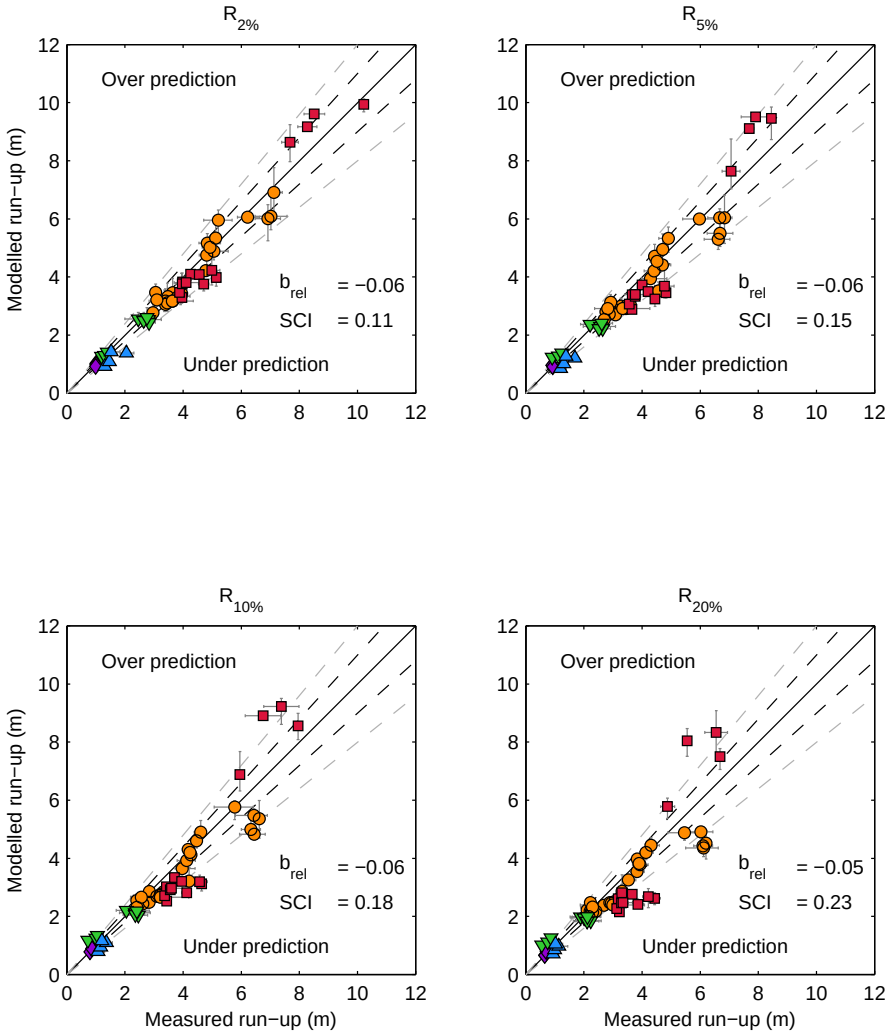

Figure 3.10: Comparison of measured (horizontal axis) and modelled (vertical axis) wave run-up heights at Chesil Beach (red □), Loe Bar (orange ◯), Slapton Sands (green ▽), Seascale (blue △) and the BARDEX-experiment (purple ♢). The solid black line indicates a perfect 1:1 relationship, and the black and grey dashed lines indicate a 10% and 20% deviation from the perfect relationship, respectively.

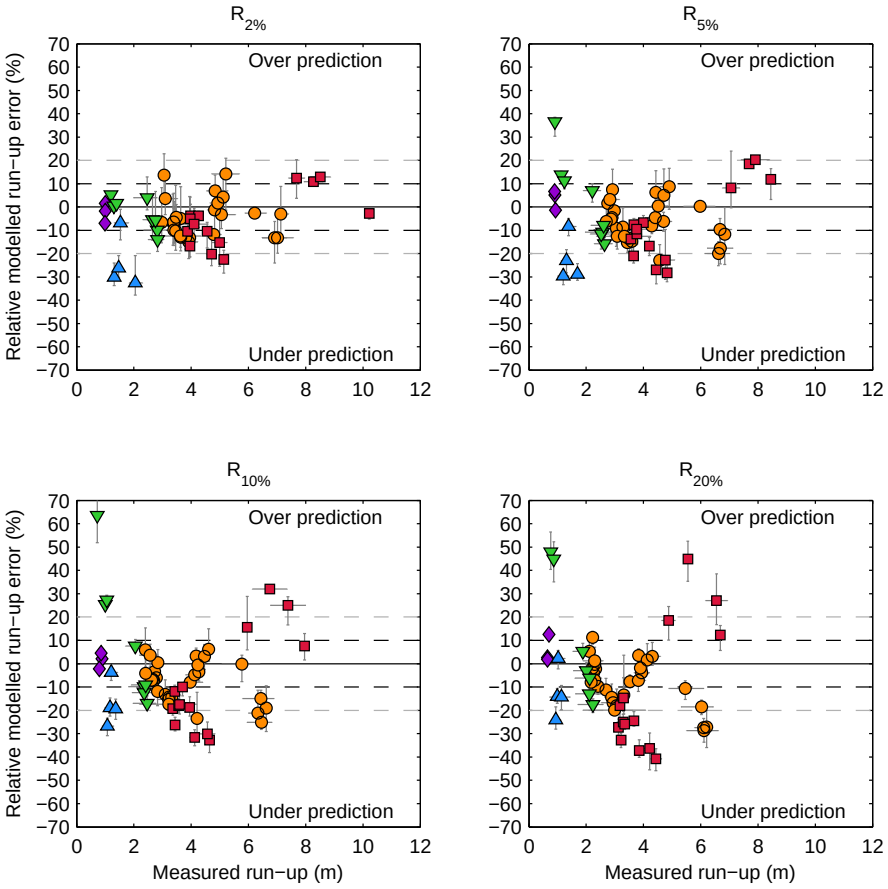

Figure 3.11: Comparison of measured wave run-up (horizontal axis) and relative model run-up prediction error (vertical axis) at Chesil Beach (red □), Loe Bar (orange ◯), Slapton Sands (green ▽), Seascale (blue △) and the BARDEX-experiment (purple ♢). The solid black line indicates a perfect 1:1 relationship, and the black and grey dashed lines indicate a 10% and 20% deviation from the perfect relationship, respectively.

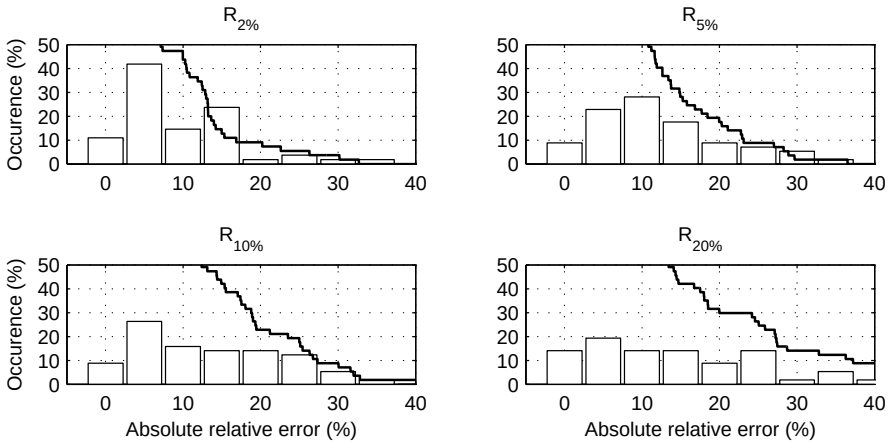

Figure 3.12: Histograms of the absolute relative error between measured and modelled wave run-up heights. The black line shows the empirical absolute relative error exceedence function.

figure shows that the median (50% exceedence) relative error for $R_{2\%}$ is 7.1%, and the maximum relative run-up error for $R_{2\%}$ is 32.7%. These values indicate that even without morphological updating, the model can potentially be applied to investigate extreme run-up levels and the possibility of wave overtopping under energetic wave conditions.

3.4.4 Wave overtopping

Time series of overtopping waves were measured by a cross-shore array of 45 bed-level sensors during the BARDEX experiment. Data provided by these instruments are the level of the bed directly below the ultrasonic sensor (when the bed is dry), or the water level below the ultrasonic sensor (when the bed is covered with water). To study the applicability of the XBeach-G model to predict overtopping waves on gravel barriers, XBeach-G simulations are set up of BARDEX measurement series BAE9 and BAE10, during which wave overtopping of the barrier crest took place. Due to lowering of the crest during the experiment, the relative freeboard of the barrier is higher in BAE9 than in BAE10, which in combination with a slight change in the beach slope results in more overtopping waves in BAE10 than in BAE9. Since considerable bed level change occurred during both measurement series, the XBeach-G simulations are limited to the first 10 minutes of overtopping waves during which the crest level was lowered less than 0.15 m from the level at the start of each series.

Comparisons of modelled and measured time series of the bed level and water level at three locations across the gravel barrier in BAE9, and four locations in BAE10 shown in Figure 3.13 and Figure 3.14 respectively. Data at the most landward sensor (BLS45) are not shown in the comparison of BAE9 due to the lack of reliable measurement data. The figures show a reduction in the number of waves, described by spikes in the time series, and their amplitude, from the most seaward sensor (BLS30)

	BAE9			BAE10			
	BLS30	BLS35	BLS40	BLS30	BLS35	BLS40	BLS45
Correct overtopping prediction	56 (90%)	31 (78%)	17 (74%)	74 (97%)	46 (85%)	8 (28%)	4 (67%)
False negative prediction	6 (10%)	9 (23%)	6 (26%)	2 (3%)	8 (15%)	21 (72%)	2 (33%)
False positive prediction	1 (2%)	4 (10%)	1 (4%)	0 (0%)	5 (9%)	0 (0%)	0 (0%)

Table 3.3: Number of overtopping waves correctly predicted by the XBeach-G model in the first 10-minutes of overtopping during the BAE9 and BAE10 measurement series simulations, the number of waves incorrectly not predicted by the model (false negative) and the number of waves incorrectly predicted by the model (false positive) at four locations on the gravel barrier. Percentages presented between parentheses are relative to the total number of measured overtopping events. The sum of correct overtopping events and false negative predictions is 100%.

to the most landward sensors (BLS40 and BLS45). This reduction in the number and the size of overtopping waves is due to infiltration of the swashes on the back barrier. Periods in which the dry bed is measured by the sensor are indicated by the horizontal sections in the time series between waves. The measurements of the dry bed show that the bed at BLS30 erodes approximately 0.15 m in the first 10 minutes of BAE9 and BAE10, and that some accretion takes place at BLS40 in both series.

Figures 3.13 and 3.14 show that the XBeach-G model is able to reproduce the time series of overtopping waves at most locations on the gravel barrier well. At the locations of BLS30 and BLS35, the model correctly predicts more than 78% of the overtopping wave occurrences that exceed the initial bed level (Table 3.3). The wave height of the majority of these overtopping events is also predicted well by the model, although accuracy of the wave height predictions at BLS30 is strongly reduced by the erosion of the bed. Wave overtopping at BLS40 is poorly predicted by the model during BAE10, where only 28% of overtopping waves are correctly reproduced by the model, however at BLS45 in the same series, the model skill improves by correctly predicting the four largest of six overtopping wave events. The reason for the improvement in the model skill from BLS40 to BLS45 is not clear. However, the approximation of the infiltration velocity in the groundwater component of the XBeach-G model, the lack of morphological updating in the XBeach-G model, and possible longshore non-uniformities in the barrier response of the BARDEX physical model, may all be considered sources for discrepancies between the the measurements and modelled results.

The results of simulations BAE9 and BAE10 show that the XBeach-G model is well capable of predicting initial wave overtopping at the crest of the gravel barrier. The model also correctly predicts the evolution of most initial overtopping waves across the back barrier. These results show that the model may be considered a useful tool with which to estimate the potential for overtopping on gravel barriers. However, since much bed level change is expected during overtopping and overwash events, the

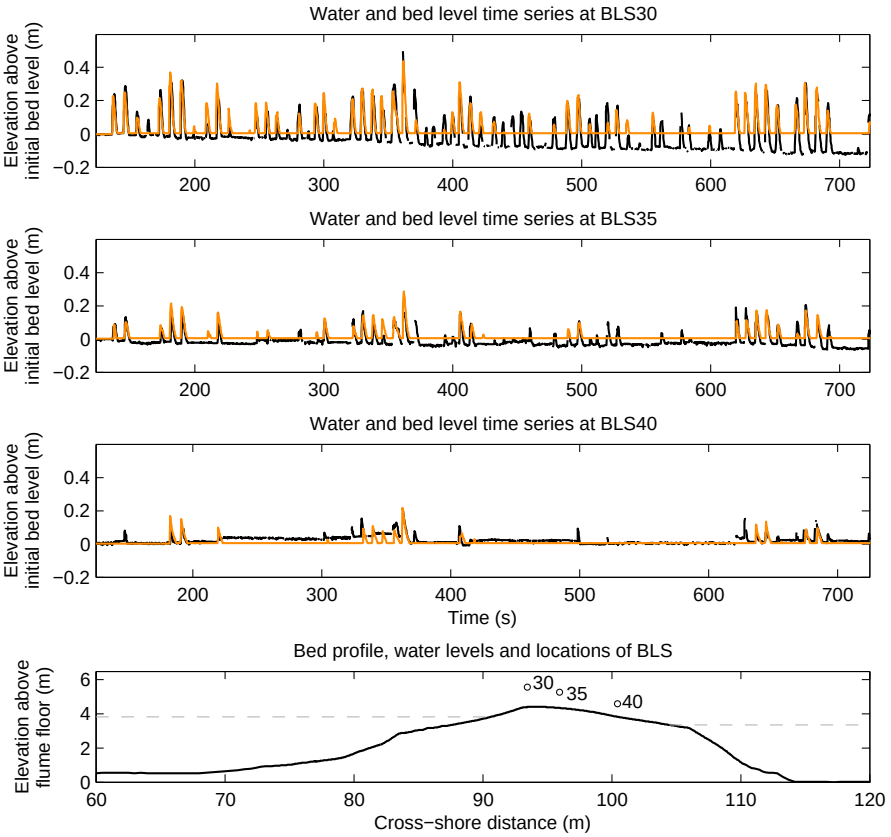

Figure 3.13: Measured (—) and modelled (—) time series of overtopping waves (spikes) and bed levels (horizontal sections) at the locations of three acoustic bed level sensors during BAE9. The locations of the bed level sensors relative to the barrier profile (—) and water levels (– –) are shown in the bottom panel. Note that the gradual erosion at BLS30 and BLS35, and accretion at BLS40 found in the measurements is not accounted for in the XBeach-G model. Sparse data were collected at BLS45 due to the proximity of the water level to the instrument and are therefore not shown in this figure.

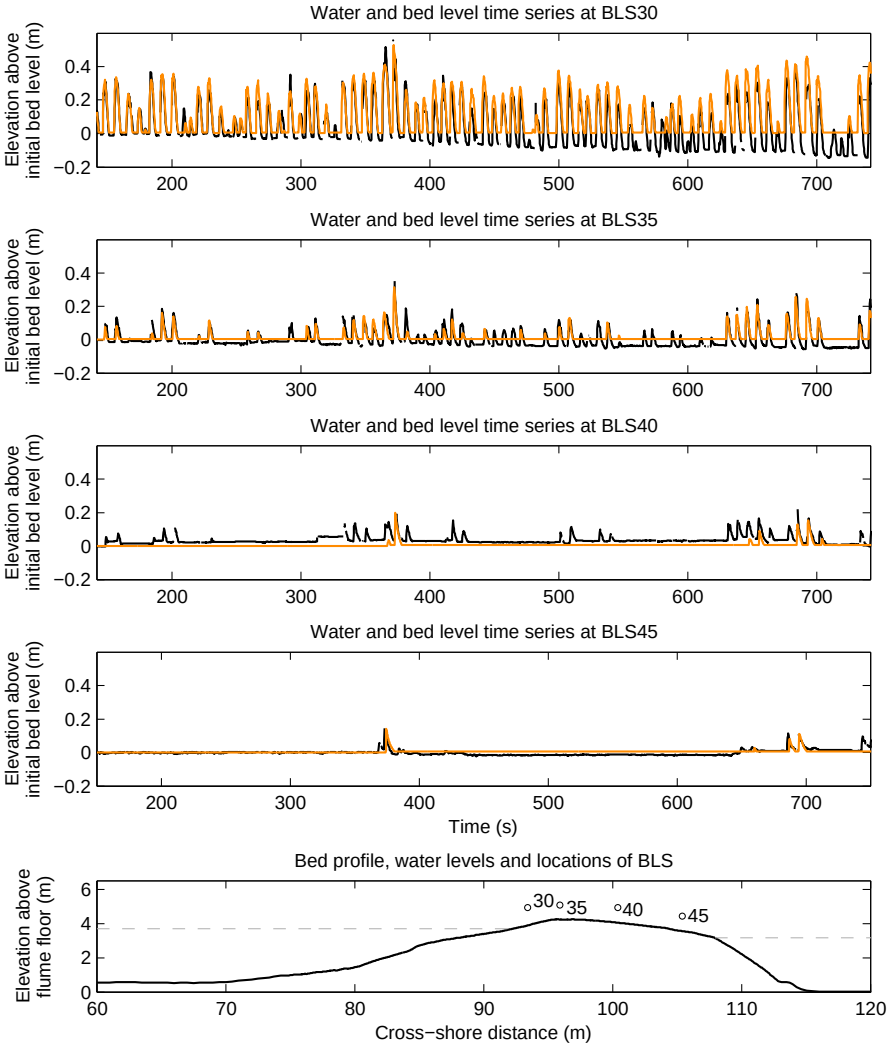

Figure 3.14: Measured (—) and modelled (—) time series of overtopping waves (spikes) and bed levels (horizontal sections) at the locations of four acoustic bed level sensors during BAE10. The locations of the bed level sensors relative to the barrier profile (—) and water levels (– –) are shown in the bottom panel. Note that the gradual erosion at BLS30 and BLS35, and accretion at BLS40 found in the measurements is not accounted for in the XBeach-G model.

addition of morphodynamic feedback in XBeach-G is considered necessary in order to properly predict the development of overtopping and overwash discharge during these events. The effect of groundwater infiltration on simulated wave overtopping and overwash is discussed in Chapter 4.

3.5 Effect of updating bed boundary condition on computed wave setup, wave transformation and wave run-up

As discussed in Section 3.4.2 and shown in Figure 3.9, application of the XBeach-G model to LB2 underestimates the measured wave set-up at the most landward pressure transducers (PT5 and PT6) by as much as 0.35 m. This underestimation of the set-up is mainly attributed to the absence of morphodynamic updating in the XBeach-G model, specifically ignoring the fact that the high tide beach morphology is significantly different from that during low tide. Here, the effect of including measured changes in bed level on the predicted set-up is investigated. The mean bed level position during LB2 is derived every 15 minutes from high-frequency (2 Hz) laser data along the model cross-shore transect from the wave run-down level to the barrier crest (cf. Almeida et al., 2013). The model is then re-run using the laser-derived time series of the bed level elevation as a time-varying bed boundary condition. Note that because no laser-derived bed elevation data exist below the wave run-down level, the assumption is made for the purpose of this sensitivity analysis that the bed level below the wave run-down level remained constant during the event.

The results of the wave set-up predicted by the XBeach-G model for LB2 with, and without, measured bed level updating are shown in the top panel of Figure 3.15 at the moment of maximum wave set-up (18:00). The figure shows that the build-up of the gravel step (derived from laser data and shown by the grey dashed line in the figure) greatly increases the predicted wave set-up in the lower swash zone (-90 m $< x <$ -70 m) with bed-level updating (black dashed line) compared to the model predictions without bed-level updating (black solid line). The wave set-up predictions in the model with bed level updating correspond more closely to the measured wave set-up levels for all tide levels (RMSE < 0.11 m for PT5 and PT6) than the results of the model without bed-level updating (RMSE < 0.24 m for PT5 and PT6).

The bottom panel of Figure 3.15 shows the measured wave height at PT5–PT8 at 18:00, as well as the wave height computed at the same PTs by the XBeach-G simulations with, and without, bed level updating. The figure shows that although bed level updating does modify the computed wave height, the model prediction of the nearshore wave height is less sensitive to bed level updating than the computed set-up. Wave heights computed by the XBeach-G simulation with bed level updating are 5–10% lower than in the XBeach-G simulation without bed level updating, leading to lower model bias and RMSE, and slightly lower SCI values in the simulation with bed level updating. The over prediction of the wave asymmetry at PT5–7 discussed in Section 3.4.1 is not reduced significantly by the application of bed level updating in the model, indicating that a modification of the HFA-model may be necessary, alongside more accurate bed level information below the waterline, in order to correctly predict the wave skewness and asymmetry in the lower swash and inner surf zone.

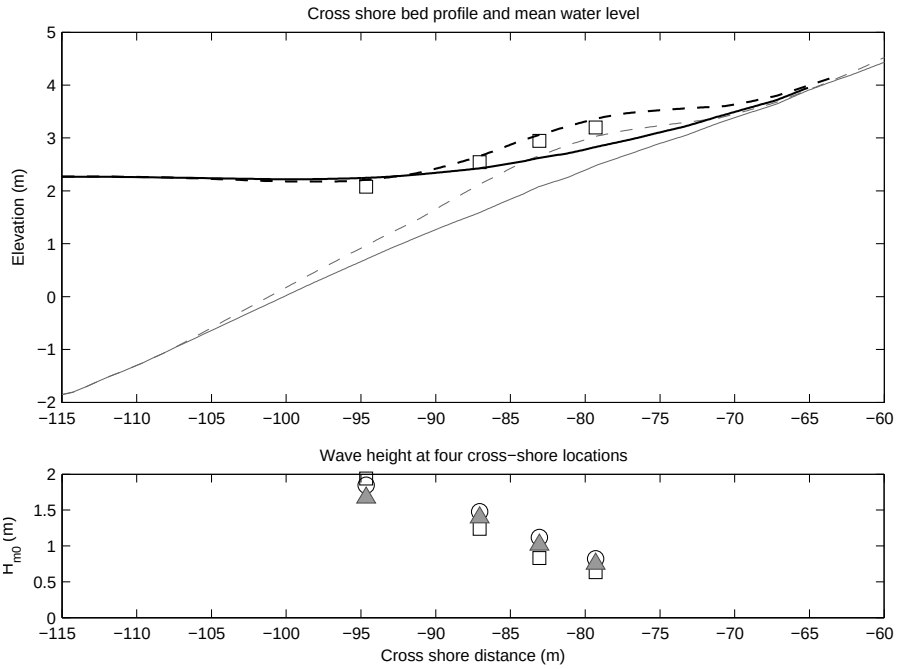

Figure 3.15: Effect of bed level updates on computed mean water levels and wave heights at Loe Bar. Top panel: measured 20-minute mean water at 18:00 during LB2(□), modelled mean water level without updated bed levels (—) and modelled mean water level with updated bed levels (– –). Bed levels corresponding to the period of the simulation without and with updated bed levels are indicated by (—) and (– –) respectively. Bottom panel: measured wave height at 18:00 during LB2(□), modelled wave height without updated bed levels (◯) and modelled wave height with updated bed levels (grey △).

The application of bed level updating in the XBeach-G model affects the computed wave run-up levels to a similar magnitude as the wave height (not shown in Figure 3.15). In the case of run-up however, the computed value is 5–10% higher in the simulation with bed level updating compared to the simulation without bed level updating, leading to slightly better predictions of the maximum run-up extent during LB2. The increase in the run-up height is explained to a great extent by the large increase in the nearshore wave set-up, in combination with relatively little wave height reduction, in the model simulation with bed level updating relative to the model simulation without bed level updating. This model observation appears contrary to measurement data presented by Poate et al. (2013), who show a reduction in the run-up height due to the development of a step during LB2. This difference between the observed and modelled behaviour may indicate a limitation of the XBeach-G model, but may also be the result of the lack of updated bed level information below the wave run-down level. It should also be noted that the difference in run-up height between both model simulations is of the same order as the model prediction error and the natural spread in run-up heights described in Section 3.4.3.

3.6 Effect of non-hydrostatic wave component and implications for modelling run-up and overwash on gravel barriers

The version of the XBeach-G model discussed in this chapter has been modified from the standard version of XBeach for sandy coasts (e.g., Roelvink et al., 2009) through two extensions to the XBeach model: (1) the application of a non-hydrostatic pressure correction term (Smit et al., 2010) that allows wave-by-wave modelling of the surface elevation and depth-averaged flow due to the incident-band short waves, instead of the use of the standard wave-action balance (surf beat) approach to model short waves; and (2) the application of a groundwater model (Chapter 4) that allows infiltration and exfiltration through the permeable gravel bed to be simulated.

In this section the effect of the application of the non-hydrostatic pressure correction term to resolve individual waves, rather than wave energy alone, is investigated for the purpose of simulating storm impact on gravel barriers. The effect of the groundwater model on storm hydrodynamics and morphodynamics is not discussed here, but separately in Chapters 4 and 5. To this end, wave run-up during CB02, LB03, SS01 and SE01, representing a broad range of natural conditions, and wave overtopping and overwash during BAE9 and BAE10 are re-examined using a modified version of XBeach-G in which waves are resolved using the wave-action balance approach of the standard XBeach model, but in which groundwater interactions are present (referred to as XBHS). The XBHS models are all forced using the same wave boundary condition information as the XBeach-G models discussed in Section 3.4. However, since XBHS uses a wave-action balance approach to model the incident waves, the total incident wave signal for these simulations is split into a high-frequency wave energy part ($f \geq 0.5f_p$) varying on the wave-group time scale, which is used as a boundary condition for the wave-action balance, and a low-frequency flux component ($f < 0.5f_p$) that is imposed as a boundary condition in the hydrostatic non-linear shallow water equations (cf. Van Thiel de Vries, 2009; Roelvink et al., 2009). It should be noted that the roller model that is used to compute the propagation and de-

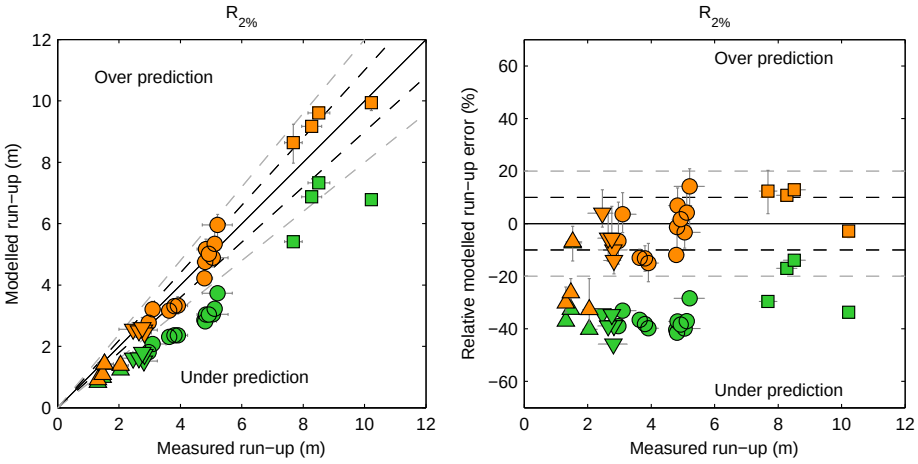

(a) Measured (horizontal) and modelled (vertical) $R_{2\%}$ run-up levels.

(b) Measured $R_{2\%}$ run-up (horizontal) and relative model run-up prediction error (vertical).

Figure 3.16: Comparison of $R_{2\%}$ run-up levels predictions using XBeach-G (orange) and XBHS (green) during CB02 (□), LB03 (◯), SS01 (▽) and SE01 (△). The solid black line indicates zero relative error, and the black and grey dashed lines indicate a 10% and 20% relative error, respectively.

cay of roller energy in the standard surf-beat version of XBeach (cf. Roelvink et al., 2009) is not used in XBHS since the roller model is designed to be used in saturated breaker zones on dissipative beaches. A discussion on the effect of the roller model on gravel beaches is given at the end of this section. All other model settings for the XBHS wave action balance model, including breaker parameters, are taken from the default values used in the standard surf-beat version of XBeach and are not varied.

Figure 3.16 shows the difference between wave run-up measured during CB02, LB03, SS01 and SE01, and wave run-up modelled by XBeach-G (orange symbols) and XBHS (green symbols). The figure shows a substantial difference between the wave run-up level prediction of XBHS and the prediction of XBeach-G during CB01, LB03 and SS01, where XBHS consistently predicts lower wave run-up levels than XBeach-G. Further analysis shows that the relative bias of XBHS for these events is -35% (under prediction), compared to -1.5% (under prediction) for XBeach-G. The figure also clearly shows that the difference between the wave run-up predictions of XBHS and XBeach-G differ substantially less for SE01, which is unsurprising given the highly dissipative nature of the sandy low-tide terrace. In the case of SE01, both models under predict the observed wave run-up in three out of four observations (relative bias XBHS -29%; XBeach-G -24%).

Measured wave overtopping time series, and wave overtopping time series modelled by XBeach-G and XBHS are shown in Figure 3.17 and 3.18 for BAE9 and BAE10,

respectively. The results of the simulations using XBHS show that the simulation of the incident waves using the non-hydrostatic wave-by-wave method greatly increases the model skill in predicting overtopping waves compared to the wave-action balance method. This effect is particularly clear in the case of BAE9 (Figure 3.17), in which XBHS does not predict any of the 63 wave overtopping events at the crest of the gravel barrier (BLS30), whereas the XBeach-G version correctly predicts 90% of the overtopping wave events (Table 3.3). The improvement of the XBeach-G model over XBHS is less pronounced in the case of BAE10 (Figure 3.18), which has a lower relative freeboard than BAE9, causing almost every wave to overtop. In this simulation, XBHS predicts wave overtopping events that are generally lower in amplitude than the measured overtopping events, and have a duration of several incident waves, corresponding to low-frequency wave-group motions. Interestingly, the model skill of XBHS is comparable to that of XBeach-G at the back of the gravel barrier (BLS45) for BAE10, indicating that the large swash events that reach the back of the barrier are related to low-frequency motions on the wave group time scale.

From these results it can be concluded that the wave-action balance approach for modelling wave propagation in the standard XBeach model under predicts observed wave run-up and overtopping compared to XBeach-G. The non-hydrostatic wave-by-wave modelling of the incident wave field is necessary to predict wave run-up levels and the start of overtopping on gravel beaches, and can only partially be replaced by a wave-action balance approach in case of very low relative freeboards and large infragravity motions due to a dissipative foreshore.

Including roller energy propagation and decay in the wave-action balance of XBHS can increase that model's prediction of wave run-up levels substantially, although not enough to lead to overtopping in BAE9, and subject to much sensitivity to numerical depth cut-off parameters. The cause of the increased wave run-up is that if the roller model is activated in XBHS, breaking wave energy is preserved in the wave-action balance equations in the form of roller energy that subsequently exerts a considerable force on the very shallow swash lens on the beach, leading to high shoreline set-up. This transfer of breaking wave energy to roller energy and subsequent decay of roller energy in XBHS is highly questionable on gravel beaches,since no validation of roller model parameters has ever been attempted on gravel beaches. Given that steep, reflective gravel beaches tend to have unsaturated and narrow surf zones with limited roller generation, it is therefore highly likely that the standard roller model parameters in XBHS will overestimate the potential for roller energy. However, although not discussed as an important parameter in earlier studies (e.g., Williams et al., 2012b; Jamal et al., 2014), the application of the standard XBeach roller model almost certainly explains why previous modelling attempts with XBeach on gravel beaches using the wave-action balance approach have proven reasonably successful.

While the concept of rollers may not be appropriate on gravel beaches, the roller model in XBHS also implicitly mimics the effect of the increase in wave radiation stress due to sawtooth-shape of broken waves. Through this process, an analogy could be made towards the swash zone of gravel beaches. Such parametrisation of the swash zone of gravel beaches for wave-action balance models could be attempted once further knowledge is gained on the hydrodynamic forces in the swash zone,

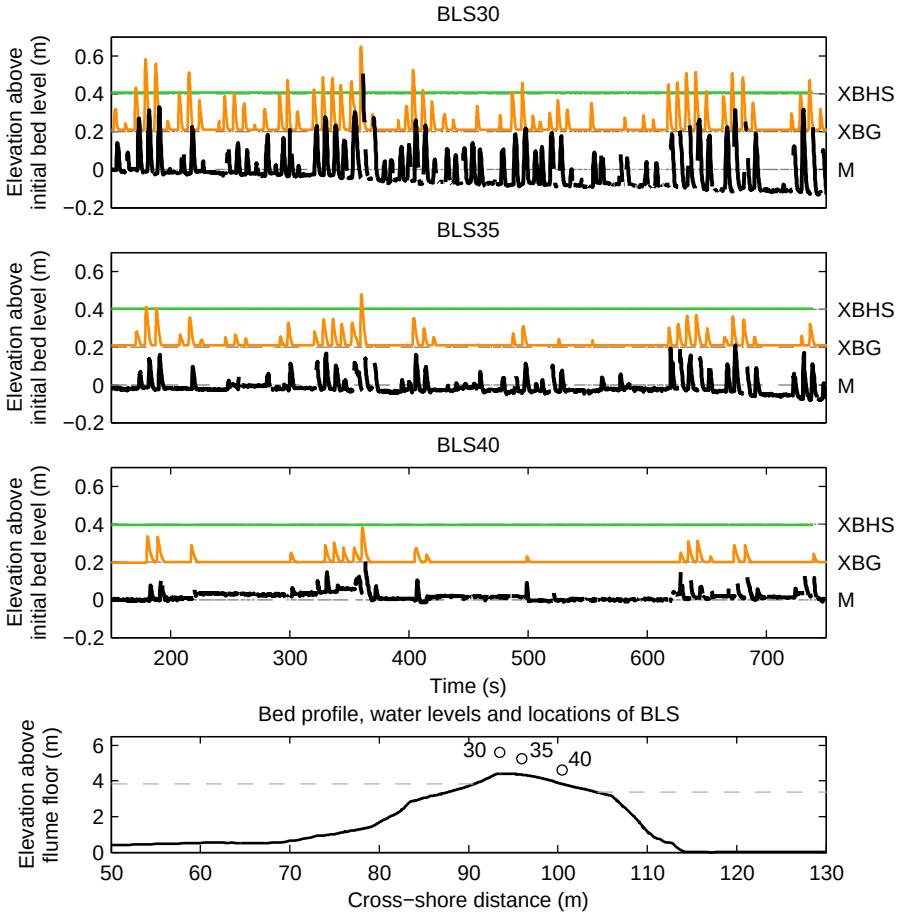

Figure 3.17: Wave overtopping time series during BAE9 at three points on the barrier, showing measured (M; bottom line, —), modelled with the XBeach-G model (XBG; central line, —) and modelled with XBHS (XBHS; wave-action balance; top line, —). Sparse data were collected at BLS45 due to the proximity of the water level to the instrument and are therefore not shown in this figure. Note that the modelled results are offset in the vertical to facilitate a comparison between the simulations.

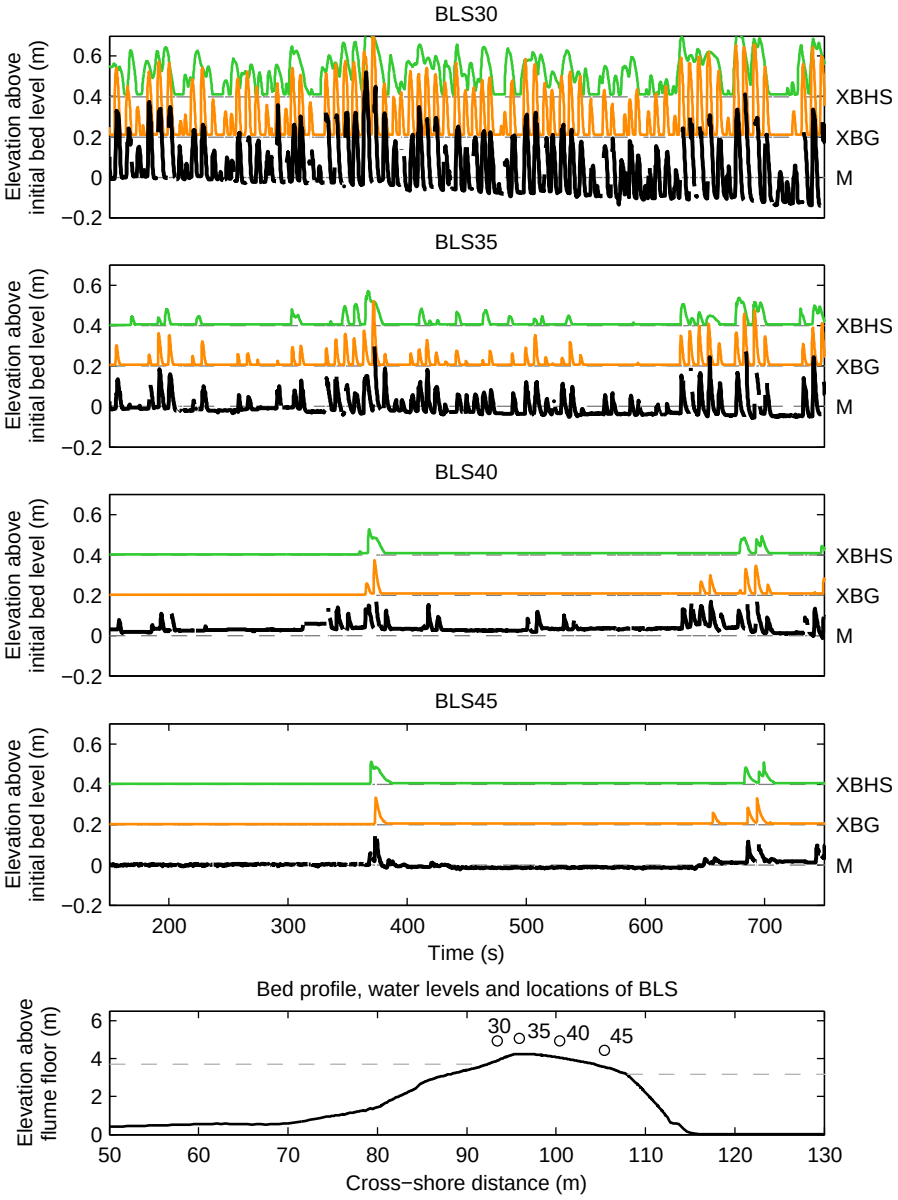

Figure 3.18: Wave overtopping time series during BAE10 at four points on the barrier, showing measured (M; bottom line, —), modelled with the XBeach-G model (XBG; central line, —) and modelled with XBHS (XBHS; wave-action balance; top line, —). Note that the modelled results are offset in the vertical to facilitate a comparison between the simulations.

the interaction between swashes, and their effect on gravel beach morphodynamics. Note that while further development and calibration of a roller model (or swash-zone radiation stress model) may be of relevance to the application of XBHS and other wave-action balance models on gravel beaches, this point is separate from a more general discussion on the need for surface roller equations in non-hydrostatic wave models (cf. Section 3.2.2).

3.7 Conclusions

The results of the model validation discussed in Section 3.4 and sensitivity simulations discussed in Section 3.6 have shown that:

1. XBeach-G is capable of reproducing observed hydrodynamics on gravel beaches across a wide range of forcing conditions well, in particular with regard to wave transformation, wave run-up and initial wave overtopping;
2. the inclusion of the non-hydrostatic correction in XBeach-G to allow wave-by-wave modelling of the surface elevation and depth-averaged flow is essential to accurately predict wave run-up and overtopping on gravel beaches and barriers.

While the results of this chapter show that without a morphodynamic component, XBeach-G can be applied to estimate the potential storm impact on gravel barriers through a prediction of wave height transformation, wave run-up levels and initial wave overtopping discharge on gravel beaches, relevant aspects of the storm response of a gravel barrier, including the development of wave overtopping and wave overwash during a storm, cannot be successfully simulated without morphodynamic updating of the bed level. The inclusion of morphodynamic updating represents an important step in the development of XBeach-G and is discussed in Chapter 5.

Chapter 4

Groundwater dynamics of XBeach-G

This chapter presents and validates a quasi-three-dimensional process-based and time dependent non-hydrostatic groundwater model, which is coupled to the XBeach-G hydrodynamic model to simulate the effect of groundwater-surface water interaction on gravel beaches and barriers. The coupled model is shown to accurately reproduce groundwater variations measured in a gravel barrier during a large-scale physical model experiment. Furthermore, the coupled model is shown to significantly improve simulated overtopping and overwash rates. The coupled model is applied to study the influence of hydraulic conductivity on wave run-up and overwash volumes. It is shown that infiltration plays a modest role in wave run-up on natural gravel beaches. Conversely, modelled overwash volumes are shown to be strongly affected by infiltration on the gravel barrier for hydraulic conductivity values greater than $0.01 ms^{-1}$.

4.1 Introduction

As discussed in Chapter 2, the interaction between surface water and groundwater is considered to play an important role in the morphology of gravel beaches (e.g., Bagnold, 1940; Mason and Coates, 2001; Jennings and Shulmeister, 2002; Buscombe and Masselink, 2006) . It is reasonable to assume that infiltration will have significant influence on wave run-up levels and overtopping volumes, and subsequent beach or barrier morphodynamics. However, the effect of the interaction between the groundwater and surface water has not been independently examined for storm conditions.

This chapter addresses the current gap in our understanding of gravel beach storm dynamics by investigating the effect of groundwater-surface water interaction on the hydrodynamics of gravel barriers during storm events. In order to study this interaction, a new groundwater model is developed and discussed in this chapter, which is coupled to the XBeach-G surface water model, discussed in Chapter 3. The groundwater model allows the simulation of groundwater dynamics in shallow aquifers, as well as the interaction between the surface water and groundwater. The coupled groundwater-surface water model is calibrated and validated using data from the BARDEX large-scale physical models experiment (Williams et al., 2012a). Since the morphodynamic component of XBeach-G and its interaction with the groundwater model will be discussed separately in Chapter 5, validation in this chapter is carried out with a fixed bed using only hydrodynamic data over short periods in which the observed bed level change is negligible.

Sections of this chapter are based on work presented in McCall et al. (2012) and McCall et al. (2014).

4.2 Groundwater model development framework

The purpose of the groundwater model developed in this chapter is to improve the accuracy of the hydrodynamic XBeach-G surface water model (Chapter 3) on gravel beaches during storms. To this end, the groundwater model is developed to simulate the following primary components of groundwater flow and groundwater-surface water interaction on gravel beaches (Figure 4.1):

- Groundwater flow in the saturated permeable gravel beach (aquifer), including the position of the groundwater table.
- Infiltration of surface water into the unsaturated beach or barrier, leading to swash asymmetry and lowering of overwash discharge, as well as increasing the groundwater table and causing wave and tidal pumping (cf. Turner et al., 1997).
- Exfiltration of groundwater from the saturated beach in the lower swash, thereby lowering the groundwater table in the saturated beach and destabilizing sediment in the lower swash.
- Exfiltration of groundwater at the groundwater exit point on the back barrier, leading to flooding of the hinterland.

Groundwater flow in the swash and surf zone has been shown in previous numerical model (e.g., Li and Barry, 2000; Lee et al., 2007) and field (e.g., Raubenheimer et al., 1998) studies to be non-hydrostatic. Furthermore, the hydrostatic pressure assumption can lead to an incorrect prediction of the groundwater table, including the groundwater exit point on the back barrier, in cases where the groundwater equipotential lines deviate from the vertical, for instance in the case of large hydraulic gradients. Therefore, a requirement of the groundwater model is that it does not use the Dupuit–Forchheimer assumption of hydrostatic groundwater pressure.

Although the requirement for non-hydrostatic pressure has the benefit of being a more accurate representation of reality, and allowing non-hydrostatic pressures to develop in the aquifer has been found in this research to increase numerical stability of the coupled groundwater-surface water model, resolving the non-hydrostatic pressure field can be very computationally expensive, particularly in three dimensional (3D) simulations. Since the groundwater model and surface water model must be coupled at sufficiently high spatial and temporal resolution to resolve individual swash and overtopping events, computationally expensive resolution of the groundwater pressure field would be prohibitive to the practical application of the coupled model.

In order to allow for a computationally efficient approximation of the non-hydrostatic groundwater pressure field, the model applies a Q3D method to predict depth-averaged horizontal groundwater fluxes, as well as the vertical distribution of the groundwater pressure and the cross-bed flow driven by groundwater-surface water pressure gradients (submarine exchange), see Figure 4.1. This implies that there is no vertical discretisation of the groundwater model and that a parametrisation is applied instead to describe variations in the vertical. Although the Q3D model is not able to resolve

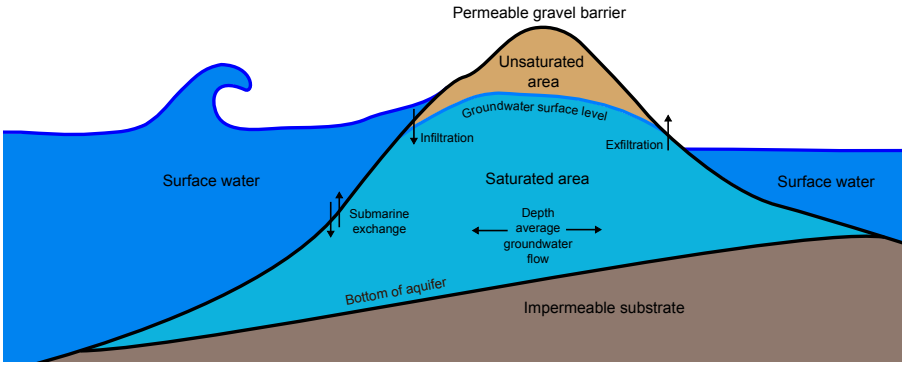

Figure 4.1: Principle components of groundwater flow model and interaction with surface water.

the true vertical variations in groundwater flow and complex vertical groundwater circulation, which play an important role in the transport of solutes, in the manner that a fully 3D non-hydrostatic model would, these processes are assumed to be of lesser importance to the response of gravel beaches and barriers to storms.

Although capillary effects may be of importance on sandy and mixed sand-gravel beaches, the capillary rise on gravel beaches is expected to be small (< 2.5 cm; Kuo, 1998) and are therefore not included in the XBeach-G groundwater model.

4.3 Groundwater model equations

This section discusses the primary model equations and parametrisations applied in the groundwater model, as well as discussing the assumptions and their implications made in the design of the model. The groundwater model closely resembles the surface water model in that the temporal and spatial evolution of the groundwater volume is computed using equations for the conservation of mass (Section 4.3.1) and equations of motion (Section 4.3.2), as well as applying a parametrisation of the non-hydrostatic groundwater pressure (Section 4.3.3). The exchange between surface water and groundwater takes place at the interface between the groundwater model and the surface water model and is discussed in Section 4.3.4. Note that both the groundwater model and the surface water model have no vertical discretisation and assume a single-valued surface. Therefore, the surface water is always assumed to lie above the groundwater, and exchange between the two models only takes place in the vertical. A full description of the numerical implementation of the groundwater model in XBeach-G is given in Appendix A.

4.3.1 Continuity

In order to solve mass continuity in the groundwater model, the groundwater is assumed to be incompressible. Continuity is achieved by imposing a non-divergent flow field:

$$\nabla \vec{U} = 0 \tag{4.1}$$

where $\vec{U}$ is the total specific discharge velocity vector, with components in the horizontal (u, v) and vertical (w) direction:

$$\vec{U} = \begin{bmatrix} u \\ v \\ w \end{bmatrix} \tag{4.2}$$

4.3.2 Equations of motion

Laminar flow of an incompressible fluid through a homogeneous medium can be described using the well-known Law of Darcy (1856):

$$\nabla H = -\frac{1}{K}\vec{U} \tag{4.3}$$

where K is the hydraulic conductivity of the medium, and H is the hydraulic head:

$$H = z + \frac{p}{\rho g} \tag{4.4}$$

In situations in which flow is not laminar, turbulent and inertial terms may become important. In these cases groundwater flow should be described using the extended Forchheimer equation (Polubarinova-Kochina, 1962):

$$\nabla H = -a\vec{U} - b\vec{U}\left|\vec{U}\right| - c\frac{\partial \vec{U}}{\partial t} \tag{4.5}$$

The contribution of laminar, turbulent and inertial resistance are described by coefficients a, b and c respectively (cf. Gu and Wang, 1991; Van Gent, 1995b):

$$\begin{aligned} a &= \tfrac{1}{K} \\ b &= \beta \tfrac{1-n_p}{n_p^3} \tfrac{1}{gD} \\ c &= \tfrac{1+\gamma \frac{1-n_p}{n_p}}{n_p g} \end{aligned} \tag{4.6}$$

where n_p is the porosity, D is a characteristic grain size and β and γ are coefficients.

In a series of laboratory experiments with gravel and rock ranging from 0.02–0.06 m diameter, Van Gent (1995b) found $\beta \backsim \mathcal{O}\left(10^0\right)$ and $\gamma \backsim \mathcal{O}\left(10^{-1} - 10^0\right)$. Although these values may not strictly be valid for all gravel beds, it is assumed that applicable values for gravel beds will not differ significantly from these values. If we

Order of magnitude of groundwater specific discharge velocity (ms^{-1})	Order of magnitude of contribution to head gradient (-)			
	Laminar	Turbulent	Inertial (waves)	Inertial (tides)
10^{-3}	$10^{-2} - 10^{0}$	$10^{-5} - 10^{-3}$	$10^{-5} - 10^{-4}$	$10^{-9} - 10^{-8}$
10^{-2}	$10^{-1} - 10^{1}$	$10^{-3} - 10^{-1}$	$10^{-4} - 10^{-3}$	$10^{-8} - 10^{-7}$
10^{-1}	$10^{0} - 10^{2}$	$10^{-1} - 10^{1}$	$10^{-3} - 10^{-2}$	$10^{-7} - 10^{-6}$
10^{0}	$10^{1} - 10^{3}$	$10^{1} - 10^{3}$	$10^{-2} - 10^{-1}$	$10^{-6} - 10^{-5}$

Table 4.1: Contribution of laminar, turbulent and inertial resistive forces in Equation 4.5 for varying groundwater velocities. Inertial contributions for waves and tides are based on periods of $\mathcal{O}\left(10^{1}\right)$ and $\mathcal{O}\left(10^{5}\right)$ seconds respectively.

assume for gravel beds that $K \sim \mathcal{O}\left(10^{-3} - 10^{-1}\right)$, $D \sim D_{50} \sim \mathcal{O}\left(10^{-3} - 10^{-1}\right)$ and $n_p \sim 0.35$, then estimates for the coefficients in Equation 4.6 are: $a \sim \mathcal{O}\left(10^{1} - 10^{3}\right)$, $b \sim \mathcal{O}\left(10^{1} - 10^{3}\right)$ and $c \sim \mathcal{O}\left(10^{-1} - 10^{0}\right)$. The contribution of the laminar, turbulent and inertial terms in Equation 4.5 are shown in Table 4.1 for varying specific discharge velocities. The table shows that in gravel beds the laminar term is dominant under low velocity conditions, and the turbulent term is of equal importance to the laminar term under high velocity conditions. The inertial term is several orders of magnitude smaller than the other terms under all flow conditions and can therefore be neglected from the calculation of groundwater dynamics in gravel beds.

If the inertial contribution to the head gradient is neglected, Equation 4.5 is simplified to the Darcy-Forchheimer law (Forchheimer, 1901):

$$\nabla H = -a\vec{U} - b\vec{U}\left|\vec{U}\right| \tag{4.7}$$

Many empirical and semi-empirical relations have been suggested for a and b (e.g., Ergun, 1952; Ward, 1964 and many others), but unfortunately no single relation has been shown to be valid for varying grain sizes without substantial calibration of coefficients. In addition, most relations give no practical guidance to users how to estimate the correct coefficients, other than to carry out laboratory experiments.

Further simplification of Equation 4.7 results in an effective hydraulic conductivity that is a function of laminar and turbulent coefficients a' and b', and the absolute specific discharge velocity $|U|$:

$$\nabla H = -\frac{1}{K\left(a', b', |U|\right)}\vec{U} \tag{4.8}$$

The approach taken in this thesis is based on Equation 4.8 and the method applied in the USGS MODFLOW-2005 groundwater model (Harbaugh, 2005), in which the turbulent hydraulic conductivity is estimated based on the laminar hydraulic conductivity K_{lam} and the Reynolds number at the onset of turbulence Re_{crit} (Halford, 2000; Kuniansky et al., 2008; Shoemaker et al., 2008):

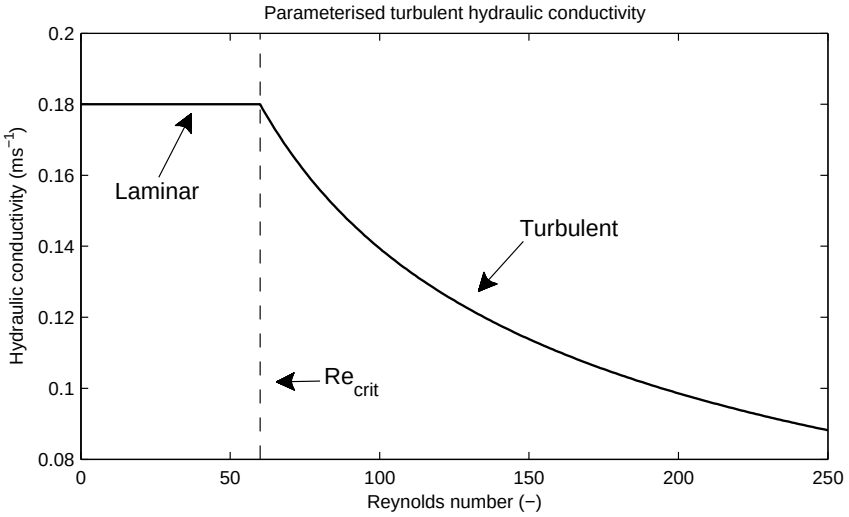

Figure 4.2: Example of the parametrisation of the hydraulic conductivity in turbulent flow conditions. In this example the laminar hydraulic conductivity is 0.18 ms^{-1} and the critical Reynolds number for the start of turbulent flow is 60.

$$K(Re) = \begin{cases} K_{lam}\sqrt{\frac{Re_{crit}}{Re}} & Re > Re_{crit} \\ K_{lam} & Re \leq Re_{crit} \end{cases} \tag{4.9}$$

where the Reynolds number Re is calculated using the median grain size D_{50}, the kinematic viscosity of water ν and the groundwater velocity in the pores $\frac{U}{n_p}$:

$$Re = \frac{|U| D_{50}}{n_p \nu} \tag{4.10}$$

and n_p is the porosity.

Since the hydraulic conductivity in the turbulent regime is dependent on the local velocity, an iterative approach is taken to find the correct hydraulic conductivity and velocity.

The advantage of the parametrisation given in Equation 4.9 is that the two physical properties of the coefficients K_{lam} and Re_{crit} are easily understood, and can be estimated relatively well in the field. An example of the relation between the Reynolds number and the hydraulic conductivity K is shown in Figure 4.2.

4.3.3 Vertical groundwater head approximation

Since the groundwater model is depth-averaged, the model cannot compute true vertical profiles of the groundwater head and velocity. In order to improve the estimate of the groundwater head variation over the vertical, a quasi-3D modelling approach is applied. In this approach the groundwater head is approximated by a curve in the vertical (Figure 4.3), which is set by three conditions:

1. There is no exchange of groundwater between the aquifer and the impermeable layer below the aquifer. Therefore the vertical velocity at the bottom of the aquifer and the vertical head gradient at the bottom of the aquifer are zero:

$$w_b = 0 \therefore \frac{\partial H}{\partial \sigma} \mid^{\sigma=0} = 0 \tag{4.11}$$

   where σ is the vertical coordinate above the bottom of the aquifer ξ_{gw}, and the subscript b refers to the location at the bottom of the aquifer. (Figure 4.3):

2. The groundwater head at the upper surface of the groundwater ($\sigma = h_{gw}$, where h_{gw} is the groundwater height above ξ_{gw}) is continuous with the head applied at the surface H_{bc}:

$$H(h_{gw}) = H_{bc} \tag{4.12}$$

3. The vertical velocity is assumed to increase or decrease linearly from the bottom of the aquifer to the upper surface of the groundwater:

$$w(\sigma) = \alpha\sigma \therefore \frac{\partial^2 H}{\partial \sigma^2} = \alpha \tag{4.13}$$

   where α is an arbitrary constant.

Conditions 1 and 2 above follow strictly from the conditions imposed on the entire groundwater model and are therefore valid within the modelling approach. However, point 3 is an assumption that may not be valid in all situations and is a limitation of this Q3D approach. The error associated with the assumption made in point 3 is considered preferable to the computational cost of a fully three-dimensional groundwater modelling approach.

The vertical groundwater head approximation can be solved for the three imposed conditions by a parabolic function:

$$H(\sigma) = \beta\sigma^2 + H_{bc} - \beta h_{gw}^2 \tag{4.14}$$

where β is the groundwater head parabolic curvature coefficient.

The depth-average value of the groundwater head $\overline{H}$ is used to calculate the horizontal groundwater flux and is found by integrating the groundwater head approximation (Equation 4.14) over the vertical:

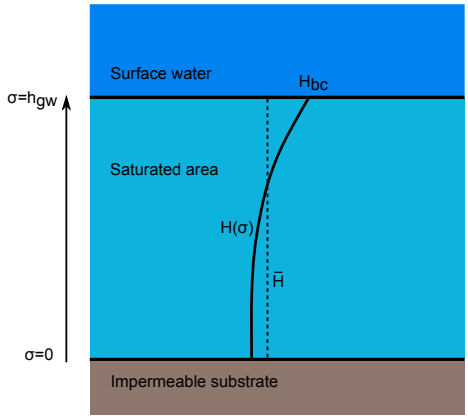

Figure 4.3: Schematic representation of quasi-3D groundwater head approximation.

$$\overline{H} = \frac{1}{h_{gw}} \int_0^{h_{gw}} H(\sigma)\, d\sigma = H_{bc} - \frac{2}{3}\beta h_{gw}^2 \tag{4.15}$$

The depth-average groundwater head $\overline{H}$ is solved alongside the unknown groundwater head parabolic curvature coefficient β by substitution of Equation 4.15 in the coupled equations of continuity (Equation 4.1) and groundwater motion (Equation 4.3), as described in Appendix A. Note that Raubenheimer et al. (1998) found a hyperbolic decay, rather than a parabolic decay function for the vertical groundwater head description in sandy beds. This approach is detailed in Appendix B, but was not found to substantially alter model results (Appendix C).

4.3.4 Exchange with surface water

In the groundwater model there are three mechanisms for the exchange of groundwater and surface water: submarine exchange, infiltration and exfiltration (Figure 4.1). The rate of exchange between the groundwater and surface water S is given in terms of surface water volume, and is defined positive when water is exchanged from the surface water to the groundwater.

The groundwater and surface water are said to be in a connected state where and when the groundwater level reaches to the top of the bed and surface water exists above the bed. This state is described by a spatially and temporally varying logical κ, which is true where groundwater and surface water are connected and false in all other situations:

$$\kappa = \begin{cases} \textbf{true} & \zeta_{gw} = \xi \wedge \zeta \geq \xi \\ \textbf{false} & \zeta_{gw} < \xi \vee h = 0 \end{cases} \tag{4.16}$$

where ζ_{gw} is the groundwater surface level.

Submarine exchange represents the high and low frequency infiltration and exfiltration through the bed due to pressure gradients across the saturated bed. This process only takes place where the groundwater and surface water are connected. The rate of submarine exchange S_s is determined by the vertical specific discharge velocity at the interface between the groundwater and surface water. The value of this velocity can be found using the vertical derivative of the Q3D groundwater head approximation (Equation 4.14) at the groundwater-surface water interface:

$$S_s = -w(h_{gw}) = K\frac{\delta H}{\delta \sigma}\,|^{\sigma=h_{gw}} = 2\beta h_{gw} K \tag{4.17}$$

Infiltration and exfiltration can only occur in locations where the groundwater and surface water are not connected. Infiltration takes place when surface water covers an area in which the groundwater level is lower than the bed level (i.e. an unsaturated bed, Figure 4.4a). The flux of surface water into the bed S_i is related to the pressure gradient across the wetting front in a manner similar to the approach taken by Packwood (1983):

$$S_i = K\left(\frac{1}{\rho g}\frac{p|^{z=\xi}}{\delta_{wf}} + 1\right) \tag{4.18}$$

where $p|^{z=\xi}$ is the surface water pressure at the bed and δ_{wf} is the thickness of the wetting front. Note that the infiltration velocity (momentarily) tends to infinity when the thickness of the wetting front is zero. In order to ensure numerical stability under such conditions, XBeach-G employs an implicit backward Euler method to compute the infiltration velocity (discussed in Appendix A, Equation A.3).

The thickness of the wetting front increases over time during the infiltration event according to the infiltration velocity:

$$\delta_{wf}(t) = \int \frac{S_i}{n_p} dt \tag{4.19}$$

Since the groundwater model is depth-averaged and cannot track multiple layers of groundwater infiltrating into the bed, the wetting front thickness is reset to zero when there is no available surface water, the groundwater exceeds the surface of the bed, or the groundwater and the surface water become connected. In addition, all infiltrating surface water is instantaneously added to the groundwater volume, independent of the distance from the bed to the groundwater table. Since the groundwater model neglects the time lag between infiltration at the beach surface and connection with the groundwater table a phase error may occur in the groundwater response to swash dynamics. However, this phase error is expected to be small on permeable gravel beaches where the distance between the waterline and the groundwater table is generally small and does not affect the modelled infiltration velocities at the beach face.

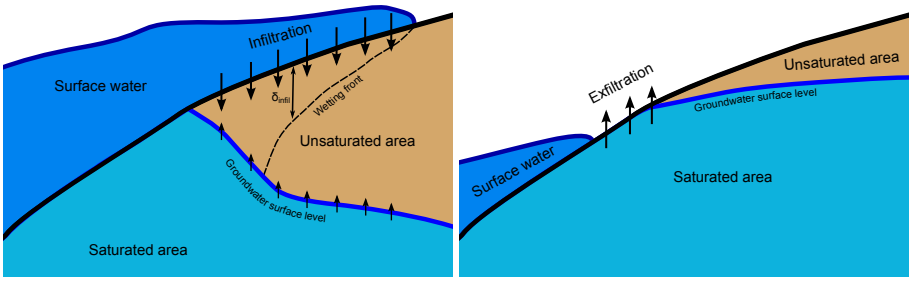

(a) Example of infiltration *(b)* Example of exfiltration

Figure 4.4: Schematic example of infiltration during a swash event (panel a) and exfiltration due to a high groundwater table (panel b).

Exfiltration occurs where the groundwater and surface water are not connected and the groundwater level exceeds the bed level (Figure 4.4b). The rate of exfiltration S_e is related to the rate of the groundwater level exceeding the bed level:

$$S_e = n_p \frac{\partial (\xi - \zeta_{gw})}{\partial t} \tag{4.20}$$

4.3.5 Calculation of groundwater and surface water levels

The curvature coefficient β in the vertical groundwater head approximation is solved using the coupled equations for continuity and motion (Eqs. 4.1 and 4.3), thereby producing the depth-average horizontal groundwater head gradients and vertical head gradients at the groundwater surface, and subsequent depth-average horizontal and vertical specific discharge. In areas where the groundwater and surface water are not connected, the groundwater level change is related to the vertical specific discharge and the infiltration and exfiltration fluxes:

$$n_p \frac{\partial \zeta_{gw}}{\partial t} = w + S_i + S_e \tag{4.21}$$

In these same areas the surface water level is modified to account for infiltration and exfiltration:

$$\frac{\partial \zeta}{\partial t} = -S_i - S_e \tag{4.22}$$

In areas where the groundwater and surface water are connected, the groundwater level remains at the level of the bed, since the computed vertical velocity at the surface w is exactly equal and opposite to the submarine exchange S_s. The surface water level is modified to account for the submarine exchange with the groundwater:

$$n_p \frac{\partial \zeta_{gw}}{\partial t} = w + S_s = 0 \tag{4.23}$$

$$\frac{\partial \zeta}{\partial t} = -S_s \tag{4.24}$$

In cases where there is insufficient surface water to permeate into the bed to ensure the groundwater level remains at the bed level, a fractional time step approach is taken in which the area is considered to be connected while there is sufficient surface water, and considered unconnected once the surface water has drained away. A similar approach is taken when the groundwater level reaches the bed level during an infiltration event.

4.3.6 Boundary conditions

Since the groundwater dynamics are described by a parabolic equation, the system of equations requires boundary conditions at all horizontal and vertical boundaries, as well as an initial condition. At the horizontal boundaries, the groundwater head is assumed to be constant (zero flux condition):

$$\begin{aligned} \tfrac{\delta H}{\delta x} \,|^{x=x_{boundary}} &= 0 \\ \tfrac{\delta H}{\delta y} \,|^{y=y_{boundary}} &= 0 \end{aligned} \tag{4.25}$$

At the bottom of the aquifer, a zero flux condition is imposed:

$$\frac{\partial H}{\partial \sigma} \,|^{\sigma=0} = 0 \tag{4.26}$$

At the surface of the groundwater, the head is set to the surface water head at the bed where the groundwater and surface water are connected, or to the atmospheric pressure head where they are not connected:

$$H_{bc} = \begin{cases} \frac{p|^{z=\xi}}{\rho g} + \xi & \kappa \\ \zeta_{gw} & \neg\kappa \end{cases} \tag{4.27}$$

The initial condition for the solution is specified by the model user in terms of the initial groundwater head.

4.4 Groundwater model validation dataset

The groundwater model coupled to the surface water model (Chapter 3) has been calibrated and validated using hydrodynamic data measured during the BARDEX physical model experiment (Williams et al., 2012a).

The hydrodynamic data of one measurement series of the BARDEX experiment

Series	Offshore water level (m)	Lagoon water level (m)	Significant wave height (m)	Peak wave period (s)
BAC6equi	2.6–2.9	3.6–3.0	-	-
BABB1	2.5	2.5	0.8	4.5
BAC1	2.5	1.0	0.8	4.5
BAC2	2.5	3.5	0.8	4.5
BAE10	3.7	3.2	0.8	7.7

Table 4.2: Wave and tide forcing conditions for groundwater calibration and validation simulations.

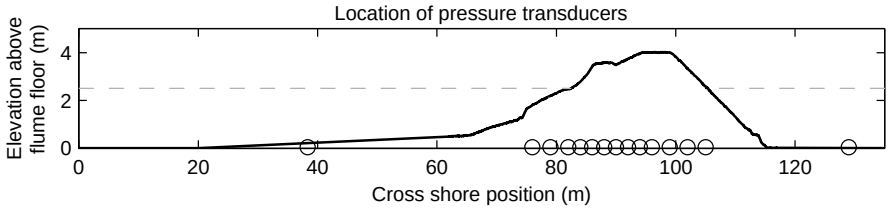

Figure 4.5: Location of buried PTs (○), and the representative water levels and cross shore profile of the BARDEX gravel barrier for series BABB1. Note that water levels and cross-shore profile varied between the experiment series discussed in this chapter.

without waves (series BAC6equi; Table 4.2) were used to calibrate the groundwater model. The model was subsequently validated using four 10-minute measurement series of the BARDEX experiment which include waves, run-up and overwash (BABB1, BAC1, BAC2 and BAE10). Modelled groundwater hydrodynamics are compared to the groundwater head measured at 15 PTs buried in the bed beneath the gravel barrier (circles in Figure 4.5).

Where modelled hydrodynamics are compared to measured hydrodynamics in this chapter, the model accuracy is expressed in terms of the root-mean-square error (RMSE) and bias as defined in Equation 3.9 and Equation 3.10. Further, the skill of a model, often referred to as the Brier Skill Score (BSS), can be described by the increase in the accuracy of the model relative to the accuracy of another existing model or best-estimate:

$$\mathrm{BSS} = 1 - \frac{\sum_{i=1}^{n} \left(x_{modelled,i} - x_{measured,i}\right)^2}{\sum_{i=1}^{n} \left(x_{estimated,i} - x_{measured,i}\right)^2} \tag{4.28}$$

Positive BSS scores imply that the model is an improvement over the estimate. A BSS of 1 implies perfect model agreement, whereas a BSS of, for instance, 0.9 implies that the variance of the model error is only 10% of the variance of the error of the estimate. A BSS of zero indicates that the model and estimate are of equal accuracy and negative skill scores imply that the model is a worsening over the estimate.

Parameter	Parameter calibration range	Calibrated value
K_{lam}	0.10 ms^{-1} – 0.24 ms^{-1}	0.155 ms^{-1}
Re_{crit}	0–300	225

Table 4.3: Parameter calibration range and best-fit calibration value for the groundwater model.

4.5 Groundwater model calibration

To calibrate the groundwater model a part of the BARDEX dataset without waves is selected in which groundwater levels vary spatially and temporally. The period selected for this calibration is measurement series BAC6equi, in which an initially large gradient in the water level across the barrier (sea level = 2.6 m; lagoon level = 3.5 m) equilibrates over a period of approximately an hour by means of groundwater flow through the barrier (sea and lagoon level = 2.9 m).

Multiple simulations of series BAC6equi are run in which the uniform hydraulic conductivity K_{lam} and critical Reynolds number Re_{crit} are varied independently within ranges found experimentally during the BARDEX experiment by Turner and Masselink (2012) and proposed by Shoemaker et al. (2008), see Table 4.3. In all calibration simulations, the water level on the lagoon boundary (cross-shore position 137 m) is forced using the measured water level in the lagoon. . The envelope of the groundwater head simulated during all calibration simulations is shown in Figure 4.6 (light orange) for four locations under the gravel barrier.

The accuracy of every calibration simulation is determined by the combined RMSE of the simulated groundwater head time series at all buried PTs under the gravel barrier (PT1–PT13). The calibrated values of the hydraulic conductivity and critical Reynolds number are determined by the simulation with the lowest combined RMSE. These values are found to be 225 for the critical Reynolds number and 0.155 ms^{-1} for the hydraulic conductivity (Table 4.3), which corresponds well with the values of hydraulic conductivity (range 0.1–0.3 ms^{-1}, mean 0.16 ms^{-1}) found by Turner and Masselink (2012).

The results of the simulation of BAC6equi using the calibrated model parameters are shown in Figure 4.6 (orange dashed). The RMSE and absolute bias at every buried PT using the calibrated model is shown to be less than 0.03 m (Table 4.4). The skill of the groundwater model relative to an estimate of zero groundwater head change (i.e., no groundwater dynamics) is very high, emphasizing the importance of including groundwater dynamics.

4.6 Groundwater model set-up and validation

The groundwater model of XBeach-G is validated using three series of the BARDEX dataset in which wave motions were limited to run-up on the beach face (series BABB1, BAC1 and BAC2), and one series in which overtopping and overwash took place (series BAE10). Since the models used in this study do not contain morpho-

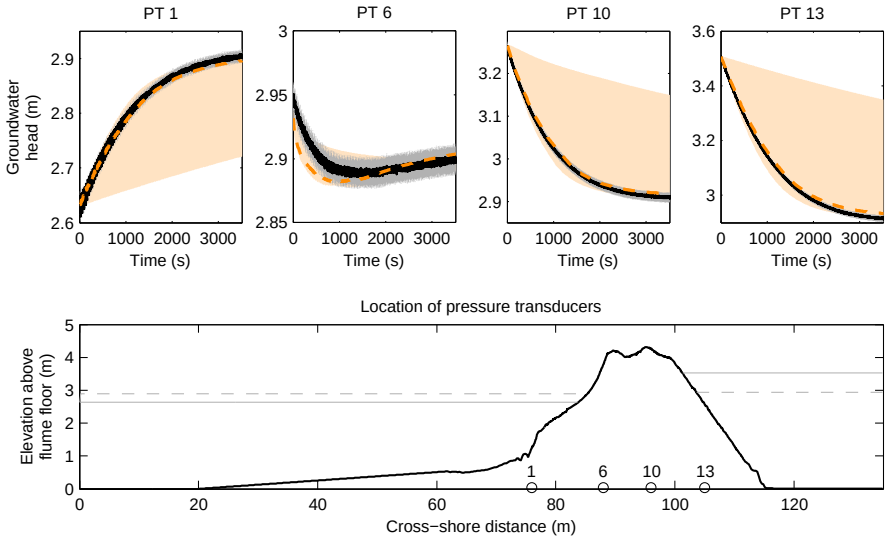

Figure 4.6: Time series of measured (—) and simulated (– –) groundwater head at the flume floor at four locations in the gravel barrier using the calibrated model for series BAC6equi. Light orange shading represents the spread in model results for the entire range of parameter settings, whereas grey shading represents uncertainty in the instrument data. The locations of the buried PTs relative to the barrier profile (—) and still water levels at the start (—) and end (– –) are shown in the bottom panel.

	RMSE (m)	Bias (m)	BSS (-)
Maximum PT1–PT13	0.03	-0.02	1.00
Median PT1–PT13	0.01	-0.01	0.99
Minimum PT1–PT13	<0.01	<0.01	0.05

Table 4.4: Error statistics of calibrated groundwater model for the groundwater head at all buried PT measurement points during series BAC6equi. The BSS is determined relative to no groundwater head change.

dynamic updating for gravel beds, all simulations are limited to 10 minutes, during which the bed profile is assumed to be quasi-stationary. All simulations use the calibrated coefficients for hydraulic conductivity and critical Reynolds number described in the previous section. The model set-up and validation of the surface water model of XBeach-G coupled to the groundwater model of XBeach-G for these simulations is discussed in Chapter 3 (Section 3.4) where the coupled model is shown to represent the measured surface water hydrodynamics well.

4.6.1 Run-up simulations

Three measurement series of the BARDEX dataset with similar waves, but varying groundwater gradients across the barrier, are simulated using the coupled groundwater-surface water model. These simulations are characterized by equal offshore and lagoon water levels (BABB1), a low lagoon water level (BAC1) and a high lagoon water level (BAC2), see Table 4.2. Validation of the wave spectrum transformation and wave run-up for these wave series is presented in Chapter 3 (Figures 3.4 and 3.10), where it is shown that the model is capable of accurately reproducing the surface water conditions during the measurement series. This is important for the validation of the groundwater model as the surface water dynamics contribute strongly to the boundary conditions for the groundwater model, through forcing of infiltration and potential for exfiltration (Equations 4.18 and 4.20) and through pressure at the surface water-groundwater interface (Equation 4.27).

The measured and modelled groundwater head time series and variance density spectra at four locations in the gravel barrier for all three run-up simulations are shown in Figures 4.7–4.9. The figures show that the coupled groundwater-surface water model can reproduce the measured groundwater dynamics on the offshore side of gravel barrier (PT1 and PT6) relatively well in all three simulations. In particular, the model is able to capture the shift from high-frequency variance at PT1 to low-frequency variance at PT6 well. Figure 4.10 shows the time-averaged modelled groundwater head and the groundwater head measured at the location of all the buried PTs. The figure shows the importance of the non-hydrostatic groundwater model in reproducing the observed groundwater head at the bottom of the flume below swash zone ($x \approx 83 - -85$ m) in BABB1 and BAC1, where a hydrostatic model would have predicted the height of the groundwater level (green line) as the groundwater head.

On the back-barrier (PT10 and PT13), the model over predicts the groundwater level in series BABB1 and BAC1, also visible in Figure 4.10. This over prediction may be due to the limitations of the Q3D approximation of the groundwater head, by spatial variations of the hydraulic conductivity of the barrier, which are not accounted for in the model and which lead to larger variations in the groundwater head than predicted by the model, or by instrument errors.

Overall, the groundwater model is capable of reproducing the measured groundwater head time series at all buried PTs in the gravel barrier with a median RMSE of 0.04–0.05 m (Table 4.4), which is approximately 2–5 times larger than the estimated accuracy of the measurements. Most importantly, the groundwater model shows clear skill over an estimate of zero groundwater head change.

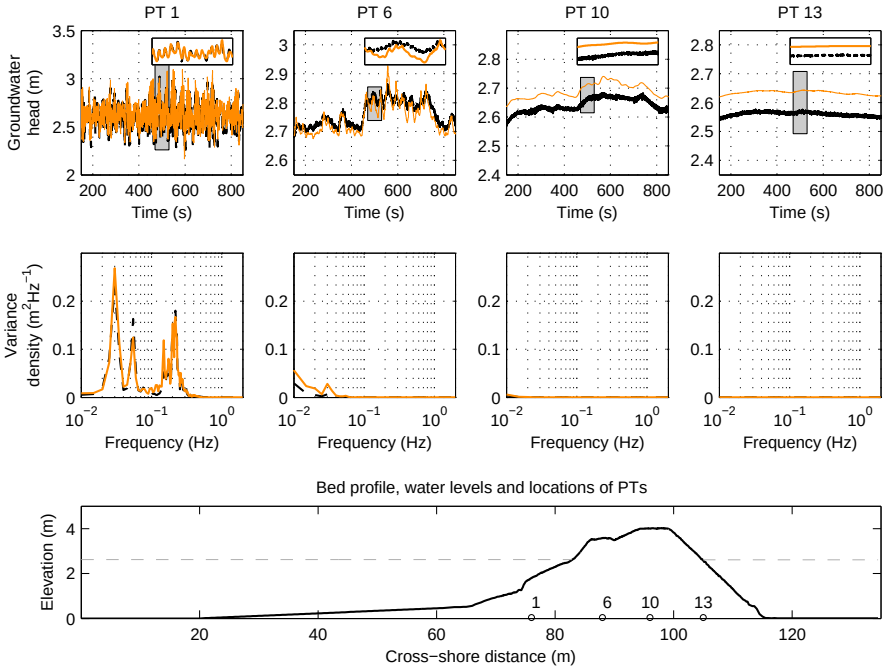

Figure 4.7: Top panels: Measured (—) and modelled (—) time series of the groundwater head relative to the flume floor at the locations of four buried PTs during series BABB1. A detailed time series, indicated by the grey shaded area, is shown in the top-right corner of each panel. Centre panels: Measured (– –) and modelled (—) variance density spectra of the groundwater head at the locations of four buried PTs during series BABB1. The locations of the buried PTs relative to the barrier profile (—) and still water levels (– –) are shown in the bottom panel.

	BABB1			BAC1			BAC2		
	RMSE (m)	Bias (m)	BSS (-)	RMSE (m)	Bias (m)	BSS (-)	RMSE (m)	Bias (m)	BSS (-)
Maximum	0.09	0.08	0.97	0.08	0.07	0.98	0.08	-0.08	0.88
Median	0.05	<0.01	0.78	0.04	<-0.01	0.89	0.05	-0.02	0.71
Minimum	0.02	<0.01	0.23	0.02	<-0.01	-0.63	<0.01	<-0.01	0.32

Table 4.5: Error statistics for the groundwater head at all buried PT measurement points (PT1–PT13) during series BABB1, BAC1 and BAC2. The BSS is determined relative to no groundwater head change.

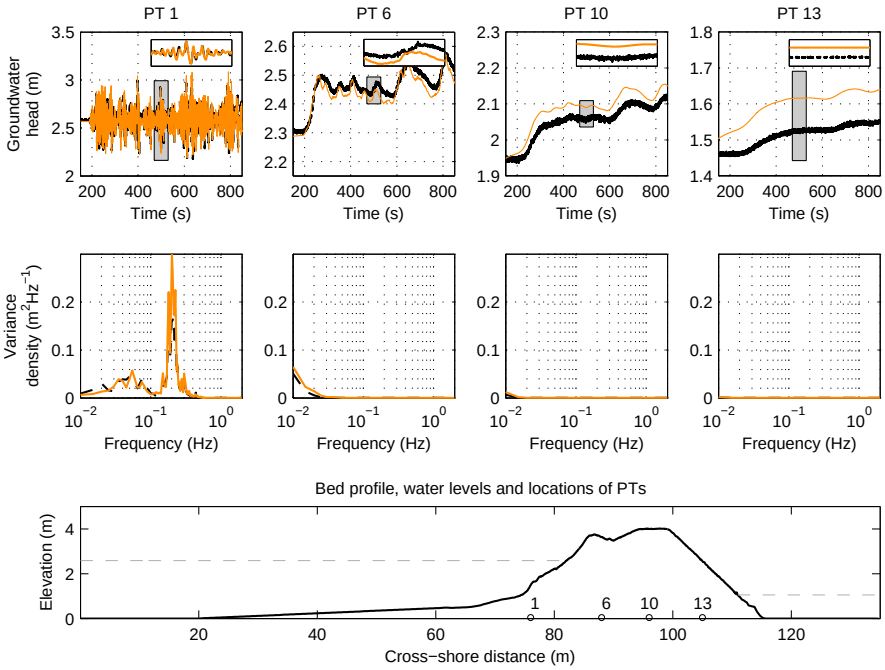

Figure 4.8: Measured (—) and modelled (—) time series of the groundwater head relative to the flume floor (top panels), and measured (– –) and modelled (—) variance density spectra of the groundwater head at the locations of four buried PTs during series BAC1 (cf. Figure 4.7).

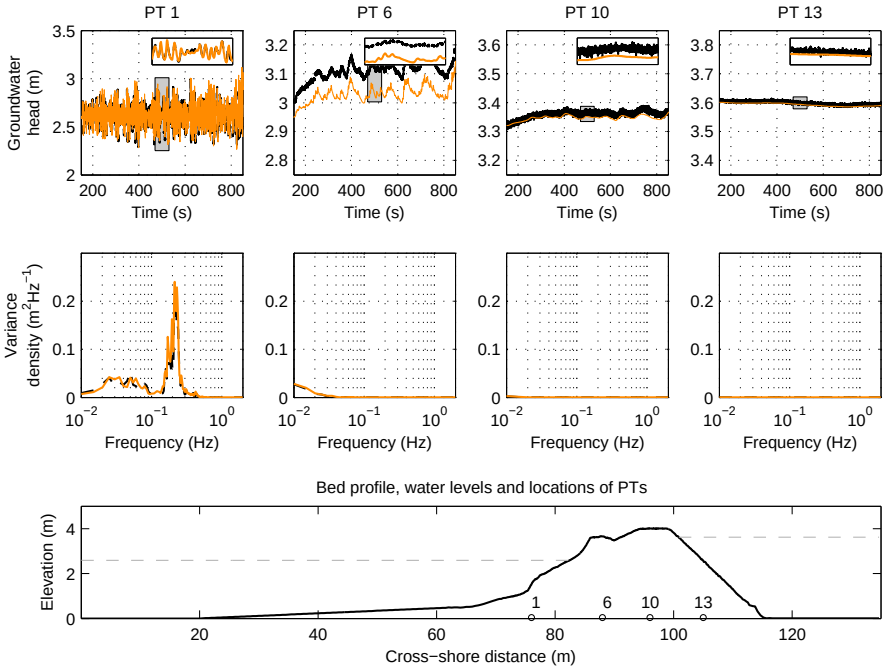

Figure 4.9: Measured (—) and modelled (—) time series of the groundwater head relative to the flume floor (top panels), and measured (– –) and modelled (—) variance density spectra of the groundwater head at the locations of four buried PTs during series BAC2 (cf. Figure 4.7).

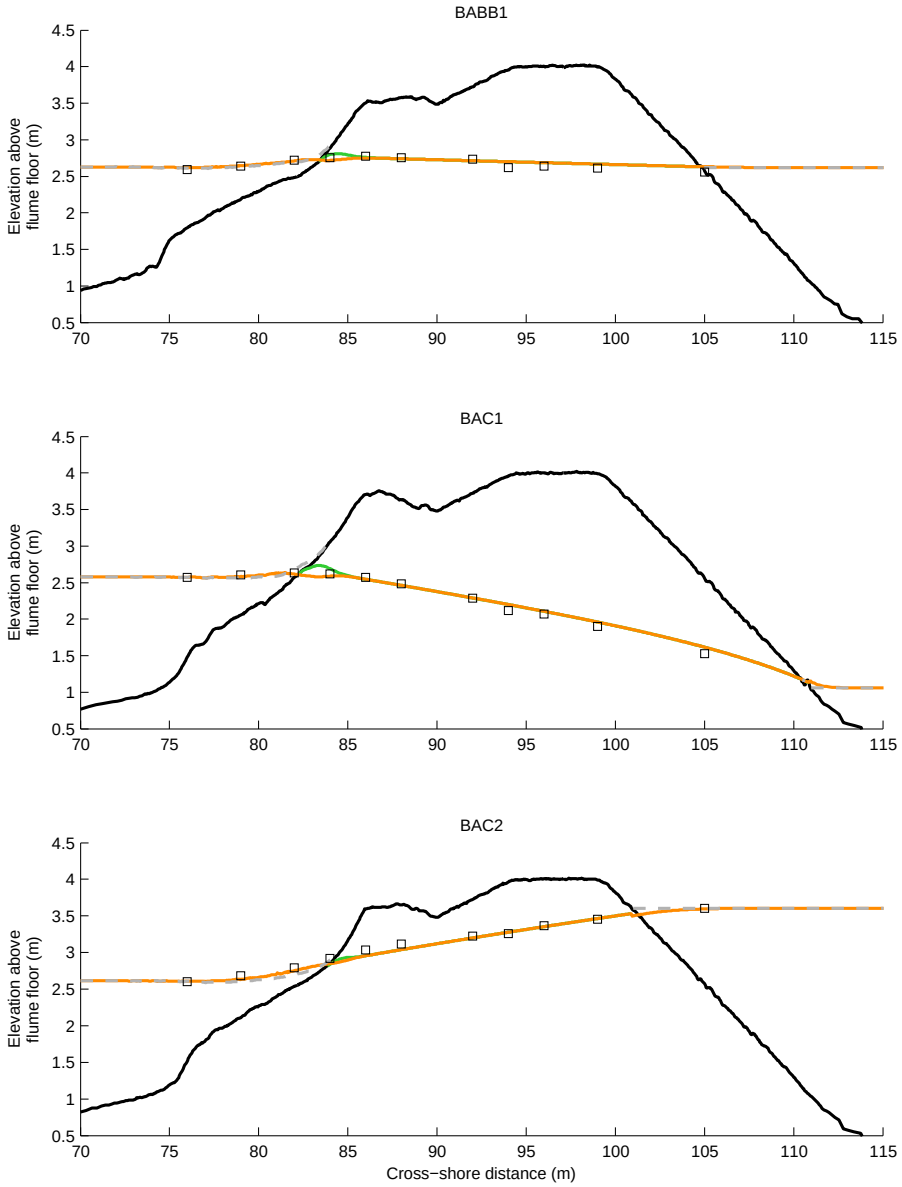

Figure 4.10: Measured mean groundwater head measured at 11 buried PTs on the flume floor (□), modelled mean groundwater head at the flume floor (—), modelled mean groundwater level (—), bed profile (—) and mean water surface levels (– –) for series BABB1 (top panel), BAC1 (centre panel) and BAC2 (bottom panel). Note the difference between the groundwater level and the groundwater head at the flume floor at ∼ 83–85 m cross-shore position in series BABB1 and BAC1.

	RMSE (m)	Bias (m)	BSS (-)
Maximum PT1–PT13	0.09	0.09	0.93
Median PT1–PT13	0.08	0.04	0.78
Minimum PT1–PT13	0.06	0.02	0.50

Table 4.6: Error statistics for the groundwater head at all buried PT measurement points (PT1–PT13) during series BAE10. Skill is determined relative to no groundwater head change.

4.6.2 Overwash simulation

One 10-minute measurement series of the BARDEX dataset in which overtopping and overwash took place (series BAE10) is selected for simulation with the XBeach-G model. As in the run-up simulations, the modelled surface water elevation spectrum at the location of the shallow water PT and overtopping time series are well resolved by the model (Chapter 3; Figures 3.4 and 3.14).

The time series and variance density spectra of measured and modelled groundwater head at four locations in the barrier are shown in Figure 4.11 and the time-averaged modelled and measured groundwater head at the locations of the buried PTs is shown in Figure 4.12. As was the case for the run-up simulations, the model shows considerable skill in reproducing the measured groundwater head variation in time and space, and the frequency shift of variance from high to low frequencies across the barrier (Figure 4.11), and the non-hydrostatic groundwater model provides a better estimate of the groundwater head beneath the swash zone ($x \approx 95$ m) than a hydrostatic approximation. Overall, the median RMSE for the groundwater head across all buried PTs under the barrier is 0.08 m (Table 4.6), which is considered satisfactory for the purpose of this model. The groundwater model shows considerable skill ($\geq$0.50) over an estimate of zero groundwater head change.

4.7 Effect of groundwater interactions and implications for modelling run-up and overwash on gravel barriers

In analogy with the sensitivity study discussed in Section 3.6 to investigate the importance of wave-resolved modelling on simulated wave run-up and overtopping, this section investigates the influence of groundwater processes on hydrodynamics on gravel beaches and barriers during storms. To this end, wave run-up during CB02, LB03, SS01 and SE01, representing a broad range of natural conditions, and wave overtopping and overwash during BAE9 and BAE10 are re-examined using a modified version of XBeach-G in which groundwater processes are excluded (referred to as NGW).

Figure 4.13 shows the difference between wave run-up measured during CB02, LB03, SS01 and SE01, and wave run-up modelled by XBeach-G (orange symbols) and NGW (green symbols). Overall, the figure shows wave run-up predictions by the NGW model to consistently higher than those of the XBeach-G model, which is in

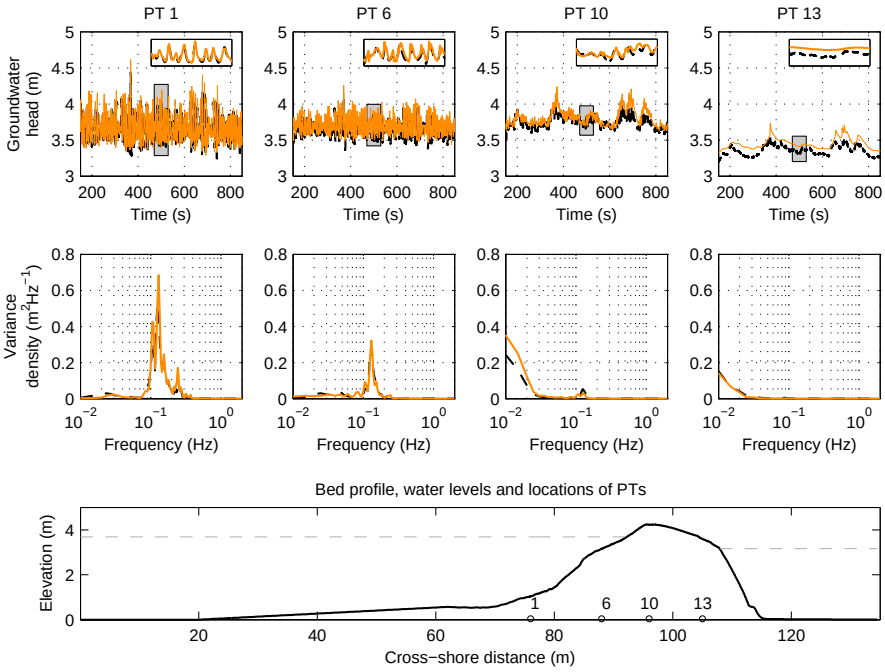

Figure 4.11: Top panels: Measured (—) and modelled (—) time series of the groundwater head relative to the flume floor at the locations of four buried PTs during series BAE10. A detailed time series, indicated by the grey shaded area, is shown in the top-right corner of each panel. Centre panels: Measured (– –) and modelled (—) variance density spectra of the groundwater head at the locations of four buried PTs during series BAE10. The locations of the buried PTs relative to the barrier profile (– –) and still water levels (– –) are shown in the bottom panel.

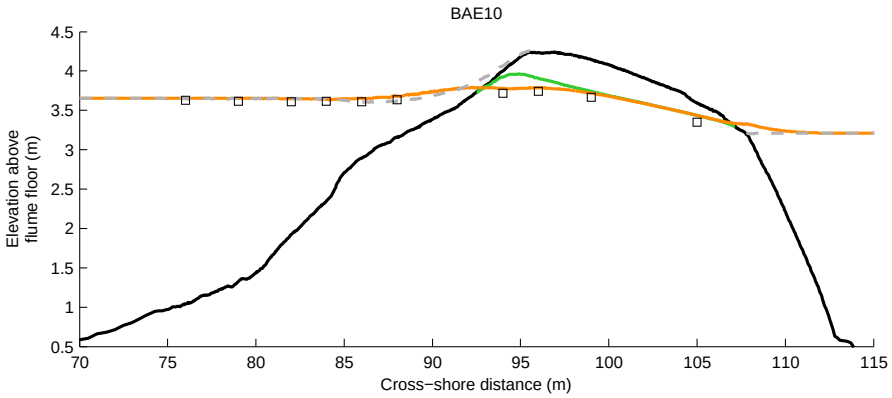

Figure 4.12: Measured mean groundwater head measured at 10 buried PTs on the flume floor (□), modelled mean groundwater head at the flume floor (—), modelled mean groundwater level (—), bed level (—), and mean water surface levels (– –) for series BAE10. Note the difference between the groundwater level and the groundwater head at the flume floor at 95 m cross-shore position.

line with earlier research (e.g., Bagnold, 1940 and many others). In relative terms the differences between the model predictions are small (median difference 8% of observed wave run-up level) compared to the differences discussed in Section 3.6, and generally fall within the range of the observed natural variation in run-up levels and modelled variation due to variations in the random wave times series applied at the model boundary (cf. Packwood, 1983).

The effect of groundwater processes on modelling overtopping and overwash is analysed by re-simulating series BAE10 with the NGW model, in a manner similar to that carried out for the run-up simulations. Figure 4.14 shows measured swash depths (black lines), swash depths predicted by XBeach-G (orange lines) and swash depths predicted by the NGW model (green lines). The figure shows that the NGW model overestimates the number of overtopping swashes, and to a lesser degree, the depth of the overtopping swashes. Table 4.7 lists the BSS of XBeach-G (including groundwater processes), relative to the NGW model, in predicting swash depth time series. The table shows that the incorporation of groundwater interaction improves the accuracy of XBeach-G at all locations (all skill values are positive), and the improvement increases in landward direction to the back of the barrier. These data suggest that for barriers with sufficient width and hydraulic conductivity, the inclusion of groundwater interaction is essential to accurately simulate the hydrodynamics on the back-barrier during overtopping and overwash events, and ultimately overwash flow velocities, discharges and sediment transport fluxes.

The results of series BAE10 show that including groundwater interaction is important to accurately predict overtopping and overwash events. Since the groundwater model in XBeach-G allows water to infiltrate into the gravel as it overtops the barrier, XBeach-G predicts fewer and less deep overwash events on the back barrier than the

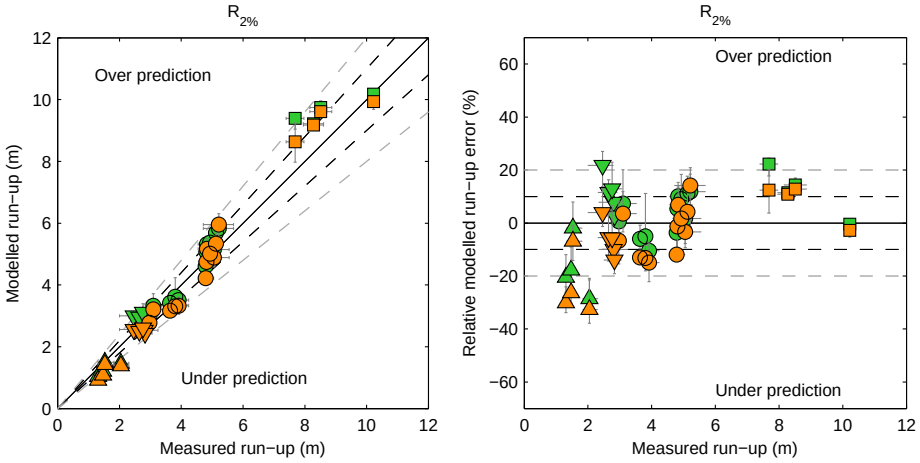

(a) Measured (horizontal) and modelled (vertical) $R_{2\%}$ run-up levels.

(b) Measured $R_{2\%}$ run-up (horizontal) and relative model run-up prediction error (vertical).

Figure 4.13: Comparison of $R_{2\%}$ run-up levels predictions using XBeach-G (orange) and NGW (green) during CB02 (□), LB03 (◯), SS01 (▽) and SE01 (△). The solid black line indicates zero relative error, and the black and grey dashed lines indicate a 10% and 20% relative error, respectively.

Instrument	BLS35	BLS36	BLS37	BLS38	BLS39	BLS40	BLS41	BLS42	BLS43	BLS44	BLS45
BSS	0.14	0.21	0.26	0.36	0.50	0.51	0.67	0.77	0.74	0.83	0.86

Table 4.7: BSS of simulated swash water depth at bed level sensors 35–45 in XBeach-G, relative to simulated water depth in the NGWmodel.

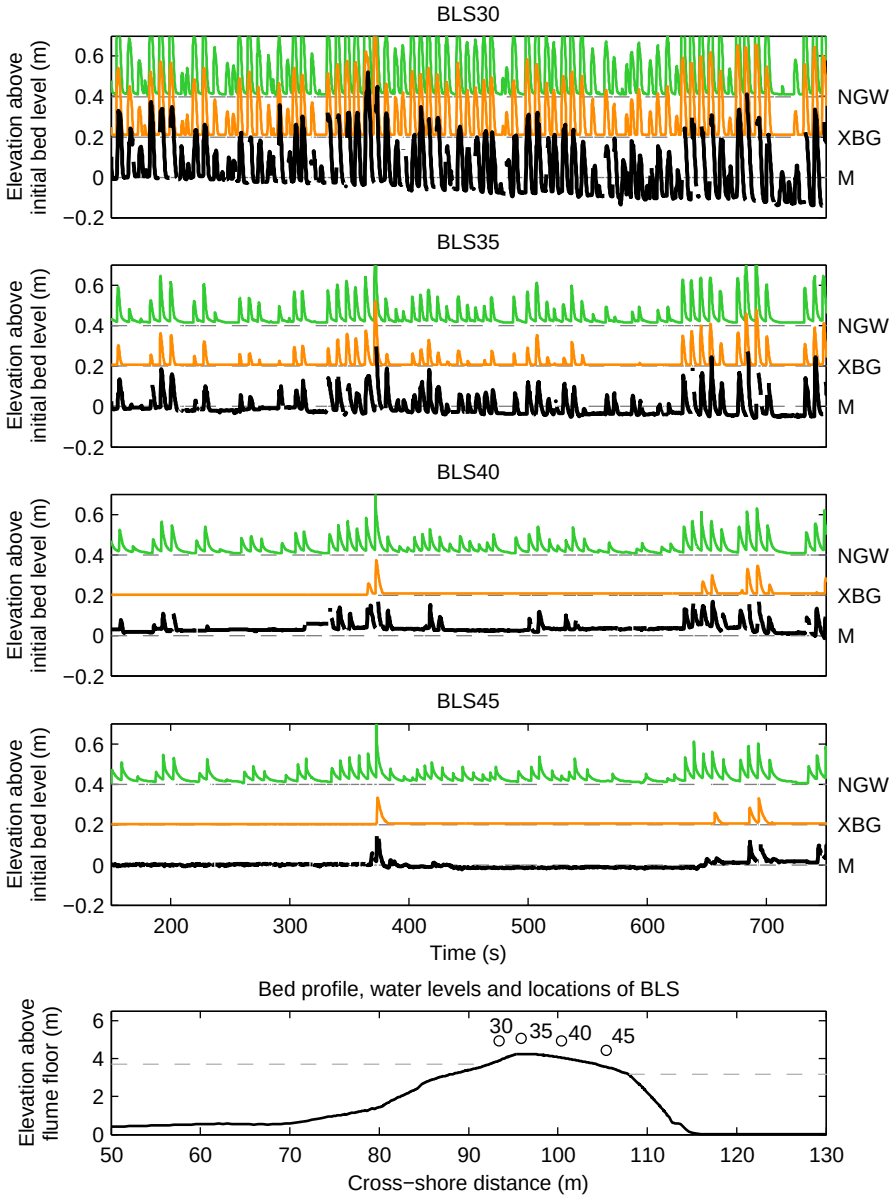

Figure 4.14: Wave overtopping time series during BAE10 at four points on the barrier, showing measured (M; bottom line, —), modelled with the XBeach-G model (XBG; central line, —) and modelled with NGW (NGW; no groundwater processes; top line, —). Note that the modelled results are offset in the vertical to facilitate a comparison between the simulations.

Model	BLS35	BLS36	BLS37	BLS38	BLS39	BLS40	BLS41	BLS42	BLS43	BLS44	BLS45
XBeach-G	25.2	21.8	15.3	11.2	8.6	7.2	6.1	5.4	5.0	4.6	4.5
NGW	41.9	41.9	41.9	41.9	41.9	41.9	41.9	41.8	41.8	41.8	41.8

Table 4.8: Modelled average overwash volumes ($ls^{-1}m^{-1}$) at bed level sensors 35–45 using XBeach-G (including groundwater processes) and NGW without groundwater interaction.

NGW model. This effect is reflected by the difference in overwash volumes across the barrier predicted by the models for series BAE10 (Table 4.8). The results show that the difference in predicted overwash volumes ranges from a factor of 1.7 at the crest to 9.3 at the back barrier. The variation in overwash discharge in the XBeach-G model (with groundwater processes) implies that approximately 72% of the water overtopping the crest infiltrates into the bed before it reaches the back of the barrier.

Since infiltration has been shown to play an important role in the simulation of overwash events and volumes in the BARDEX series, it is relevant to study whether this is also true for barriers with less (or more) permeable sand and gravel matrices. In order to do so, series BAE10 is re-simulated using the same initial and hydraulic boundary conditions as described in the previous section, but with values for the hydraulic conductivity K_{lam} varying from $5 \cdot 10^{-4}$ ms^{-1} – $5 \cdot 10^{-1}$ ms^{-1}.

The results for these sensitivity simulations are shown in Figure 4.15, in which overwash volumes at the barrier crest and on the back barrier are shown relative to a case with no groundwater interaction. Clearly, the importance of infiltration increases with hydraulic conductivity. However, the figure also shows that infiltration effects start to become important in series BAE10 at a hydraulic conductivity of approximately $1 \cdot 10^{-2}$ ms^{-1}, which corresponds to typical values for fine gravel and well-sorted sand-gravel mixtures (e.g., Coduto, 1999). Interestingly, similar values were found by Masselink and Li (2001) when determining a minimum threshold hydraulic conductivity for significant infiltration effects in the swash zone. Since the gravel barrier in series BAE10 is relatively narrow, and infiltration is enhanced by increasing cross-barrier width, it is expected that in real-world cases infiltration may become important at even lower values of hydraulic conductivity.

From the considerations above, it would appear essential to include groundwater interaction when studying overwash on gravel barriers. In practical applications this requires relatively accurate estimates of the effective hydraulic conductivity of the barrier, which can be determined in-situ by permeability tests, or from detailed groundwater time series (e.g., Fetter, 1988; Austin et al., 2013). Since even half an order of magnitude error can lead to large disparities in predicted overwash volumes, sensitivity simulations, in combination with predicted and measured run-up data, will remain indispensable for most real-world cases.

4.8 Conclusions

The results of simulations using XBeach-G including groundwater processes have shown that the incorporation of groundwater processes is essential to accurately sim-

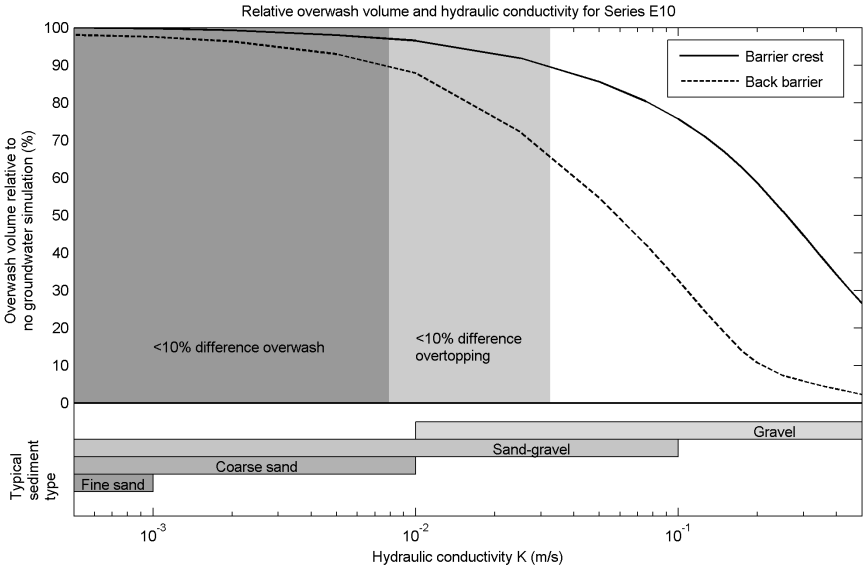

Figure 4.15: Relationship between hydraulic conductivity and relative overwash volumes at the barrier crest (BLS 35, —) and on the back barrier (BLS 45, – –) for series BAE10. Shaded areas show less than 10% difference in overwash volume at the barrier crest (light grey) and on the back barrier (dark grey). Sediment types are estimates for given hydraulic conductivity (e.g., Coduto, 1999).

ulate storm impacts on gravel beaches. In particular, infiltration of overtopping waves can lead to a significant reduction of the overwash discharge on the back barrier, which can only be properly accounted for if groundwater processes are resolved. The effect of infiltration on modelled wave run-up exceedence levels is modest, but discernible (5–10% higher values relative to a model with groundwater processes), and therefore relevant to the correct prediction of the overtopping threshold. The reduction of overwash discharge across the barrier crest and back barrier was shown to be strongly dependent on the hydraulic conductivity in one sensitivity study, and to become significant (>10% difference) for a hydraulic conductivity $K_{lam} > 1 \cdot 10^{-2}$ ms^{-1} for a relatively narrow gravel barrier. Other factors including barrier geometry (barrier width, crest slope, etc.) and aquifer properties (aquifer depth, etc.) are likely to affect this threshold hydraulic conductivity value.

Chapter 5

Morphodynamics of XBeach-G

This chapter presents and validates a sediment transport and morphology module for XBeach-G. The model is validated by simulating the morphodynamic response of one laboratory and four natural gravel barriers to ten separate storm events, where the observed morphodynamic response ranged from berm building to barrier rollover. Model results show that the model is capable of reproducing the type of morphodynamic response of the barrier well in qualitative and quantitative sense (median BSS 0.75), with higher skill for more energetic storm conditions. The inclusion of groundwater processes is shown to be essential for predicting the morphodynamic response of most gravel barriers, although the effect of varying hydraulic conductivity within estimated and published ranges is shown to be of secondary importance. Inclusion of acceleration forces on coarse gravel beaches is shown to significantly increase model skill and may be essential in modelling these types of beaches. The range of validation cases and lack of site-specific calibration show that XBeach-G can be applied to predict storm impacts on pure gravel beaches and barriers with reasonable to high confidence for a range of hydrodynamic forcing conditions and barrier response types.

5.1 Introduction

The XBeach-G model was developed, discussed and validated in terms of hydrodynamics, without morphological updating in Chapters 3 and 4. In those chapters, model simulations were restricted to situations in which bed level changes are assumed sufficiently small not to affect the overall hydrodynamic storm impact parameters (e.g., wave run-up and initial overtopping rates). While useful as an indicator of the potential for coastal flooding, a morphostatic model (without bed level updating) can neither be used to predict the full morphodynamic response of gravel coasts to a given storm, nor be used to investigate the relative influence of physical parameters on coastal morphodynamics. To address this shortfall, this chapter introduces and validates a new morphodynamic module for XBeach-G that allows the model to compute bed level changes on pure gravel beaches (cf. Jennings and Shulmeister, 2002) during storm events. The validated model is subsequently used to investigate the effect of groundwater processes on the magnitude and type of morphodynamic response of gravel coasts to storms.

This chapter first gives a description of the morphodynamic module development framework (Section 5.2), as well as the central equations of the module (Section 5.3). The model is validated using data collected during a large-scale physical model experiment (BARDEX; Williams et al., 2012a), as well as storm impact data collected at three gravel beach locations along the UK coast during the 2012–2013 and 2013–2014 storm season, and at one location on the coast of Brittany (Stéphan et al., 2010)

Sections of this chapter are based on work presented in McCall et al. (2015b).

in Sections 5.4–5.6. Section 5.7 discusses the importance of including groundwater processes in modelling the morphodynamic response of gravel beaches and barriers to storms. Finally, Section 5.8 discusses the sensitivity of a newly-developed sediment transport parameter used in the validation of XBeach-G.

5.2 Morphodynamic module development framework

The purpose of the morphodynamic module developed in this chapter is to allow XBeach-G to accurately predict the morphodynamic response of gravel beaches and barriers to storms, as well as to help investigate the influence of physical parameters of the beach and hydrodynamic forcing on the observed morphodynamic response of gravel coasts. To this end, the following framework was set out for the development of the morphodynamic module:

- The development of the morphodynamic module should be such that the XBeach-G model is capable of predicting the morphodynamic response of gravel coasts to any type of storm forcing condition, i.e., the morphodynamic module should allow the simulation of all five stages of morphodynamic storm response (berm formation – barrier rollover) discussed in Chapter 2 (Figure 2.2).

- Since XBeach-G is a process-based model, processes that are important for the morphodynamic response of gravel coasts should be described as best as possible in terms of their physics, rather than through empirical relations. As such, the module should contain processes that relate the effect of groundwater-surface water interactions to sediment transport and morphology in order to fully describe and understand the role of groundwater processes on gravel beaches during storms (cf., Chapter 2). Similarly, differences in uprush and downwash sediment transport should be explained as best as possible in terms of physical processes, rather than separate calibration coefficients for uprush and downwash transport (cf. Pedrozo-Acuña et al., 2007).

- For the model to be used practically in a predictive role, e.g., in forecasting safety against coastal flooding, the model should require minimal to no calibration of event-specific model parameter settings and relatively little calibration of site-specific model parameter settings.

- Since the XBeach-G model is developed to predict the morphodynamics of pure gravel beaches, the morphodynamic module should include bed load and sheet flow transport, but will not need to compute suspended sediment transport. Future development of the XBeach-G model for MSG beaches would require the development of a complementary suspended sediment transport module to compute suspended sand transport.

In an earlier version of a morphodynamic module for XBeach-G (see Appendix D and Masselink et al., 2014) a relatively simple approach was taken to describe bed load transport using the swash-zone sediment transport relation of Nielsen (2002). This approach highlighted the importance of including flow acceleration forces in the determination of gravel sediment transport, also acknowledged as a potential transport

mechanism by Pedrozo-Acuña et al. (2007). Although this approach yielded reasonable results for erosion of the the upper beach, shortcomings included poor representation the lower beach face, overestimation of crest build-up and barrier rollover, and considerable sensitivity to free model calibration parameters. The results of this approach are detailed in Appendix D, but are not discussed further in this chapter.

5.3 Model equations

The following section discusses the governing model equations of the XBeach-G morphodynamic module, as well as a description of the bed shear stress that is both used to compute the surface flow dynamics (cf., Section 3.2.2) as well as forming the principal forcing component for gravel sediment transport. In line with Chapters 3 and 4, and as discussed in Chapter 1, this section will restrict the description and implementation of the equations to their 1D form.

5.3.1 Sediment transport

Sediment mobility is defined in XBeach-G using the Shields parameter θ:

$$\theta = \frac{\tau_b}{\rho g \Delta_i D_{50}} \tag{5.1}$$

where Δ_i is the relative effective weight of the sediment. To account for the effect of through-bed flow on particle weight (cf., Chapter 2), the effective weight of the grains is modified by the vertical groundwater pressure gradient according to Turner and Masselink (1998):

$$\Delta_i = \frac{\rho_s - \rho}{\rho} + \alpha \frac{S}{K} = \Delta + \alpha \frac{S}{K} \tag{5.2}$$

where ρ_s is the density of the sediment and α is an empirical constant relating the surface seepage force to the seepage force in the bed, set to 0.5 in this study following Martin and Aral (1971).

To account for bed slope effects on sediment transport, the effective Shields parameter θ' is modified according to Fredsøe and Deigaard (1992):

$$\theta' = \theta \cos\beta \left(1 \pm \frac{\tan\beta}{\tan\phi}\right) \tag{5.3}$$

where β is the local angle of the bed, ϕ is the angle of repose of the sediment (approximately 30º–40º), and the right-hand term is less than 1 for up-slope transport, and greater than 1 for down-slope transport.

Sediment transport is computed using the bed load transport equation of Van Rijn (2007a), excluding coefficients for silt:

$$q_b = \gamma D_{50} D_*^{-0.3} \sqrt{\frac{\tau_b}{\rho}} \frac{\theta' - \theta_{cr}}{\theta_{cr}} \frac{\tau_b}{|\tau_b|} \tag{5.4}$$

where q_b is the volumetric bed load transport rate (excluding pore space), γ is a calibration coefficient, set to 0.5 in Van Rijn (2007a), $D_* = D_{50} \left(\frac{\Delta g}{\nu^2}\right)^{\frac{1}{3}}$ is the non-dimensional grain size, and θ_{cr} is the critical Shields parameter for the initiation of transport, in this thesis computed using the relation of Soulsby and Whitehouse (1997):

$$\theta_{cr} = \frac{0.30}{1 + 1.2 D_*} + 0.055 \left(1 - e^{-0.020 D_*}\right) \tag{5.5}$$

Note that other bed load transport equations, including Meyer-Peter and Müller (1948), Engelund and Fredsøe (1976), Nielsen (2002) and Wong and Parker (2006) were examined (cf., Appendix D), but were found to be less accurate than the formulation of Van Rijn (2007a).

5.3.2 Bed shear stress

The bed shear stress τ_b is required to compute the Shields parameter (Equation 5.1) as well as the surface water momentum balance (Equation 3.2). In order to account for the force of the water column on particles in the bed, the bed shear stress is described in terms of a drag and an inertia component (cf. Morison et al., 1950; Puleo et al., 2003). This approach allows the effect of acceleration on sediment transport to be explicitly taken into account in the bed shear stress, rather than in a modification of the effective Shields parameter (e.g., Van Gent, 1995a; Nielsen, 2002; Pedrozo-Acuña et al., 2007):

$$\tau_b = \tau_{bd} + \tau_{bi} \tag{5.6}$$

where τ_{bd} and τ_{bi} are bed shear stress terms due to drag and inertia, respectively. Note that the inertia component of the bed shear stress does not represent the actual inertia of the particles, but refers to the force on particles in the bed due to pressure gradients, as well as due to the disturbance of the accelerating flow, following potential flow theory (cf. Morison et al., 1950; O'Brien and Morison, 1952). The bed shear stress component due to drag τ_{bd} is computed using:

$$\tau_{bd} = c_f \rho u |u| \tag{5.7}$$

where c_f is the dimensionless friction factor.

The bed friction factor c_f is computed following the description of Conley and Inman (1994) to account for modified bed shear stress due to ventilated boundary layer effects in areas of infiltration and exfiltration (cf. Chapter 2):

$$c_f = c_{f,0}\left(\frac{\Phi}{e^{\Phi}-1}\right) \tag{5.8}$$

where $c_{f,0}$ is the dimensionless bed friction factor without ventilated boundary layer effects, $\Phi = -\frac{1}{2}\frac{b_{CI}}{c_{f,0}}\frac{S}{|u|}$ is a non-dimensional ventilation parameter and $b_{CI} = 0.9$ is a constant. Note that the value of the ventilation enhancement and reduction factor $\frac{\Phi}{e^{\Phi}-1}$ is limited to a minimum value of 0.1 and maximum value of 3.0, based on maximum and minimum recorded experimental values (Conley, pers. comm.).

The dimensionless bed friction factor without ventilated boundary layer effects is computed as:

$$c_{f,0} = \frac{g}{\left(18\log\left(\frac{12h}{k}\right)\right)^2} \tag{5.9}$$

where k is the characteristic roughness height, assumed to be equal to $3D_{90}$, as for flat beds (Van Rijn, 1982). Since the morphodynamic change on gravel beaches is predominantly confined to the swash zone and gravel step, this assumption is considered acceptable to compute storm-induced morphological change. However, it should be noted that the drag component of the bed friction may be underestimated in deeper water, where unresolved sub-grid bed forms may exist.

Bed shear due to inertia effects is computed through analogy with the force exerted by water on a sphere in non-stationary flow (cf. O'Brien and Morison, 1952; Kobayashi and Otta, 1987; Van Gent, 1995a). In this case, the force on an object due to inertia F_i can be computed from the local flow acceleration:

$$F_i = \rho c_m c_v D^3 \frac{\partial u}{\partial t} \tag{5.10}$$

where $c_m = 1 + c_a$ is an inertia coefficient, c_a is the added mass coefficient ($c_a = 0.5$ for spheres with zero autonomous acceleration), c_v is the volume shape factor ($c_v = \frac{\pi}{6}$ for spheres) and D is the characteristic grain size. Note that the inertial force is therefore the sum of the Froude–Krylov force $\rho c_v D^3 \frac{\partial u}{\partial t}$ and the hydrodynamic mass force $\rho c_a c_v D^3 \frac{\partial u}{\partial t}$. For the purpose of XBeach-G, the shear stress on the bed due to inertia is computed by assuming the characteristic grain size to be the median sediment grain size D_{50} and the number of grains affected by flow acceleration per unit area to scale with $c_n D_{50}^{-2}$ ($c_n \approx \mathcal{O}(1)$) such that:

$$\tau_{bi} = \rho c_m c_v c_n D_{50} \frac{\partial u}{\partial t} \tag{5.11}$$

Since in most practical cases the individual values of c_m, c_v and c_n cannot be derived from measurement data, these parameters are replaced by one calibration coefficient for inertia $c_i = c_m c_v c_n \approx \mathcal{O}(1)$, which is used to describe the added mass of the

grains, as well as the shape of the grains and number of grains on the surface of the bed affected by flow acceleration.

Although Equation 5.11 follows the line of reasoning of earlier research, the equation should reasonably be considered a proxy for more complex physical processes acting on grains on the bed, including near-bed pressure gradients and turbulence. In particular, Equation 5.11 ignores the contribution of the advective acceleration term to the total inertia force on particles in the bed, which may be relevant in the swash (see Baldock et al., 2005 in their discussion of Puleo et al., 2003), although initial sensitivity simulations with XBeach-G show the effect of this term to be small on all but very coarse gravel beaches (not discussed further in this thesis). Furthermore, the equation does not explicitly account for relative velocity differences between the surface water flow and sediment motion, other than through a user-defined variation of the coefficient of added mass c_a. Despite these simplifications, the application of shear stress on the bed due to inertia following Equation 5.11 is demonstrated later in this chapter to substantially improve model simulation of sediment transport and to be particularly important for the simulation of coarse-grained gravel beaches.

5.3.3 Bed level change

Bed level change due to sediment transport is computed from the spatial gradient in the bed load transport (Exner equation):

$$\frac{\partial \xi}{\partial t} + \frac{1}{(1-n_p)} \frac{\partial q_b}{\partial x} = 0 \tag{5.12}$$

Bed level change due to geotechnical slope collapse is simulated by avalanching material down-slope when the bed slope exceeds the angle of repose (cf. Roelvink et al., 2009):

$$\begin{aligned} |\tan\beta| &> \phi \quad avalanching \\ |\tan\beta| &\leq \phi \quad no\,avalanching \end{aligned} \tag{5.13}$$

5.4 Case study sites and storm data

The data used in this chapter to set-up XBeach-G models and to validate the model results have been collected during the BARDEX physical model experiment (Williams et al., 2012a), as well as at three natural gravel beaches along the coast of the UK (Chesil Beach, Loe Bar and Slapton Sands) during the 2012–2013 and 2013–2014 winter storm seasons, and at one gravel barrier on the Brittany coast (Sillon de Talbert; Stéphan et al., 2010). In contrast to Chapters 3 and 4, where model validation periods are selected during which little bed level change occurred, this chapter focusses on model validation periods with a strong morphodynamic response. The location of each site discussed in this chapter is given in Figure 5.1 (similar to Figure 3.1). Although longshore sediment transport may be present at all four natural gravel beaches, the sites selected for this study have been chosen such that the longshore

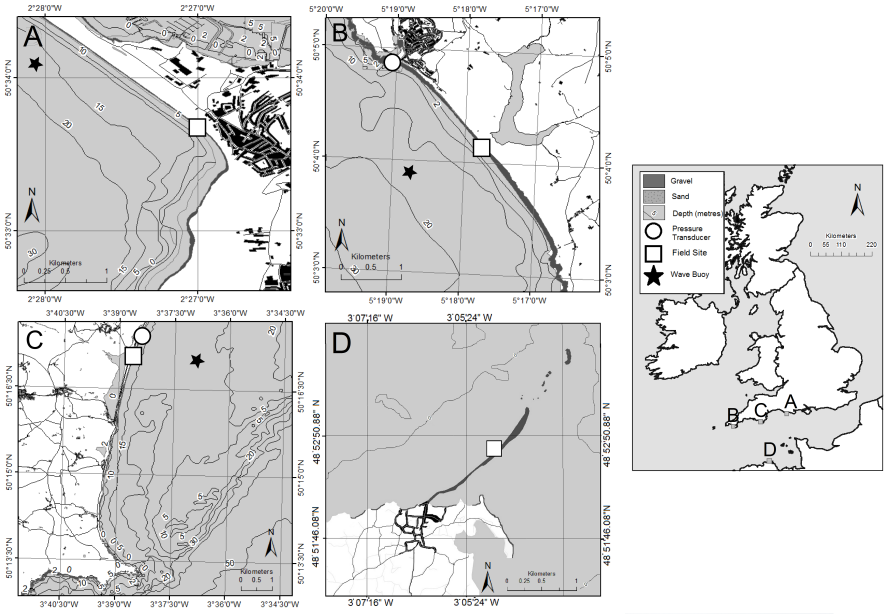

Figure 5.1: Location of field data collection sites: (A) Chesil Beach, (B) Loe Bar, (C) Slapton Sands and (D) Sillon de Talbert. Note that the location of the wave buoy at Chesil Beach is beyond the extent of map A and has been depicted closer to the field location, but at the correct water depth (cf., Figure 3.1).

sediment transport gradient during the storm events is expected to have the least effect. A summary of the key hydrodynamic and geometric parameters of the beaches and storms investigated in this chapter is given in Table 5.1 (similar to Table 3.1).

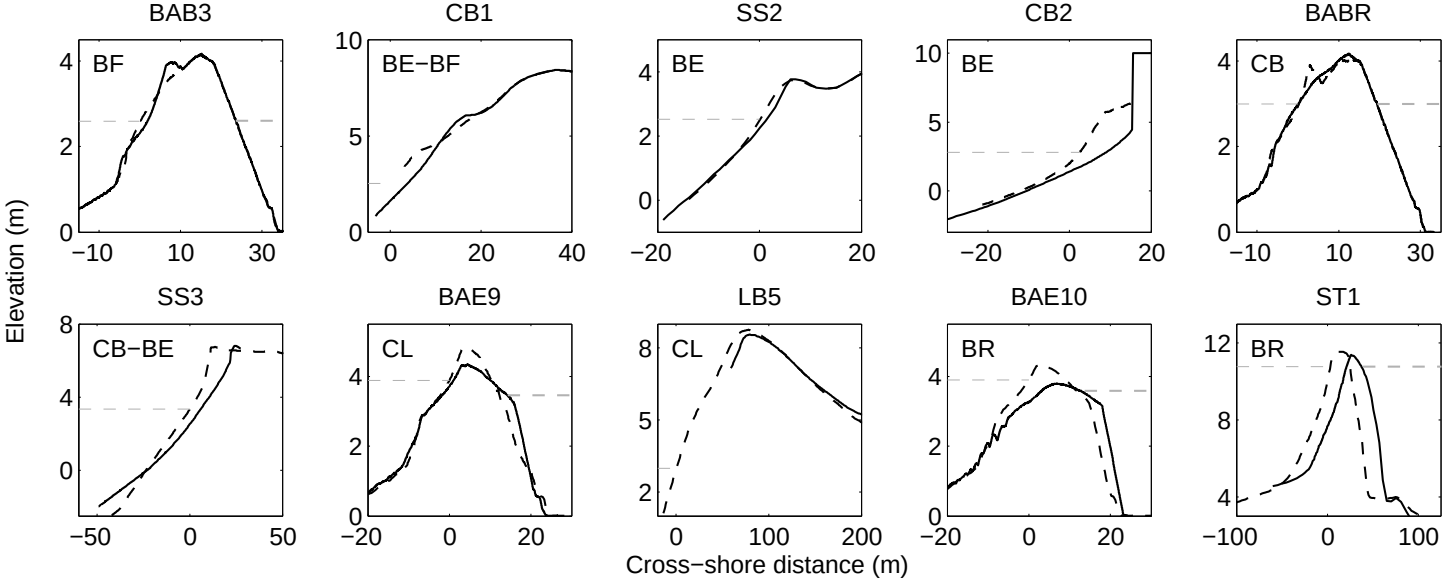

Figure 5.2: Overview of the morphological response of the gravel barriers during the 10 storm events discussed in this chapter. The panels show the pre-storm cross-shore profile (– –), measured post-storm cross-shore profile (—) and maximum still water levels (– –) for each event. The abbreviation in the top left corner of each panel refers to the observed morphological response: berm formation (BF), beach erosion (BE), crest build-up (CB), crest lowering (CL), or barrier rollover (BR). Note that the horizontal and vertical scale varies per panel and that detailed plots of each storm event are given in Figures 5.3–5.12.

Beach characteristics					Storm simulation			Hydrodynamic forcing conditions			Relative forcing and response		
Location	Sediment type	D_{50} (mm)	K (mms^{-1})	$\tan\beta_b$	Simulation	Storm date	Simulated storm duration (h)	H_{m0} (m)	T_p (s)	$[H_{m0}/\lambda_p]_0$	R_c/H_{m0}	$\xi_{p,0}$	Morphodynamic response
BARDEX[a,b]	Medium gravel	11	155	0.19	BAB3	3 Jul. 2008	1.7	0.8	4.3	0.029	2.0	1.1	Berm formation
					BABR	2 Jul. 2008	0.1	1.0§	10.0	0.005	1.0	2.6	Crest build-up
					BAE9#	28 Jul. 2008	1.2	0.8	7.7	0.007	1.2‡	2.2	Crest lowering
					BAE10#	29 Jul. 2008	1.2	0.8	7.7	0.007	0.5‡	2.2	Barrier rollover
Chesil Beach[c,d,e]	Very coarse gravel	40	400 (200–600)	0.20	CB1*	15 Dec. 2012	25.0	2.9	8.6	0.027	2.9	1.2	Beach erosion and berm formation
					CB2*,♁	5–6 Feb. 2014	21.5	7.6	13.9	0.025	1.0†	1.3	Beach erosion
Loe Bar[f,g,h]	Very fine gravel	2	10 (3–30)	0.12	LB5	5 Feb. 2014	122.8	8.0	14.5	0.024	0.6	0.8	Crest lowering
Slapton Sands[h,i,j]	Fine gravel	6	75 (19–150)	0.15	SS2#	21 Oct. 2013	9.8	2.0	6.9	0.029	2.0	0.9	Beach erosion
					SS3	5 Feb. 2014	36.0	4.6	9.5	0.035	0.7	0.8	Crest build-up and beach erosion
Sillon de Talbert[k,l,m]	Cobbles	80	400 (200–600)	0.11	ST1	10 Mar. 2007	74.0	9.5	16.0	0.024	0.2‡	0.7	Barrier rollover

Table 5.1: Overview of beach characteristics for each of the gravel beach sites, list of storm simulations, maximum hydrodynamic forcing conditions during the storms, and morphological response of the barrier to each of the storm events. In the case of hydraulic conductivity (K), the "high" and "low" estimates are indicated between parentheses. Sediment type is classified according to the Wentworth scale. Literature referenced in this table are: a)Williams et al. (2012a), b) Turner and Masselink (2012), c) Heijne and West (1991), d) Hook et al. (1994), e) Carr (1974), f) Poate et al. (2013), g) Poate et al. (2014), h) Austin et al. (2013), i) Austin and Masselink (2006b), j) Austin (2005), k) Stéphan et al. (2010), l) Stéphan et al. (2012), m) Chanson (2006). In the case of BAE9, BAE10 and SS2 # indicates that the simulation periods are longer than those described in Chapter 3, whereas in the case of CB1 and CB2 * indicates that the simulations in Chapter 3 include periods that are not included in the morphodynamic simulations. In the case of CB2 ♁ indicates that the location of the cross-shore profile is different to that discussed in Chapter 3 and † is relative to the top of the sea wall. In the case of BAE9, BAE10 and ST1 ‡ is relative to the pre-storm crest level. In the case of BABR § represents monochromatic wave conditions.

As discussed in Chapter 3, the hydrodynamics and morphodynamics of a medium gravel ($D_{50} = 11$ mm) barrier were measured during the BARDEX experiment under varying hydraulic boundary conditions, ranging from wave run-up to wave overtopping and overwash (see Williams et al., 2012a for details). This chapter focuses on four BARDEX experiment series with significant and distinct morphological change (Table 3.1 and Figure 5.2 for an overview). In BARDEX series BAB3 a berm was generated at the wave run-up extent on an initially plain slope under relatively mild wave conditions. In series BABR, a 3-minute burst of large and long period monochromatic waves was used to remove a berm on the barrier beach in order to generate a smooth and slightly convex beach face. The removal of the berm was accompanied by wave overtopping and accretion on the barrier crest. At the start of series BAE9, overwash of the gravel barrier was triggered by an increase of the offshore water level and wave period. Conditions for overwash increased over the duration of the series through the crest-lowering response of the gravel barrier. Barrier rollover finally occurred during series BAE10, when high wave and water level conditions lead to barrier crest lowering and retreat, and substantial washover deposition on the back barrier (Matias et al., 2012).

Data on the morphodynamic response of three UK gravel beaches to energetic and storm conditions were collected during the winter of 2012–2013 and 2013–2014 (Poate et al., 2015). The three beaches discussed in this chapter are Chesil Beach (CB), a very coarse ($D_{50} = 40$ mm) gravel barrier with a crest height approximately 12 meters above ODN (Ordnance Datum Newlyn; approximately equal to 0.2 m below mean sea level – MSL); Loe Bar (LB), a very fine gravel barrier ($D_{50} = 2$ mm) with a crest height approximately 9 meters above ODN; and Slapton Sands (SS), a fine gravel barrier ($D_{50} = 6$ mm) with a crest height approximately 7 meters above ODN. CB and LB have a SW orientation (Figure 5.1), and face into the typically SW winter swells, whereas SS has an E orientation and is partly sheltered from SW swells.

During CB1 (Table 3.1 and Figure 5.2), the beach experienced landward migration of the berm under energetic wave conditions combined with spring tides. In CB2, extremely energetic wave conditions lead to beach erosion and approximately 2 meters of scour at the base of a seawall. Eyewitness accounts and amateur videos[1] confirm that other sections of Chesil Beach that were not protected by the seawall experienced wave overtopping during this event. Offshore wave data and surge level data for both events were provided by a directional wave buoy, a shore-mounted PT and the West Bay Harbour tide gauge, as discussed in Chapter 3 (Section 3.3). During CB1, the morphology of the beach was measured every low tide by RTK-GPS survey, whereas during CB2 the morphology of the beach was continuously measured by a tower-mounted cross-shore laser scanner (see Almeida et al., 2015 for comparable measurements and methodology).

The storm system that caused event CB2, led to overwash at Loe Bar in event LB5, where overwashing waves caused crest lowering of 0.2 m and up to 0.4 m of accretion on the back barrier. Offshore wave data for this event were provided by a directional

[1] For example those found on internet: `https://youtu.be/rRYbDtqusX4`; `https://youtu.be/84EQtsgA0_8`

wave buoy maintained by CCO, located approximately 500 m from the study site in 15–20 m water depth (Figure 5.1). Tide and surge data for LB5 were derived from tidal predictions for Loe Bar combined with time series of measured surge at Newlyn tide gauge, approximately 20 km from the study site. Pre-storm topographic data for LB5 were collected two days prior to the storm by means of an RTK-GPS survey. Post-storm topographic data were collected by RTK-GPS survey 13 days after LB5, during which time recovery of the beach took place in the form of a cusp and horn system. Unfortunately, no wave data are available for the period between LB5 and the post-storm survey. However, evaluation of the two nearest CCO wave buoys in operation during this period (Looe Bay and Start Bay) indicate that LB5 was the largest wave event in this period. Eye-witness reports confirm substantial overwash at Loe Bar during LB5 (Earlie, pers. comm.).

The morphodynamic response to SS2 was characterised by moderate erosion of a berm on the supratidal beach. More substantial morphological change occurred during SS3, which was caused by the same storm system that led to CB2 and LB5. During SS3, the beach was heavily eroded and the barrier overtopped, leading to temporary closure of the main road on the barrier crest. Offshore wave data for both events were provided by a directional wave buoy maintained by CCO, located approximately 500 m from the study site in 10–15 m water depth (Figure 5.1). Tide and surge data for SS2 were collected by a pressure transducer located approximately 1 km from the study site, as discussed in Chapter 3 (Section 3.3). Tide and surge data for SS3 were derived from tidal predictions for Slapton Sands combined with the magnitude of the measured surge at Devonport and West Bay Harbour tide gauges, approximately 40 km and 80 km from the study site, respectively. Topographic data for SS2 were collected by means of low tide RTK-GPS surveys prior to and following SS2. Pre-storm topographic data for SS3 were collected 27 days prior to the storm by means of an RTK-GPS survey, during which period no wave events above storm threshold were measured by the wave buoy. Post-storm topographic data were collected by RTK-GPS survey 2 days after SS3, during which period washover deposits on the road had been removed to the back barrier.

Sillon de Talbert is a NW-facing gravel-cobble spit on the macro-tidal (maximum tidal range 10.85 m) coast of Brittany, France, fronted by an approximately 1 km-wide intertidal rocky platform. The barrier was heavily overwashed during ST1, when highly energetic wave conditions coincided with spring tide. The storm led to barrier rollover of approximately 15 m along the central section of the barrier (Stéphan et al., 2010, 2012). Topographic, bathymetric and hydrodynamic forcing conditions for ST1 were provided by l'Université de Bretagne Occidentale (Stéphan and Suanez, pers. comm.). Topographic data of the barrier consist of supratidal and intertidal RTK-GPS measurements of the barrier measured in September 2007 (six months prior to ST1) and September 2008 (six months after ST1). Unpublished cross-shore profile measurements carried out on 19 March 2008 (nine days after the storm) indicate qualitatively that the overall lowering of the crest of the barrier during ST1 was approximately 1 m (Stéphan et al., 2012). These data are supplemented with LiDAR data of the intertidal rocky platform measured in 2002 (Boersma and Hoenderkamp, 2003) and bathymetry data provided by the Service Hydrographique et Océanographique de la Marine. Time series of the storm surge level were derived

from surge measured at the Roscoff tide gauge, located approximately 65 km from the study site, alongside tidal predictions at the location of the barrier. Wave conditions offshore of the barrier were extracted from a nested WAVEWATCH III® model (Tolman and Chalikov, 1996), forced by ECMWF wind fields. Model validation results on buoys off Brittany indicate an overall relative root-mean-square error of 12% for wave height with a bias less than 2% (Ardhuin and Accensi, 2011).

A summary of the measured or estimated median grain diameter D_{50}, hydraulic conductivity K and beach slope $\tan(\beta)$ at all five gravel barriers is given in Table 3.1. The table furthermore lists all storm simulations discussed in this chapter, alongside the maximum hydrodynamic forcing conditions (significant wave height at the wave buoy, H_{m0}; peak wave period at the wave buoy, T_p; and the peak deep water wave steepness, $[H_{m0}/\lambda_p]_0$) and a description of the relative forcing and storm morphology (relative freeboard ,R_c/H_{m0}; deep water Iribarren number $\xi_{p,0} = \frac{\tan\beta_b}{\sqrt{\frac{H_{m0}}{\lambda_{p,0}}}}$; and the morphodynamic response type) for each of the simulated storms.

5.5 Model setup

Wave and water level boundary conditions time series for the four BARDEX simulations are derived from measured time series of waves imposed at the wave paddle and still water levels measured by pressure transducers on the flume floor, in the same manner as applied in Chapter 3. Wave boundary conditions for the Chesil Beach, Loe Bar, Slapton Sands and Sillon de Talbert models are imposed by means of wave spectra time series measured at the nearest wave buoy (CB, LB and SS), or wave spectrum parameters provided by a large-scale wave model (ST; described in the Section 5.4). Tide and surge boundary conditions for these models are derived from measurements (CB1, SS2), or tidal predictions combined with measured surge at locations near the model site (CB2, LB5, SS3, ST1), as described in Section 5.4.

Where feasible, the model simulations are set up to simulate the entire period of the storm between the pre-storm and post-storm survey (BARDEX, Chesil Beach and SS2). In these cases, the initial cross-shore profile in the XBeach-G model is set to the cross-shore profile measured at low-tide prior to the simulated storm, or at the start of the simulated wave measurement series. In the case of LB5, the duration of the simulation has been set to the period from the pre-storm measurement to the end of the storm peak, after which no measured wave boundary conditions are available. As discussed in Section 5.4, this simulation includes the largest storm event of the period between the pre-storm and post-storm measurements, during which the crest lowering and overwash most probably occurred. In the case of SS3, the initial cross-shore profile in the model is set equal to the cross-shore profile measured 27 days before the storm. To reduce computational requirements and to account for the fact that the XBeach-G model is designed to simulate storm events, and does not include processes to model medium to long-term shoreline change (e.g. longshore transport gradients), the duration of the simulation is shortened to 36 hours surrounding the peak of the storm. As discussed in Section 5.4, no other large wave energy events occurred in the period between the cross-shore profile measurements. In the case of ST1, the initial cross-shore profile is set equal to the cross-shore profile measured 6

months before ST1. Again, using the same reasoning as for SS3, the duration of the simulation is set to 74 hours surrounding the peak of ST1, rather than the duration between cross-shore profile measurements. Due to the large period between ST1 and the post-storm profile measurement, the modelled post-storm cross-shore profile cannot be directly compared to the measured change. However, the observed barrier rollover can be attributed to ST1, which was the largest storm event in this period (Stéphan et al., 2010), and the model results can be compared to the measurements in a qualitative sense.

The cross-shore resolution of the models is set to vary gradually in the cross-shore direction, from $\frac{\lambda_m}{25} \approx 2-3$ m at the offshore boundary of the model, where λ_m is the wave length related to the mean wave period, to 0.3 m near the waterline in order to correctly capture swash processes in the model. In the case of the BARDEX simulations, the resolution has been increased to 0.5 m at the wave generator and 0.1 m at the beach. In the case of CB2 and ST1, the seawall and rocky foreshore, respectively, are included in the cross-shore profile as non-erodible objects.

The hydraulic conductivity and median grain size at BARDEX, Chesil Beach, Loe Bar and Slapton Sands are based on ranges found in literature for these sites (Table 3.1). Since the reported values of hydraulic conductivity for the natural gravel beaches are relatively uncertain and show considerable spread, all simulations at the natural gravel beaches are computed with three estimates (high, medium and low; Table 3.1) for the hydraulic conductivity. Due to lack of detailed data for Sillon de Talbert, the median grain size for this barrier is assumed equal to 0.08 m (Chanson, 2006) and the hydraulic conductivity is set equal to that of Chesil Beach, which is the most similar barrier in this study in terms of sediment composition.

The three free model parameters relating to sediment transport are the inertia coefficient c_i, which acts on sediment transport through the bed shear stress; the angle of repose ϕ, which controls avalanching and affects sediment transport on sloping beds; and the bed load transport calibration coefficient γ, which linearly scales transport rates and gradients. Where sufficient data are available, these model parameters can be calibrated at every gravel barrier to provide the most accurate reproduction of measured cross-shore profile change. However, in order to assess the predictive skill of the numerical model one value is used in this chapter for the sediment transport parameters ($c_i = 1.0; \phi = 35^o$; $\gamma = 0.5$) at all four natural gravel sites. In the case of BARDEX, the bed load transport calibration coefficient is increased ($\gamma = 1.0$) in order to capture the apparently highly mobile gravel in the laboratory. Although the reason for the high sediment mobility in the laboratory is uncertain, at this stage it is assumed to be related to the use of angular gravel of fluvial, rather than marine, origin, as well as the 2D nature of the processes, with no longshore smoothing due to variability in swash direction. The remaining two parameters are kept equal to those of the natural gravel sites.

5.6 Model validation

In the following section the results of the XBeach-G simulations of the storm events presented in Section 5.4 are discussed. The results have been grouped according to

the morphodynamic response of the gravel barrier: berm formation, beach erosion, crest build-up, crest lowering and barrier rollover (Figure 2.2). All model simulations are run using the model parameters described in Section 5.5. Although higher model accuracy may be achieved by calibration of the free model parameters at each case study site, this is not considered the main objective of this investigation.

To assess the skill of the model in simulating morphological change, the cross-shore profile change predicted by the model at the end of the storm event is compared to the measured post-storm cross-shore profile change. As discussed in Section 5.4, the post-storm profiles for LB5 and ST1 were measured 13 days and 6 months after the respective storm events, during which changes to the beach face (LB5, ST1) and barrier crest (ST1) may have occurred. In these cases the analysis of the model skill is limited to a quantitative (LB5) and qualitative (ST1) analysis of the profile change of the barrier crest and back barrier, and the front of the barrier is not considered. All comparisons at the natural gravel beaches reported in this chapter are based on the model simulation corresponding to the "mid range" estimate for the hydraulic conductivity (cf. Table 5.1), unless stated otherwise.

For all simulations, the absolute profile change prediction error at each point in the profile $\left|\varepsilon_{\Delta\xi}\right|_i$ is computed from the measured and modelled bed level change, as well as an estimate of the measurement error and natural profile variability ε_0, similar to Van Rijn et al. (2003):

$$\left|\varepsilon_{\Delta\xi}\right|_i = max\left(\left|\Delta\xi_{modelled,i} - \Delta\xi_{measured,i}\right| - \varepsilon_0, 0\right) \tag{5.14}$$

where $\Delta\xi_{modelled}$ and $\Delta\xi_{measured}$ are the modelled and measured bed level change, respectively, $\varepsilon_0 = max\left(\varepsilon_{inst}, 3D_{50}\right)$ and ε_{inst} is the estimated instrument error (0.030 m for RTK-GPS surveys, 0.015 m for laser scanner data, and 0.005 m for the mechanical roller profiler; cf. Poate et al., 2013; Almeida et al., 2015).

The measured and modelled bed level change and absolute profile change prediction error are subsequently used to compute (1) the root-mean-square error (RMSE; defined in Equation 5.15); (2) the relative bias, normalised by the absolute mean of the observations (Rel. bias; Equation 5.16); (3) the correlation coefficient (ρ; Equation 5.17) and (4) the Brier Skill Score (BSS; Equation 5.18) of the model simulations in a method similar to Roelvink et al. (2009).

	RMSE	Rel. bias	ρ	BSS (qualifier†)
BAB3	0.16 m	-0.00	0.65	0.38 (fair)
CB1	0.36 m	-0.62	0.98	0.69 (good)
SS2	0.11 m	-0.66	0.96	0.63 (good)
CB2a	0.45 m	-0.71	0.89	0.46 (fair)
CB2b	1.11 m	0.45	0.95	0.77 (good)
CB2c	0.33 m	0.14	1.00	0.98 (excellent)
CB2d	0.17 m	-0.06	0.99	0.99 (excellent)
BABR	0.05 m	-0.00	0.89	0.91 (excellent)
SS3	0.35 m	-0.06	0.92	0.88 (excellent)
BAE9	0.17 m	-0.03	0.83	0.77 (good)
LB5	0.08 m	-0.22	0.99	0.93 (excellent)
BAE10	0.34 m	-0.00	0.82	0.66 (good)

Table 5.2: Root-mean-square error (RMSE), relative bias (Rel. bias), correlation coefficient (ρ) and Brier Skill Score (BSS) of the model cross-shore profile change predictions relative to the measured profile change. Note that ST1 is not included in the statistical analysis. † Refers to the qualification of Van Rijn et al. (2003).

$$RMSE = \sqrt{\frac{1}{n}\sum_{i=1}^{n}\left(\left|\varepsilon_{\Delta\xi}\right|_i\right)^2} \tag{5.15}$$

$$Rel.bias = \frac{\frac{1}{n}\sum_{i=1}^{n}\left(\left|\varepsilon_{\Delta\xi}\right|_i sgn\left(\Delta\xi_{i,modelled} - \Delta\xi_{i,measured}\right)\right)}{\frac{1}{n}\sum_{i=1}^{n}\left(\left|\Delta\xi_{i,measured}\right|\right)} \tag{5.16}$$

$$\rho = \frac{cov\left(\Delta\xi_{modelled}, \Delta\xi_{measured}\right)}{\sigma_{\Delta\xi_{modelled}}\sigma_{\Delta\xi_{measured}}} \tag{5.17}$$

$$BSS = 1 - \frac{\frac{1}{n}\sum_{i=1}^{n}\left|\varepsilon_{\Delta\xi}\right|_i^2}{\frac{1}{n}\sum_{i=1}^{n}\left(\Delta\xi_{i,measured}\right)^2} \tag{5.18}$$

where all statistics are computed using data interpolated to a regularly-spaced grid, and only include points where the measured or modelled bed level changes are greater than ε_0.

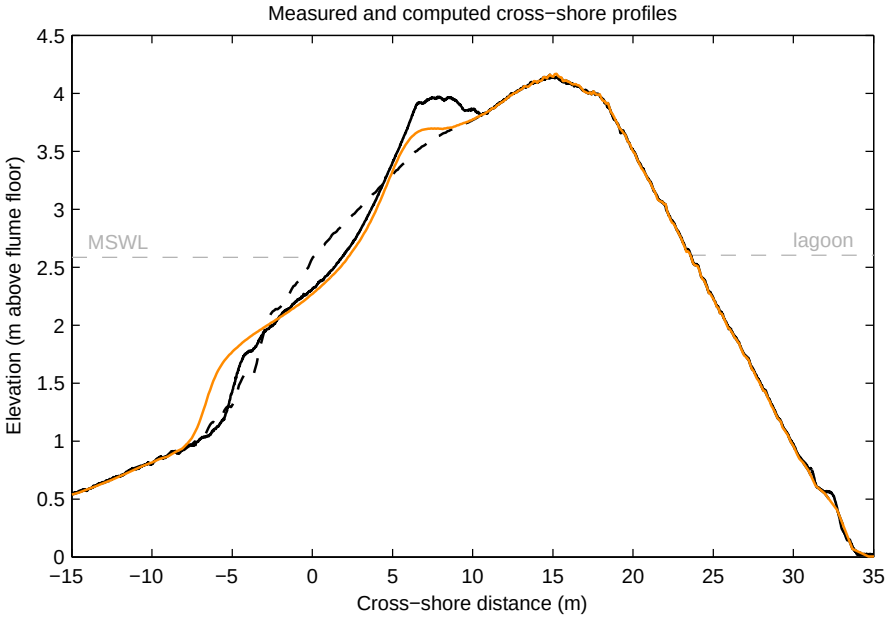

Figure 5.3: Initial cross-shore profile (– –), cross-shore profiles measured (—) and modelled (—) at the end of wave series BAB3, and the maximum still water levels imposed on the front and the back barrier (– –).

5.6.1 Berm formation

Two storm events discussed in Section 5.4 are characterised by berm formation: BAB3, where an initially mild beach slope was reworked into steep beach slope with a berm, and CB1, where an existing berm was eroded and a new berm created higher on the beach profile.

The results of BAB3 are shown in Figure 5.3. The figure shows that the model can qualitatively reproduce the observed change from a mild beach slope to a steep beach slope with a berm. However, in a quantitative sense, XBeach-G underestimates the volume of the berm, where the volume of the berm accretion is predicted to be 0.4 m^3m^{-1} and the measured berm accretion is 1.4 m^3m^{-1}. The underestimation of the berm volume by XBeach-G is mirrored by an overestimation of sediment deposition below the still water level, the probable cause of which is discussed in Section 7.2.3. Despite these discrepancies, the overall skill of the model prediction is reasonable (Table 5.2), with a BSS of 0.38. Note that BAB3 has low relative bias because the measurements and model results encompass the full mass balance.

The model prediction of cross-shore profile change during CB1 is shown in Figure 5.4. The figure shows that the model correctly predicts the erosion of the pre-storm berm, as well as a general steepening of the beach towards a berm-like feature at an elevation of 5 m + ODN. However, in similarity with BAB3, the model greatly under

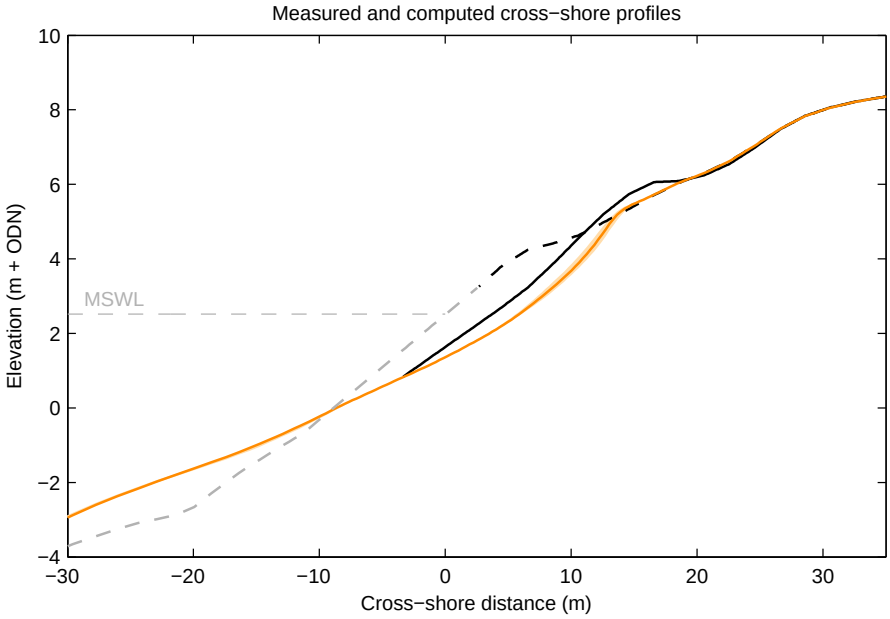

Figure 5.4: Pre-storm (– –), measured post-storm (—) and modelled post-storm (—) cross-shore profiles for CB1, and maximum still water level (– –). The range in post-storm model profiles due to varying the hydraulic conductivity (Table 3.1) is shown in shading ( ). The estimated pre-storm profile below the elevation of measurements (– –) is shown for comparative purposes.

predicts the volume of the post-storm berm above the pre-storm profile (modelled, 0.2 m^3m^{-1}; measured, 2.0 m^3m^{-1}), and the model predicts a more landward position of the post-storm beach. These model discrepancies are reflected in a relatively large model RMSE and relative bias (Table 5.2), but not by low ρ or BSS values. The latter two represent the fact that despite that the berm is not being well represented, the majority of the shape of the cross-shore profile change is captured relatively well by the model.

The results of BAB3 and CB1 show that although XBeach-G is able to reproduce berm formation relatively well in a qualitative sense without site-specific calibration of the model sediment transport parameters, the quantitative skill of the model is not particularly high (mean BSS 0.54). Although it is expected that site-specific calibration of the inertia coefficient c_i and angle of repose ϕ may lead to a better representation of the berm formation at both sites, processes related to wave breaking and gravel step dynamics may be required to further improve model predictions (discussed in Section 5.8).

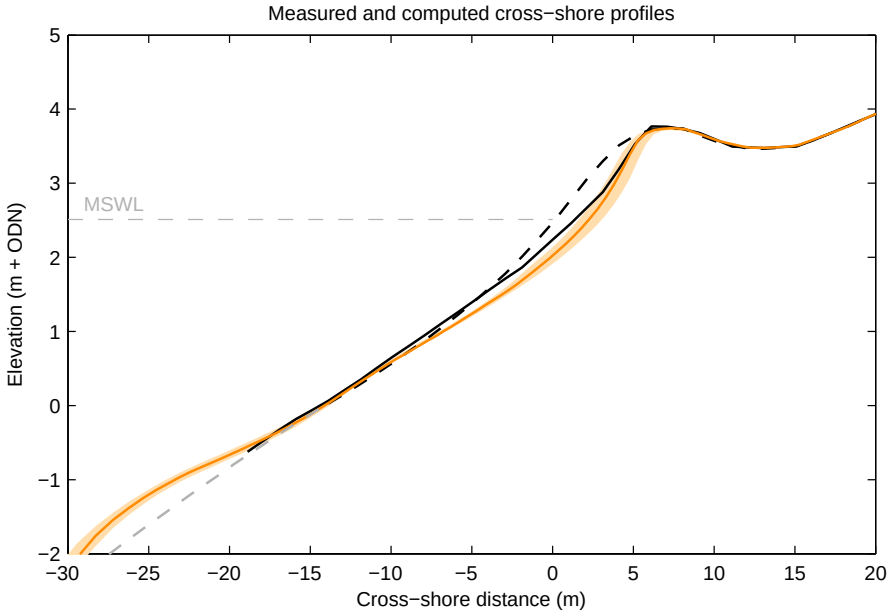

Figure 5.5: Pre-storm (– –), measured post-storm (—) and modelled post-storm (—) cross-shore profiles for SS2, and maximum still water levels (– –). The range in post-storm model profiles due to varying the hydraulic conductivity (Table 3.1) is shown in shading ( ) and the estimated pre-storm profile below the elevation of measurements (– –) is given for comparative purposes.

5.6.2 Beach erosion

Two storm events are characterised primarily by beach erosion: SS2, where an existing berm was partially eroded by energetic waves, and CB2, where substantial beach erosion took place at the base of a sea wall during highly energetic wave conditions.

Figure 5.5 shows the modelled and measured cross-shore profiles for SS2. The figure shows approximately 2 m horizontal retreat of the upper beach face above maximum storm still water level due to the partial erosion of the pre-storm berm, which is well reproduced by the XBeach-G model. Between MSL (0.38 m + ODN) and maximum storm still water level, the model slightly overpredicts the magnitude of erosion by approximately 0.2 m. To a large extent, the error in the model prediction falls within the variation of model predictions due to imposed variations in hydraulic conductivity of the beach. The overall BSS for SS2 is good (0.63; Table 5.2) and is primarily reduced by the relatively large relative bias (-66%) caused by the overestimation of beach erosion below maximum still water level.

The morphodynamic impact of CB2 on a beach backed by a sea wall is shown in Figure 5.6. The figure shows substantial lowering ($\backsim$ 2 m) of the post-storm cross-shore profile at the base of the sea wall relative to the pre-storm profile (d; top panel).

The figure also shows that the maximum erosion depth at the base of the sea wall was largest at low tide during CB2 ($\backsim$ 3 m; Figure 5.6b, bottom centre panel) when wave conditions were at their most energetic. Figure 5.6 and Table 5.2 show that although the maximum erosion at the base of the seawall is somewhat under predicted, XBeach-G generally reproduces the measured cross-shore profile very well (BSS: fair–excellent) with high ρ values and low bias.

5.6.3 Crest build-up

Two storm events discussed in Section 5.4 are principally characterised by crest build-up: BABR (Figure 5.7), where an existing berm was reworked by high water levels and energetic waves to the crest, and SS3 (Figure 5.5), where energetic waves eroded much of the beach and overtopped the gravel barrier.

Figure 5.7 shows up to 0.5 m measured erosion of the berm during BABR between 0 and 5 m cross-shore distance and 0.1–0.2 m deposition on the initially flat barrier crest. The figure shows good agreement between the modelled and measured profile development: the model correctly removes the berm, achieves the correct beach face slope, and deposits sediment on the top of the barrier. This agreement is reflected in the computed and measured erosion (1.0 m^3m^{-1} and 1.1 m^3m^{-1}, respectively) and deposition (0.5 m^3m^{-1} and 0.9 m^3m^{-1}, respectively) above SWL and high BSS (0.91; Table 5.2).

Figure 5.8 shows the modelled and measured cross-shore profiles for SS3. The figure shows substantial beach erosion in the post-storm measurements, leading to a retreat of the crest of 11 m and a thin layer of deposition on top of the barrier. The figure also shows that the results of the XBeach-G model are very similar to the measured cross-shore profile development, expressed in the total eroded volume above maximum still water level (modelled, 31.1 m^3m^{-1}; measured, 31.8 m^3m^{-1}), crest retreat (modelled, 13.9 m ; measured, 10.7 m) and deposition layer thickness on the barrier crest (modelled and measured 0.3 m). Although the post-storm beach slope below MSL (0.38 m + ODN) is predicted correctly by the XBeach model, the beach slope above MSL is less well represented by the model, which is comparable with the results of SS2. As with the simulation of SS2, the majority of the prediction error on the beach slope above MSL lies within the variation of model predictions due to imposed variations in hydraulic conductivity of the beach. The overall skill of the XBeach-G model for SS3 is high, with a high BSS (0.88; Table 5.2) and low relative bias (-6%).

5.6.4 Crest lowering

During BAE9 and LB5 crest lowering and washover occurred under energetic wave conditions in combination with high water levels. During these events the upper part of the barrier beach and crest was eroded, but the crest of the barriers did not move landward significantly.

Figure 5.9 shows the modelled and measured cross-shore profiles for BAE9. The measurements show that during BAE9, the crest was lowered by 0.5 m and 4.5 m^3m^{-1} of gravel washed over the crest of the barrier, where washover volume is defined as the volume of sediment accretion landward of the initial barrier crest. The figure shows that in qualitative and quantitative sense, the XBeach-G simulates the observed

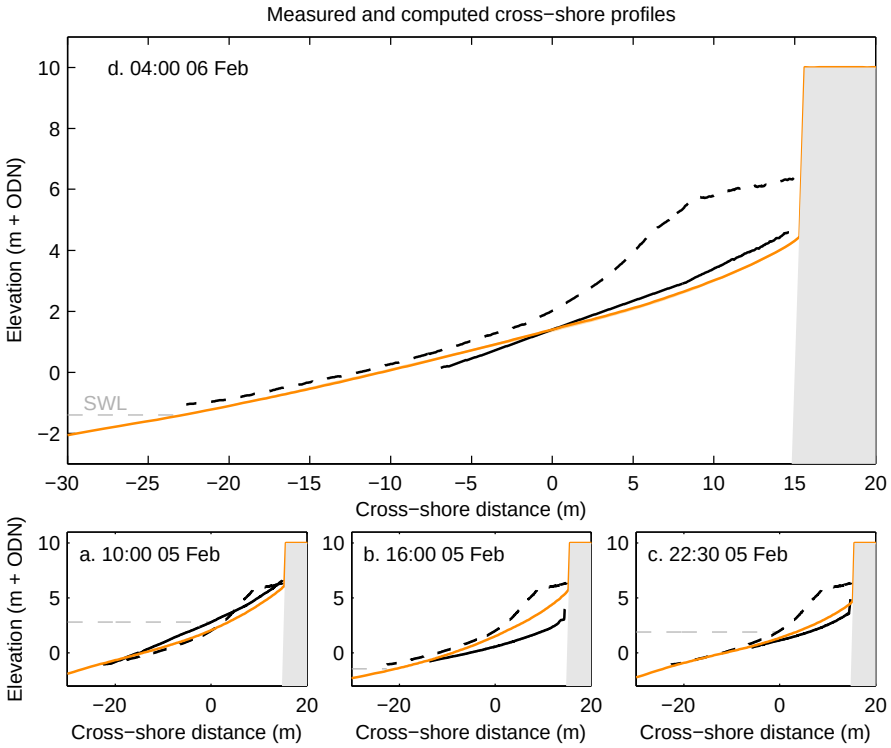

Figure 5.6: Pre-storm (- - -), measured post-storm (—) and modelled post-storm (—) cross-shore profiles for CB2. The top panel shows modelled and measured profiles at low tide after CB2 (d). The bottom three panels show from left to right: modelled and measured profiles at the first high tide of CB2 (a), low tide of CB2 (b) and the second high tide of CB2 (c). The range in post-storm model profiles due to varying the hydraulic conductivity (Table 3.1) is shown in light orange shading ( ) and the non-erodible sea wall is shown in grey shading ( ). The tide level for each panel is represented by the dashed grey line.

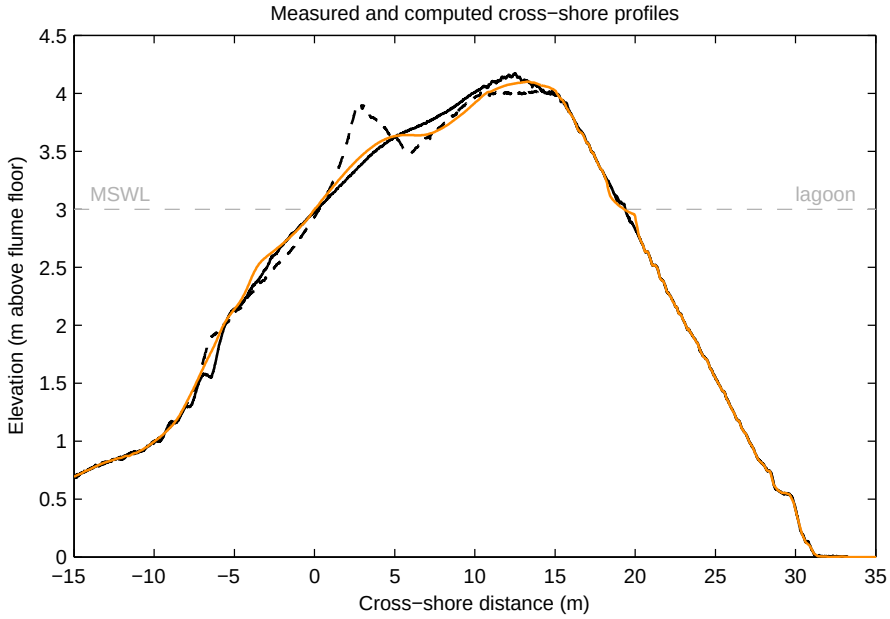

Figure 5.7: Initial cross-shore profile (– –), cross-shore profiles measured (—) and modelled (—) at the end of wave series BABR, and maximum still water levels (– –) .

cross-shore profile change well. The model correctly predicts washover sediment deposition (3.2 m^3m^{-1}) on the back barrier, and lowering of the barrier crest (0.4 m). The model does not quite manage to correctly predict the crest of the barrier, as the model predicts 2.7 m rollback of the crest. Overall, the model skill for BAE9 is high (Table 5.2), with relatively small RMSE (0.17 m) and high BSS (0.77).

The morphological response of Loe Bar to LB5 is shown in Figure 5.10. The figure shows substantial erosion of the the upper beach face and barrier crest, as well as crest lowering and washover deposits on the back barrier (black solid line). Note that the post-storm lower beach face is not shown in the figure due to the recovery of the beach and generation of beach cusps in the period between LB5 and the post-storm survey, as discussed in Section 5.4, which is not modelled in XBeach-G. Figure 5.10 shows great similarity between modelled and measured post-storm erosion of the barrier crest and deposition on the back barrier. The model correctly predicts a crest lowering of 0.2 m, and predicts crest retreat (modelled, 2.0 m; measured, 1.9 m) and washover volume (modelled, 9.6 m^3m^{-1}; measured, 10.8 m^3m^{-1}) well. The overall model skill for LB5 is high (Table 5.2), with little relative bias (-5%), low RMSE (0.05 m) and high BSS score (0.96).

5.6.5 Barrier rollover

Barrier rollover occurred during two events discussed in Section 5.4: BAE10 and ST1, where high water levels and energetic waves lead to crest lowering and substan-

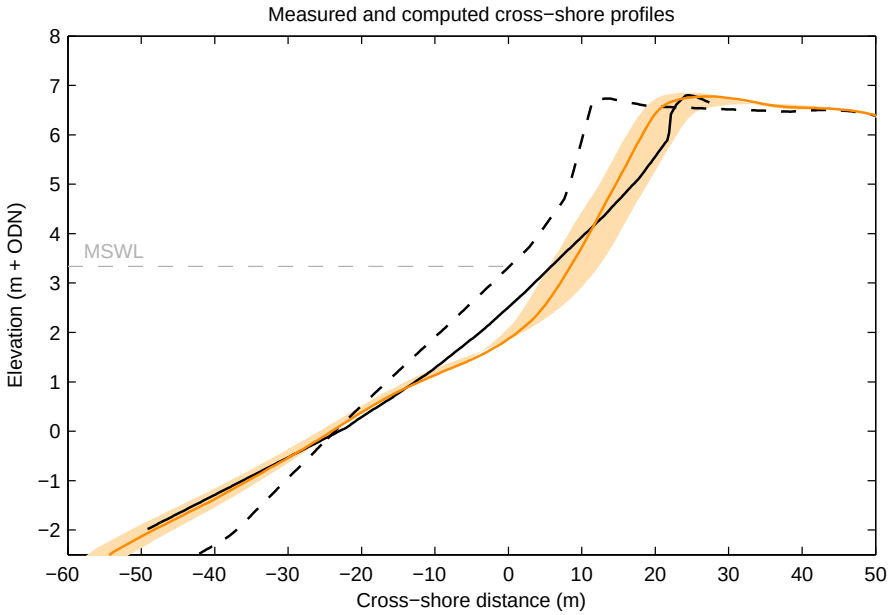

Figure 5.8: Pre-storm (– –), measured post-storm (—) and modelled post-storm (—) cross-shore profiles for SS3, and maximum still water level (– –). The range in post-storm model profiles due to varying the hydraulic conductivity (Table 3.1) is shown in shading ( ).

Figure 5.9: Initial cross-shore profile (– –), cross-shore profiles measured (—) and modelled (—) at the end of wave series BAE9, and maximum still water levels (– –).

tial crest retreat.

The results of the simulation of BAE10 are shown in Figure 5.11. The figure shows a situation with a very low relative freeboard (0.5 m; Table 3.1), leading to crest lowering (0.5 m), crest retreat (3.4 m) and substantial washover deposits on the back barrier (8.2 m^3m^{-1}). The results of the simulation show that the XBeach-G model reproduces the observed profile change well in qualitative sense, and reasonably well in quantitative sense. The model predicts lowering and retreat of the barrier crest, as well as washover deposition on the back barrier, although these are all slightly less than found in the measurements (0.5 m, 3.3 m and 4.1 m^3m^{-1}, respectively). The greatest difference between the measurements and the model predictions is the response of the foreshore between -10 m and 0 m cross-shore distance (Figure 5.11), where the model under predicts the observed erosion. The lack of erosion in the foreshore leads to an under estimation of washover deposition on the back barrier. Both errors contribute to one of the lowest values of the correlation coefficient (ρ; Table 5.2) of the simulations discussed in this chapter. However, overall model skill remains high for BAE10, with a BSS of 0.66.

As discussed at the beginning of this section, the period between the pre-storm and post-storm measurement at Sillon de Talbert, as well as the large duration between ST1 and the post-storm measurement, mean that this case cannot be used to validate the XBeach-G model in a quantitative sense. However, ST1 was the largest

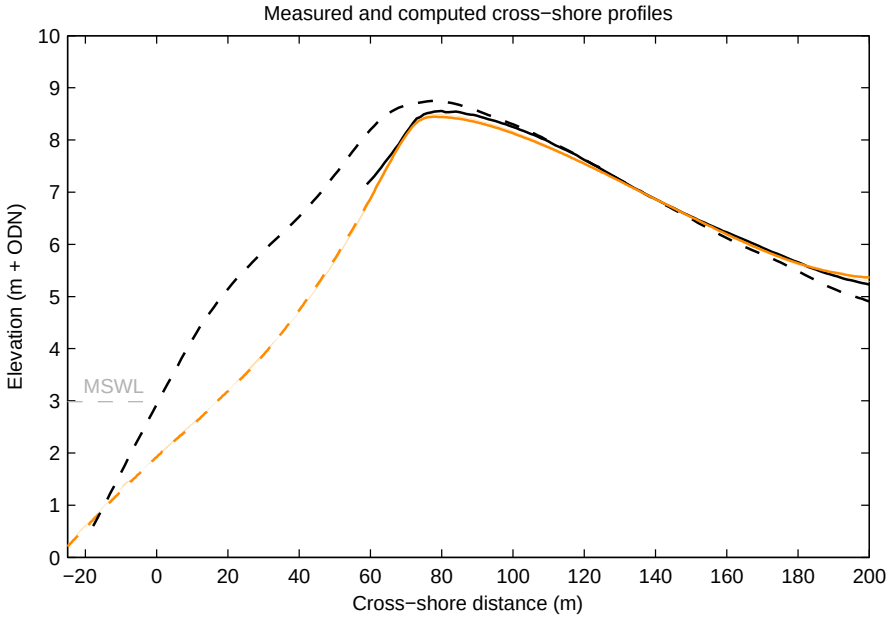

Figure 5.10: Pre-storm (– –), measured post-storm (—) and modelled post-storm (—) cross-shore profiles for LB5, maximum still water level (– –), and the section of the beach face that may have been reworked in the period between LB5 and the post-storm survey (– –), which is not included in the analysis of the model skill. The range in post-storm model profiles due to varying the hydraulic conductivity (Table 3.1) is shown in shading ( ).

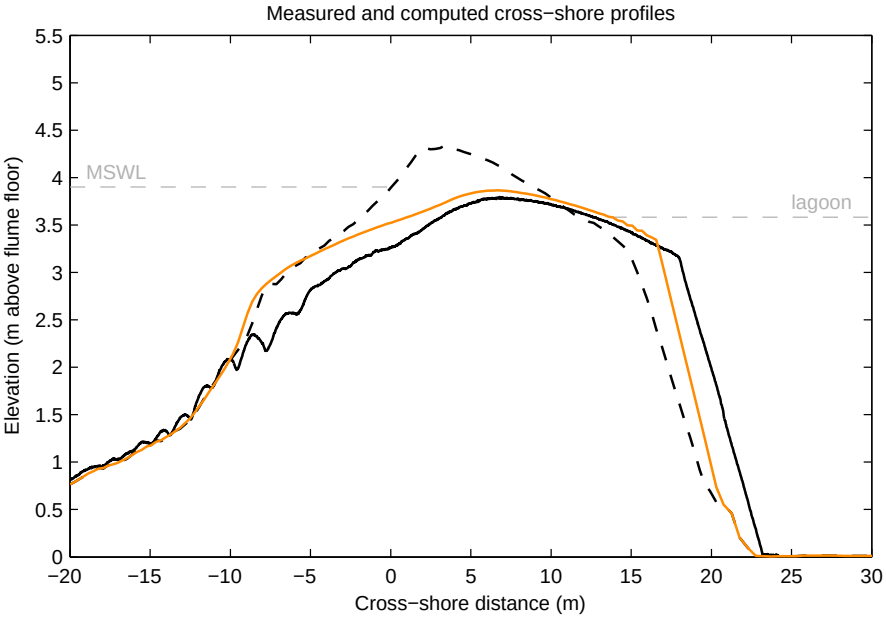

Figure 5.11: Initial cross-shore profile (– –), cross-shore profiles measured (—) and modelled (—) at the end of wave series BAE10, and maximum still water levels (– –).

storm event during the period between the pre- and post-storm measurements, and is responsible for the observed barrier rollover (Stéphan et al., 2010). The measured and modelled pre- and post-storm cross-shore profiles of ST1 are shown in Figure 5.12. The figure shows a measured crest retreat of 10.7 m, and a washover volume of 130 m^3m^{-1}. The measured crest lowering is just 0.2 m, less than the approximate 1 m lowering measured nine days after ST1 reported by Stéphan et al. (2012), which may be a result of recovery in the six months between ST1 and the post-storm measurements. The results of the model presented in Figure 5.12 show good qualitative agreement with the measurements; the model shows crest retreat (3.7 m), crest lowering (0.5 m) and washover deposition (80 m^3m^{-1}) on the back barrier. Since the measurements do not allow for an objective quantitative assessment of the overall model skill, values for the four model skill parameters are not presented in Table 5.2 for ST1.

5.7 Effect of groundwater interactions and implications for modelling gravel beach storm response

The results of the model simulations discussed in the previous section (5.6) show that XBeach-G is able to predict the morphodynamic response of gravel beaches and barriers to storms with high quantitative skill, if the model is given a reasonable estimate of the hydraulic conductivity of the beach or barrier (light orange shading in Figures 5.3–5.12 and hydraulic conductivity ranges indicated in Table 5.1). In this section,

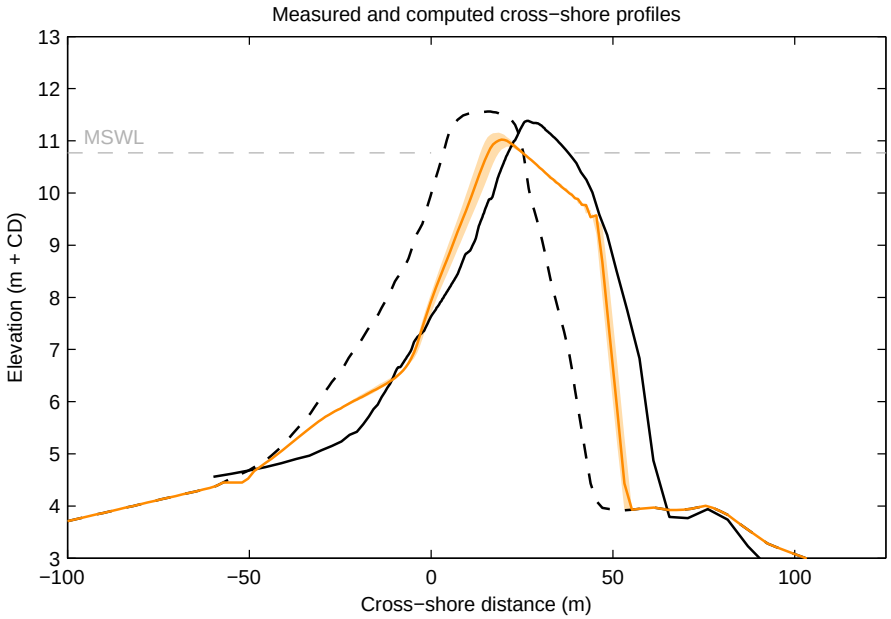

Figure 5.12: Pre-storm (– –), measured post-storm (—) and modelled post-storm (—) cross-shore profiles for ST1, and maximum still water levels (– –). The range in post-storm model profiles due to varying the hydraulic conductivity (Table 3.1) is shown in shading ( ).

the full effect of groundwater processes on modelled morphodynamics is investigated through sensitivity simulations of the 10 storm events discussed earlier, in which all groundwater processes are removed from the model (cf., NGW model in Section 4.7). Further sensitivity studies regarding particular groundwater processes, viz. the turbulent groundwater flow parametrisation, ventilated boundary layer effects and the effect of the surface seepage forces on the relative weight of grains, are presented in Appendix E.

Figure 5.13 shows the cross-shore profile development predicted by the XBeach-G model with groundwater processes (orange) and by the NGW model without groundwater processes (green) for all 10 storm events. The figure shows that including groundwater processes significantly improves the skill of the model in predicting the observed cross-shore profile change. In particular, berm formation is underestimated (CB1) and beach erosion and crest lowering are overestimated (SS2, SS3, BAE10) in the NGW model without groundwater processes compared to the regular XBeach-G model. Furthermore, through exclusion of groundwater processes, the NGW model predicts the wrong morphodynamic response type, e.g., beach erosion in the case of BAB3, crest lowering in the case of BABR and barrier rollover in the case of BAE9.

The effect of including groundwater processes appears to be particularly large in the case of BAE9 and BAE10. This observation may be explained by the high hydraulic conductivity of the BARDEX gravel beach and the design of the imposed wave and tide conditions during BAE9 and BAE10 around the threshold of barrier crest lowering. Since the threshold between crest build-up and crest lowering is highly sensitive to groundwater (infiltration) processes, disruption of these processes in the NGW simulations leads toward a shift in regimes, where crest lowering at the start of the NGW simulation is amplified to even greater crest lowering and barrier rollover through positive feedback mechanisms (i.e., more and greater overtopping flows).

The computed morphodynamic responses during CB2, LB5 and ST1 are shown not to be sensitive to the presence of groundwater processes in the model. In the case of LB5, this may be explained by the low hydraulic conductivity of the barrier ($K_{lam} = 0.003$ ms^{-1}) and is in line with earlier model observations (cf., Section 4.7). However, the difference in the profile response predicted by XBeach-G and the NGW model is not solely determined by the value of the hydraulic conductivity of the gravel beach or barrier. This is illustrated by events CB2 and ST1 where the barriers have high hydraulic conductivity ($K_{lam} = 0.40$ ms^{-1}), but the effect of including groundwater processes is substantially smaller than on less permeable beaches with similar morphodynamic response types (SS2 and BAE10; $K_{lam} = 0.075$ ms^{-1}and $K_{lam} = 0.155$ ms^{-1}, respectively). Although this may in first instance be unexpected, the relative insensitivity of the model to groundwater processes in these cases may be hypothesised to be caused by a relatively high groundwater table due to the presence of a seawall (CB2) and the high back barrier SWL (ST1). Under such conditions the upper beach may become fully saturated, which in turn leads to low infiltration rates into the beach face. Since the processes through which the model accounts for groundwater effects on hydrodynamics and sediment mobility are primarily controlled by infiltration, the predicted morphodynamic response of the XBeach-G model with groundwater processes will approach that of the NGW model in cases with limited infiltration rates.

Therefore, the potential for infiltration could be considered a better predictor for the relative effect of groundwater processes than the hydraulic conductivity *per se*.

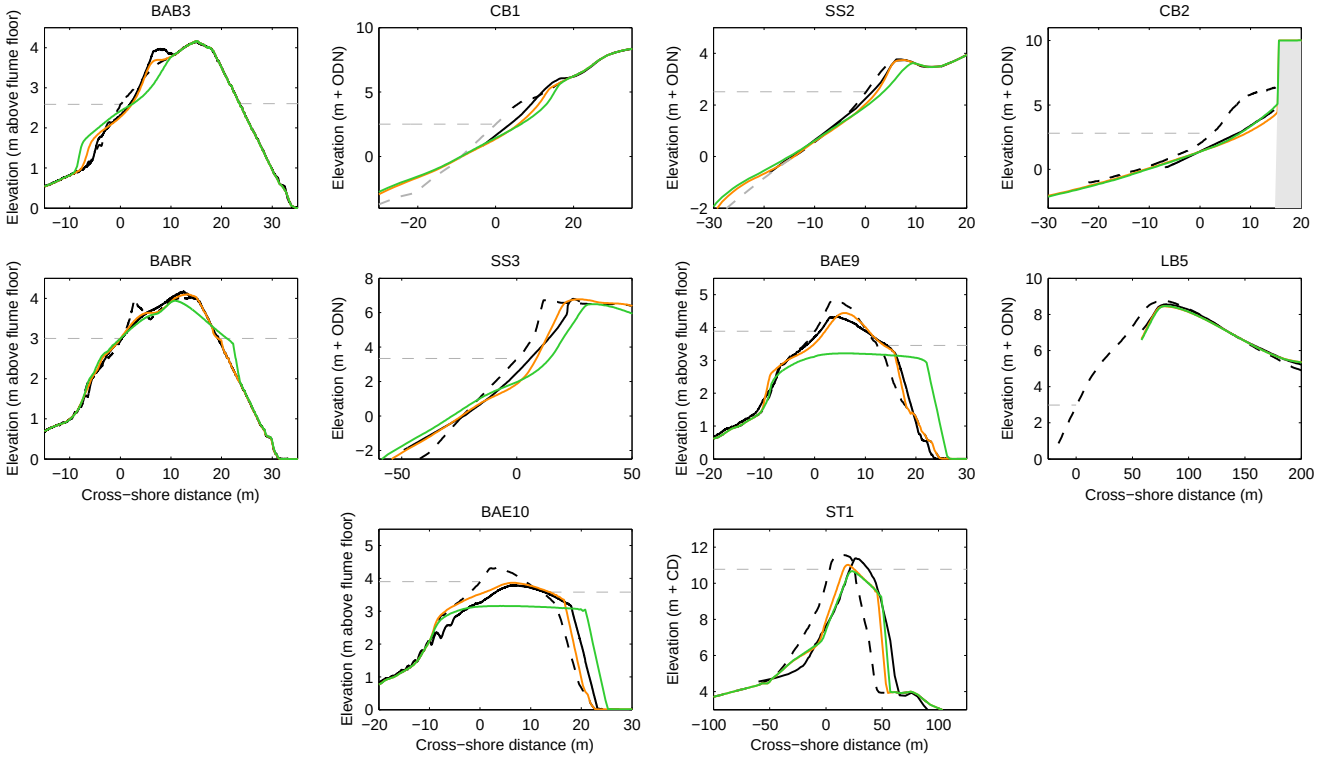

Figure 5.13: Sensitivity of modelled cross-shore profile response to the inclusion of groundwater processes: measured pre-storm profiles (– –), measured post-storm profiles (—), modelled profiles with groundwater processes (XBeach-G; —), modelled without groundwater processes (NGW; —), and maximum still water level (– –).

The results of the sensitivity studies further show that although groundwater processes may not necessarily affect wave run-up levels strongly (Section 4.7), their effect on the computed morphodynamic response of the beach face upon which wave run-up occurs is substantial (e.g., BAB3, CB1, SS2). This difference is further examined in Figure 5.14, which presents time series of water depth, horizontal velocity, bed shear stress and bed load transport rates computed by the XBeach-G model with groundwater processes (orange) and by the NGW model without groundwater processes (green) at three locations on the barrier (upper surf zone – upper swash) during BAB3. Note that the data presented in Figure 5.14 are based on simulations without bed level updating, in order to ensure comparability between the modelled hydrodynamics and sediment transport rates. The figure shows that during periods of the highest computed water depth in the upper swash (top right panel), the maximum water depth is not strongly dependent on the presence of groundwater processes in the model, highlighting the earlier conclusion that maximum wave run-up levels are not strongly affected by infiltration processes (cf. Packwood, 1983). However, examination of the horizontal velocity, bed shear stress and bed load transport rate shows more substantial differences between the XBeach-G model with groundwater processes and the NGW model. In particular, the presence of groundwater processes in the model leads to lower maximum negative (offshore-directed) velocities, as well as higher positive (onshore-directed) and lower negative bed shear stress and bed load transport rates in the swash zone (locations B and C), and lower maximum negative bed shear stress and bed load transport rates in the upper surf zone (location A). This reduction in offshore sediment transport and increase in onshore transport in the upper surf zone and swash enhances the potential for net onshore sediment transport, and thus for the berm formation-type morphodynamic response of the gravel barrier.

Sensitivity simulations presented in Appendix E show that the principle mechanism through which groundwater processes affect the simulated morphodynamics of gravel beaches and barriers is by modification of the surface water dynamics (i.e., reduction of backwash volume) through the exchange of mass between the surface water and groundwater (e.g., S_i, S_e and S_s). Ventilated boundary layer effects (Equation 5.8) and the effect of through-bed flow on the submerged particle weight (Equation 5.2) are generally shown to be of secondary importance in determining the predicted cross-shore profile response, which is contrary to the findings of Masselink and Turner (2012). In the case of BAE9 and BAE10, the ventilated boundary layer and submerged particle weight effects lead to less crest lowering, which is potentially both due to increased onshore transport towards the crest in the swash due to ventilated boundary layer effects, as to decreased back barrier transport due to increased particle weight through infiltration. It should be noted however that in all cases the magnitude of the change in bed shear stress due to ventilated boundary layer effects has been limited to those discussed in Section 5.3.2 and the model may therefore be underestimating the net effect of this process. Further detailed investigation of ventilated boundary layers on permeable gravel slopes (e.g., Sparrow et al., 2012, 2013) may lead to more appropriate bed shear stress relations under highly ventilated conditions.

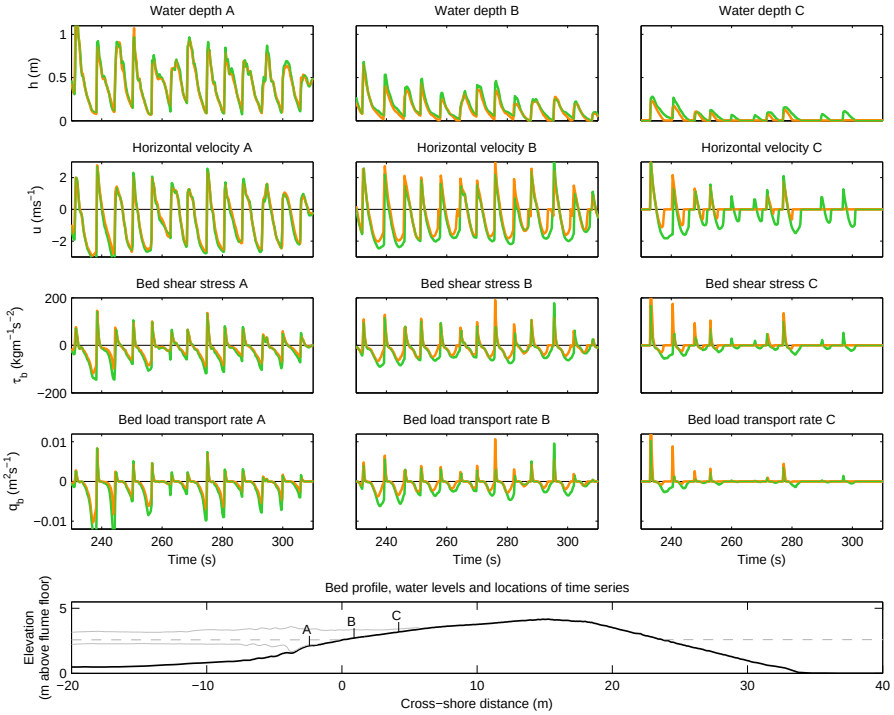

Figure 5.14: Time series of water depth, horizontal velocity, bed shear stress and volumetric bed load transport rate computed by the model with groundwater processes (XBeach-G; —) and without groundwater processes (NGW; —) at three locations on the barrier (A – upper surf zone; B – lower swash; C – upper swash) during BAB3. The locations of points A, B and C relative to the barrier profile (—) and water levels (SWL, – –; maximum and minimum, —) are shown in the bottom panel. Note that the simulations presented in this figure are carried out without morphological updating in order to ensure a consistent comparison between the models.

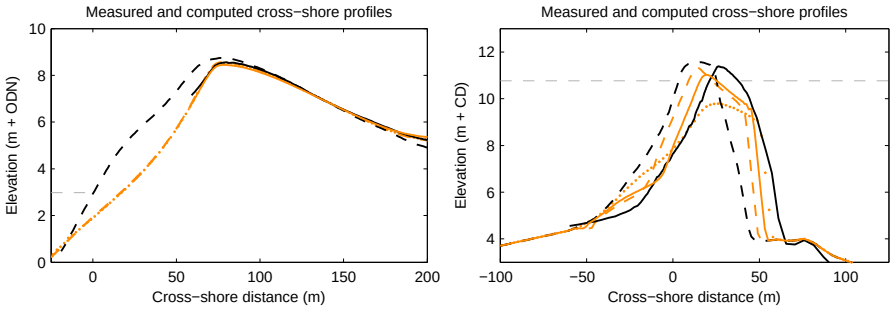

(a) Fine-grained barrier (LB5) *(b)* Coarse-grained barrier (ST1)

Figure 5.15: Sensitivity of modelled cross-shore profile response to the value of the inertia parameter. The figure shows the pre-storm (– –), measured post-storm (—) and modelled post-storm (default inertia parameter; —) cross-shore profiles, as well as the maximum still water level (– –). The range in post-storm model profiles due to varying the inertia parameter is shown for $c_i = 2.0$ (– –) and $c_i = 0.5$ (·····).

5.8 Model sensitivity

To study the effect of varying the inertia parameter c_i on cross-shore profile development in XBeach-G, sensitivity simulations are carried out for a storm event on a fine-grained barrier (LB5) and a storm event on a coarse-grained barrier (ST1). Since the bed shear due to inertia effects scales linearly with the median grain size (Equation 5.11), it can be expected that the sensitivity of the model to the inertia parameter is greater for ST1 than for LB5. In the sensitivity simulations presented in this section, the inertia parameter was varied between 0.5–2.0, while all other model parameters were kept constant. The results of these simulations are shown in Figure 5.15. The results of further sensitivity simulations in which the sensitivity of all 10 storm events to variations in the inertia parameter are investigated are shown in Appendix F (Figures F.4–F.10).

The results of the sensitivity studies show that on fine-grained barriers (e.g., left panel in Figure 5.15), the effect of modifying the inertia parameter is relatively small and does not lead to significantly different cross-shore profile development. However, the response of coarse-grained barriers (e.g., right panel in Figure 5.15) is strongly affected by the inertia parameter, where a low value of c_i leads to substantially more crest lowering and retreat than measured. This difference in the case of ST1 is the result of an imbalance between onshore transport (driven by acceleration) and offshore transport (caused by wave backwash) at the start of the storm, leading to more beach erosion and crest lowering in the case of a low value of c_i, which in turn leads to greater overwash during the peak of the storm.

The increased potential for onshore transport with the inertia parameter in ST1 is highlighted in Figure 5.16, which presents time series of water depth, horizontal ve-

locity, bed shear stress and bed load transport rates computed by the XBeach-G model with the use of inertia parameter ($c_i = 1$; orange) and without use of the inertia parameter ($c_i = 0$; green) at three locations on the barrier, ranging from the upper surf zone to the upper swash, during the peak of the first storm tide. Note that the data presented in Figure 5.16 are based on simulations without bed level updating, in order to ensure comparability between the modelled hydrodynamics and sediment transport rates. The figure shows that the inclusion of the inertia parameter greatly increases the onshore directed bed shear stress (Equations 5.11 and 5.6) and hence bed load transport (Equation 5.4) in the upper surf zone and lower swash. The maximum onshore as well as offshore-directed velocities are decreased by the inertia parameter across the beach profile, which is caused by increased bed friction (τ_{bi}) in the momentum balance equation (Equation 3.2). Furthermore, the inclusion of the inertia parameter reduces maximum velocities and wave run-up levels in the upper swash, thereby reducing the potential for wave overtopping and overwash.

The result of this sensitivity study highlights the importance of including acceleration forces on coarse-grained gravel beaches in order to correctly model sediment transport magnitudes and directions during storms (cf. Van Gent, 1995a; Pedrozo-Acuña et al., 2007). This importance has previously been found for the threshold of motion of boulders in storms (e.g., Etienne and Paris, 2010) in the equations of Nott (2003) (note however that the equations of Nott do not account for the Froude–Krylov force, resulting in an underestimation of the acceleration forces on boulders under storm waves). Although the current choice of value for the inertia parameter ($c_i = 1$) appears to represent the morphodynamic response of the broad range of gravel barriers discussed in this chapter reasonably well, further calibration and validation of the inertia parameter using data collected at coarse-grained beaches would increase confidence in applying the model on coarse gravel and cobble beaches. Such analysis would also highlight the potential for more accurate predictions of morphological change given site-specific calibration of the inertia coefficient.

5.9 Conclusions

The model results presented in this chapter show that the morphodynamic component of the XBeach-G model has considerable skill (median BSS 0.75) in predicting the morphodynamic response of gravel barriers across a wide range of forcing conditions and barrier response types. Interestingly, the results show that the model is more accurate in predicting the response to very energetic storms (beach erosion – barrier rollover; median BSS 0.83) than to less energetic storm conditions (berm formation; median BSS 0.54), although it should be acknowledged that this may in part be due to the larger observed cross-shore profile changes in the former relative to the reference zero-change prediction (cf. Bosboom et al., 2014). The range of validation cases and lack of site-specific calibration show that XBeach-G can be applied to predict storm impacts on pure gravel beaches and barriers with reasonable to high confidence for a range of hydrodynamic forcing conditions and barrier response types.

Model sensitivity simulations have highlighted the importance of groundwater processes in the process-based modelling of gravel beaches. In particular, they have shown that:

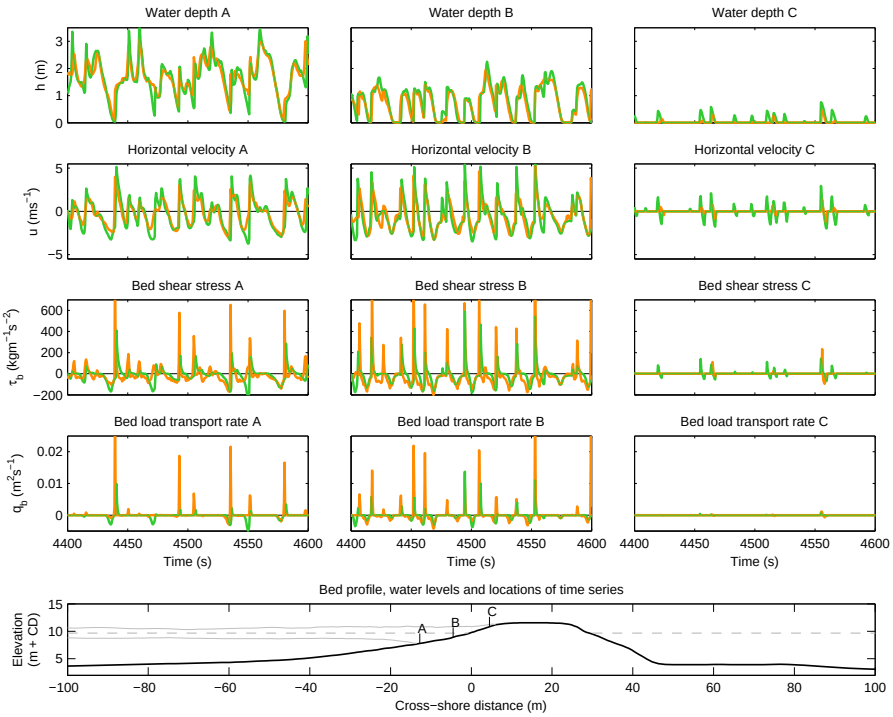

Figure 5.16: Time series of water depth, horizontal velocity, bed shear stress and volumetric bed load transport rate computed by XBeach-G with (—) and without (—) use of the inertia parameter three locations on the barrier (A – upper surf zone; B – lower swash; C – upper swash) during ST1. The locations of points A, B and C relative to the barrier profile (black) and water levels (SWL – dashed grey; maximum and minimum – solid grey) are shown in the bottom panel. Note that the simulations presented in this figure are carried out without morphological updating in order to ensure a consistent comparison between the models.

1. The inclusion of groundwater processes in XBeach-G significantly improves the predictive skill of the model through enhancing berm formation and crest build-up, and reducing beach erosion, crest lowering and barrier rollover.
2. The error associated with omitting groundwater processes in the model is not solely dependent on the hydraulic conductivity of the gravel barrier, but can be better described by the *potential* for infiltration, which is dependent on the combination of hydraulic conductivity, hydrodynamic forcing, and aquifer geometry.
3. The morphodynamic effect of the inclusion of groundwater processes is primarily caused by the by modification of the surface water dynamics through the exchange of mass between the surface water and groundwater, leading to higher onshore-directed and lower offshore-directed bed shear stress and bed load transport rates in the swash.
4. Ventilated boundary layer effects and the effect of through-bed flow on the submerged particle weight that enhance maximum onshore bed load transport rate in the upper swash are of secondary importance in determining the overall cross-shore profile response during storms.
5. Order-of-magnitude estimates of the hydraulic conductivity of the modelled gravel barrier, e.g., within a range of values found in literature, are sufficient to predict the overall morphodynamic response of the barrier, although the magnitude of the cross-shore profile response may vary.

Model sensitivity results furthermore showed the importance of including a term to account for acceleration forces on the bed on coarse-grained beaches, where omission of these lead to significant underestimation of onshore transport in the swash. Further calibration and validation of this term using data collected at coarse-grained beaches is highly recommended and would increase confidence in applying the model on coarse gravel and cobble beaches.

Chapter 6

Gravel barrier overwash thresholds

An analysis is performed in this chapter of overwash thresholds for gravel barriers using XBeach-G. Model results show that the difference between the potential wave run-up level and the height of the crest (Overwash Potential) is essential, but not sufficient, to predict the occurrence of barrier crest build-up (overtopping) and crest lowering (overwash). The results suggest that barrier width, barrier composition and the incident wave energy flux are essential parameters needed in addition to Overwash Potential to identify overtopping and overwash events. Through numerical model analysis, this chapter suggests improvements to the parametrisation of wave run-up in order to better quantify the Overwash Potential. The chapter furthermore presents schematic examples and relations to determine upper and lower overwash thresholds based on Overwash Potential, barrier width and grain size. Finally, model sensitivity simulations with and without groundwater effects show that groundwater processes contribute strongly to overwash thresholds on gravel barriers, and effectively increase the capacity of gravel barriers to withstand storms with 1–3 m higher surge levels than if groundwater processes did not occur.

6.1 Introduction

While gravel beaches and barriers are considered by many to be sustainable forms of coastal defence (Johnson, 1987; Powell, 1990; Aminti et al., 2003; Pranzini and Farrell, 2006), coastal managers currently have very limited guidance when predicting the response of gravel barriers and beaches to storms, in particular for predicting under what conditions a gravel barrier will withstand a certain storm event, be overwashed, or even breached (Masselink et al., 2014). Currently, one empirical model called the Barrier Inertia Model (BIM, cf. Section 2.3; Bradbury, 2000) is commonly used by coastal managers and engineers in the UK to compute the potential for barrier overwash during storms (DEFRA, 2008). Although the BIM has been used in many locations in the UK with some success (e.g., Cope, 2005), the data used to derive the threshold overwash relation are specific to the site and conditions where they were measured (Hurst Spit on the south coast of England). The model is therefore not necessarily valid for other sections of the coast of the UK, or the rest of the world.

The suitability of the BIM to predict overwash thresholds at other sites along the UK coastline was examined by McCall et al. (2013). In that study, a comparison was made between the overwash threshold of the BIM and critical overtopping discharges using the XBeach-G model without morphodynamic feedback (cf., Chapter 4). Following engineering design guidelines for the stability of rip-rap structures under overwash conditions (Simm, 1991; Frizell et al., 1998), critical average discharge

Sections of this chapter are based on work presented in McCall et al., 2013, McCall et al., 2015a and Poate et al. (in prep.).

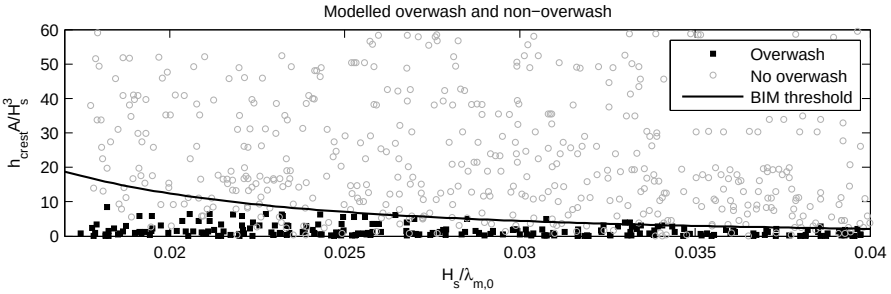

Figure 6.1: Simulated cases of overwash (black squares) and non-overwash (grey circles) computed by the morphodynamic XBeach-G model of Chapter 5 in comparison to the BIM overwash threshold. According to the BIM, overwash is unlikely to occur in the parameter space above the black curve (Equation 2.7 on page 18). The results show similarity in that only 3.6% of overwash predictions (0.6% of the total number of simulations) made by XBeach-G exceed the BIM overwash threshold.

levels were estimated for the start of damage on the back barrier (20 $ls^{-1}m^{-1}$) and severe damage on the back barrier slope (100 $ls^{-1}m^{-1}$), which were tentatively used as criteria to predict barrier overwash in the morphostatic XBeach-G model. The results of the model simulations showed that for barrier geometries and forcing conditions resembling those of Hurst Spit and the data from which the BIM was derived, the BIM and morphostatic XBeach-G model produced similar predictions for overwash. Subsequent comparison between the prediction of overwash by the morphodynamic XBeach-G model of Chapter 5 (defined as simulations in which the maximum absolute bed level change on the back barrier is greater than $3D_{50}$, after 20 minutes simulation time) and the BIM, not discussed by McCall et al. (2013), but shown in Figure 6.1, confirm the similarity between the two models for the range of barrier geometries and forcing conditions that was used to derive the BIM.

Despite the similarity between XBeach-G and the BIM in conditions similar to Hurst Spit, McCall et al. (2013) showed through the schematic (morphostatic) simulation of 25 documented storm events on the UK coast, ranging from beach scour to severe overwash (Table 6.1), that overwash predictions of the two models differed substantially for forcing conditions and barrier geometries that were significantly different from the data used to derive the BIM. In these storm simulations, the study showed that while the morphostatic XBeach-G model was not perfect, it presented a significant improvement over the BIM in predicting six of ten observed overwash events (black and red coloured symbols in Figure 6.2, namely HS, BE10, C79, S01, and two out of five events at MMo), whereas the BIM predicted only two of the ten observed overwash events, of which one was at Hurst Spit (symbols lying below the solid black line in Figure 6.2). The principal reason suggested by McCall et al. for the under estimation of the potential for overwash by the BIM was the lack of parameters relating

Location	Year	Abbreviation	Recorded storm impact category
Hurst Spit	1989	HS	Breach + severe overwash damage
BARDEX	2008	BE10	Breach + severe overwash damage
Chesil Beach	1979	C79	Breach + severe overwash damage
Chesil Beach	1978	C78	Overwash damage + crest lowering
Slapton Sands	2001	S01	Overwash damage + crest lowering
Medmerry	1994–2001 (five separate events)	MMo	Overwash damage + crest lowering
Hayling Island	2005	HI	Overtopping + crest build-up
Slapton Sands	2004	S04	Overtopping + crest build-up
BARDEX	2008	BE1	Overtopping + crest build-up
BARDEX	2008	BC1	Scour + no change to crest
Chesil Beach	2007–2010 (four separate events)	CB07	Scour + no change to crest
Loe Bar	2011–2012 (four separate events)	LB	Scour + no change to crest
Medmerry	1993–2002 (three separate events)	MMs	Scour + no change to crest

Table 6.1: Summary of storm hindcasts simulations by McCall et al. (2013).

to wave run-up (e.g., beach slope and the water depth at the toe of the gravel barrier[1]) and the evolution of overtopping flows (e.g., the hydraulic conductivity).

The results of McCall et al. (2013) clearly show that the application of the BIM on coastal sections that differ from Hurst Spit may lead to incorrect estimates for the potential for barrier overwash. This chapter attempts to improve current understanding of conditions leading to overwash with the aim of providing the potential for more accurate parametric overwash models in the future. The morphodynamic XBeach-G model of Chapter 5 is used in lieu of extensive field and physical model data on overwash conditions to investigate the role of hydrodynamic forcing and barrier geometry and composition on overwash.

6.2 Objective and model analysis set-up

Following the reasoning of McCall et al. (2013), current estimates of gravel barrier overwash thresholds (e.g., BIM) may be improved through better description of the wave run-up relative to the barrier crest, and the evolution of overtopping flows and the morphodynamic response of the barrier crest. To this end, a numerical model analysis is carried out composed of two parts. In Part I of the model analysis (Section 6.3.1), XBeach-G simulations are carried out in which the hydraulic forcing conditions (significant wave height and wave steepness) and beach geometry and composition (beach slope, grain size and hydraulic conductivity) of a schematic gravel beach (Figure 6.3) are varied to compute wave run-up levels for varying combinations of beach type and forcing (Table 6.2). These simulations are carried out to give insight into the relation between the forcing and barrier parameters on the potential wave

[1]Note that the sensitivity simulations of McCall et al. (2013) that were used to identify missing physical parameters in the BIM used wave conditions derived at a constant water depth as input for the BIM, rather than at the toe of the beach, which may affect their conclusions with respect to the effect of shallow foreshores on predicted overwash, but not necessarily improve the applicability of the BIM in such environments.

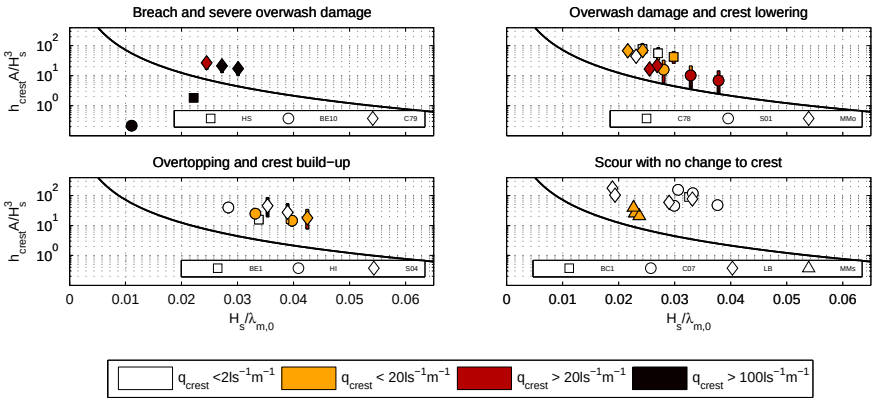

Figure 6.2: Simulated overtopping discharges across the barrier crest for 25 documented storm events and comparison of the performance of the BIM and XBeach-G with observations. The black curve represents the BIM threshold. Marker colours relate to the simulated overtopping volumes q_{crest} across the barrier crest in the morphostatic version of XBeach-G. . Note that C79, C78, S01, HI, S01, C07 and LB have three markers each to show the range of uncertainty in wave steepness. Where sensitivity simulations have been carried out with equal wave steepness, error bars indicate the range of simulated overtopping discharge and barrier inertia parameter values. Note that the vertical scale is logarithmic. Data plots are based on McCall et al. (2013) and Masselink et al. (2014).

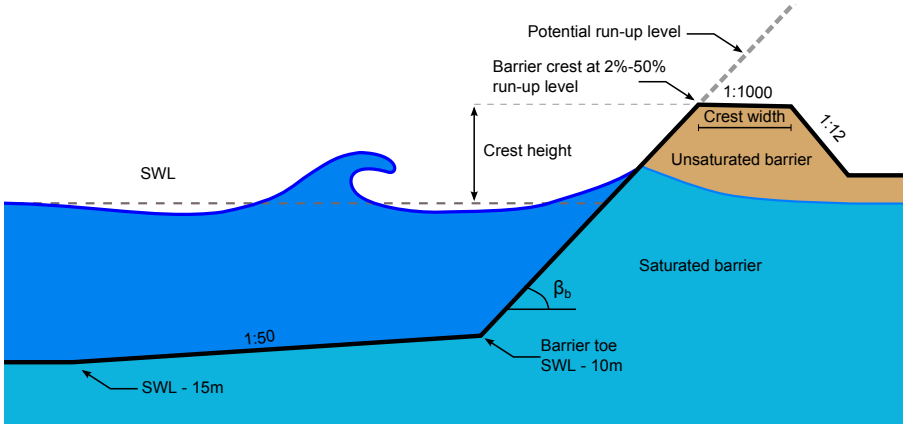

Figure 6.3: Schematic of a gravel barrier geometry for Part I and II of the numerical model analysis showing the angle of the barrier beach β_b, crest height and width. The dashed grey line represents the infinite beach slope used to compute potential run-up for this barrier type in Part I.

run-up, and are therefore simulated on a sufficiently high gravel beach (i.e., an "infinite" beach slope) so that no overtopping can take place. Furthermore, the simulations carried out in Part I of the analysis are computed without morphological updating (morphostatic simulation, cf., Chapters 3 and 4).

The morphodynamic evolution of the gravel barrier crest is investigated in Part II of the model analysis (Section 6.3.2), where simulations are carried out using the morphodynamic XBeach-G model of Chapter 5 in which the hydrodynamic forcing conditions and beach geometry and composition are varied as in Part I. However, in Part II the cross-shore profile of the gravel beach is modified to that of a barrier, where the crest height is varied between the 2% and 50% potential wave run-up exceedence heights computed in Part I, and the width of the barrier crest is varied between 2.5 m and 25 m (Table 6.2 and Figure 6.3). An important assumption made in the analysis of the results of Part II is that barrier overwash can be evaluated through analysis of the change of the maximum crest level only, where a distinction is made between crest build-up related to wave overtopping, and crest lowering that is related to overwash (Figure 6.4). While this simplification is in line with previous research (e.g., Matias et al., 2012), incorporation of other indicators of overwash (e.g., back barrier deposition, or maximum discharge levels) may be useful in future studies.

In order to minimize the parameter space to be investigated and to remove unlikely and unnatural combinations of geotechnical parameters in Parts I and II, the beach slope is assumed to correlate linearly (e.g., Shepard, 1963; McLean and Kirk, 1969; Jennings and Shulmeister, 2002) with the logarithmic phi scale of the median grain size (Krumbein and Sloss, 1963), where the phi scale is defined as $\phi = -\log_2\left(D_{50}/0.001\right)$, and the hydraulic conductivity is assumed to correlate quadratically (e.g., Hazen, 1892) with the median grain size. These variables are therefore not varied independ-

Parameter	Range
Significant wave height H_{m0}	2–6 m
Deep water peak wave steepness $s_{p,0}$	1–5%
Median grain size D_{50}	2–40 mm
Crest width W_{crest}*	2.5–25 m
Crest height h_{crest}*	2% – 50% wave run-up exceedence height (m above SWL)

Table 6.2: Hydraulic forcing and barrier properties parameter range. *Indicates parameters varied during Part II only.

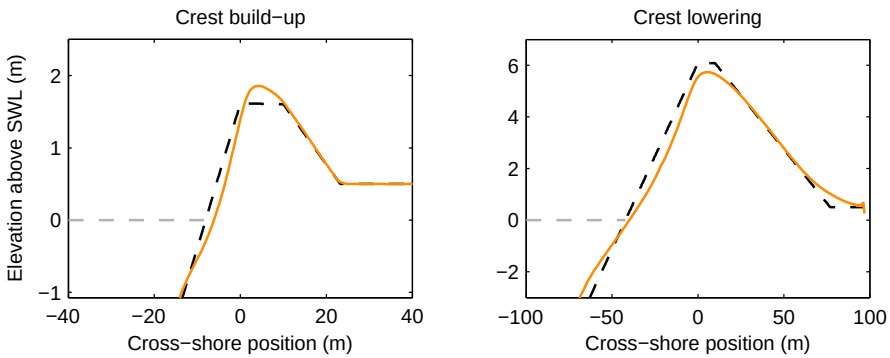

Figure 6.4: Example of a simulation with crest build-up (overtopping; left panel) and crest lowering (overwash; right panel); pre-storm profile (– –), post-storm profile (—) and still water level (– –). Note the difference in horizontal and vertical scale between the panels.

Median grain size (D_{50}; mm)	Beach slope ($\tan\beta_b$; -)	Hydraulic conductivity (K_{lam}; cms^{-1})
2.00	0.100	1.00
6.22	0.138	4.71
10.4	0.155	8.83
14.7	0.167	13.1
18.9	0.175	17.5
21.1	0.182	21.9
27.3	0.187	26.4
31.6	0.192	30.9
35.8	0.196	34.4
40.0	0.200	40.0

Table 6.3: Beach slope and hydraulic conductivity dependency on grain size. For comparative purposes, the median grain diameter, beach slope and hydraulic conductivity at Loe Bar, Slapton Sands and Chesil Beach are: 2 mm, 0.12, and 1.0 cms^{-1}; 6 mm, 0.15, and 7.5 cms^{-1}; 40 mm, 0.20, and 40.0 cms^{-1}; respectively.

ently of the grain size in the model analysis. The relation between grain size, beach slope and hydraulic conductivity used in this analysis are approximately based on values found at Loe Bar, Slapton Sands and Chesil Beach (cf., Chapter 3) and is shown in Table 6.3.

6.3 Model simulations

6.3.1 Part I: Potential wave run-up

Part I of the numerical model analysis is applied to determine the wave run-up in the event of an infinite beach slope (e.g., no overtopping of the barrier crest; Figure 6.3), which is henceforth referred to as the POTENTIAL WAVE RUN-UP. To this end, 250 simulations are carried out in XBeach-G in which the offshore significant wave height at 15 m water depth of a standard JONSWAP wave spectrum H_{m0} is varied in the range 2–6 m, the wave steepness related to the deep water wave length of the peak period wave $s_{p,0} = \frac{2\pi H_{m0}}{gT_p^2}$ is varied in the range 0.01–0.05, and the median grain size D_{50} is varied in the range 2–40 mm (Table 6.2). Note that the beach slope and hydraulic conductivity of the simulated barriers are directly correlated to the grain size, following Table 6.3. The SWL is kept constant in all simulations, as are the offshore water depth (15 m below SWL), depth at the toe of the gravel barrier (10 m below SWL) and the seabed slope (1/50). The resulting relative wave run-up $\frac{R_{2\%}}{H_{m0,0}}$, where $H_{m0,0}$ is the deep water spectral significant wave height found by deshoaling the wave height at 15 m water depth to deep water using the peak wave frequency, is computed from one-hour time series of the shoreline elevation after 20 minutes of model spin-up time.

The results of the 250 simulations is shown in Figure 6.5 as scatter plots of the re-

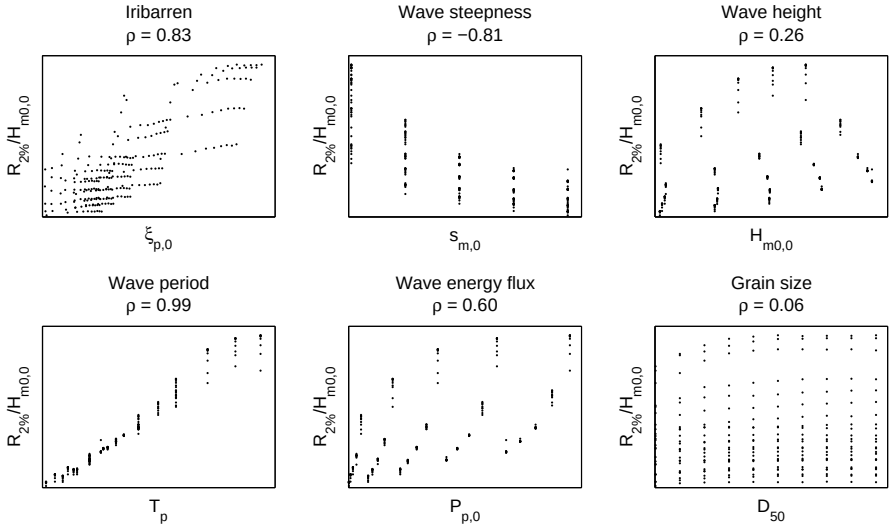

Figure 6.5: Correlation between relative wave run-up predicted by the XBeach-G model and hydrodynamic forcing conditions and barrier properties. The correlation coefficient ρ between the relative wave run-up and hydrodynamic variables and barrier properties is given in the title of each panel.

lative wave run-up $\frac{R_{2\%}}{H_{m0,0}}$ versus a range of parameters: (1) the deep water Iribarren parameter $\xi_{p,0} = \frac{\tan\beta_b}{\sqrt{H_{m0,0}/\lambda_{p,0}}}$; (2) the steepness of the mean period wave $s_{m,0}$; (3) the deep water wave height $H_{m0,0}$; (4) the peak wave period T_p; (5) the deep water wave energy flux based on the group velocity at the peak frequency $P_{p,0} = \frac{1}{8}\rho g H_{m0,0}^2 c_{g,p,0}$; and (6) the median grain size D_{50}. The figure shows strong correlation (high absolute value of the correlation coefficient ρ) between the relative wave run-up and the Iribarren parameter (cf. Battjes, 1974; Holman, 1986; Stockdon et al., 2006), and between the relative wave run-up and the wave steepness (cf. Powell, 1990; Nielsen and Hanslow, 1991). Interestingly, a significantly higher correlation is found between the (dimensional) peak wave period and the relative wave run-up than those found for the non-dimensional Iribarren parameter or wave steepness. The minor positive correlation between the relative wave run-up and grain size indicates that the effect of the parametrised increase of beach slope with grain size outweighs the effect of the parametrised increase in hydraulic conductivity with grain size on wave run-up, but that these effects are minor compared to effect of variations in wave forcing. Importantly, the figure shows a positive correlation between the relative wave run-up, which is normalised by the incident wave height, and the incident wave height, indicating that according to the model simulations, wave run-up depends on wave height in a non-linear fashion.

The effect of variations in the offshore wave height on the simulated relative wave run-up is further examined in Figure 6.6, where the computed relative wave run-up

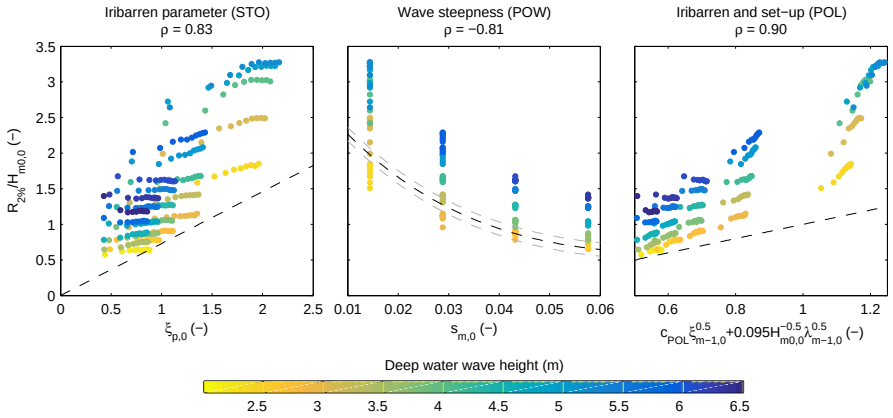

Figure 6.6: Relation between the relative wave run-up predicted by the XBeach-G model (coloured dots) and the Iribarren parameter (left panel) and STO model (dashed line); the mean wave steepness (centre panel) and POW model (dashed line); and the Iribarren-type set-up and swash parameter of the POL model (right panel and dashed line). In the centre panel, the grey lines indicate model spread for deep water, rather than offshore wave heights. Colours indicate variations in deep water wave height. The correlation coefficient ρ between the relative wave run-up and Iribarren or wave steepness variables is given in the title of each panel.

is plotted as a function of the deep water wave height (colours) and the deep water Iribarren parameter as used in the empirical model of Stockdon et al. (STO; 2006) for steep beaches[2] (Equation 2.1b; left panel), the wave steepness as used in the model of Powell (POW; 1990) to compute the berm elevation (Equation 2.3; centre panel), and the Iribarren-type wave set-up component and incident swash component used in the model of Polidoro et al. (POL; 2013), where c_{POL} represents coefficients relating to the shape of the wave spectrum (Equation 2.4; right panel). The relative wave run-up prediction of each empirical model is shown in the figures by the dashed black line. The figure points to two important findings: first, all three empirical run-up relations tend to estimate lower wave run-up (dashed line) compared to the XBeach-G simulations (coloured dots), with the exception of POW for low-steepness and low energy ($H_{m0,0} < 3$ m) waves. Secondly, the XBeach-G simulations show increased relative wave run-up for increasing deep water wave height, which is partially independent of the Iribarren number and wave steepness. The three empirical relations do not, and cannot due to the nature of their equations, show this behaviour.

The dependency of the relative wave run-up on the deep water wave height in the predictions of the XBeach-G model is shown in Figure 6.7 (left panel), where the

[2]Application of the empirical model for mild slope beaches (Equation 2.1a), or the combined empirical equation for all types of beaches (Equation 2.2) leads to lower predictions of wave run-up than those of the equation for steep beaches and is not discussed further in this chapter.

correlation coefficient ρ is shown to increase from 0.83 between the relative wave run-up and the Iribarren parameter (refer to Figure 6.6, left panel) to 0.92 between the relative wave run-up and the the Iribarren parameter scaled by the square root of the deep water wave height. It should be noted that the relation depicted in the left panel of Figure 6.7 is equivalent to relating the relative wave run-up to the incident wave period and beach slope as $\sqrt{H_{m0,0}}\frac{\tan\beta_b}{\sqrt{H_{m0,0}/\lambda_{m-1,0}}} = \sqrt{\frac{g}{2\pi}}T_{m-1,0}\tan\beta_b$ through substitution of $\lambda_{m-1,0} = \frac{gT_{m-1,0}^2}{2\pi}$. In the centre panel of Figure 6.7, wave run-up predictions by XBeach-G are shown to be better described ($\rho = 0.89$) by the square root of the beach slope and wave steepness ($\frac{\xi_{m-1,0}}{\sqrt{\tan\beta_b}} = \sqrt{\frac{\tan\beta_b}{H_{m0,0}/\lambda_{m-1,0}}}$), than by the standard Iribarren parameter, although considerable scatter due to variations in deep water wave height is still visible. Finally, the right-hand panel in Figure 6.7 shows a very strong correlation ($\rho = 0.97$) between the relative wave run-up predicted by the XBeach-G model and a modification of the Iribarren parameter through inclusion of both scaling to the square root of the deep water wave height and a reduction of the influence of the beach slope term.

While some scatter is still present, relative wave run-up predictions of the XBeach-G model are relatively well described (b_{rel} = 0.08; SCI = 0.12) by a linear function of the Iribarren parameter and square root of the deep water wave height and beach slope:

$$\frac{R_{2\%}}{H_{m0,0}} = 0.33\sqrt{\frac{H_{m0,0}}{\tan\beta_b}}\xi_{m-1,0} \tag{6.1}$$

Note that the constant in Equation 6.1 has dimensions $m^{-0.5}$ to convert to non-dimensional relative wave run-up. Equation 6.1 can also be described in terms of beach slope and incident wave period:

$$\frac{R_{2\%}}{H_{m0,0}} = 0.33\sqrt{\frac{g}{2\pi}}\sqrt{\tan\beta_b}T_{m-1,0} \tag{6.2}$$

While Equation 6.1 appears to describe the relative wave run-up predictions of XBeach-G well, the parametrisation of the XBeach-G model results in this manner suffers from two limitations in practical applications. First, the XBeach-G model prediction dataset from which the parametrisation is derived is limited in the number and range of variables varied in the model simulations, and is based on highly schematic representations of the beach geometry. Secondly, the constant in the equation is not non-dimensional, which suggests that the equation would not necessarily be valid at non-prototype scales (e.g., Froude-scaled laboratory experiments). Currently, no physically suitable length scale (Equation 6.1), or time scale (Equation 6.2) has been found to non-dimensionalise the constant in the parametrisation of the XBeach-G relative wave run-up predictions.

Despite the fact that Equation 6.1 is based only on model-generated data, the improvement of Equation 6.1 over run-up predictions based on the Iribarren parameter

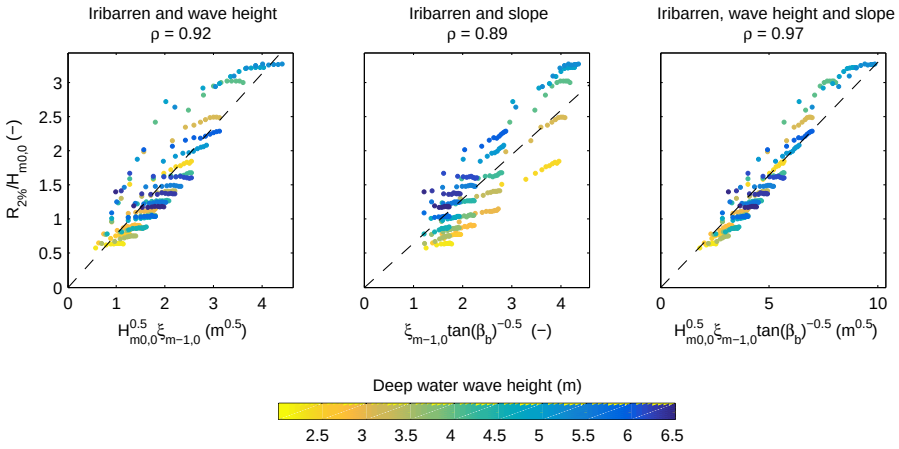

Figure 6.7: Relation between relative wave run-up predicted by the XBeach-G model and three modified Iribarren parameters. The dashed black lines in each panel represent a linear fit through the model data and the origin. The correlation coefficient ρ for each comparison is given in the title of each panel.

is substantial and is shown in Figure 6.8, where predicted $R_{2\%}$ wave run-up levels are shown relative to wave run-up levels extracted from 743 17-minute camera pixel stack time series collected at Chesil Beach, Loe Bar and Slapton Sands between 2012 and 2014 (Poate et al., in prep.). Note that the data presented in Chapter 3 (Figure 3.10 on page 45) for Chesil Beach, Loe Bar and Slapton Sands represent a subset of the data presented in Figure 6.8. The figure shows that the STO model (left panel) tends to under estimate the measured wave run-up (b_{rel} = -23%) and has high scatter (SCI = 0.49), which is consistent with the results shown in Figure 6.6.

To rule out the effects of scalable model bias and the bimodality of the wave spectrum at the measurement locations, the STO model is modified through the application of the Iribarren parameter $\xi_{m-1,0}$, which is based on the spectral wave period $T_{m-1,0}$ (cf. Polidoro et al., 2013), and an increase of the empirical constant in Equation 2.1b such that the bias of the model predictions with respect to the measurements is zero, leading to the relation:

$$\frac{R_{2\%}}{H_{m0,0}} = 1.15\xi_{m-1,0} \tag{6.3}$$

The results of this modified STO model (Figure 6.8; centre panel) show that the model predictions still have considerable scatter (SCI = 0.40). Furthermore, although the modified parametrisation is by definition not biased over the entire dataset, the modified model tends to under estimate the run-up levels during high energy events ($H_{m0,0}$ >3 m, n = 153; b_{rel} = -33%) and over estimate run-up levels during low-energy events ($H_{m0,0}$ ≤3 m, n = 590; b_{rel} = 9%). Again, this is consistent with the

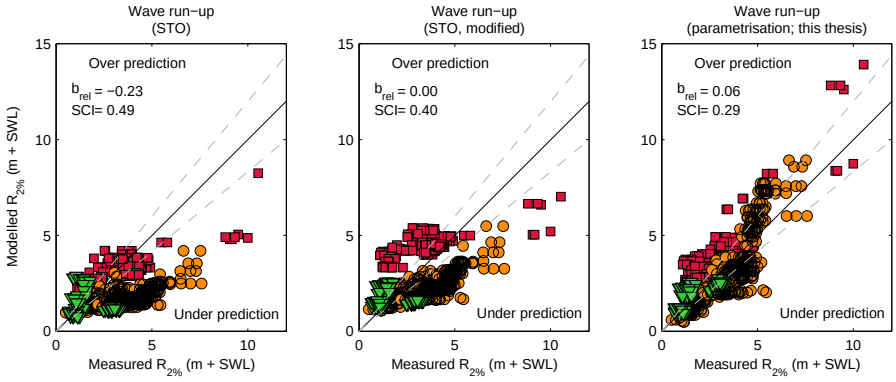

Figure 6.8: Comparison of $R_{2\%}$ run-up levels predictions using empirical model of Stockdon et al. (2006) for steep beaches (Equation 2.1b; left panel), a modified version of the empirical model of Stockdon with zero bias (Equation 6.3; centre panel), and Equation 6.1 (right panel) for 743 run-up data points collected at Chesil Beach (red □), Loe Bar (orange ◯) and Slapton Sands (green ▽) between 2012 and 2014 (Poate et al., in prep.). The solid black line indicates zero relative error, and the grey dashed lines indicate 20% relative error.

results presented in Figure 6.6, which shows that relative wave run-up levels appear to be dependent on the deep water wave height and thus that an Iribarren-type wave run-up equation calibrated to a set of measurement data is likely to under predict wave run-up for high-energy wave conditions.

Finally, Figure 6.8 (right panel) shows the predicted wave run-up using Equation 6.1. The figure shows reasonable correspondence between measured and modelled wave run-up levels (SCI = 0.29) and low model bias (b_{rel} = 0.06) across the whole dataset, although the model tends towards greater over prediction of wave run-up during high-energy wave events (b_{rel} = 14%) than during low-energy wave events (b_{rel} = 4%). The results in Figure 6.8 thus show that despite the fact that Equation 6.1 is derived from XBeach-G model simulations that are only schematically based on conditions observed at the three gravel beaches and not on measurement data, the general modification to Iribarren-type run-up formulations proposed in Equation 6.1 (viz. scaling of the Iribarren parameter with the square root of the deep water wave height and the beach slope) substantially increases the predictive skill of wave run-up levels compared to Iribarren-type equations calibrated to the measurement data.

The reason for increasing values of relative wave run-up with increasing deep water wave height observed in the XBeach-G simulation results may be speculated to be a result of for instance increasing infragravity wave dominance, or increasing wave groupiness and swash interactions with increasing wave height. Further investigation of these processes is highly recommended in both numerical model simulations and field data analysis, but is not discussed further in this chapter. However, the high

model skill of XBeach-G in simulating observed wave run-up on gravel beaches during storms (Chapter 3), as well as the improved predictive skill of the wave run-up parametrisation (Equation 6.1) provides some measure of confidence that the relative wave run-up on gravel beaches during storms can be better described by a new approach that includes these effects alongside the standard Iribarren and wave steepness parameters.

6.3.2 Part II: Morphology of the barrier crest

Part II of the numerical model analysis examines the simulated response of gravel barriers, defined in terms of crest level change, to variations in forcing conditions and barrier geometry and composition. To this end 12,250 simulations were carried out with the same variations in offshore significant wave height H_{m0}, deep water wave steepness $s_{p,0}$ and median grain size D_{50} as applied in Part I, as well as varying the width of the crest of a schematic barrier W_{crest} (Figure 6.3) in the range 2.5–25 m. Furthermore, the height of the crest of the schematic barrier above SWL h_{crest} in each simulation is related to the wave run-up computed in Part I for the combination of H_{m0}, $s_{p,0}$ and D_{50} of the barrier and forcing conditions, and varied in the range of the $R_{50\%,pot}$–$R_{2\%,pot}$ wave run-up exceedence level, where the subscript *pot* refers to potential run-up levels in case of an infinite beach. Note that the run-up level used is the level computed by XBeach-G, rather than that of the run-up parametrisation of Equation 6.1. In an identical manner to Part I, the beach slope and hydraulic conductivity of the simulated barriers are directly correlated to the grain size, following Table 6.3, and the SWL, offshore water depth, depth at the toe of the gravel barrier and the seabed slope are kept constant and at the same value as in Part I. Additionally, the barrier crest is given a constant landward-dipping slope of 1:1000 to ensure overtopping water drains from the crest, and the slope of the back barrier is set at 1:12 in all simulations. All simulations are run for one hour of morphological updating after 20 minutes of model spin-up. The simulated crest level change Δh_{crest} is found by comparing the maximum elevation in the post-storm profile to the maximum elevation in the pre-storm cross-shore profile, where positive values indicate an increase in maximum elevation. Since the barrier crest has a landward-dipping slope, even small amounts of erosion of the barrier crest lead to a lowering of the maximum crest level, which would not be the case had the initial barrier crest been horizontal. To distinguish between this lowering due to erosion of the beach face and choice of barrier slope, and crest lowering due to overtopping and overwash, Δh_{crest} is only considered negative (i.e., crest lowering) if the maximum post-storm elevation is below the initial elevation of the landward edge of the barrier crest. All simulations with a maximum post-storm elevation that lies between the initial elevation of the landward edge and seaward edge of the barrier crest are considered to have Δh_{crest} equal to zero.

Previous research on a gravel barrier (Matias et al., 2012) has shown the difference between the potential wave run-up height and the crest height, the so-called Overwash Potential (OP), to be a good indicator of overtopping and overwash. Figure 6.9 shows the computed crest level change of a narrow (5 m) and a wide (20 m) gravel barrier, as a function of the OP and the median grain size D_{50}, where the Overwash Potential in this analysis is defined as:

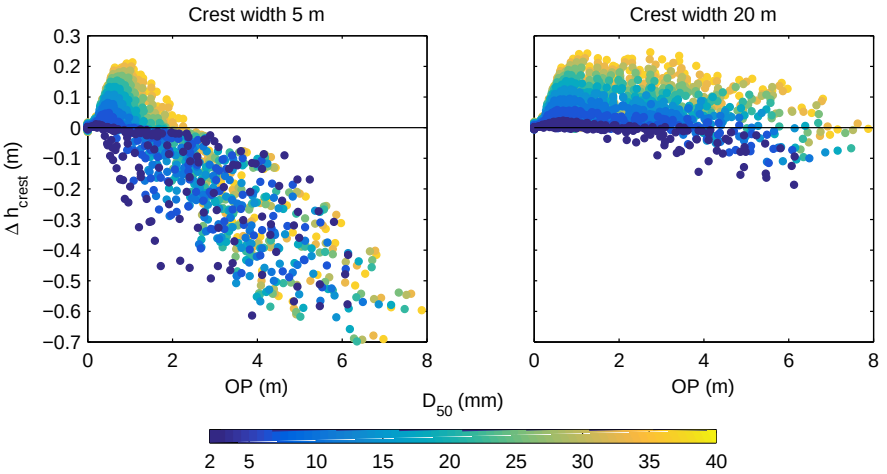

Figure 6.9: Computed crest level change as a function of the OP and grain size for a narrow (left panel) and wide (right panel) barrier. Positive values indicate crest build-up.

$$\mathrm{OP} = R_{2\%,pot} - h_{crest,i} \tag{6.4}$$

where $h_{crest,i}$ is the initial crest height above SWL. The figure shows that higher crest build-up is achieved by gravel barriers composed of coarse sediment than those composed of fine sediment, and that coarse and wide gravel barriers can continue crest build-up under higher OP conditions than fine and narrow gravel barriers. However, the figure also shows considerable spread in predicted crest level change for a given combination of OP and grain size.

The computed crest level change is shown in Figure 6.10 as a function of the grain size and the relative potential run-up freeboard (RPRF), defined as:

$$\mathrm{RPRF} = {}^{R_{2\%,pot}}\!/_{h_{crest,i}} \tag{6.5}$$

. The figure shows that both in the case of the narrow barrier and the wide barrier, maximum crest build-up occurs when the RPRF is approximately 0.5, i.e. the crest elevation lies half way between the still water level and the 2% wave run-up exceedence height. However, the figure also shows that the spread in predicted crest level change is greatest at a RPRF of 0.5, where in the case of the narrow barrier the predicted crest level change varies between 70 cm lowering to 20 cm crest build-up. Predicted crest level change is generally negative (crest lowering) for all grain sizes and barrier crest widths when the RPRF is less than approximately 0.4–0.5.

The variation in model results presented in Figures 6.9 and 6.10 are further examined in Figures 6.11 and 6.12, where the computed crest level change is shown as a function of the incident deep water wave energy flux $P_{p,0}$ and the OP and RPRF, respect-

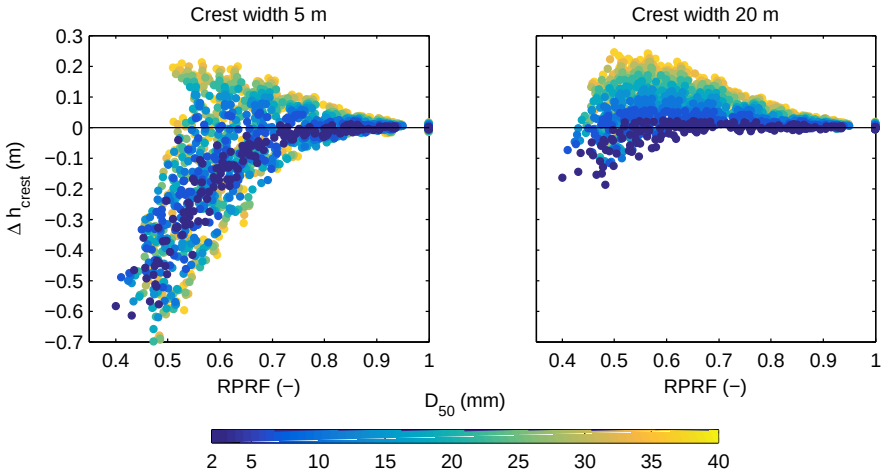

Figure 6.10: Computed crest level change as a function of the RPRF and grain size for a narrow (left panel) and wide (right panel) barrier. Positive values indicate crest build-up.

ively. The figures show that for constant wave energy flux, very fine gravel barriers experience increasing crest lowering with increasing OP (e.g., increase of the still water level relative to the crest) and decreasing RPRF (e.g., increasing number of overtopping waves). Crest build-up on very fine gravel barriers is only shown to occur in very small amounts on wide barriers under conditions with low incident wave flux. In the case of very coarse gravel barriers however, increasing values of OP and decreasing values of RPRF can lead to more crest build-up, rather than crest lowering, on all simulated barrier widths. The range of incident wave energy flux conditions in which crest build-up can occur on very coarse gravel barriers is determined by the barrier width, e.g. only in conditions of low values of incident wave energy flux for narrow barriers ($W_{crest} \leq 5$ m) and for all simulated wave energy fluxes for wider gravel barriers. This process of crest build-up on coarse barriers may be hypothesized to play a role in the recovery of gravel barriers after large overwash events, where in the days following the storm the wave conditions will abate (lower incident wave energy flux), whereas the OP will remain high due to overwash-induced crest lowering during the storm and the increased width of the barrier caused by washover deposition enhances the ability of the barrier to captured sediment and increase the height of the crest.

Interestingly, Figure 6.11 shows that increasing incident wave energy flux while maintaining a constant OP does not lead to increased crest level change (less crest build-up or lowering). While counter-intuitive, this can be explained by the fact that the OP is not independent of the incident wave energy flux and that under high energy flux conditions, and therefore high values of $R_{2\%,pot}$, relatively fewer waves overtop a crest at a given distance below the 2% run-up level (constant OP), than in the case of lower wave energy flux, since the spread in wave run-up levels increases with increasing wave energy flux.

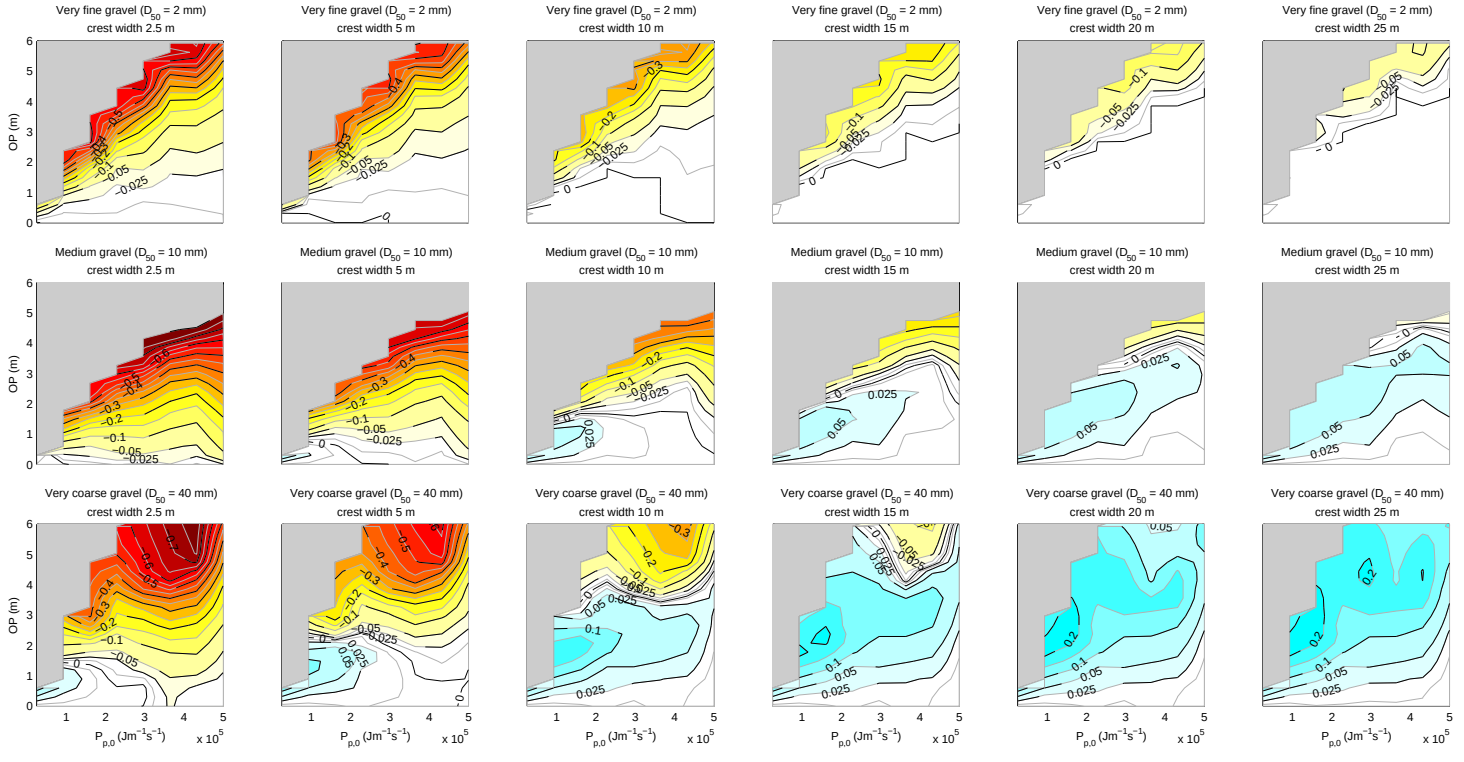

Figure 6.11: Simulated crest level change for a very fine gravel barrier (top row), medium gravel barrier (middle row) and very coarse gravel barrier (bottom row) for varying OP, incident wave energy flux and crest widths (columns). Hot colours indicate crest lowering, cool colours indicate crest build-up and grey represents areas without data.

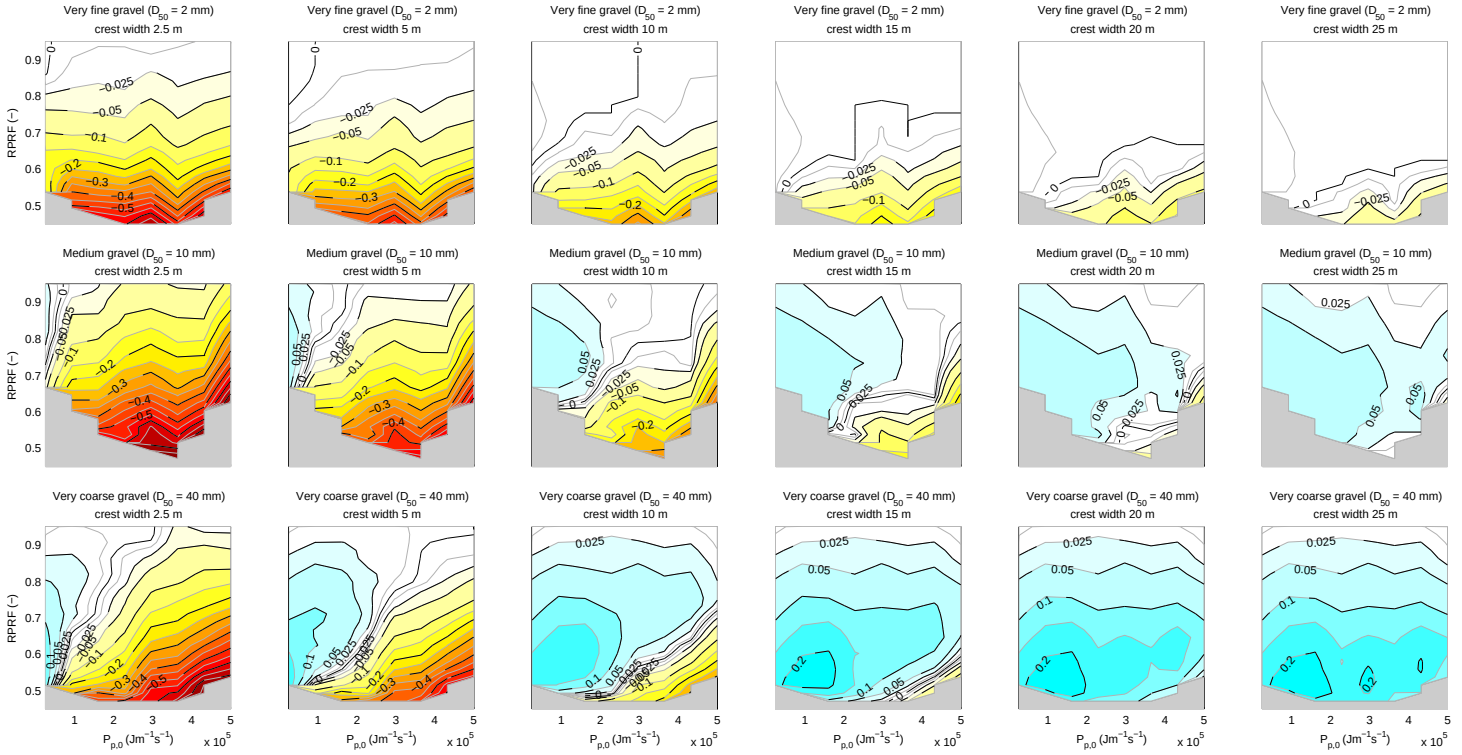

Figure 6.12: Simulated crest level change for a very fine gravel barrier (top row), medium gravel barrier (middle row) and very coarse gravel barrier (bottom row) for varying RPRF, incident wave energy flux and crest widths (columns). Hot colours indicate crest lowering, cool colours indicate crest build-up and grey represents areas without data.

While the results presented in Figures 6.11 and 6.12 give insight into the relative effects of the barrier geometry and composition (W_{crest} and D_{50}) and hydrodynamic forcing conditions (OP, RPRF and $P_{p,0}$) on gravel barrier storm response, the morphodynamic response of gravel barriers can also be further simplified to identify maximum and minimum threshold OP values for crest level lowering. An estimate of these thresholds, based on the XBeach-G model results of Part II is depicted in Figure 6.13, where the left panels depict the minimum OP (top row) and maximum RPRF (bottom row) leading to crest level lowering in the model simulation results, and the right panels depict the maximum OP (top row) and minimum RPRF (bottom row) *not* leading to crest lowering. The results of the left and right columns can be used to identify upper and lower bounds for the start of overwash (crest lowering) on a gravel barrier, where for instance a barrier with crest width of 10 m and grain size of 20 mm may experience crest lowering at a lower OP threshold of 2.0 m (top left panel) and crest lowering will almost certainly have taken place once an upper OP threshold of 2.9 m is reached (top right panel). Similarly, the same gravel gravel barrier may experience crest lowering at an upper RPRF threshold of 0.80 (bottom left panel) and crest lowering will almost certainly have taken place once a lower RPRF threshold of 0.58 m is reached (bottom right panel).

It should be noted that while the threshold conditions described in Figure 6.13 do illustrate the potential to use of the XBeach-G model to investigate conditions for barrier overwash, the absolute values of the OP thresholds are likely only applicable for the schematic storm simulations carried out in Part II of this numerical model analysis. The temporal variation of the storm and storm duration in particular are important parameters for the determination of the morphological response of gravel barriers that are not well described in the current model analysis framework (one-hour simulations of constant maximum storm conditions). However, the development of overwash threshold diagrams based on less schematic model simulations, in combination with the development of more accurate wave run-up equations for gravel beaches, could have very practical applications for the assessment of flood risk on gravel coasts.

6.4 Effect of groundwater interactions and implications for overwash thresholds

In analogy with Sections 4.7 and 5.7, this section examines the effect of groundwater-surface water interaction, primarily infiltration in the upper swash and on the barrier crest, on overwash thresholds of gravel barriers during storms. To this end the hydraulic forcing conditions and barrier properties of Part II of the numerical model analysis are re-simulated using the XBeach-G model without groundwater processes (cf., NGW model of Section 5.7). It should be noted that in this analysis, the crest height of the simulated gravel barriers, as well as the assumed OP and RPRF are identical to those used in Part II of the model analysis and do not account for increased potential wave run-up levels in the NGW model with respect to the XBeach-G model with groundwater processes. This analysis method facilitates simple comparison of identical gravel barriers that differ only in respect to their hydraulic conductivity. A short analysis in which the crest level of simulated gravel barriers is modified (increased) to account for higher wave run-up levels in the NGW model is given in Appendix G, but does not alter the overall conclusion of this section.

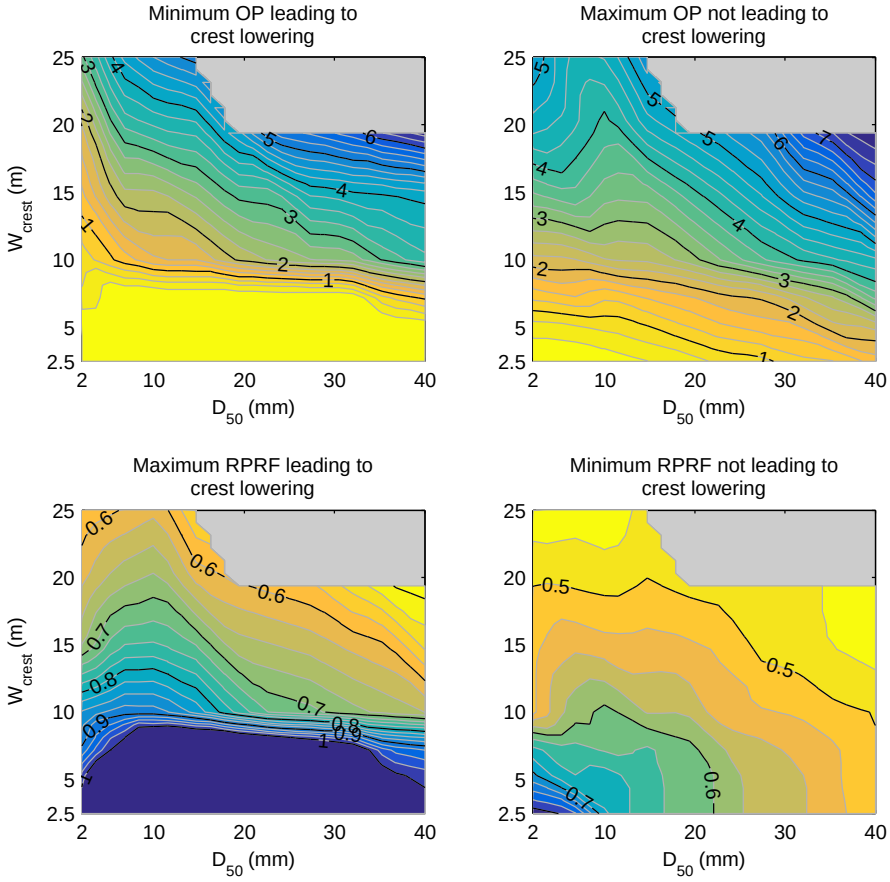

Figure 6.13: Minimum OP resulting in crest lowering (top left panel), maximum OP not resulting in crest lowering (top right panel), maximum RPRF resulting in crest lowering (bottom left panel) and minimum RPRF not resulting in crest lowering (bottom right panel) in XBeach-G model simulations of Part II, as a function of the barrier crest width and median grain size.

A comparison of the simulated bed level change with and without the groundwater model is shown in Figure 6.14, for the case of a barrier with a crest width of 10 m. The results show that the inclusion of groundwater processes consistently leads to less crest lowering, or greater crest build-up of the gravel barrier. Furthermore, the figure shows that the absolute difference in crest level change (panels in the third column) increases with increasing grain size (and hydraulic conductivity) and increasing OP. The relative difference due to groundwater processes, defined as the absolute crest level change difference normalised by the maximum of the absolute crest level change in the XBeach-G model and NGW model, on very fine gravel barriers with low hydraulic conductivity is substantially less (10–20% difference for conditions of maximum simulated crest level change) than the effect on very coarse gravel barriers (40–50% difference for conditions of maximum simulated crest level change). The difference in the magnitude of the effect of groundwater processes on the crest level change aside, both types of barrier are characterised by a maximum *relative* difference due to groundwater processes near the zero-crest level change contour (i.e., the threshold between overtopping and overwash) and a maximum *absolute* difference due to groundwater processes under conditions of greatest crest lowering.

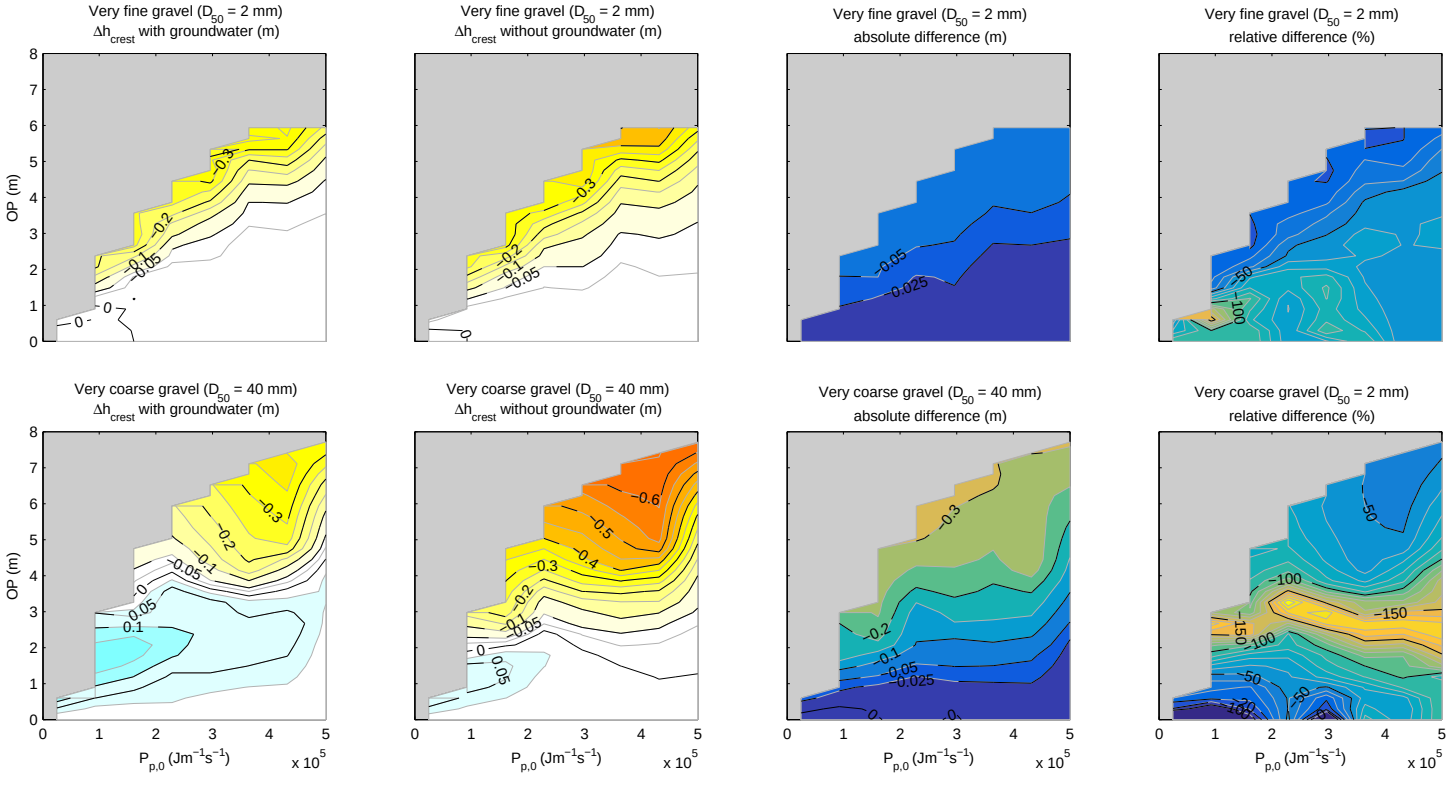

Figure 6.14: Effect of including groundwater effects in the computed crest level change as a function of the OP, incident wave energy flux and grain size, shown for barriers with 10 m crest width. In the leftmost two columns, hot colours indicate crest lowering and cool colours indicate crest build-up. In the absolute and relative difference plots, negative values indicate that the crest of the model without groundwater is lower than the model with groundwater. Grey represents areas without data.

The effect of groundwater processes on the upper and lower OP and RPRF thresholds discussed in Section 6.3.2 is shown in Figure 6.15, where solid orange lines represent contour lines of the XBeach-G model simulations, and the dashed black lines those of the NGW model simulations. The figure shows that although the threshold contour lines of both models have similar trends, the absolute values of the thresholds differ substantially. The figure shows for instance that for a barrier with crest width of 10 m and grain size of 20 mm, the lower OP threshold for the start of overwash (top left panel) drops from 1.5 m to 0.5 m, whereas the upper OP threshold for overwash (top right panel) drops from 2.3 m to 1.0 m. In cases of wide barriers ($W_{crest} > 15$ m) the difference in OP threshold levels can exceed 2 m for fine gravel barriers and 3 m for coarse gravel barriers.

6.5 Conclusions

The numerical model analysis carried out in this chapter was designed to develop further understanding of gravel barrier overwash thresholds for use in future empirical models. Although the range of the parameter space analysed in this investigation is not all-encompassing, in particular with respect to storm duration, wave spectrum type and coastal geometry, the analysis is based only on one indicator for overwash, namely crest level change, and the analysis is based on results of the XBeach-G model, rather than field observations, the results of this analysis point towards several interesting observations that merit further investigation in the future:

1. (a) The XBeach-G simulations carried out in Part I of this analysis on gravel beaches with beach slope ranging from 0.1–0.2 and beach toe located at SWL - 10 m, show markedly different predictions of wave run-up than empirical formulations based on the Iribarren parameter (e.g., Stockdon et al., 2006; Polidoro et al., 2013) and wave steepness (Powell, 1990). In general, wave run-up predictions of the XBeach-G model exceed those of the empirical models, in particular for high-energy ($H_{m0,0} > 3$ m) offshore wave conditions.

   (b) Relative wave run-up predictions of the XBeach-G model simulations show greater correspondence ($\rho = 0.97$) with an empirical relation based on a non-linear relation with the offshore wave height (Equation 6.1), or based on the wave period (Equation 6.2), than with the Iribarren parameter ($\rho = 0.80$) and the mean wave steepness ($\rho = -0.79$).

   (c) Comparison between wave run-up derived from 743 17-minute camera pixel stack time series collected at Chesil Beach, Loe Bar and Slapton Sands and a wave run-up parametrisation based on the Iribarren parameter (STO; Equation 2.1b) and a parametrisation based on the XBeach-G simulation results of Part I (Equation 6.1) shows that measured wave run-up is predicted with greater accuracy (less bias and scatter) by the parametrisation derived in Part I of this analysis than by the STO model. Calibration of the STO model to ensure zero bias with the measured wave run-up data does not reduce the model prediction scatter to lower values than those of the parametrisation derived in Part I of this analysis and under estimates observed wave run-up during high energy wave con-

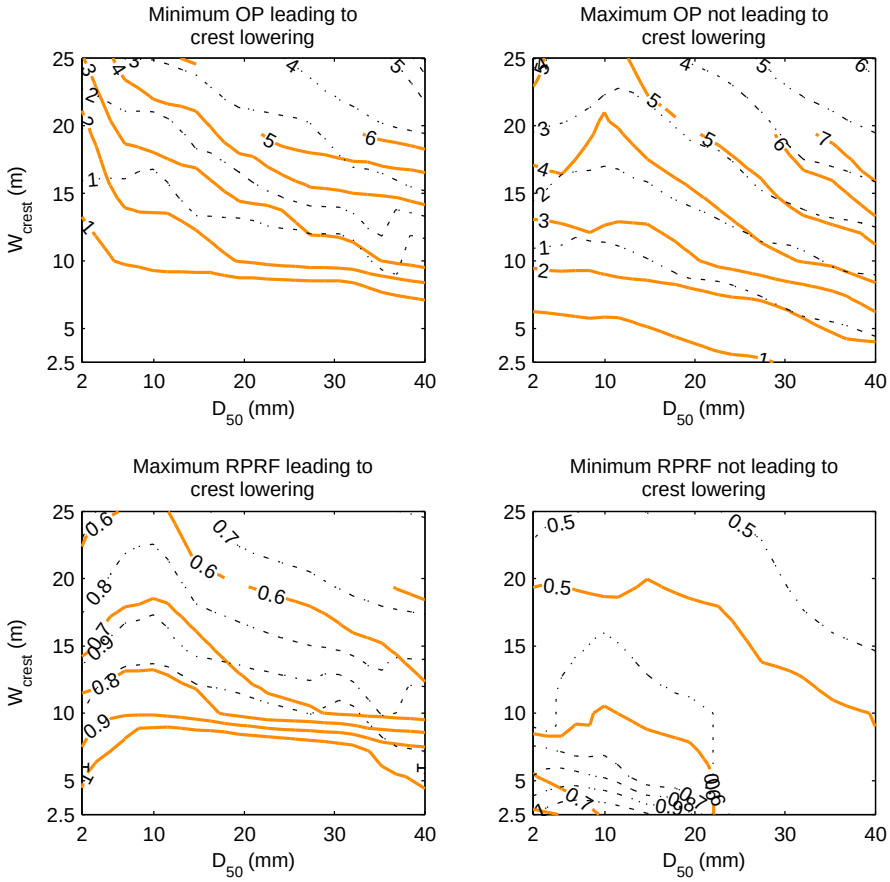

Figure 6.15: Minimum OP resulting in crest lowering (top left panel), maximum OP not resulting in crest lowering (top right panel), maximum RPRF resulting in crest lowering (bottom left panel) and minimum RPRF not resulting in crest lowering (bottom right panel) in XBeach-G model simulations (—) and the NGW model simulations (– –), as a function of the barrier crest width and median grain size.

ditions (Figure 6.8). These facts, combined with the reliability of the XBeach-G model in simulating observed wave run-up on gravel beaches during storms (Chapter 3), suggest that alternative empirical equations, such as that presented in Equation 6.1, may be necessary to describe wave run-up on gravel beaches during storms.

2. XBeach-G simulations carried out in Part II of this analysis show that while the difference between the potential wave run-up and barrier crest height, either defined as Overwash Potential (OP), or relative potential run-up freeboard (RPRF), is essential to help predict barrier overwash, it is not *sufficient* to predict barrier overwash. Model results show that barrier width, barrier grain size and the incident wave energy flux all affect gravel barrier crest response and lead to different thresholds for overwash for constant values of OP and RPRF. This is especially well demonstrated by narrow and coarse gravel barriers, where variations in the incident wave energy flux can distinguish between crest build-up and crest lowering for constant OP values (Figure 6.11). Future overwash threshold prediction models (e.g., Figure 6.13) should account for variations in these parameters.

3. Sensitivity simulations using the XBeach-G and NGW models show that the role of groundwater processes on gravel barriers during overwash is substantial with respect to the morphology of the barrier crest. The model results suggest that these processes are essential mechanisms for the resilience of gravel barriers to overwash events. In the case of coarse gravel barriers, groundwater processes lead to 40–50% less crest lowering under conditions of maximum change than would be the case if groundwater processes did not occur. Groundwater processes on gravel barriers have an equivalent effect on barrier overwash processes as a reduction of the OP by 1–3 m (Figure 6.15), which effectively increases the capacity of gravel barriers to withstand storms with 1–3 m higher surge levels than if groundwater processes did not occur. Reducing the width of a barrier leads to a lowering of this capacity, thereby reducing the resilience of the barrier to extreme storm events.

It should again be noted that the results and conclusions of this chapter are based on schematic barrier geometries with a constant foreshore, uni-modal wave forcing and limited storm duration. Variations in natural barrier geometries and forcing beyond the range investigated in this study mean that some conclusions of this analysis may, in cases, not be applicable. In particular, variation of the foreshore slope and depth, for instance in the case of composite sand-gravel beaches, and variation in storm duration can significantly alter the threshold of barrier resilience in respect to offshore wave conditions. Further validation of the model results is envisaged through comparison with field and laboratory data.

Chapter 7

Discussion

This chapter discusses the potential use of XBeach-G in research and engineering projects and the value of the model over existing empirical models for gravel beaches. While no new data are presented, it is argued that the use of XBeach-G over empirical models is appropriate in the case of high-impact storm events. The chapter furthermore addresses three main limitations of the model with respect to the absence of longshore processes, morpho-sedimentary dynamics, and processes at the beach step, as well as presenting model development strategies to overcome these limitations.

This thesis has primarily focussed on the development and validation of XBeach-G as a process-based storm-impact model for gravel beaches (Chapters 3–5) and with the exception of Chapter 6, has not addressed the use of the model as a means of testing hypotheses in research projects, or as a practical design and analysis tool in engineering projects. In this chapter, the value of XBeach-G is discussed as an engineering tool with respect to commonly-used storm impact models in the UK (e.g., BIM, Bradbury, 2000; and SHINGLE, Powell, 1990), as well as its application to investigate physical relations on gravel beaches. The chapter subsequently addresses the principal limitations of the model and their constraints on its application. The chapter concludes with the potential for future research and model development to mitigate or overcome the current model limitations.

7.1 Application of XBeach-G in research and engineering projects

The results of Chapters 3, 4 and 5 show that XBeach-G is capable of qualitatively and quantitatively reproducing observed hydrodynamics and cross-shore profile change on gravel beaches under varying hydrodynamic forcing conditions and with varying morphodynamic responses. However, as should be the norm for all newly-developed models, further testing of XBeach-G is recommended on other gravel beaches to ensure its physical validity, and testing by other modellers is recommended to ensure its universal applicability. The development of a freeware graphical user interface for XBeach-G[1] (Masselink et al., 2014) forms a first step in this direction by allowing for relatively fast uptake of the model by engineers and scientists and promoting discussion of the capabilities of the model.

To a certain extent, the value of XBeach-G as an engineering tool over existing models has been shown by McCall et al. (2013 ; cf. Section 6.1). In this study, XBeach-G was shown to significantly outperform the empirical Barrier Inertia Model (BIM; Bradbury, 2000) in predicting historic flooding events, despite the lack of accurate

[1] Free to download from the XBeach website: www.xbeach.org.

boundary and initial conditions with which to run the model. More importantly, the results of the analysis showed that application of the BIM generally resulted in an under prediction of the potential for flooding on many gravel beaches, which is highly undesirable from the point of view of flood-safety, and that XBeach-G could be used to identify the dominant parameters causing underestimation by the BIM. While further research on this topic is invaluable, the results of McCall et al. (2013) appear to be a strong argument for choosing XBeach-G over the BIM to study potential coastal flooding and overwash.

The value of XBeach-G as an engineering tool compared to the SHINGLE model (Powell, 1990) is less well defined as there has been no direct comparison between the two models. It is well-known that in some conditions, the SHINGLE model is inaccurate and an inappropriate model choice for overwash conditions (Bradbury and Powell, 1992; Van Rijn and Sutherland, 2011), and for such conditions XBeach-G will likely provide more accurate predictions (cf. Chapter 5). However, in cases where the SHINGLE model is known to work well (e.g., periods with little swell on medium gravel beaches, leading to berm-building and beach erosion), the empirical SHINGLE model may outperform XBeach-G in predicting the morphodynamic response of the beach (cf. Section 7.2.3). Until a comprehensive comparison between the models has been carried out, it is recommended to apply both models in parallel to ensure a conservative approach.

Chapter 6 showed the potential use of XBeach-G as a numerical laboratory for investigating physical dependencies. It goes without saying that in this aspect XBeach-G cannot replace physical models and field data collection, since the model is bound by predefined physical assumptions and is only able to provide answers that are described by those relations. However, the model can be used in other manners to advance our scientific understanding of gravel beaches. Firstly, the model can be used to generate synthetic data (cf. Chapter 6 and Masselink et al., 2014) for areas of parameter spaces where observational data are lacking and difficult to obtain, and calculation of the desired data from physical principles is too complex. By definition, the model is sparsely validated for such conditions, and hence the reliability of the model results must be inferred from our projected understanding of the physical system. However, if correctly applied, the generation of such data can lead to constructive new insights into the behaviour of gravel beach processes (cf. wave run-up in Section 6.3.1). Secondly, the model can be used to give weight to hypotheses regarding the relation between physical processes and their importance on larger-scale behaviour. In this thesis, the influence of groundwater processes on the hydrodynamics and morphodynamics of gravel beaches was examined in this manner by switching on and off groundwater flow (Sections 4.7, 5.7 and 6.4). Again, the reliability of the model cannot be considered in isolation as the model sensitivity to process-interactions may not be the same as those in reality. Thirdly, and no less importantly, the model and its inaccuracies can be used to highlight gaps in our knowledge of gravel beach processes and thereby help to steer coordinated research and measurement campaigns.

7.2 Model limitations

Although the results of Chapters 3–5 appear to show that the model represents the physics of gravel beaches relatively well, XBeach-G is inherently a simplification of reality. This section discusses the most important simplifications applied by the model and the limitations they impose on the use and reliability of the model.

7.2.1 The longshore dimension: sediment transport gradients, wave angle and longshore flows

Chapter 5 discusses the development and validation of a morphodynamic module for XBeach-G. The development of this module focussed on the simulation of cross-shore sediment transport rates and gradients, and validation of the model was carried out using data collected on beaches with near-normally incident waves (BARDEX, Loe Bar, Chesil Beach) and on beach profiles where the net longshore transport gradient was close to zero (Slapton Sands). Since XBeach-G has been developed to simulate storm-impacts, where cross-shore sediment transport rate gradients typically dominate the short-term morphodynamic response of the cross-shore profile (cf. Dean, 1977; Vellinga, 1986), the omission of longshore sediment transport gradients is a reasonable approximation for the initial development of the model as an engineering tool. However, on curved coastlines, coasts with large longshore gradients in wave forcing, or coasts with interrupted longshore sediment transport pathways, the longshore sediment transport gradient may be sufficiently large to significantly affect the overall morphodynamic response of the beach (cf. de Alegria-Arzaburu and Masselink, 2010; Den Heijer, 2013). In such situations the current assumption of alongshore uniformity in sediment transport rates, which is inherent to all 1D and 2DV cross-shore profile models, may lead to substantial errors in the predicted cross-shore profile response.

Due to the manner in which the equations of motion for flow (Equations 3.1 and 3.2) are solved in only one dimension, XBeach-G does not currently account for variations in forcing terms in the longshore direction. In a very practical sense, this means that in its present form, the model does not account for refraction of obliquely-incident waves, since the wave crests are assumed to be longshore-uniform. The result is that the model will overestimate the incident wave energy during conditions with large angles of wave incidence, and will not compute wave-driven longshore currents. Furthermore, since XBeach-G only computes the cross-shore components of the flow and sediment transport, the contribution of a longshore uniform, but non-zero, longshore component of the flow to the bed shear stress and sediment mobility is ignored. While this is in line with the 1D and 2DV cross-shore profile models discussed in Section 2.3, field measurements (Austin et al., 2011) and numerical model studies (Den Heijer, 2013) on sandy beaches have confirmed that under certain conditions the longshore component of the flow can enhance cross-shore sediment transport rates and hence affect the predicted cross-shore profile response.

The result of the simplifications listed above mean that the model cannot readily be applied in situations with significant longshore gradients in sediment transport, nor in situations with large angles of wave incidence. A general guideline based loosely on the simulations run in this thesis is that conditions with waves incident at angles

up to 30º may still to be resolved reasonably well by the model, but that larger angles should be avoided.

7.2.2 MSG beaches and morpho-sedimentary dynamics

As stated in the research approach in Chapter 1, the development of XBeach-G has focussed on pure gravel beaches (cf. Jennings and Shulmeister, 2002), rather than MSG and composite beaches. Therefore, even though the model may be able to represent hydrodynamic indicators of storm impact (e.g., wave run-up, overtopping) on MSG and composite beaches (cf. Seascale in Chapter 3), it is unlikely that the model will correctly predict the morphodynamic response of such beaches and their complex sedimentological interactions. In particular, the model discussed in this thesis contains no physics related to suspended sediment transport, which is commonly regarded as essential to model the dynamics of sand fractions, particularly under storm conditions (Vellinga, 1986; Van Thiel de Vries, 2009). Furthermore, the model currently accounts for only one sediment type, with one representative grain size distribution, porosity and hydraulic conductivity, and has no physics relating to how different-sized or shaped grains may interact to affect sediment mobility (e.g., hiding, exposure and armouring, or implementation of more general concepts such as grain acceptance and rejection) and beach permeability (e.g., modifying hydraulic conductivity and porosity). At this stage therefore, the basic drivers necessary for the concept of morpho-sedimentary dynamics, instead of pure morphodynamics, are missing from the model.

7.2.3 Berm formation and step development

The results of BAB3 and CB1 in Chapter 5 show that although XBeach-G is capable of reproducing berm formation in general, the model tends to under predict the volume of the berm. In the case of BAB3, where measured data are available of the submerged profile before and after the wave series, the lack of volume in the post-storm berm is mirrored by an overestimation of the deposition at, and below, the beach step. This observation appears to indicate that the step and berm are morphodynamically related and that accurate modelling of step dynamics may be required to accurately model berm-building. This hypothesis is in line with previous research (refer to Buscombe and Masselink, 2006 and Chapter 2 for an overview) that has highlighted the importance of the step in maintaining steep, reflective beach slopes through preferential onshore sediment transport mechanisms. Interestingly, the underestimation of the berm development is mirrored to greater or lesser degree by other process-based models (e.g., Van Gent, 1995a; Pedrozo-Acuña et al., 2007; Van Rijn and Sutherland, 2011; Jamal et al., 2014), which may point to a common discrepancy between modelled and naturally-occurring processes at the step.

At present, it appears that XBeach-G is unable to accurately simulate the development of the gravel step, including the onshore movement of the step during LB2 (cf. Section 3.5, Poate et al., 2013 and Almeida et al., 2015, but not discussed in Chapter 5). A likely source for this error is the limitation of XBeach-G with respect to the representation of the highly complex hydrodynamics under breaking waves (e.g., wave overturning, turbulence generation, air entrainment, strong vertical velocity gradients) in a depth-averaged model, as noted in Section 3.2.2. As a result, the

fine balance between onshore and offshore sediment transport in the swash may be incorrectly represented by the model. While this appears to have little influence on the predicted morphodynamic response of gravel barriers under relatively energetic wave conditions (e.g., crest build-up – barrier rollover) when transport in the swash may be more dominantly controlled by offshore wave forcing and the SWL, the accuracy of the modelled morphodynamic response under less energetic wave conditions will likely be improved through better representation of gravel step dynamics. However, until a more accurate representation of step dynamics in the model is achieved, caution is advised in the application of the model to study beach morphodynamics that are more strongly controlled by step dynamics. Similarly, the use of the model to study post-storm beach recovery, as well as to investigate thresholds between berm-building and beach erosion and the morphodynamic effect of swash-swash interactions, is discouraged until further investigation of modelled step dynamics has been carried out.

7.3 Directions for future model development

The current model limitations discussed in the previous section show that further development of XBeach-G will increase the potential application of the model in many engineering applications, as well as help the scientific community to study the complex physical processes at the heart of the morphodynamic response of gravel beaches and barriers. This section addresses model development strategies to tackle the three main limitations of the model discussed in the previous section.

7.3.1 The longshore dimension

The most accurate and complete method of including the effect of wave obliquity, longshore flow and sediment transport in XBeach-G is through modification of the model equations from the 1D-form to their 2DH equivalent, thereby converting the model from a cross-shore profile model to an area model. There is high potential for such development since 2DH equations for flow in the surface water (Smit et al., 2010) and groundwater (Appendix A) have already been implemented in the model. The remaining development required for a full 2DH version of XBeach-G is therefore the development and implementation of 2DH equations for sediment transport (cf. Section 5.3). Such development will allow the model to resolve the effect of interactions between mean longshore and intra-wave cross-shore flows on the sediment transport magnitude and direction (cf. Soulsby and Damgaard, 2005). It should be noted however that the 2DH development of the sediment transport module is not trivial and that due consideration should be taken of cross-shore – longshore interactions in the computation of the bed shear stress, bed slope effects, sediment mobility and sediment transport direction (cf. De Vet, 2014).

While a fully-2DH version of XBeach-G would improve the representation of the naturally-occurring physical processes in the model, this would also increase the computational costs of running simulations. Therefore, a second model development approach could be initiated to include the dominant longshore gradients in a "quasi-2DH" model, where cross-shore processes are explicitly resolved as in the current 1D-version of XBeach-G, and longshore processes are included in a para-

metric form. An example of this modelling approach would be to use an empirical (e.g., Kamphuis, 1991; Damgaard and Soulsby, 1996; Van Wellen et al., 2000b), or process-based (e.g., Van Wellen et al., 2000a), longshore sediment transport relation alongside user-defined longshore gradients in coastline angle and wave direction to derive longshore sediment transport rate gradients. These transport gradients could be used to update bed-level changes in the XBeach-G model, allowing for net erosion or accretion in the cross-shore profile. It goes without saying that further model validation would be required to support the use of such quasi-2DH methods, as well as of a fully-2DH approach.

7.3.2 MSG beaches and morpho-sedimentary dynamics

While there is still much uncertainty relating to the physical processes of MSG beaches (cf. Mason and Coates, 2001), there are several relatively simple developments that can be carried out in the XBeach-G in order to increase the applicability of the model on such beaches. In first instance, the model can be developed to use the multiple sediment fraction approach of the standard XBeach model (Roelvink et al., 2009; Deltares, 2015) to track the location and concentrations of sand and gravel fractions[2]. Without considering complex grain interactions, the XBeach-G sediment transport module could be extended with the suspended transport equations of Van Rijn (2007b), or the Van Thiel de Vries–Van Rijn transport relations (Deltares, 2015), alongside the suspended sediment advection scheme of Galapatti and Vreugdenhil (1985) used in the standard XBeach model, to simulated suspended transport of the sand fraction. In further stages of model development, empirical relations for armouring and grain sheltering and exposure (e.g., Parker et al., 1982; Garcia and Parker, 1991) can be included to better approximate sediment pick-up functions on MSG beaches, whereas the spatially and temporally-varying hydraulic conductivity of MSG beaches could be computed by an integrated empirical model that allows for variations in the grain size distribution (e.g., Carrier, 2003). Most importantly however, the addition of new sediment transport modules to account for morpho-sedimentary dynamics on gravel and MSG beaches requires extensive validation datasets collected in the field (e.g., Roberts et al., 2013) and in the laboratory (e.g., López de San Román-Blanco et al., 2006) to prevent the model becoming overdetermined by the increase in model parameters.

7.3.3 Step dynamics

Since the hydrodynamics thought to develop and maintain gravel steps is essentially two-dimensional (2DV; e.g., step vortex generation, plunging breakers), representation of these processes in a depth-averaged model presents some difficulties. Important factors not accounted for in the XBeach-G model that all enhance onshore sediment transport across the step region are: (1) bore turbulence; (2) net onshore flow across the seaward face of the step due to the vortex (Larson and Sunamura, 1993); (3) vertical velocity under breaking waves; and potentially (4) breaker pressure pulses

[2]Note that proof of concept simulations were carried out successfully with this multiple sediment fraction approach for a pure gravel outside the context of this thesis. While no data were available for comparison, the model produced qualitatively correct behaviour in sorting the gravel fractions by their size.

(Pedrozo-Acuña et al., 2008). In order to better represent gravel step dynamics in the model, these processes can be approximated through parametrisation of breaker-induced turbulence (cf. Reniers et al., 2013), suspending sediment at wave breaking using the local vertical velocity, and a parametrisation of plunging breaker pressure pulses on the mobilisation of sediment (cf. Pedrozo-Acuña et al., 2010). Adaptation of the model to explicitly compute, rather than parametrise, plunging wave breaking and hydrodynamics at the step, however, would require extensive modification of the surface water flow module from a 2DH-type model to a 3D Volume of Fluid–type (VOF) model. While such modelling approaches have been shown to be technically feasible and accurate (e.g., Lara et al., 2010), this modification would incur a significant increase in the associated computational expense (Van den Bos et al., 2014) and would effectively represent an entirely different model to the one discussed in this thesis. It is therefore not foreseen that these processes will be explicitly resolved in future versions of XBeach-G.

Chapter 8

Conclusions

The research discussed in this thesis concerns the development of a process-based morphodynamic model for storm impacts on gravel beaches and barriers, called XBeach-G. The model represents an improvement over existing process-based models for gravel coasts in that it has been extensively validated for surface water dynamics (Chapter 3), groundwater dynamics (Chapter 4) and morphodynamics (Chapter 5), using data collected in physical model experiments, as well as data collected in the field during storms. XBeach-G is shown to have high model skill in simulating storm impacts on gravel beaches, and to the author's knowledge, is the only model to date to have been shown to correctly simulate varying stages of morphodynamic storm-response, ranging from berm-building to barrier rollover (cf. Figure 2.2).

The model was used to investigate swash hydrodynamics on gravel beaches during storms. In Chapter 3 it was shown that the incident-band motions need to be explicitly resolved in the model to correctly predict wave run-up levels, and that a simple parametrisation of the incident-band variance in a phase-averaged approach leads to substantial underestimation of the wave run-up. This observation corresponds well with current hypotheses that the swash zone on gravel beaches may be unsaturated during storm conditions, leading to substantial variance of the wave run-up elevation at the incident-band frequency (Chapter 2). Further analysis of wave run-up levels in Chapter 6 has highlighted a disparity between the prediction of current models of wave run-up on gravel beaches based on the Iribarren parameter or wave steepness, and those simulated by XBeach-G and observed in the field, particularly during storms. Both findings are highly relevant to the development and potential application of phase-averaged morphodynamic models on gravel beaches (e.g., Hicks et al., 2010; Van Rijn and Sutherland, 2011; Williams et al., 2012b; Jamal et al., 2014).

Model sensitivity analysis has underlined the importance of groundwater processes on the hydrodynamics of barrier overtopping (Section 4.7) and the morphodynamic response of gravel coasts (Section 5.7). Although model sensitivity relations may not be exactly the same as those in reality (cf. Section 7.1), research in this thesis appears to support the hypothesis that infiltration in the swash is a key driver for the berm-building response of gravel beaches and helps to reduce erosion of the upper beach during storms (e.g., Bagnold, 1940; Grant, 1948; Carter and Orford, 1993). Further sensitivity simulations in Chapter 6 show that groundwater processes can lead to a reduction in crest-lowering of 40–50% during overwash events and effectively increases the capacity of gravel barriers to withstand storms with 1–3 m higher surge levels than if groundwater processes did not occur. The model shows that on most gravel beaches the morphodynamic impact of groundwater processes is primarily due to first-order

effects of infiltration (i.e., loss of backwash volume), rather than second-order effects (i.e., modified boundary layer and effective particle weight), which is contradictory to that found by Masselink and Turner (2012), indicating a need for further research in this field (cf. Sparrow et al., 2012, 2013). Despite its strong influence on gravel beach morphodynamics, research in Chapter 4 found that infiltration plays a relatively small role on wave run-up levels on most natural gravel beaches (median $R_{2\%}$ run-up level reduction of 8%; Section 4.7), suggesting that other parameters, such as beach slope and nearshore water depth are more important in controlling wave run-up and the potential for wave overtopping.

Due to the lack of sediment transport measurements on gravel beaches during storms, the sediment transport module in XBeach-G was indirectly validated by comparison of predicted and observed morphological change. The results of the morphodynamic validation presented in Chapter 5 show that in general, the observed morphological change during storms is well represented by the model using gradients in simulated bed load transport to update bed levels. Simulated morphological change is found to mimic reality more accurately if the local acceleration, as a potential proxy for near-bed pressure gradients and bore-induced turbulence, is used in addition to the drag force on the bed to mobilise and transport sediment (cf. Van Gent, 1995a; Nielsen, 2002; Puleo et al., 2003; Pedrozo-Acuña et al., 2007), than if it is neglected. Furthermore, results of the model show that the importance of including the local acceleration component in the computation of the bed shear stress increases with the size of the sediment, where the effect of the acceleration term is significant for medium gravel and coarser beaches (Appendix F).

Application of the model to simulate historical flooding events (McCall et al., 2013) has emphasised the value of using the process-based XBeach-G model in coastal flooding analysis over the use of empirical tools. Much of the coastal reach of the UK and of other countries around the world is not well described by the parameter-space used to derive the only existing empirical overwash model for gravel barriers (e.g., BIM; Bradbury, 2000). In these areas, application of the empirical model can lead to substantial mis-estimation of the potential for coastal flooding. While no model can be considered entirely accurate, application of XBeach-G in all hindcast overwash simulations reported so far, has lead to reasonable estimates of overtopping discharge (Chapter 3 and McCall et al., 2013) and of morphological change (Chapter 5). Moreover, the results of simulations with XBeach-G are useful in themselves to help derive improved parametric formulations for the analysis of flood safety, for instance in relation to wave run-up (Section 6.3.1) and barrier overwash thresholds (Section 6.3.2).

To enable further development and validation of the model, as well as to facilitate the use of the model in practical applications, the XBeach-G model, the open-source XBeach-G code (Fortran95) and a graphical user interface for the XBeach-G model have been made available for free and for public download on the XBeach project website[1].

[1] www.xbeach.org

Appendix A

Groundwater model numerical implementation

A.1 Numerical grid

In order to solve the equations in Section 4.3, the spatial and temporal domain of the groundwater system is split into the same spatial grid and time steps as the XBeach-G surface water model it is coupled to. At each time step in the numerical model, the depth average groundwater head is calculated in the centre of the groundwater cells, and the fluxes (specific discharge, submarine exchange, infiltration and exfiltration) are calculated on the cell interfaces (Figure A.1).

A.2 Infiltration and exfiltration

At the start of the time step, every cell is evaluated whether the groundwater and surface water are connected:

$$\kappa_{i,j} = \zeta_{gw,i,j} \geq \xi_{i,j} - \varepsilon \wedge h_{i,j} \geq \varepsilon \tag{A.1}$$

where $\varepsilon = O\left(10^{-3}\right)$ is a numerical smoothing constant used to deal with numerical round off errors near the bed, and i and j represent cross-shore and longshore coordinates in the numerical solution grid, respectively.

Infiltration is calculated in cells where the groundwater and surface water are not connected and there exists surface water. As shown in Equation 4.18, the infiltration

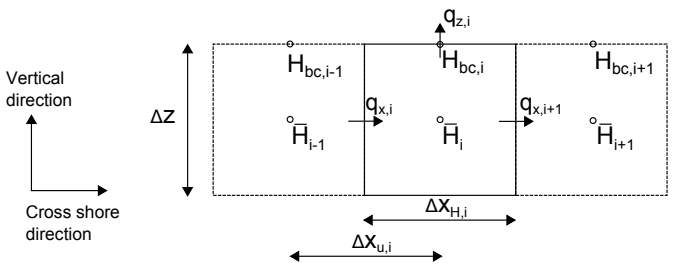

Figure A.1: Example of the numerical grid representation of the groundwater model.

rate is a function of the thickness of the wetting front δ_{wf} , which is zero at the start of infiltration, and increases as a function of the infiltration rate. The equations for the infiltration rate and the thickness of the wetting front are approximated by first-order schemes, in which the wetting front is updated using a backward-Euler scheme, which ensures numerical stability:

$$\begin{aligned} S^n_{i,i,j} &= K_{i,j}\left(\frac{1}{\rho g}\frac{p_{i,j}\big|^{z=\xi}}{\delta^n_{wf,i,j}}+1\right) \\ \delta^n_{wf,i,j} &= \delta^{n-1}_{wf,i,j}+S^n_{i,i,j}\frac{\Delta t}{n_p} \end{aligned} \tag{A.2}$$

where the superscript n corresponds to the time step number and Δt is the size of the time step. The infiltration rate in the coupled relationship in Equation A.2 can be solved through substitution:

$$S^n_{i,i,j} = \frac{-\delta^{n-1}_{wf,i,j}+\frac{\Delta t}{n_p K_{i,j}}+\sqrt{\left(\delta^{n-1}_{wf,i,j}\right)^2+\frac{2}{n_p}\frac{\Delta t}{\delta^{n-1}_{wf,i,j}K_{i,j}}+\frac{4\rho g}{n_p}\frac{\Delta t}{p_{i,j}\big|^{z=\xi}K_{i,j}}+\frac{\Delta t^2}{K^2_{i,j}}}}{\frac{2\Delta t}{n_p}} \tag{A.3}$$

At the end of infiltration, i.e. when the groundwater and surface water become connected or there is no surface water left, the wetting front thickness δ_{wf} is reset to zero.

If the infiltration rate exceeds the Reynolds number for the start of turbulence, the local hydraulic conductivity is updated using the local Reynolds number:

$$K_{i,j} = K_{lam}\sqrt{\frac{Re_{crit}}{\max\left(Re_{i,j},Re_{crit}\right)}} \tag{A.4}$$

Equations A.3 and A.4 are iterated until a minimum threshold difference between iterations is found. Infiltration in one time step is limited to the amount of surface water available in the cell and to the amount of water required to raise the groundwater level to the level of the bed:

$$S^n_{i,i,j} = min\left(S^n_{i,i,j},\frac{\zeta_{i,j}-\xi_{i,j}}{\Delta t},\frac{\xi_{i,j}-\zeta_{gw,i,j}}{n_p\Delta t}\right) \tag{A.5}$$

If during infiltration the groundwater level reaches the bed level, the fraction of the time step required to do so is estimated ($\Lambda_{t_{i,j}}$) and the remaining fraction is used in the submarine exchange (Equation A.15):

$$\Lambda_{t_{i,j}} = \frac{n_p\left(\xi_{i,j} - \zeta_{gw,i,j}\right)}{K_{i,j}\left(\frac{1}{\rho g}\frac{p_{i,j}\big|^{z=\xi}}{\xi_{i,j}-\zeta_{gw,i,j}} + 1\right)}\frac{1}{\Delta t} \quad 0 \leq \Lambda_{t_{i,j}} \leq 1 \tag{A.6}$$

Exfiltration is calculated in cells where the groundwater and surface water are not connected and the groundwater level exceeds the bed level:

$$S_{e,i,j} = n_p\frac{\xi_{i,j} - \zeta_{gw,i,j}}{\Delta t} \tag{A.7}$$

After infiltration and exfiltration have been calculated, the groundwater level and surface water level are updated:

$$\begin{aligned}\zeta_{gw,i,j}^{n+\frac{1}{2}} &= \zeta_{gw,i,j}^{n} + \tfrac{\Delta t}{n_p}\left(S_i + S_e\right)\\ \zeta_{i,j}^{n+\frac{1}{2}} &= \zeta_{i,j}^{n} - \Delta t\left(S_i + S_e\right)\end{aligned} \tag{A.8}$$

All updated cells are subsequently re-evaluated on whether the surface water and groundwater are connected or unconnected.

A.3 Horizontal flow and submarine exchange

The horizontal specific discharge on each cell interface can be found using the approximation of the groundwater head gradient, where in this example a parabolic approximation of the vertical head variation is used (cf., Section 4.3.3):

$$\begin{aligned}q_{gw,i,j}^{x} &= -K_{u,i,j}\Delta z_{u,i}\frac{H_{i+1,j}-H_{i,j}}{\Delta x_{u,i,j}} = -K_{u,i,j}\Delta z_{u,i,j}\frac{H_{bc,i+1,j}-\frac{2}{3}\beta_{i+1,j}\Delta z_{H,i+1,j}^2 - H_{bc,i,j}+\frac{2}{3}\beta_{i,j}\Delta z_{H,i,j}^2}{\Delta x_{u,i,j}}\\ q_{gw,i,j}^{y} &= -K_{v,i,j}\Delta z_{v,i,j}\frac{H_{i,j+1}-H_{i,j}}{\Delta y_{v,i,j}} = -K_{v,i,j}\Delta z_{v,i,j}\frac{H_{bc,i,j+1}-\frac{2}{3}\beta_{i,j+1}\Delta z_{H,i,,j+1}^2 - H_{bc,i,,j}+\frac{2}{3}\beta_{i,j}\Delta z_{Hi,,j}^2}{\Delta y_{v,i,j}}\end{aligned} \tag{A.9}$$

where the superscripts x and y refer to the components of the variable in the cross-shore and longshore direction, respectively, the subscripts u and v refer to variables approximated at the horizontal cell interfaces in the cross-shore and longshore direction, respectively, and the subscript H refers to variables approximated at the cell centres (Figure A.1). The hydraulic conductivity may be different at each cell interface and is therefore computed at every interface ($K_{u,i,j}$; $K_{v,i,j}$), where every K is calculated separately using Equation A.4. The cell height at the centre of the groundwater cells $\Delta z_{H,i,j}$ is calculated from the groundwater level and the bottom of the aquifer ξ_{gw} in the centre of the cell, whereas the cell heights at the horizontal cell interfaces are calculated using an upwind procedure:

$$\Delta z_{H,i,j} = \zeta_{gw,i,j} - \xi_{gw,i,j} = h_{gw,i,j} \tag{A.10}$$

$$\Delta z_{u,i,j} = \begin{cases} \Delta z_{H,i+1,j} & q^x_{gw,i,j} < 0 \\ \Delta z_{H,i,j} & q^x_{gw,i,j} \geq 0 \end{cases}$$
$$\Delta z_{v,i,j} = \begin{cases} \Delta z_{H,i,j+1} & q^y_{gw,i,j} < 0 \\ \Delta z_{H,i,j} & q^y_{gw,i,j} \geq 0 \end{cases} \tag{A.11}$$

As described in Section 4.3.6, the head applied on the top boundary of the groundwater domain H_{bc} depends on whether the groundwater and surface water are connected or unconnected:

$$H_{bc,i,j} = \begin{cases} \xi_{i,j} + \frac{p_{i,j}\big|^{z=\xi}}{\rho g} & \kappa_{i,j} \\ \zeta_{gw,i,j} & \neg\kappa_{i,j} \end{cases} \tag{A.12}$$

The vertical submarine exchange at the top of the numerical groundwater cell, is found using Equation 4.17:

$$q^z_{gw,i,j} = -2\beta_{i,j} K_{w,i,j} \Delta z_{H,i,j} \Delta x_{H,i,j} \left(1 - \Lambda_{t_{i,j}}\right) \tag{A.13}$$

where the superscript z refers to the vertical component of the variable, the subscript w refers to a numerical approximation at the vertical cell interfaces, and $\Lambda_{t_{i,j}}$ is zero, unless infiltration has caused the groundwater surface to connect to the surface water (Equation A.6).

Continuity in the groundwater cell is found following Equation 4.1:

$$q^x_{gw,i-1,j} - q^x_{gw,i,j} + q^y_{gw,i,j-1} - q^y_{gw,i,j} - q^z_{gw,i,j} = 0 \tag{A.14}$$

All variables in Equation A.14 contain an unknown value for the groundwater pressure head, described in terms of a known head at the surface of the groundwater H_{bc} and the unknown curvature of the vertical groundwater head function β. Since water is incompressible, the groundwater pressure driving Equation A.14 must be solved for all cells simultaneously using matrix algebra:

$$Ax + b = 0 \tag{A.15}$$

where A is a matrix containing coefficients for the horizontal and vertical specific discharge, x is a vector containing the unknown groundwater head curvature, and b contains the known forcing terms.

For a one dimensional cross-shore case, A is reduced to a tridiagonal matrix:

$$A = \begin{bmatrix} \ddots & & & & & & \\ & a_{i-1} & a_i & a_{i+1} & 0 & & \\ & 0 & a_{j-1} & a_j & a_{j+1} & 0 & \\ & & 0 & a_{k-1} & a_k & a_{k+1} & \\ & & & & & & \ddots \end{bmatrix} \tag{A.16}$$

where

$$\begin{gathered} a_{i-1} = -K_{u,i}\frac{2\triangle z_{H,i-1}^2}{3\Delta x_{u,i}}\Delta z_{u,i} \\ a_i = K_{u,i}\frac{2\triangle z_{H,i}^2}{3\Delta x_{u,i}}\Delta z_{u,i} + K_{u,i+1}\frac{2\triangle z_{H,i}^2}{3\Delta x_{u,i+1}}\Delta z_{u,i+1} + 2K_{w,i}\Delta z_{H,i}\Delta x_{H,i}\left(1-\Lambda_{t_{i,j}}\right) \\ a_{i+1} = -K_{u,i+1}\frac{2\triangle z_{H,i+1}^2}{3\Delta x_{u,i+1}}\Delta z_{u,i+1} \\ etc. \end{gathered} \tag{A.17}$$

The vector of unknown groundwater head curvature is given by:

$$x = \begin{bmatrix} \cdots \\ \beta_{i-1} \\ \beta_i \\ \beta_{i+1} \\ \cdots \end{bmatrix} \tag{A.18}$$

The vector of known forcing consists of the numerical gradients in the contribution of the head applied on the top boundary of the groundwater domain to the horizontal specific discharge:

$$b = \begin{bmatrix} \cdots \\ K_{u,i-1}\Delta z_{u,i-1}\frac{-H_{bc,i-1}+H_{bc,i-2}}{\Delta x_{u,i-1}} + K_{u,i}\Delta z_{u,i}\frac{-H_{bc,i-1}+H_{bc,i}}{\Delta x_{u,i}} \\ K_{u,i}\Delta z_{u,i}\frac{-H_{bc,i}+H_{bc,i-1}}{\Delta x_{u,i}} + K_{u,i+1}\Delta z_{u,i+1}\frac{-H_{bc,i}+H_{bc,i+1}}{\Delta x_{u,i+1}} \\ K_{u,i+1}\Delta z_{u,i+1}\frac{-H_{bc,i+1}+H_{bc,i}}{\Delta x_{u,i+1}} + K_{u,i+2}\Delta z_{u,i+2}\frac{-H_{bc,i+1}+H_{bc,i+2}}{\Delta x_{u,i+2}} \\ \cdots \end{bmatrix} \tag{A.19}$$

In the one dimensional case, the solution to the tridiagonal matrix A in Equation A.15 can be computed using the efficient Thomas algorithm (Thomas, 1949). In the

two dimensional case, matrix A contains two additional diagonals that are not placed along the main diagonal, and vector b contains additional forcing terms from the alongshore contribution. The solution to the two dimensional case requires a more complex and less computationally efficient matrix solver. In this case the Strongly Implicit Procedure (Stone, 1968) is used in a manner similar to Zijlema et al. (2011b). The derivation of the solution matrix for two dimensional cases, as well as for one and two dimensional cases using a hyperbolic, rather than parabolic, approximation for the description of the vertical groundwater head decay (Section 4.3.3), are given in Appendix B.

The horizontal and vertical groundwater fluxes are calculated using the solution of x and Equations A.9 and A.13. Since some local velocities may exceed the critical Reynolds number for the start of turbulence Re_{crit}, the turbulent hydraulic conductivity K is updated using the local Reynolds number. The solution to Equation A.15 and the update of the turbulent hydraulic conductivity are iterated until a minimum threshold difference between iterations is found.

The iterated solution for the specific vertical discharge is used to update the groundwater level and surface water level:

$$\begin{aligned}
\zeta_{gw,i,j}^{n+1} &= \begin{cases} \zeta_{gw,i,j}^{n+\frac{1}{2}} & C_{i,j} \\ \zeta_{gw,i,j}^{n+\frac{1}{2}} + \frac{\Delta t}{n_p} \frac{q_{i,j}^{z}}{\Delta x_{H,i,j}} & \neg C_{i,j} \end{cases} \\
\zeta_{i,j}^{n+1} &= \begin{cases} \zeta_{i,j}^{n+\frac{1}{2}} + \Delta t \frac{q_{i,j}^{z}}{\Delta x_{H,i,j}} & C_{i,j} \\ \zeta_{i,j}^{n+\frac{1}{2}} & \neg C_{i,j} \end{cases}
\end{aligned} \tag{A.20}$$

If the groundwater and surface water are connected, and the submarine exchange from the surface water to the groundwater estimated in Equation A.15 is greater than the amount of surface water available in the cell, continuity is enforced by lowering the groundwater level to compensate for the lack of permeating water:

$$\zeta_{gw,i,j}^{n+1} = \zeta_{gw,i,j}^{n+1} + \frac{1}{n_p} \left(\zeta_{i,j}^{n+\frac{1}{2}} - \xi_{i,j} - \Delta t \frac{q_{i,j}^{z}}{\Delta x_{H,i,j}} \right) \qquad if \qquad \kappa_{i,j} \wedge \zeta_{i,j}^{n+\frac{1}{2}} - \xi_{i,j} < \Delta t \frac{q_{i,j}^{z}}{\Delta x_{H,i,j}} \tag{A.21}$$

Appendix B

Vertical groundwater head approximation: equations expanded

In Chapter 4, Section 4.3.3, an approximation method for the vertical groundwater head variation is introduced and discussed in 1D cross-shore form. In this appendix, the approximation is expanded for 2DH application, as well as for a hyperbolic, rather than parabolic approximation of the groundwater head.

B.1 Equations for the description of the vertical groundwater head

As stated in Section 4.3.3, the vertical groundwater head function is bound by three assumptions:

1. The vertical groundwater velocity at bottom of the aquifer is zero:

$$\left.\frac{\partial H}{\partial \sigma}\right|^{\sigma=0} = 0 \tag{B.1}$$

2. The groundwater head at top of groundwater is defined by boundary condition:

$$H_s = H_{bc} \tag{B.2}$$

3. The assumed shape of the vertical groundwater head profile. In Chapter 4 the profile is assumed parabolic, but in this appendix new equations are derived for an exponential-type profile (cf., Raubenheimer et al., 1998):

$$\begin{aligned} H(\sigma) &= \alpha_2\sigma^2 + \alpha_1\sigma + \alpha_0 \quad \text{parabolic} \\ H(\sigma) &= \alpha_1 cosh(\sigma) + \alpha_0 \quad \text{exponential} \end{aligned} \tag{B.3}$$

   where α_0, α_1 and α_2 are unknown shape coefficients.

From these three constraints it is possible to find two relations for the groundwater head function:

$$H(\sigma) = \begin{cases} \beta\sigma^2 + H_{bc} - \beta h_{gw}^2 & \text{parabolic} \\ \beta cosh(\sigma) + H_{bc} - \beta cosh(h_{gw}) & \text{exponential} \end{cases} \tag{B.4}$$

where in the parabolic-type equation $\beta = \alpha_2$, and in the exponential type equation $\beta = \alpha_1$.

Similarly, two expressions of the depth-average groundwater head can be derived through integration across the vertical:

$$\overline{H} = \frac{1}{h_{gw}} \int_0^{h_{gw}} H(\sigma)\, dz = \begin{cases} H_{bc} - \frac{2}{3}\beta h_{gw}^2 & \text{parabolic} \\ \frac{\beta}{h_{gw}} sinh(h_{gw}) + H_{bc} - \beta cosh(h_{gw}) & \text{exponential} \end{cases} \tag{B.5}$$

Finally, the vertical head gradient at the surface of the groundwater is computed from Equation B.4:

$$\frac{\partial H}{\partial \sigma} \Big|^{\sigma = h_{gw}} = \begin{cases} 2\beta h_{gw} & \text{parabolic} \\ \beta sinh(h_{gw}) & \text{exponential} \end{cases} \tag{B.6}$$

As discussed in Section 4.3, the groundwater model must solve the system of equations for conservation of mass and of motion:

$$\begin{aligned} \nabla \vec{U} &= 0 \\ \nabla H &= -\tfrac{1}{K} \vec{U} \end{aligned} \tag{B.7}$$

B.2 Numerical equations in 2DH

In one cell in a 2DH model the equation for the conservation of mass can rewritten as:

$$\begin{aligned} h_{u,gw}^{i-1,j} \Delta y_u^{i-1,j} u_{gw}^{i-1,j} - h_{u,gw}^{i,j} \Delta y_u^{i,j} u_{gw}^{i,j} \\ + h_{v,gw}^{i,j-1} \Delta x_v^{i,j-1} v_{gw}^{i,j-1} - h_{v,gw}^{i,j} \Delta x_v^{i,j} v_{gw}^{i,j} - \Delta x y_c^{i,j} w_{gw}^{i,j} = 0 \end{aligned} \tag{B.8}$$

where the variables u and v refer to the cross-shore and long-shore groundwater specific discharge velocity, respectively, Δxy is the area of the cell, the subscripts u and v refer to variables approximated at the horizontal cell interfaces in the cross-shore and longshore direction, respectively, and the subscript c refers to variables approximated at the cell centres.

If Equation B.8 is combined with the equation of motion following a parabolic approximation of the groundwater head, the system of equations becomes:

$$
\begin{aligned}
&-h_{u,gw}^{i-1,j}\Delta y_u^{i-1,j}K_{x,u}^{i-1,j}\frac{H_{bc}^{i,j}-\frac{2}{3}\beta^{i,j}\left(h_{gw}^{i,j}\right)^2-H_{bc}^{i-1,j}+\frac{2}{3}\beta^{i-1,j}\left(h_{gw}^{i-1,j}\right)^2}{\Delta s_u^{i-1,j}}\\
&+h_{u,gw}^{i,j}\Delta y_u^{i,j}K_{x,u}^{i,j}\frac{H_{bc}^{i+1,j}-\frac{2}{3}\beta^{i+1,j}\left(h_{gw}^{i+1,j}\right)^2-H_{bc}^{i,j}+\frac{2}{3}\beta^{i,j}\left(h_{gw}^{i,j}\right)^2}{\Delta s_u^{i,j}}\\
&-h_{v,gw}^{i,j-1}\Delta x_v^{i,j-1}K_{y,v}^{i,j-1}\frac{H_{bc}^{i,j}-\frac{2}{3}\beta^{i,j}\left(h_{gw}^{i,j}\right)^2-H_{bc}^{i,j-1}+\frac{2}{3}\beta^{i,j-1}\left(h_{gw}^{i,j-1}\right)^2}{\Delta n_v^{i,j-1}}\\
&+h_{v,gw}^{i,j}\Delta x_v^{i,j}K_{y,v}^{i,j}\frac{H_{bc}^{i,j+1}-\frac{2}{3}\beta^{i,j+1}\left(h_{gw}^{i,j+1}\right)^2-H_{bc}^{i,j}+\frac{2}{3}\beta^{i,j}\left(h_{gw}^{i,j}\right)^2}{\Delta n_v^{i,j}}\\
&+2\Delta xy_c^{i,j}K_{z,c}^{i,j}\beta^{i,j}h_{gw}^{i,j}=0
\end{aligned}
\tag{B.9}
$$

Whereas if Equation B.8 is combined with the equation of motion following a exponential approximation of the groundwater head, the system of equations becomes:

$$
\begin{aligned}
&-h_{u,gw}^{i-1,j}\Delta y_u^{i-1,j}K_{x,u}^{i-1,j}\frac{\frac{\beta^{i,j}}{h_{gw}^{i,j}}sinh\left(h_{gw}^{i,j}\right)+H_{bc}^{i,j}-\beta^{i,j}cosh\left(h_{gw}^{i,j}\right)-\frac{\beta^{i-1,j}}{h_{gw}^{i-1,j}}sinh\left(h_{gw}^{i-1,j}\right)-H_{bc}^{i-1,j}+\beta^{i-1,j}cosh\left(h_{gw}^{i-1,j}\right)}{\Delta x_u^{i-1,j}}\\
&+h_{u,gw}^{i,j}\Delta y_u^{i,j}K_{x,u}^{i,j}\frac{\frac{\beta^{i+1,j}}{h_{gw}^{i+1,j}}sinh\left(h_{gw}^{i+1,j}\right)+H_{bc}^{i+1,j}-\beta^{i+1,j}cosh\left(h_{gw}^{i+1,j}\right)-\frac{\beta^{i,j}}{h_{gw}^{i,j}}sinh\left(h_{gw}^{i,j}\right)-H_{bc}^{i,j}+\beta^{i,j}cosh\left(h_{gw}^{i,j}\right)}{\Delta x_u^{i,j}}\\
&-h_{v,gw}^{i,j-1}\Delta x_v^{i,j-1}K_{y,v}^{i,j-1}\frac{\frac{\beta^{i,j}}{h_{gw}^{i,j}}sinh\left(h_{gw}^{i,j}\right)+H_{bc}^{i,j}-\beta^{i,j}cosh\left(h_{gw}^{i,j}\right)-\frac{\beta^{i,j-1}}{h_{gw}^{i,j-1}}sinh\left(h_{gw}^{i,j-1}\right)-H_{bc}^{i,j-1}+\beta^{i,j-1}cosh\left(h_{gw}^{i,j-1}\right)}{\Delta y_v^{i,j-1}}\\
&+h_{v,gw}^{i,j}\Delta x_v^{i,j}K_{y,v}^{i,j}\frac{\frac{\beta^{i,j+1}}{h_{gw}^{i,j+1}}sinh\left(h_{gw}^{i,j+1}\right)+H_{bc}^{i,j+1}-\beta^{i,j+1}cosh\left(h_{gw}^{i,j+1}\right)-\frac{\beta^{i,j}}{h_{gw}^{i,j}}sinh\left(h_{gw}^{i,j}\right)-H_{bc}^{i,j}+\beta^{i,j}cosh\left(h_{gw}^{i,j}\right)}{\Delta y_v^{i,j}}\\
&+\Delta xy_c^{i,j}K_{z,c}^{i,j}\beta^{i,j}sinh\left(h_{gw}^{i,j}\right)=0
\end{aligned}
\tag{B.10}
$$

As discussed in Appendix A, the system of equations is solved by matrix algebra for the unknown parameter β .

$$Ax+b=0 \tag{B.11}$$

where A is a matrix containing coefficients for the horizontal and vertical specific discharge, x is a vector containing the unknown parameter β, and b contains the known forcing terms.

B.2.1 Solution matrix for 1D exponential-type

The 1D solution for the parabolic groundwater head approximation has been given in Appendix A. This section list the 1D solution for the exponential groundwater head approximation:

$$A = \begin{bmatrix} \ddots & & & & \\ & a_{i-1} & a_i & a_{i+1} & \\ & & & & \ddots \end{bmatrix} \tag{B.12}$$

where

$$a_{i-1} = -h^{i-1}_{u,gw} K^{i-1}_{x,u} \frac{cosh\left(h^{i-1}_{gw}\right) - \frac{1}{h^{i-1}_{gw}} sinh\left(h^{i-1}_{gw}\right)}{\Delta x^{i-1}_u}$$

$$a_i = h^{i-1}_{u,gw} K^{i-1}_{x,u} \frac{cosh\left(h^{i}_{gw}\right) - \frac{1}{h^{i}_{gw}} sinh\left(h^{i}_{gw}\right)}{\Delta x^{i-1}_u} + h^{i}_{u,gw} K^{i}_{x,u} \frac{cosh\left(h^{i}_{gw}\right) - \frac{1}{h^{i}_{gw}} sinh\left(h^{i}_{gw}\right)}{\Delta x^{i}_u} + \Delta x^i_c K^i_{z,c} sinh\left(h^i_{gw}\right)\left(1 - \Lambda_{t_{i,j}}\right)$$

$$a_{i+1} = -h^{i}_{u,gw} K^{i}_{x,u} \frac{cosh\left(h^{i+1}_{gw}\right) - \frac{1}{h^{i+1}_{gw}} sinh\left(h^{i+1}_{gw}\right)}{\Delta x^{i}_u}$$

The vector of unknown groundwater head curvature is given by:

$$x = \begin{bmatrix} \cdots \\ \beta_{i-1} \\ \beta_i \\ \beta_{i+1} \\ \cdots \end{bmatrix} \tag{B.13}$$

And the vector of known forcing components is:

$$b = \begin{bmatrix} \cdots \\ -h^{i-2}_{u,gw} K^{i-2}_{x,u} \frac{H^{i-1}_{bc} - H^{i-2}_{bc}}{\Delta x^{i-2}_u} + h^{i-1}_{u,gw} K^{i-1}_{x,u} \frac{H^{i}_{bc} - H^{i-1}_{bc}}{\Delta x^{i-1}_u} \\ -h^{i-1}_{u,gw} K^{i-1}_{x,u} \frac{H^{i}_{bc} - H^{i-1}_{bc}}{\Delta x^{i-1}_u} + h^{i}_{u,gw} K^{i}_{x,u} \frac{H^{i+1}_{bc} - H^{i}_{bc}}{\Delta x^{i}_u} \\ -h^{i}_{u,gw} K^{i}_{x,u} \frac{H^{i+1}_{bc} - H^{i}_{bc}}{\Delta x^{i}_u} + h^{i+1}_{u,gw} K^{i+1}_{x,u} \frac{H^{i+2}_{bc} - H^{i+1}_{bc}}{\Delta x^{i+1}_u} \\ \cdots \end{bmatrix} \tag{B.14}$$

B.2.2 Solution matrix for 2DH parabolic-type

This section list the 2DH solution for the parabolic groundwater head approximation:

$$A = \begin{bmatrix} \ddots & & & & & & \\ & a_{i-1,j} & a_{i,j} & a_{i+1,j} & \cdots & a_{i,j-1} & a_{i,j+1} & \\ & & & & & & \ddots \end{bmatrix} \tag{B.15}$$

where

$$a_{i-1,j} = -h_{u,gw}^{i-1,j} \Delta y_u^{i-1,j} K_{x,u}^{i-1,j} \frac{\frac{2}{3}\left(h_{gw}^{i-1,j}\right)^2}{\Delta x_u^{i-1,j}}$$

$$a_{i+1,j} = -h_{u,gw}^{i,j} \Delta y_u^{i,j} K_{x,u}^{i,j} \frac{\frac{2}{3}\left(h_{gw}^{i+1,j}\right)^2}{\Delta x_u^{i,j}}$$

$$a_{i,j} = h_{u,gw}^{i-1,j} \Delta y_u^{i-1,j} K_{x,u}^{i-1,j} \frac{\frac{2}{3}\left(h_{gw}^{i,j}\right)^2}{\Delta x_u^{i-1,j}} + h_{u,gw}^{i,j} \Delta y_u^{i,j} K_{x,u}^{i,j} \frac{\frac{2}{3}\left(h_{gw}^{i,j}\right)^2}{\Delta x_u^{i,j}} + h_{v,gw}^{i,j-1} \Delta x_v^{i,j-1} K_{y,v}^{i,j-1} \frac{\frac{2}{3}\left(h_{gw}^{i,j}\right)^2}{\Delta y_v^{i,j-1}}$$
$$+ h_{v,gw}^{i,j} \Delta x_v^{i,j} K_{y,v}^{i,j} \frac{\frac{2}{3}\left(h_{gw}^{i,j}\right)^2}{\Delta y_v^{i,j}} + 2\Delta xy_c^{i,j} K_{z,c}^{i,j} h_{gw}^{i,j} \left(1 - \Lambda_{t_{i,j}}\right)$$

$$a_{i,j-1} = -h_{v,gw}^{i,j-1} \Delta x_v^{i,j-1} K_{y,v}^{i,j-1} \frac{\frac{2}{3}\left(h_{gw}^{i,j}\right)^2}{\Delta y_v^{i,j-1}}$$

$$a_{i,j+1} = -h_{v,gw}^{i,j} \Delta x_v^{i,j} K_{y,v}^{i,j} \frac{\frac{2}{3}\left(h_{gw}^{i,j}\right)^2}{\Delta y_v^{i,j}}$$

The vector of unknown groundwater head curvature is given by:

$$x = \begin{bmatrix} \cdots \\ \beta_{i-1,j} \\ \beta_{i,j} \\ \beta_{i+1,j} \\ \ldots \\ \beta_{i,j-1} \\ \beta_{i,j+1} \\ \ldots \end{bmatrix} \tag{B.16}$$

And the vector of known forcing components is:

$$
b = \begin{bmatrix}
\cdots \\
-h_{u,gw}^{i-2,j}\Delta y_u^{i-2,j}K_{x,u}^{i-2,j}\frac{H_{bc}^{i-1,j}-H_{bc}^{i-2,j}}{\Delta x_u^{i-2,j}} + h_{u,gw}^{i-1,j}\Delta y_u^{i-1,j}K_{x,u}^{i-1,j}\frac{H_{bc}^{i,j}-H_{bc}^{i-1,j}}{\Delta x_u^{i-1,j}} \\
-h_{v,gw}^{i-1,j-1}\Delta x_v^{i-1,j-1}K_{y,v}^{i-1,j-1}\frac{H_{bc}^{i-1,j}-H_{bc}^{i-1,j-1}}{\Delta y_v^{i-1,j-1}} + h_{v,gw}^{i-1,j}\Delta x_v^{i-1,j}K_{y,v}^{i-1,j}\frac{H_{bc}^{i-1,j+1}-H_{bc}^{i-1,j}}{\Delta y_v^{i-1,j}} \\
\\
-h_{u,gw}^{i-1,j}\Delta y_u^{i-1,j}K_{x,u}^{i-1,j}\frac{H_{bc}^{i,j}-H_{bc}^{i-1,j}}{\Delta x_u^{i-1,j}} + h_{u,gw}^{i,j}\Delta y_u^{i,j}K_{x,u}^{i,j}\frac{H_{bc}^{i+1,j}-H_{bc}^{i,j}}{\Delta x_u^{i,j}} \\
-h_{v,gw}^{i,j-1}\Delta x_v^{i,j-1}K_{y,v}^{i,j-1}\frac{H_{bc}^{i,j}-H_{bc}^{i,j-1}}{\Delta y_v^{i,j-1}} + h_{v,gw}^{i,j}\Delta x_v^{i,j}K_{y,v}^{i,j}\frac{H_{bc}^{i,j+1}-H_{bc}^{i,j}}{\Delta y_v^{i,j}} \\
\\
-h_{u,gw}^{i,j}\Delta y_u^{i,j}K_{x,u}^{i,j}\frac{H_{bc}^{i+1,j}-H_{bc}^{i,j}}{\Delta x_u^{i,j}} + h_{u,gw}^{i+1,j}\Delta y_u^{i+1,j}K_{x,u}^{i+1,j}\frac{H_{bc}^{i+2,j}-H_{bc}^{i+1,j}}{\Delta x_u^{i+1,j}} \\
-h_{v,gw}^{i+1,j-1}\Delta x_v^{i+1,j-1}K_{y,v}^{i+1,j-1}\frac{H_{bc}^{i+1,j}-H_{bc}^{i+1,j-1}}{\Delta y_v^{i+1,j-1}} + h_{v,gw}^{i+1,j}\Delta x_v^{i+1,j}K_{y,v}^{i+1,j}\frac{H_{bc}^{i+1,j+1}-H_{bc}^{i+1,j}}{\Delta y_v^{i+1,j}} \\
\\
\cdots \\
\\
-h_{u,gw}^{i-1,j-1}\Delta y_u^{i-1,j-1}K_{x,u}^{i-1,j-1}\frac{H_{bc}^{i,j-1}-H_{bc}^{i-1,j-1}}{\Delta x_u^{i-1,j-1}} + h_{u,gw}^{i,j-1}\Delta y_u^{i,j-1}K_{x,u}^{i,j-1}\frac{H_{bc}^{i+1,j-1}-H_{bc}^{i,j-1}}{\Delta x_u^{i,j-1}} \\
-h_{v,gw}^{i,j-2}\Delta x_v^{i,j-2}K_{y,v}^{i,j-2}\frac{H_{bc}^{i,j-1}-H_{bc}^{i,j-2}}{\Delta y_v^{i,j-2}} + h_{v,gw}^{i,j-1}\Delta x_v^{i,j-1}K_{y,v}^{i,j-1}\frac{H_{bc}^{i,j}-H_{bc}^{i,j-1}}{\Delta y_v^{i,j-1}} \\
\\
-h_{u,gw}^{i-1,j+1}\Delta y_u^{i-1,j+1}K_{x,u}^{i-1,j+1}\frac{H_{bc}^{i,j+1}-H_{bc}^{i-1,j+1}}{\Delta x_u^{i-1,j+1}} + h_{u,gw}^{i,j+1}\Delta y_u^{i,j+1}K_{x,u}^{i,j+1}\frac{H_{bc}^{i+1,j+1}-H_{bc}^{i,j+1}}{\Delta x_u^{i,j+1}} \\
-h_{v,gw}^{i,j}\Delta x_v^{i,j}K_{y,v}^{i,j}\frac{H_{bc}^{i,j+1}-H_{bc}^{i,j}}{\Delta y_v^{i,j}} + h_{v,gw}^{i,j+1}\Delta x_v^{i,j+1}K_{y,v}^{i,j+1}\frac{H_{bc}^{i,j+2}-H_{bc}^{i,j+1}}{\Delta y_v^{i,j+1}} \\
\\
\cdots
\end{bmatrix} \tag{B.17}
$$

B.2.3 Solution matrix for 2DH exponential-type

This section list the 2DH solution for the exponential groundwater head approximation:

$$A = \begin{bmatrix} \ddots & & & & & & & \\ & a_{i-1,j} & a_{i,j} & a_{i+1,j} & \cdots & a_{i,j-1} & a_{i,j+1} & \\ & & & & & & & \ddots \end{bmatrix} \tag{B.18}$$

where:

$$a_{i-1,j} = -h_{u,gw}^{i-1,j}\Delta y_u^{i-1,j}K_{x,u}^{i-1,j}\frac{cosh\left(h_{gw}^{i-1,j}\right)-\frac{1}{h_{gw}^{i+1,j}}sinh\left(h_{gw}^{i-1,j}\right)}{\Delta x_u^{i-1,j}}$$

$$a_{i+1,j} = -h_{u,gw}^{i,j}\Delta y_u^{i,j}K_{x,u}^{i,j}\frac{cosh\left(h_{gw}^{i+1,j}\right)-\frac{1}{h_{gw}^{i+1,j}}sinh\left(h_{gw}^{i+1,j}\right)}{\Delta x_u^{i,j}}$$

$$a_{i,j} = h_{u,gw}^{i-1,j}\Delta y_u^{i-1,j}K_{x,u}^{i-1,j}\frac{cosh\left(h_{gw}^{i,j}\right)-\frac{1}{h_{gw}^{i,j}}sinh\left(h_{gw}^{i,j}\right)}{\Delta x_u^{i-1,j}} + h_{u,gw}^{i,j}\Delta y_u^{i,j}K_{x,u}^{i,j}\frac{cosh\left(h_{gw}^{i,j}\right)-\frac{1}{h_{gw}^{i,j}}sinh\left(h_{gw}^{i,j}\right)}{\Delta x_u^{i,j}} + h_{v,gw}^{i,j-1}\Delta x_v^{i,j-1}K_{y,v}^{i,j-1}\frac{cosh\left(h_{gw}^{i,j}\right)-\frac{1}{h_{gw}^{i,j}}sinh\left(h_{gw}^{i,j}\right)}{\Delta y_v^{i,j-1}}$$
$$+h_{v,gw}^{i,j}\Delta x_v^{i,j}K_{y,v}^{i,j}\frac{cosh\left(h_{gw}^{i,j}\right)-\frac{1}{h_{gw}^{i,j}}sinh\left(h_{gw}^{i,j}\right)}{\Delta y_v^{i,j}} + \Delta xy_c^{i,j}K_{z,c}^{i,j}sinh\left(h_{gw}^{i,j}\right)\left(1-\Lambda_{t_{i,j}}\right)$$

$$a_{i,j-1} = -h_{v,gw}^{i,j-1}\Delta x_v^{i,j-1}K_{y,v}^{i,j-1}\frac{cosh\left(h_{gw}^{i,j-1}\right)-\frac{1}{h_{gw}^{i,j-1}}sinh\left(h_{gw}^{i,j-1}\right)}{\Delta y_v^{i,j-1}}$$

$$a_{i,j+1} = -h_{v,gw}^{i,j}\Delta x_v^{i,j}K_{y,v}^{i,j}\frac{cosh\left(h_{gw}^{i,j+1}\right)-\frac{1}{h_{gw}^{i,j+1}}sinh\left(h_{gw}^{i,j+1}\right)}{\Delta y_v^{i,j}}$$

The vector of unknown groundwater head curvature is given by:

$$x = \begin{bmatrix} \cdots \\ \beta_{i-1,j} \\ \beta_{i,j} \\ \beta_{i+1,j} \\ \cdots \\ \beta_{i,j-1} \\ \beta_{i,j+1} \\ \cdots \end{bmatrix} \tag{B.19}$$

And the vector of known forcing components is:

$$
b = \begin{bmatrix}
\cdots \\
-h_{u,gw}^{i-2,j}\Delta y_u^{i-2,j}K_{x,u}^{i-2,j}\frac{H_{bc}^{i-1,j}-H_{bc}^{i-2,j}}{\Delta x_u^{i-2,j}} + h_{u,gw}^{i-1,j}\Delta y_u^{i-1,j}K_{x,u}^{i-1,j}\frac{H_{bc}^{i,j}-H_{bc}^{i-1,j}}{\Delta x_u^{i-1,j}} \\
-h_{v,gw}^{i-1,j-1}\Delta x_v^{i-1,j-1}K_{y,v}^{i-1,j-1}\frac{H_{bc}^{i-1,j}-H_{bc}^{i-1,j-1}}{\Delta y_v^{i-1,j-1}} + h_{v,gw}^{i-1,j}\Delta x_v^{i-1,j}K_{y,v}^{i-1,j}\frac{H_{bc}^{i-1,j+1}-H_{bc}^{i-1,j}}{\Delta y_v^{i-1,j}} \\
\\
-h_{u,gw}^{i-1,j}\Delta y_u^{i-1,j}K_{x,u}^{i-1,j}\frac{H_{bc}^{i,j}-H_{bc}^{i-1,j}}{\Delta x_u^{i-1,j}} + h_{u,gw}^{i,j}\Delta y_u^{i,j}K_{x,u}^{i,j}\frac{H_{bc}^{i+1,j}-H_{bc}^{i,j}}{\Delta x_u^{i,j}} \\
-h_{v,gw}^{i,j-1}\Delta x_v^{i,j-1}K_{y,v}^{i,j-1}\frac{H_{bc}^{i,j}-H_{bc}^{i,j-1}}{\Delta y_v^{i,j-1}} + h_{v,gw}^{i,j}\Delta x_v^{i,j}K_{y,v}^{i,j}\frac{H_{bc}^{i,j+1}-H_{bc}^{i,j}}{\Delta y_v^{i,j}} \\
\\
-h_{u,gw}^{i,j}\Delta y_u^{i,j}K_{x,u}^{i,j}\frac{H_{bc}^{i+1,j}-H_{bc}^{i,j}}{\Delta x_u^{i,j}} + h_{u,gw}^{i+1,j}\Delta y_u^{i+1,j}K_{x,u}^{i+1,j}\frac{H_{bc}^{i+2,j}-H_{bc}^{i+1,j}}{\Delta x_u^{i+1,j}} \\
-h_{v,gw}^{i+1,j-1}\Delta x_v^{i+1,j-1}K_{y,v}^{i+1,j-1}\frac{H_{bc}^{i+1,j}-H_{bc}^{i+1,j-1}}{\Delta y_v^{i+1,j-1}} + h_{v,gw}^{i+1,j}\Delta x_v^{i+1,j}K_{y,v}^{i+1,j}\frac{H_{bc}^{i+1,j+1}-H_{bc}^{i+1,j}}{\Delta y_v^{i+1,j}} \\
\\
\cdots \\
\\
-h_{u,gw}^{i-1,j-1}\Delta y_u^{i-1,j-1}K_{x,u}^{i-1,j-1}\frac{H_{bc}^{i,j-1}-H_{bc}^{i-1,j-1}}{\Delta x_u^{i-1,j-1}} + h_{u,gw}^{i,j-1}\Delta y_u^{i,j-1}K_{x,u}^{i,j-1}\frac{H_{bc}^{i+1,j-1}-H_{bc}^{i,j-1}}{\Delta x_u^{i,j-1}} \\
-h_{v,gw}^{i,j-2}\Delta x_v^{i,j-2}K_{y,v}^{i,j-2}\frac{H_{bc}^{i,j-1}-H_{bc}^{i,j-2}}{\Delta y_v^{i,j-2}} + h_{v,gw}^{i,j-1}\Delta x_v^{i,j-1}K_{y,v}^{i,j-1}\frac{H_{bc}^{i,j}-H_{bc}^{i,j-1}}{\Delta y_v^{i,j-1}} \\
\\
-h_{u,gw}^{i-1,j+1}\Delta y_u^{i-1,j+1}K_{x,u}^{i-1,j+1}\frac{H_{bc}^{i,j+1}-H_{bc}^{i-1,j+1}}{\Delta x_u^{i-1,j+1}} + h_{u,gw}^{i,j+1}\Delta y_u^{i,j+1}K_{x,u}^{i,j+1}\frac{H_{bc}^{i+1,j+1}-H_{bc}^{i,j+1}}{\Delta x_u^{i,j+1}} \\
-h_{v,gw}^{i,j}\Delta x_v^{i,j}K_{y,v}^{i,j}\frac{H_{bc}^{i,j+1}-H_{bc}^{i,j}}{\Delta y_v^{i,j}} + h_{v,gw}^{i,j+1}\Delta x_v^{i,j+1}K_{y,v}^{i,j+1}\frac{H_{bc}^{i,j+2}-H_{bc}^{i,j+1}}{\Delta y_v^{i,j+1}} \\
\cdots
\end{bmatrix} \tag{B.20}
$$

Appendix C

Vertical groundwater head approximation: comparison

In Chapter 4, Section 4.3.3, a parabolic-type approximation method for the vertical groundwater head variation is introduced. An exponential-type approximation is described in Appendix B. In this appendix, a comparison is made between the parabolic-type approximation and exponential-type approximation, using the data and models of the BARDEX experiment presented in Chapter 4.

Figure C.1 shows time series and variance density spectra of measured and modelled groundwater head at four locations in the BARDEX gravel barrier during measurement series BAE10, using the parabolic-type approximation (orange) and the exponential-type approximation (green). Figure C.2 shows the time-averaged modelled groundwater head, using both vertical approximations, and the groundwater head measured at the location of all the buried PTs. The figures show that while there are some minor differences between the results of the two vertical groundwater head approximation methods, they generally produce similar results. The results of the exponential-type approximation are not found to be more accurate than the results of the parabolic-type approximation, and are instead found to be slightly less accurate than those of the parabolic-type approximation in certain locations (e.g., PT10).

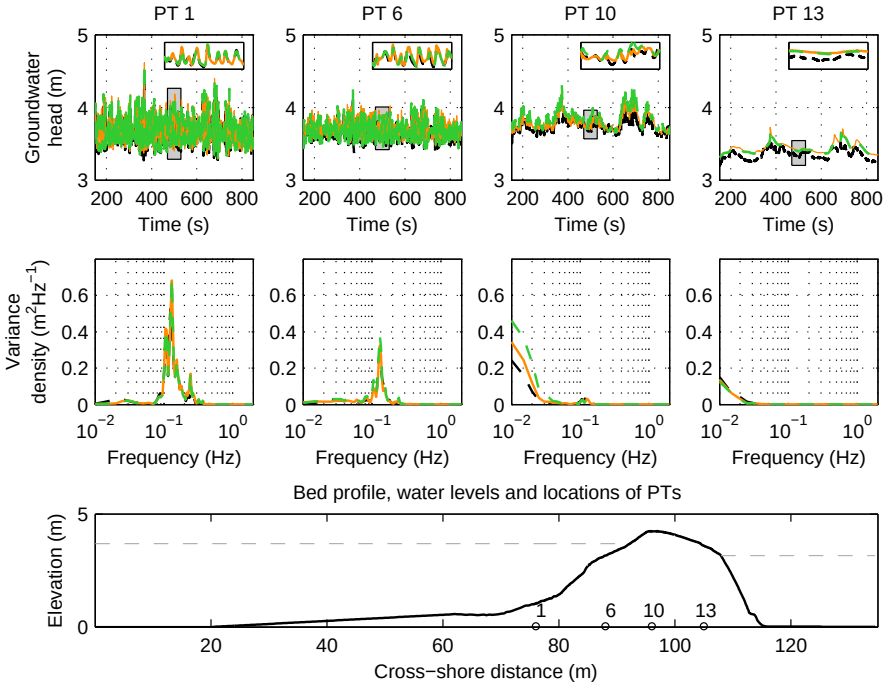

Figure C.1: Top panels: Measured (– –), modelled with parabolic-type approximation (—) and modelled with exponential-type approximation (– –) time series of the groundwater head relative to the flume floor at the locations of four buried PTs during series BAE10. A detailed time series, indicated by the grey shaded area, is shown in the top-right corner of each panel. Centre panels: Measured (– –) and modelled (—, – –) variance density spectra of the groundwater head at the locations of four buried PTs during series BAE10. The locations of the buried PTs relative to the barrier profile (—) and still water levels (– –) are shown in the bottom panel.

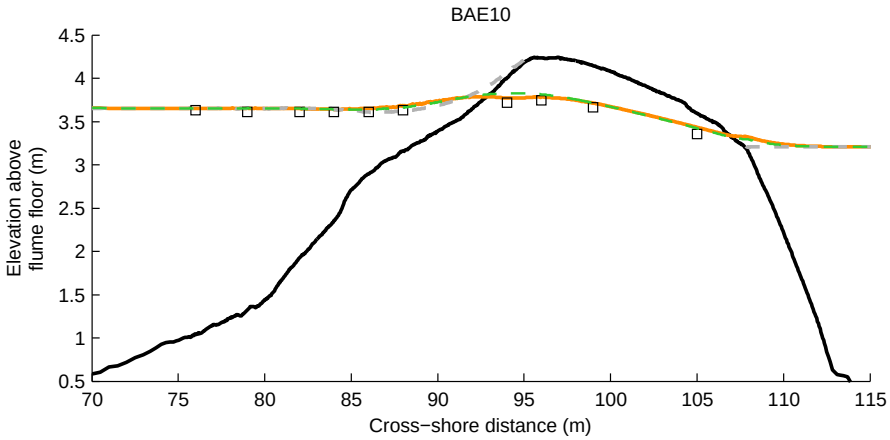

Figure C.2: Measured mean groundwater head measured at 10 buried PTs on the flume floor (□), modelled mean groundwater head at the flume floor using the parabolic-type approximation (—), modelled mean groundwater head at the flume floor using the exponential-type approximation (– –), bed profile (—), and mean water surface levels (– –) for series BAE10.

Appendix D

Morphodynamic sensitivity to sediment transport relations

D.1 Introduction

It is widely accepted that the selection of an appropriate sediment transport formulation is essential for the application of process-based morphodynamic models, since morphodynamic variations due to different sediment transport formulae can be substantially larger than those due to different hydrodynamic models. The sensitivity of the XBeach-G model to changes in the sediment transport formula, as well as a substantiation of the choice for the Van Rijn (2007a) transport equation in Chapter 5 are addressed in this appendix. In this appendix, morphodynamic sensitivity simulations are carried out using four alternative sediment transport relations (Meyer-Peter and Müller, 1948; Engelund and Fredsøe, 1976; Nielsen, 2002; Wong and Parker, 2006) to the Van Rijn equation, as well as a variation of the morphodynamic module based on the Nielsen (2002) bed load transport model, as presented in Masselink et al. (2014).

Since the principle driver of morphological change in the XBeach-G model is the spatial gradient in bed load transport (Equation 5.12), the sensitivity of the model to sediment transport formulae is strongly dependent on the variation of predicted transport rates to changes in the hydrodynamic forcing. Figures D.1 and D.2 show the predicted bed load transport rate and the predicted bed load transport rate gradient, respectively, for three grain sizes as a function of the Shields parameter θ for the Nielsen (N; purple), Meyer-Peter and Müller (MPM; red), Engelund and Fredsøe (EF; green), Wong and Parker (WP; blue) and Van Rijn (VR; orange) bed load transport equations. The figures show that the transport equations show considerable spread in predicted transport rates and transport rate gradients with respect to θ (both up to a factor of 10 for $\theta \leqq 2$ and $D_{50} = 50$ mm).

The morphodynamic sensitivity of the XBeach-G model to the transport equations discussed above is discussed per transport equation in the following sections.

Sections of this chapter are based on work presented in Masselink et al. (2014).

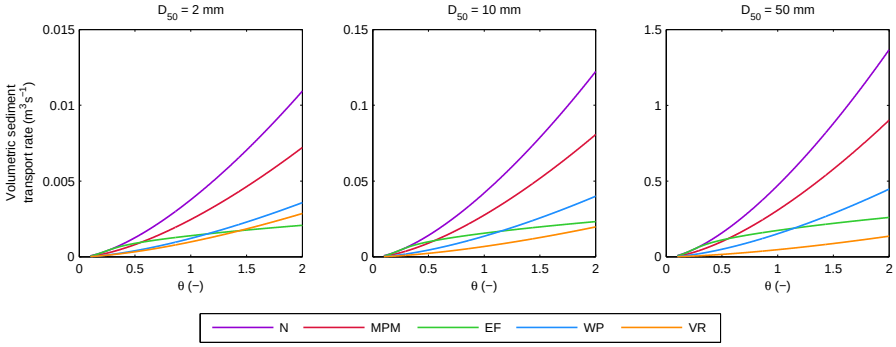

Figure D.1: Bed load transport rates as a function of the Shields parameter for three grain sizes: Nielsen (2002 ; purple), Meyer-Peter and Müller (1948 ; red), Engelund and Fredsøe (1976 ; green), Wong and Parker (2006 ; blue) and Van Rijn (2007a ; orange).

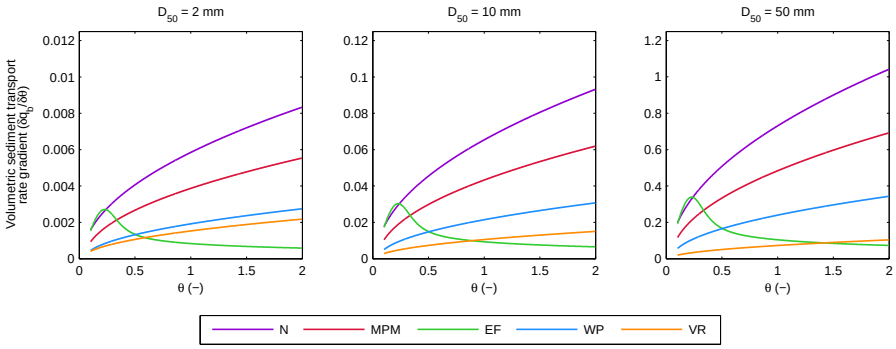

Figure D.2: Gradient in bed load transport rates as a function of the Shields parameter for three grain sizes: Nielsen (2002 ; purple), Meyer-Peter and Müller (1948 ; red), Engelund and Fredsøe (1976 ; green), Wong and Parker (2006 ; blue) and Van Rijn (2007a ; orange).

D.2 Nielsen

D.2.1 Model equations for sediment transport

In the case of the Nielsen equation, the sediment transport model is modified slightly from that presented in Chapter 5. In this model the total gravel sediment transport is computed using a modification of the Meyer-Peter and Müller (1948) equation for bed load transport derived by Nielsen (2002):

$$q_b = 12\left(\theta' - 0.05\right)\sqrt{\theta'}\sqrt{\Delta g D_{50}^3}\frac{u_*}{|u_*|} \tag{D.1}$$

In contrast to the sediment transport model described in Chapter 5, in this model the Shields parameter θ is computed from the friction velocity u_*, rather than bed shear stress as:

$$\theta = \frac{u_*^2}{\Delta g D_{50}} \tag{D.2}$$

where u_* is computed following Nielsen (2002) to account for boundary layer expansion and contraction in the swash, pressure gradient effects, and the presence of turbulent fronts:

$$u_* = \sqrt{\frac{f_s}{2}}\left(cos\left(\varphi\right)u + \frac{T_{m-1,0}}{2\pi}sin\left(\varphi\right)\frac{\partial u}{\partial t}\right) \tag{D.3}$$

where f_s is a user-defined sediment friction factor, $T_{m-1,0}$ is the offshore spectral period based on the first negative moment of the energy spectrum and φ is a user-defined phase lag angle. Note that the friction velocity u_* and the bed shear stress τ_b used in the NLSWE (Eq. 3.2) are not coupled in this model.

The Shields parameter is subsequently adjusted for bed slope effects following Fredsøe and Deigaard (1992) (cf., Equation 5.3):

$$\theta' = \theta cos\left(\beta\right)\left(1 \pm \frac{tan\left(\beta\right)}{tan\left(\phi\right)}\right) \tag{D.4}$$

D.2.2 Morphodynamic sensitivity

Figure D.3 shows the cross-shore profile development predicted by the XBeach-G model with the Van Rijn transport equation (solid orange lines) and by the XBeach-G model with the Nielsen transport model (dashed orange lines) for all 10 storm events discussed in Chapter 5. After calibration, the free model parameters in the Nielsen model are set as $f_s = 0.0125$ and $\varphi = 25°$ for all 10 storm events. The figure shows that while the Nielsen model reproduces much of the observed morphodynamic response of the gravel barriers, the Nielsen model over predicts the erosion of the beach during BAB3, CB2, SS3, BAE9 and LB5, over predicts crest build-up during SS3

and over predicts barrier rollover during ST1. Furthermore, in a quantitative sense the computed BSS of the Nielsen model (Table D.1) is lower than that of the Van Rijn transport equation (Table 5.2).

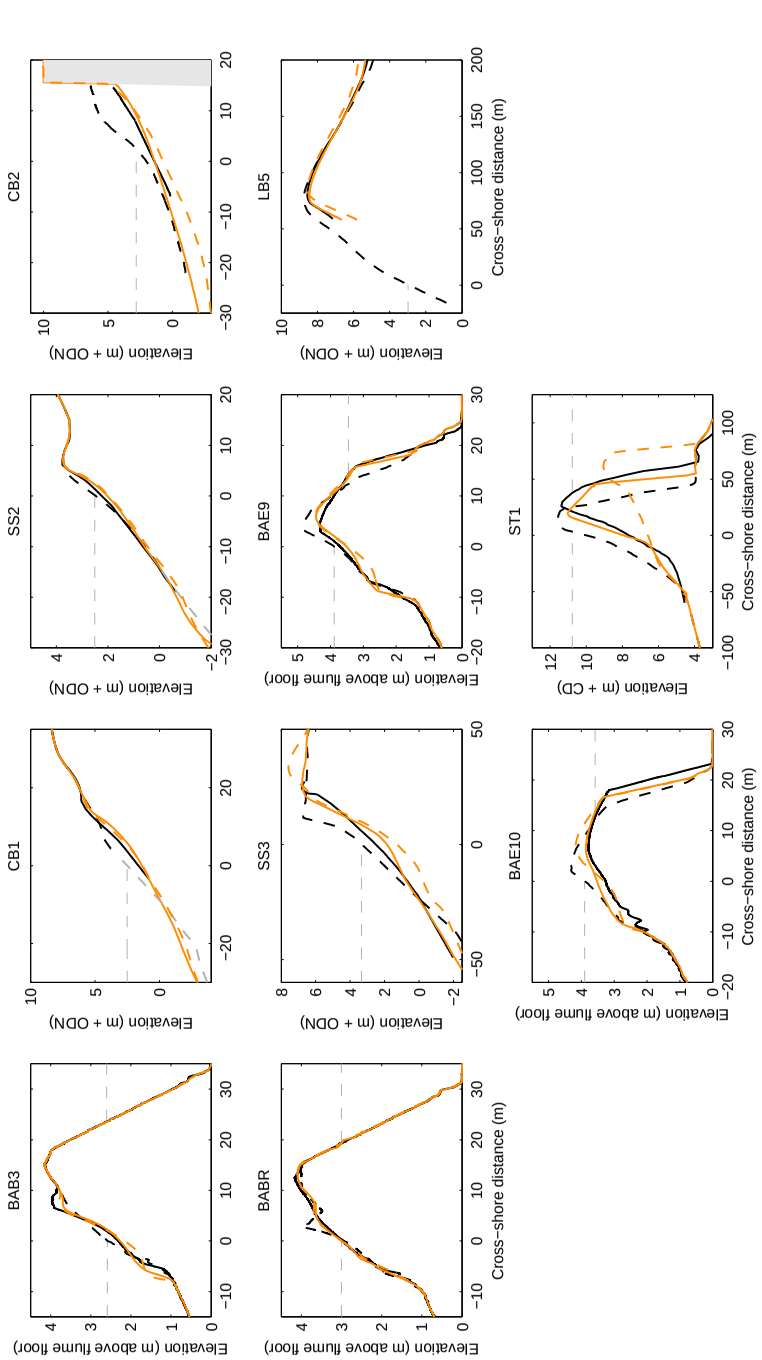

Figure D.3: Sensitivity of modelled cross-shore profile response to sediment transport relations: measured pre-storm (– –) and measured post-storm (—) cross-shore profiles, modelled profiles with the Van Rijn formulation (—) and Nielsen transport relation (– –), and maximum still water level (– –).

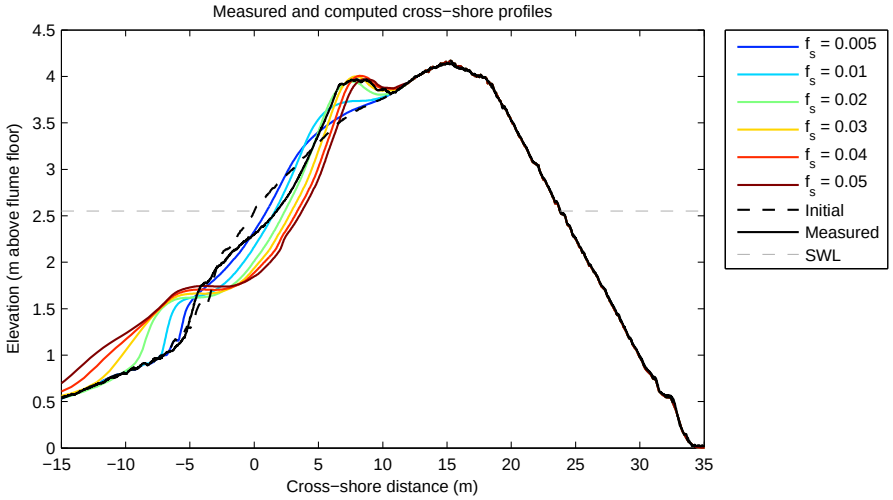

Figure D.4: Sensitivity of Nielsen sediment transport model to the sediment friction factor during BAB3.

Sensitivity to free model parameters

The Nielsen transport model applied in this thesis has two different free model parameters from the sediment transport and morphology module discussed in Chapter 5: the user-defined sediment friction factor f_s and the user-defined phase lag angle φ. The sensitivity of the XBeach-G model using the Nielsen transport model to these parameters is shown in Figures D.4 and D.5 for the case of BAB3. Figure D.5 in particular, shows a strong dependence of the predicted morphodynamics on φ, where larger values of φ lead to substantially greater berm volumes. Note that the lower beach face is incorrectly modelled in all sensitivity simulations with the Nielsen transport model.

D.3 Meyer-Peter and Müller

D.3.1 Model equations for sediment transport

In the case of the Meyer-Peter and Müller equation, the morphodynamic module discussed in Chapter 5 is used, with the exception that the total gravel sediment transport is computed using the equation for bed load transport derived by Meyer-Peter and Müller (1948):

$$q_b = 8\left(\theta' - \theta_{cr}\right)^{1.5}\sqrt{\Delta g D_{50}^3}\frac{\tau_b}{|\tau_b|} \tag{D.5}$$

D.3.2 Morphodynamic sensitivity

Figure D.6 shows the cross-shore profile development predicted by the XBeach-G model with the Van Rijn transport equation (solid orange lines) and by the XBeach-G

	RMSE	Rel. bias	ρ	BSS (qualifier†)
BAB3	0.18 m	-0.02	0.64	0.13 (poor)
CB1	0.18 m	-0.28	1.00	0.93 (excellent)
SS2	0.18 m	-1.29	0.94	-0.04 (bad)
CB2a	1.02 m	-1.42	0.05	-1.80 (bad)
CB2b	1.29 m	0.34	0.16	0.69 (good)
CB2c	0.68 m	-0.10	0.77	0.90 (excellent)
CB2d	0.46 m	-0.31	0.98	0.92 (excellent)
BABR	0.04 m	0.03	0.93	0.95 (excellent)
SS3	0.85 m	-0.85	0.83	0.27 (poor)
BAE9	0.17 m	-0.05	0.85	0.73 (good)
LB5	0.34 m	0.31	0.99	-0.52 (bad)
BAE10	0.35 m	0.01	0.79	0.64 (good)

Table D.1: Root-mean-square error (RMSE), relative bias (Rel. bias), correlation coefficient (ρ) and Brier Skill Score (BSS) of the model cross-shore profile change predictions using the Nielsen transport equation relative to the measured profile change. Note that ST1 is not included in the statistical analysis. † refers to the qualification of Van Rijn et al. (2003).

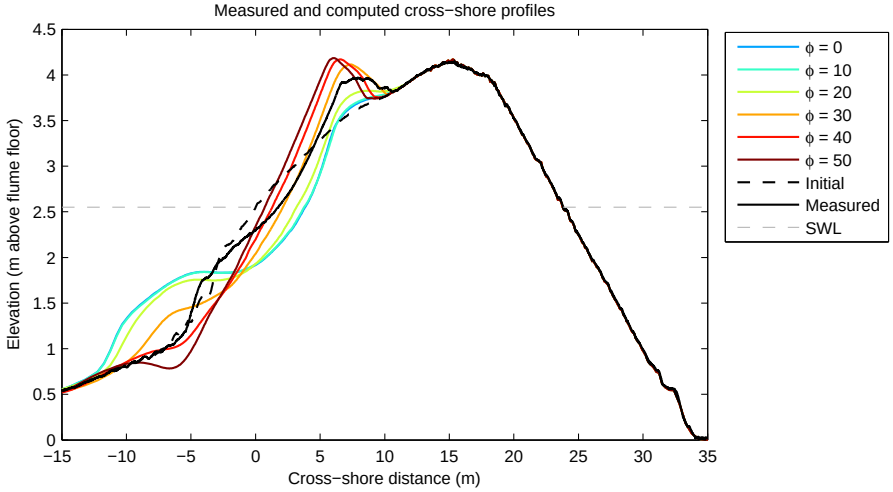

Figure D.5: Sensitivity of Nielsen sediment transport model to the boundary layer phase lag parameter during BAB3.

model with the Meyer-Peter and Müller transport equation (dashed orange lines) for all 10 storm events discussed in Chapter 5. The figure shows that the Meyer-Peter and Müller transport equation generally over predicts the observed morphodynamic response. In a quantitative sense the computed BSS of the Meyer-Peter and Müller transport equation (Table D.2) is substantially lower than that of the Van Rijn transport equation (Table 5.2).

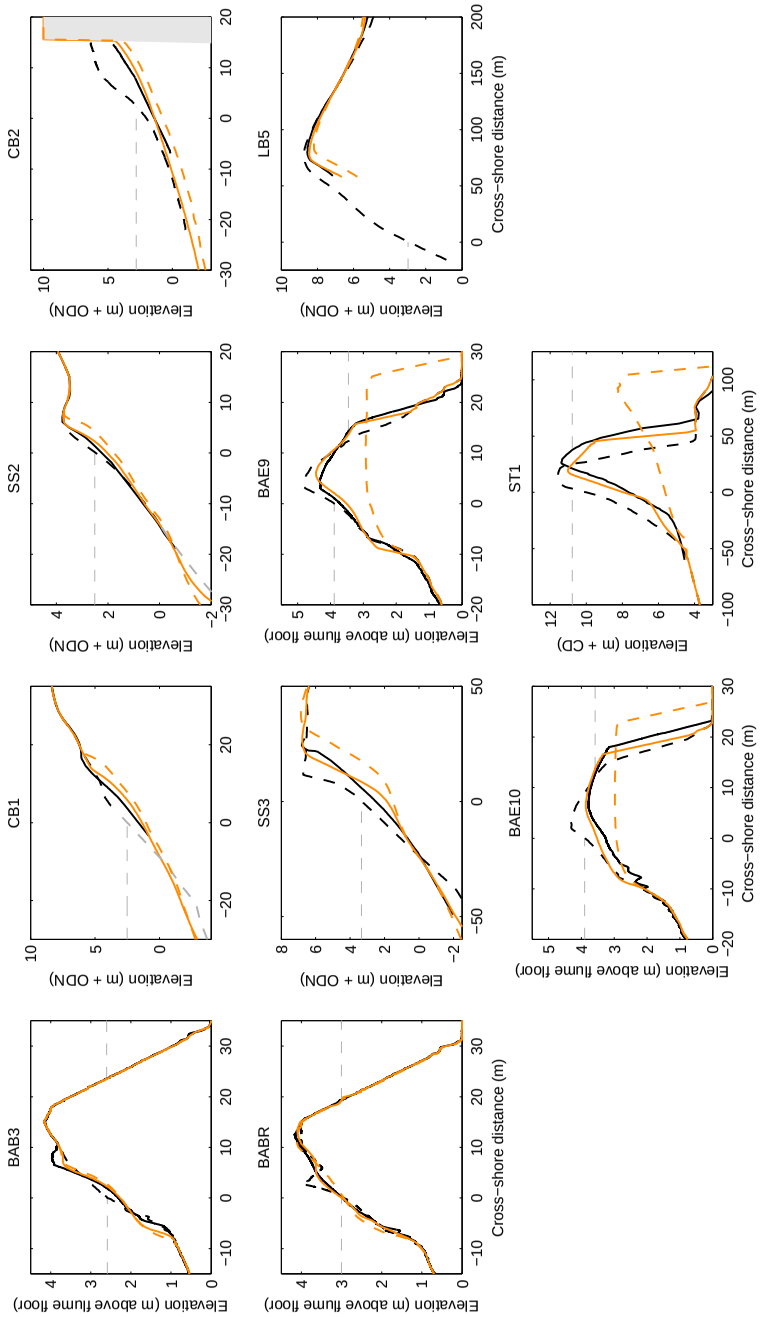

Figure D.6: Sensitivity of modelled cross-shore profile response to sediment transport relations: measured pre-storm (– –) and measured post-storm (—) cross-shore profiles, modelled profiles with the Van Rijn formulation (—) and Meyer-Peter and Müller transport relation (– –), and maximum still water level (– –).

D.4 Engelund and Fredsøe

D.4.1 Model equations for sediment transport

In the case of the Engelund and Fredsøe equation, the morphodynamic module discussed in Chapter 5 is used, with the exception that the total gravel sediment transport is computed using the equation for bed load transport derived by Engelund and Fredsøe (1976):

$$q_b = 5n_{EF}\left(\sqrt{\theta'} - 0.7\sqrt{\theta_{cr}}\right)\sqrt{\Delta g D_{50}^3}\frac{\tau_b}{|\tau_b|} \tag{D.6}$$

where

$$n_{EF} = \left(1 + \left(0.5236\frac{0.5}{\theta' - \theta_{cr}}\right)^4\right)^{-\frac{1}{4}} \tag{D.7}$$

D.4.2 Morphodynamic sensitivity

Figure D.7 shows the cross-shore profile development predicted by the XBeach-G model with the Van Rijn transport equation (solid orange lines) and by the XBeach-G model with the Engelund and Fredsøe transport equation (dashed orange lines) for all 10 storm events discussed in Chapter 5. The figure shows that similarly to the Meyer-Peter and Müller equation, the Engelund and Fredsøe transport equation generally over predicts the observed morphodynamic response. In a quantitative sense the computed BSS of the Engelund and Fredsøe transport equation (Table D.3) is substantially lower than that of the Van Rijn transport equation (Table 5.2).

	RMSE	**Rel. bias**	ρ	**BSS (qualifier†)**
BAB3	0.20 m	-0.01	0.57	-0.06 (bad)
CB1	1.07 m	-1.90	0.85	-1.70 (bad)
SS2	0.39 m	-2.75	0.90	-4.15 (bad)
CB2a	1.06 m	-1.87	0.81	-2.04 (bad)
CB2b	0.29 m	-0.12	1.00	0.98 (excellent)
CB2c	0.31 m	-0.12	1.00	0.98 (excellent)
CB2d	0.64 m	-0.44	0.99	0.84 (excellent)
BABR	0.14 m	0.07	0.75	0.31 (fair)
SS3	1.05 m	-0.89	0.93	-0.12 (bad)
BAE9	1.16 m	-0.18	0.35	-11.41 (bad)
LB5	0.41 m	-1.08	0.99	-1.04 (bad)
BAE10	0.77 m	-0.09	0.76	-0.75 (bad)

Table D.2: Root-mean-square error (RMSE), relative bias (Rel. bias), correlation coefficient (ρ) and Brier Skill Score (BSS) of the model cross-shore profile change predictions using the Meyer-Peter and Müller transport equation relative to the measured profile change. Note that ST1 is not included in the statistical analysis. † refers to the qualification of Van Rijn et al. (2003).

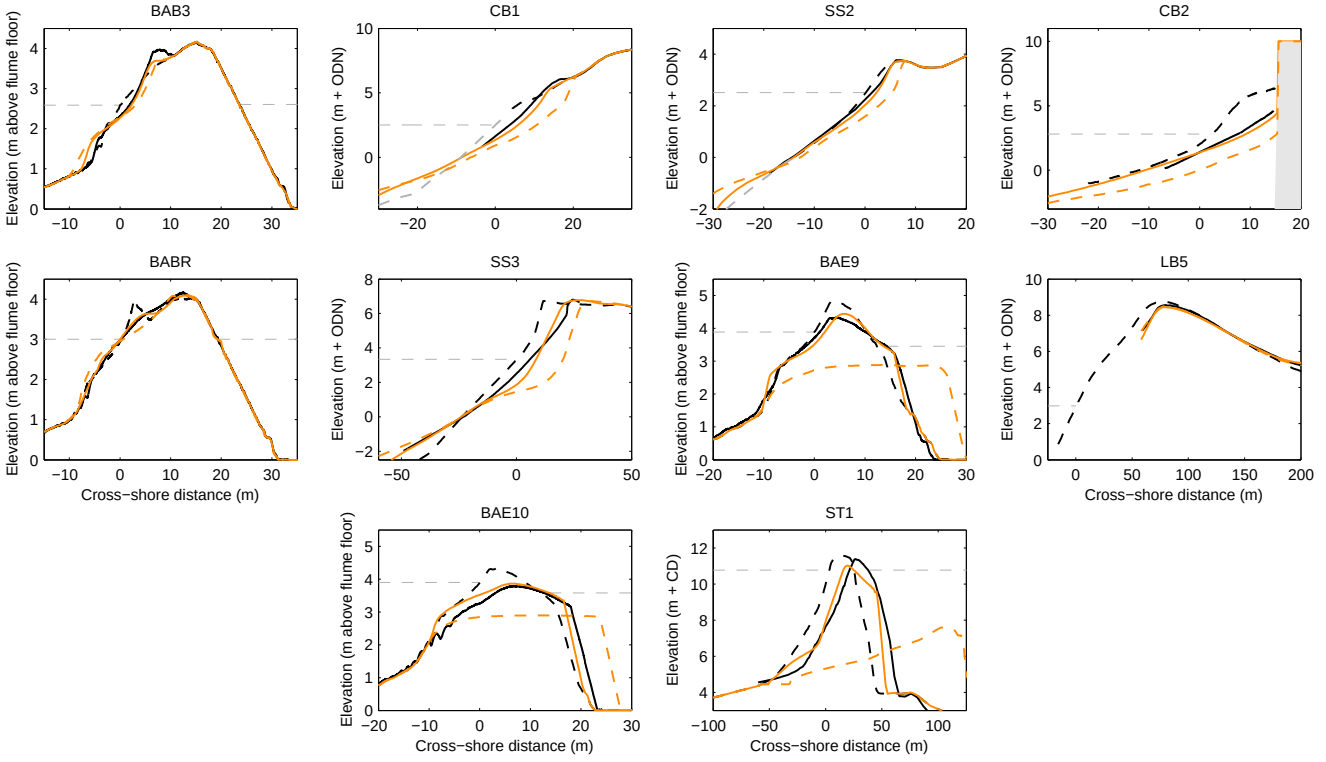

Figure D.7: Sensitivity of modelled cross-shore profile response to sediment transport relations: measured pre-storm (– –) and measured post-storm (—) cross-shore profiles, modelled profiles with the Van Rijn formulation (—) and Engelund and Fredsøe transport relation (– –), and maximum still water level (– –).

D.5 Wong and Parker

D.5.1 Model equations for sediment transport

In the case of the Wong and Parker equation, the morphodynamic module discussed in Chapter 5 is used, with the exception that the total gravel sediment transport is computed using the equation for bed load transport based on a modification of the Meyer-Peter and Müller (1948) equation for bed load transport and derived by Wong and Parker (2006):

$$q_b = 3.97\left(\theta' - \theta_{cr}\right)^{1.5}\sqrt{\Delta g D_{50}^3}\frac{\tau_b}{|\tau_b|} \tag{D.8}$$

D.5.2 Morphodynamic sensitivity

Figure D.8 shows the cross-shore profile development predicted by the XBeach-G model with the Van Rijn transport equation (solid orange lines) and by the XBeach-G model with the Wong and Parker transport equation (dashed orange lines) for all 10 storm events discussed in Chapter 5. The figure shows that the Wong and Parker transport equation gives quite reasonable model predictions compared to the observations, the Van Rijn model, and the Meyer-Peter and Müller model upon which it is based. Given the similarity between the Wong and Parker equation and the Van Rijn equation in terms of the bed load transport gradient relative to θ, this results is not entirely surprising. However, in a quantitative sense the computed BSS of the Wong and Parker transport equation (Table D.2) is lower than that of the Van Rijn transport equation (Table 5.2).

	RMSE	Rel. bias	ρ	BSS (qualifier†)
BAB3	0.26 m	-0.03	0.40	-0.86 (bad)
CB1	1.63 m	-3.30	0.56	-6.27 (bad)
SS2	0.54 m	-3.72	0.88	-8.63 (bad)
CB2a	1.86 m	-2.99	0.78	-8.13 (bad)
CB2b	1.01 m	-0.51	1.00	0.81 (excellent)
CB2c	1.03 m	-0.54	0.99	0.78 (good)
CB2d	1.39 m	-0.98	0.98	0.23 (poor)
BABR	0.17 m	0.10	0.66	-0.10 (bad)
SS3	1.22 m	-1.00	0.94	-0.51 (bad)
BAE9	1.20 m	-0.32	0.34	-12.31 (bad)
LB5	0.06 m	-0.24	0.99	0.96 (excellent)
BAE10	0.83 m	-0.19	0.74	-1.04 (bad)

Table D.3: Root-mean-square error (RMSE), relative bias (Rel. bias), correlation coefficient (ρ) and Brier Skill Score (BSS) of the model cross-shore profile change predictions using the Engelund and Fredsøe transport equation relative to the measured profile change. Note that ST1 is not included in the statistical analysis. † refers to the qualification of Van Rijn et al. (2003).

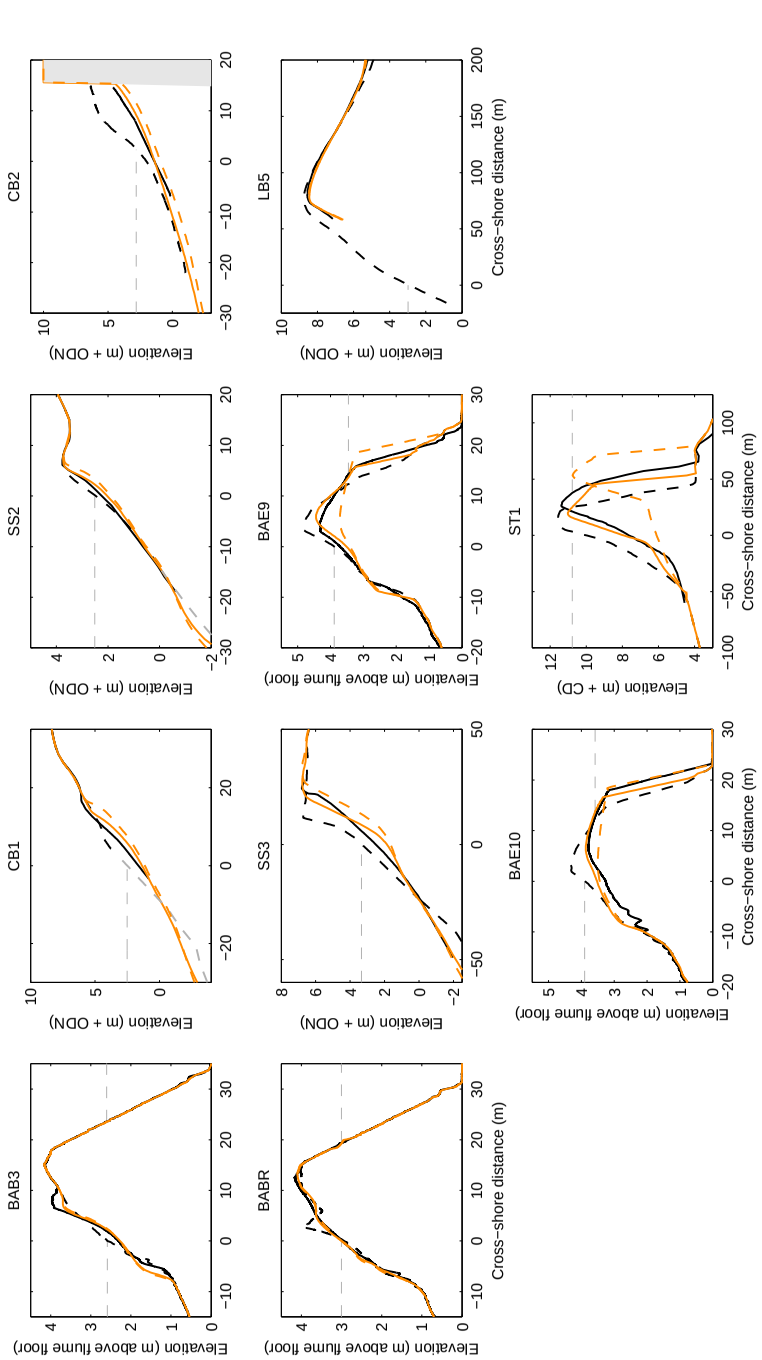

Figure D.8: Sensitivity of modelled cross-shore profile response to sediment transport relations: measured pre-storm (– –) and measured post-storm (—) cross-shore profiles, modelled profiles with the Van Rijn formulation (—) and Wong and Parker transport relation (– –), and maximum still water level (– –).

D.6 Conclusions

The results of the sensitivity simulations discussed in this appendix show that the XBeach-G model is sensitive to the choice of the sediment transport relation in the morphodynamic module. The predictive skill of the XBeach-G model is greater when using the Van Rijn transport formulation than when using the Nielsen, Meyer-Peter and Müller, Engelund and Fredsøe, or Wong and Parker transport equations.

	RMSE	**Rel. bias**	ρ	**BSS (qualifier†)**
BAB3	0.18 m	-0.02	0.58	0.14 (poor)
CB1	0.92 m	-1.60	0.85	-1.02 (bad)
SS2	0.23 m	-1.64	0.95	-0.99 (bad)
CB2a	0.92 m	-1.52	0.92	-1.09 (bad)
CB2b	0.29 m	0.06	0.99	0.98 (excellent)
CB2c	0.21 m	-0.08	0.99	0.99 (excellent)
CB2d	0.53 m	-0.34	0.99	0.89 (excellent)
BABR	0.06 m	0.05	0.87	0.87 (excellent)
SS3	0.61 m	-0.49	0.97	0.63 (good)
BAE9	0.41 m	-0.01	0.80	-0.51 (bad)
LB5	0.08 m	-0.23	0.99	0.93 (excellent)
BAE10	0.20 m	0.03	0.93	0.88 (excellent)

Table D.4: Root-mean-square error (RMSE), relative bias (Rel. bias), correlation coefficient (ρ) and Brier Skill Score (BSS) of the model cross-shore profile change predictions using the Wong and Parker transport equation relative to the measured profile change. Note that ST1 is not included in the statistical analysis. † refers to the qualification of Van Rijn et al. (2003).

Appendix E

Sensitivity to groundwater parameters

Chapter 5 (Section 5.7) discusses the effect of including groundwater processes on the simulated morphodynamic response of five gravel barriers to ten storm events. The appendix elaborates upon the findings of Chapter 5 by examining the effect of the first-order groundwater processes (e.g., the exchange of mass between the surface water and groundwater; infiltration and exfiltration) and second-order groundwater processes that act upon sediment mobility (e.g., modification of the bed shear stress through ventilated boundary layer effects and modification of the relative particle weight by through-bed flow). Furthermore, this appendix presents results of the XBeach-G model in the case that the a laminar groundwater flow model is used, instead of the turbulent groundwater model discussed in Section 4.3.2 (Equation 4.9), which leads to larger simulated infiltration and exfiltration velocities.

E.1 Groundwater parameters and bed shear stress

Figure E.1 presents time series of water depth, horizontal velocity, bed shear stress and bed load transport rates computed by the standard XBeach-G model, including all groundwater processes discussed in Chapters 4 and 5 (XBG; orange), by the model using a laminar groundwater model instead of a turbulent groundwater model (LAM; blue), by the model using a turbulent groundwater model, but no second-order groundwater processes related to sediment mobility (NSO; green) and by the model without any groundwater processes (NGW; red). In analogy with Figure 5.14, Figure E.1 presents time at three locations on the barrier (upper surf zone – upper swash) during BAB3. The figure shows that including first-order groundwater processes (XBG, LAM, NSO) groundwater processes in the model leads to lower maximum negative (offshore-directed) bed load transport rates at all three locations (A–C), as well as higher positive (onshore-directed) bed load transport rates in the upper swash zone (locations C). While not apparent for the reduction of offshore bed load transport, the magnitude of the onshore bed load transport in the upper swash zone is increased by the presence of second-order groundwater processes (compare XBG and NSO), as well as by the infiltration rate (compare XBG and LAM), where the laminar groundwater model leads to higher onshore bed load transport rates.

E.2 Groundwater processes and storm morphology

In this section, the effect of groundwater processes on modelled morphodynamics is investigated through sensitivity simulations of the ten storm events discussed in Chapter 5. In contrast with Section 5.6, the results of this sensitivity analysis are grouped per barrier, thus highlighting the effect of differences in grain size and hy-

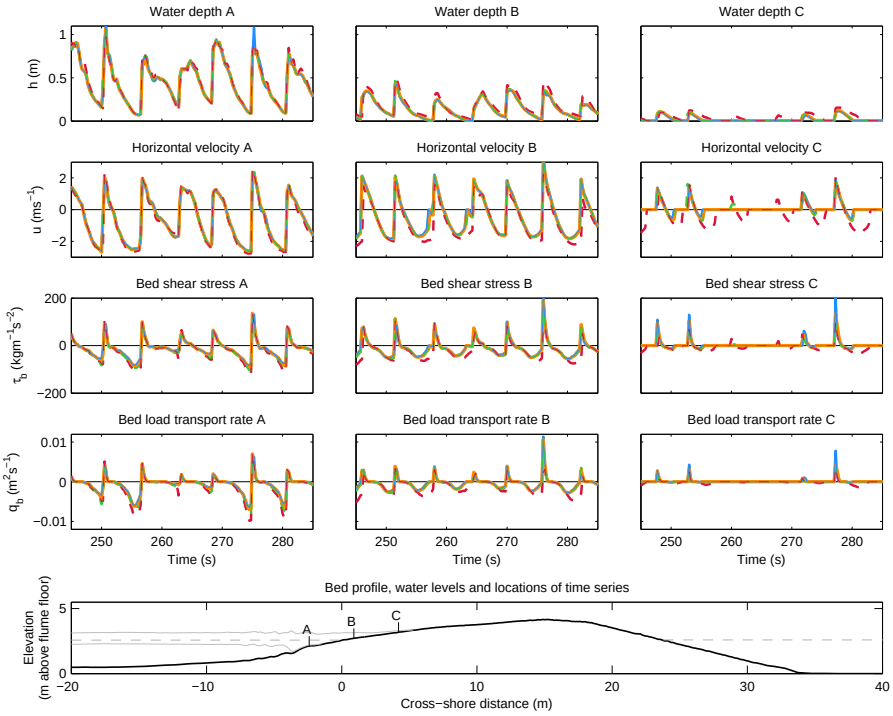

Figure E.1: Time series of water depth, horizontal velocity, bed shear stress and volumetric bed load transport rate computed with XBG (—), LAM (—), NSO (– –) and NGW (– –) at three locations on the barrier (A – upper surf zone; B – lower swash; C – upper swash) during BAB3. The locations of points A, B and C relative to the barrier profile (—) and water levels (– –) are shown in the bottom panel. Note that the simulations presented in this figure are carried out without morphological updating in order to ensure a consistent comparison.

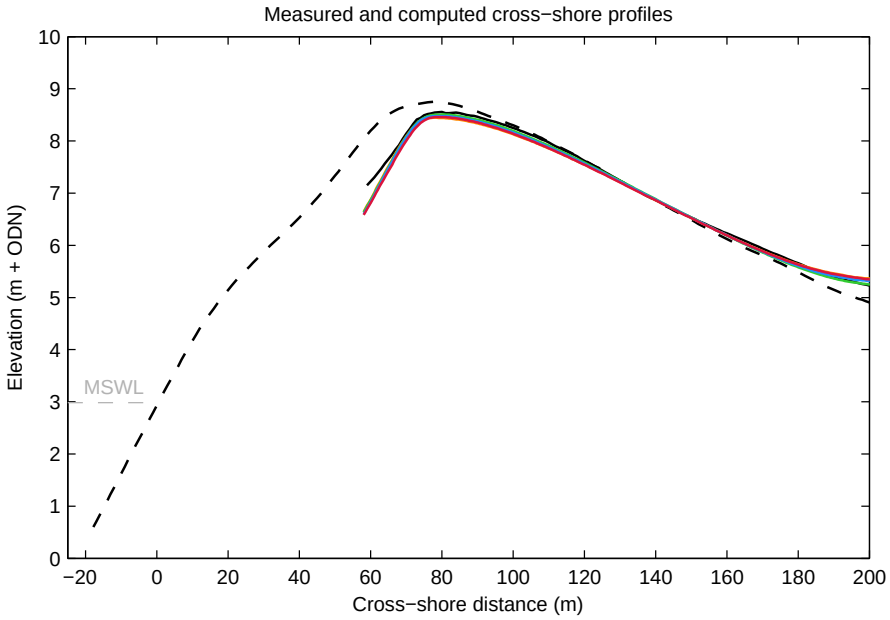

Figure E.2: Pre-storm (– –), measured post-storm (—) and modelled with XBG (—), LAM (—), NSO (—) and NGW (—) cross-shore profiles for LB5, and maximum still water level (– –).

draulic conductivity.

E.2.1 Loe Bar (very fine gravel barrier)

Figure E.2 shows the results of the XBG, LAM, NSO and NGW models for LB5. In this case, the difference between the models is relatively minor due to the low hydraulic conductivity of the barrier, as discussed in Chapter 5. Second-order groundwater processes and the turbulent groundwater model do not substantially increase or lower the predictive skill of the model.

E.2.2 Slapton Sands (fine gravel barrier)

Figures E.3 and E.4 show the results of the XBG, LAM, NSO and NGW models for SS2 and SS3, respectively. The figures show that in these cases, the effects of the second-order groundwater processes (compare XBG and NSO) and turbulent groundwater model (compare XBG and LAM) are relatively minor. However, the inclusion of the first-order groundwater processes is essential to accurately model the observed morphodynamic response of the barrier.

E.2.3 BARDEX (medium gravel barrier)

Figures E.5, E.6, E.7 and E.8 show the results of the XBG, LAM, NSO and NGW models for BAB3, BABR, BAE9 and BAE10, respectively. The figures show that in the case of BAB3 and BABR, the inclusion of the first-order groundwater processes

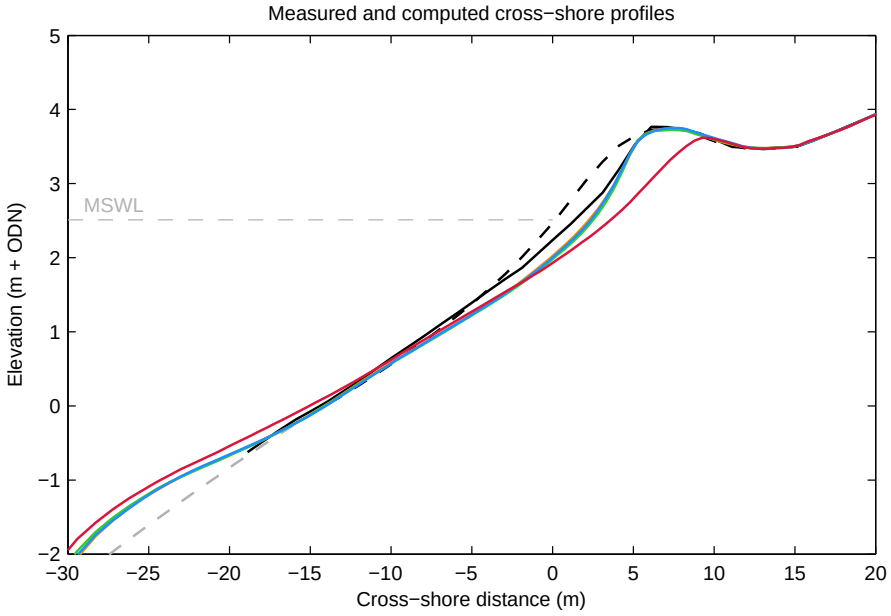

Figure E.3: Pre-storm (– –), measured post-storm (—) and modelled with XBG (—), LAM (—), NSO (—) and NGW (—) cross-shore profiles for SS2, and maximum still water level (– –). The estimated pre-storm profile below the elevation of measurements (– –) is given for comparative purposes.

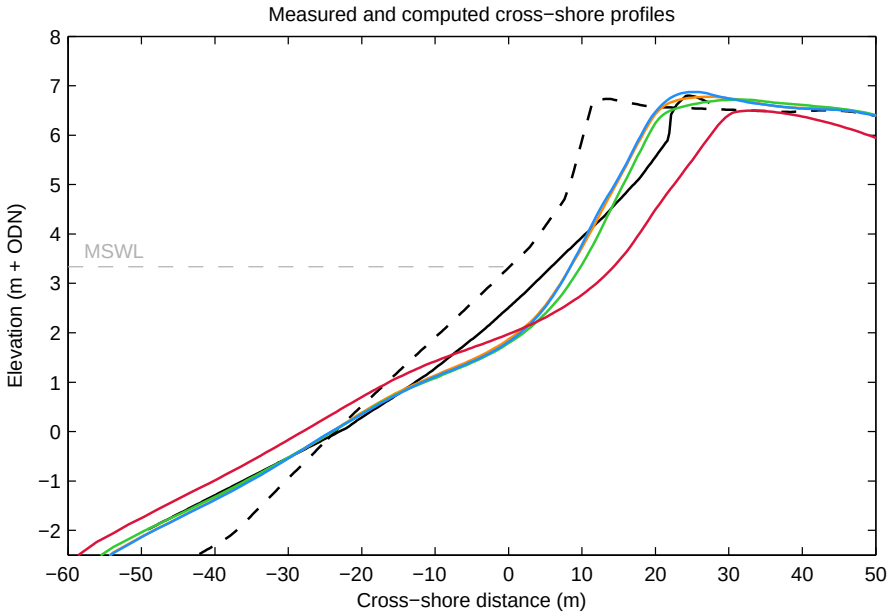

Figure E.4: Pre-storm (– –), measured post-storm (—) and modelled with XBG (—), LAM (—), NSO (—) and NGW (—) cross-shore profiles for SS3, and maximum still water level (– –).

(e.g., XBG, LAM and NSO) allows the model to develop a berm and to increase the level of the crest. The inclusion of second-order processes and the turbulent groundwater model affect the size of the berm in BAB3 and the height of the crest in BABR slightly. However, in the case of BAE9 and BAE10 (Figures E.7 and E.8), there is a distinct difference in the amount of crest lowering between the models with first-order groundwater processes (XBG, LAM and NSO). The figures show that the inclusion of second-order groundwater processes leads to less crest lowering (compare XBG and NSO), and that the increased infiltration (and exfiltration) rate of the LAM model leads to almost no crest lowering at all in the case of BAE9, and less crest lowering in the case of BAE10.

E.2.4 Chesil Beach (very coarse gravel barrier)

Figures E.9 and E.10 show the results of the XBG, LAM, NSO and NGW models for CB13 and CB2, respectively. The figures show that in the case of CB1, the inclusion of groundwater processes allows the model to develop a berm. The effect of the inclusion of second-order processes is very minimal and is less pronounced than the increased berm-building capacity of the laminar groundwater model (compare XBG and LAM). In the case of CB2, the effect of the groundwater model parameters is very limited for reasons discussed in Chapter 5.

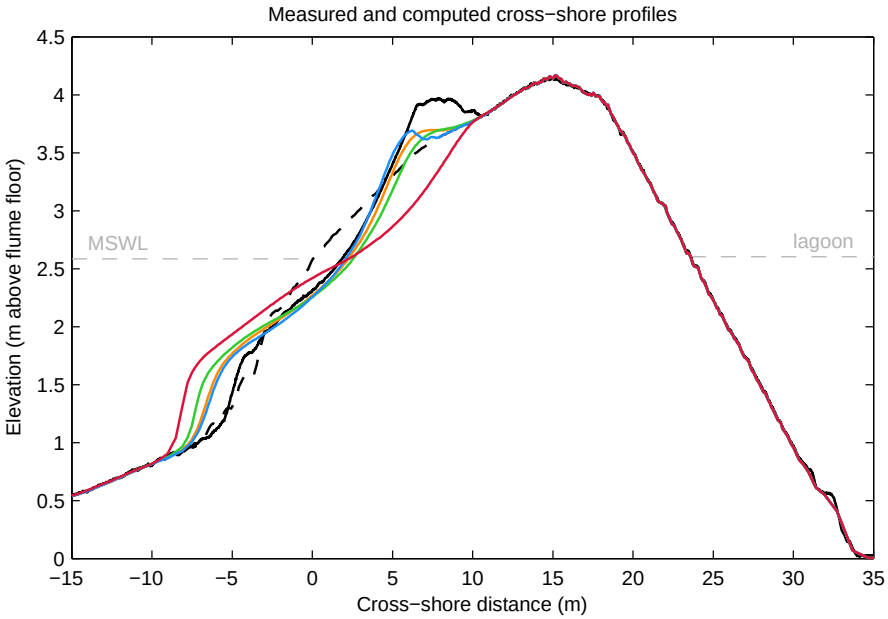

Figure E.5: Initial cross-shore profile (– –) and cross-shore profiles measured (—) and modelled with XBG (—), LAM (—), NSO (—) and NGW (—) at the end of wave series BAB3, and maximum still water level (– –).

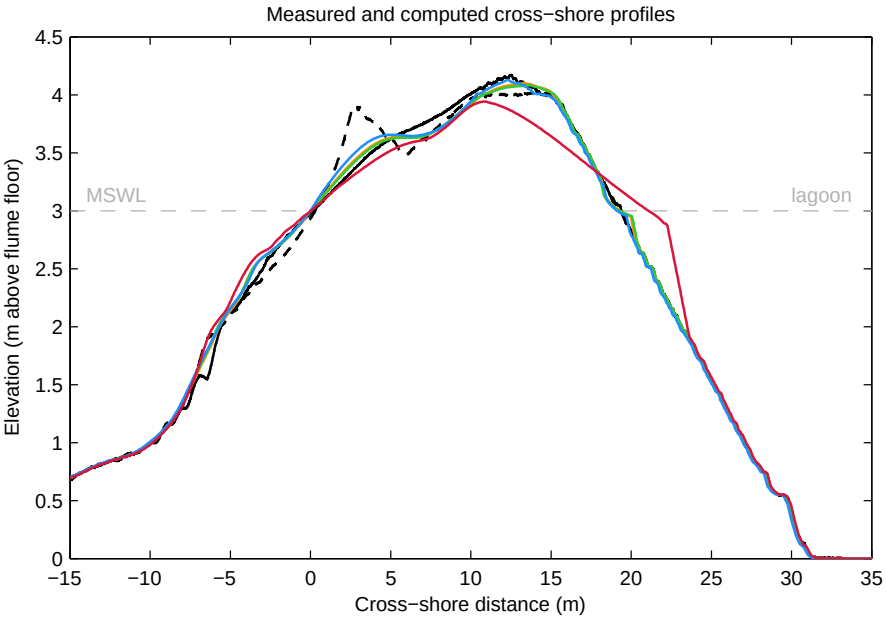

Figure E.6: Initial cross-shore profile (– –) and cross-shore profiles measured (—) and modelled with XBG (—), LAM (—), NSO (—) and NGW (—) at the end of wave series BABR, and maximum still water level (– –).

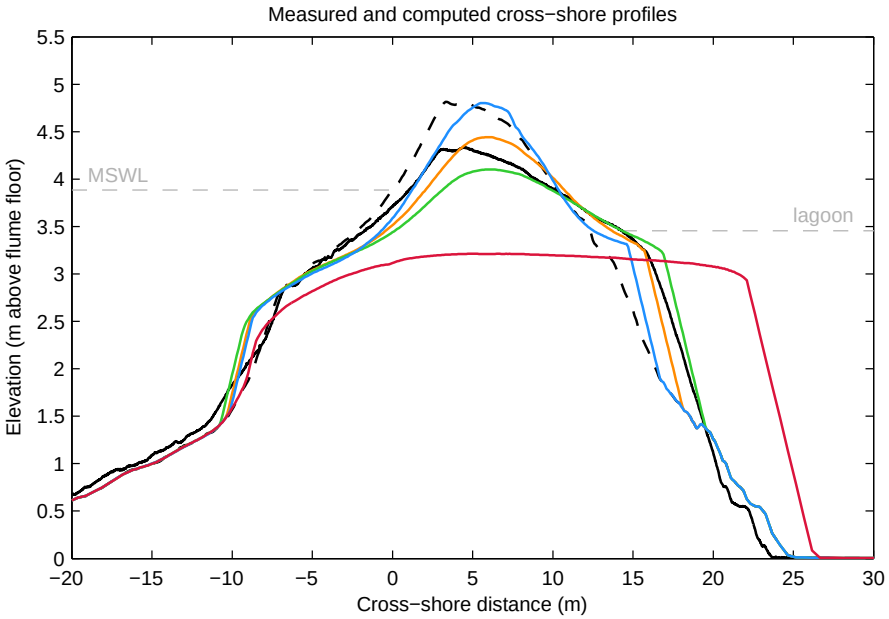

Figure E.7: Initial cross-shore profile (– –) and cross-shore profiles measured (—) and modelled with XBG (—), LAM (—), NSO (—) and NGW (—) at the end of wave series BAE9, and maximum still water level (– –).

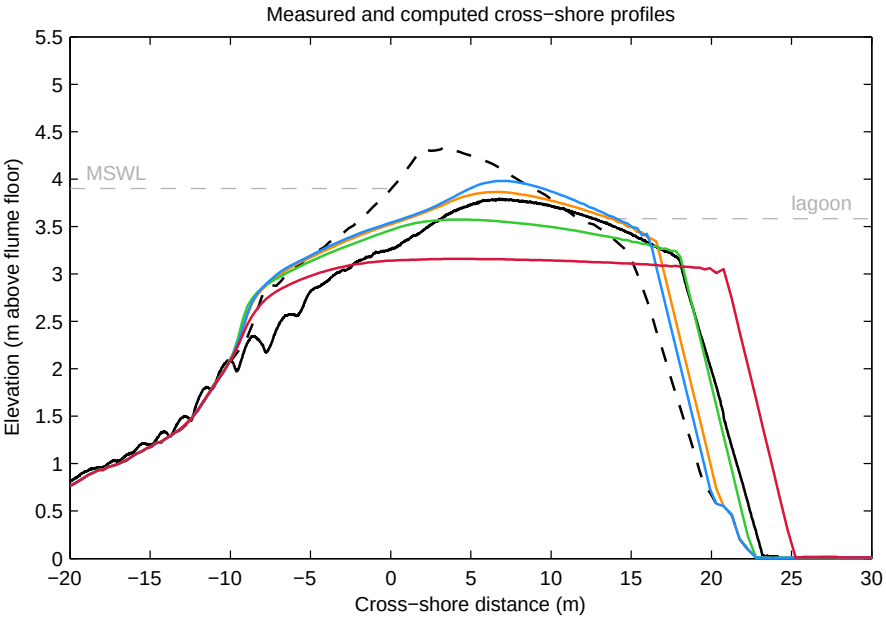

Figure E.8: Initial cross-shore profile (– –) and cross-shore profiles measured (—) and modelled with XBG (—), LAM (—), NSO (—) and NGW (—) at the end of wave series BAE10, and maximum still water level (– –).

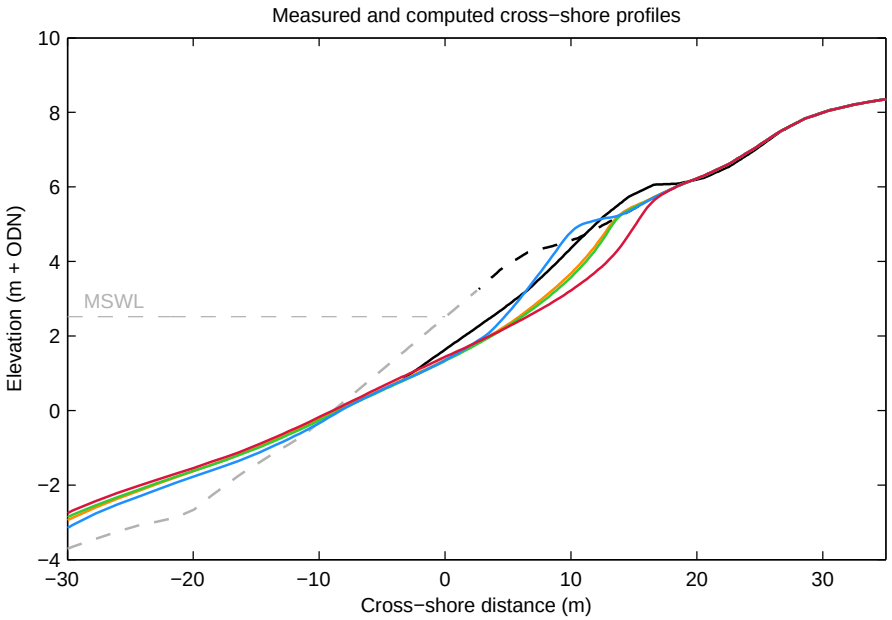

Figure E.9: Pre-storm (– –), measured post-storm (—) and modelled with XBG (—), LAM (—), NSO (—) and NGW (—) cross-shore profiles for CB1, and maximum still water level (– –). The estimated pre-storm profile below the elevation of measurements (– –) is given for comparative purposes.

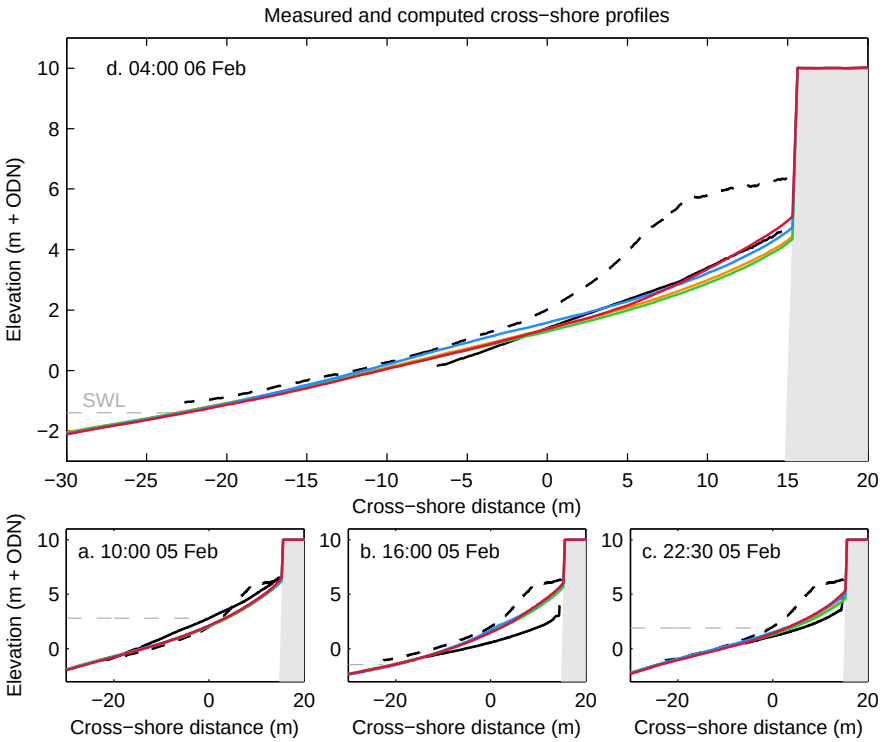

Figure E.10: Pre-storm (– –), measured post-storm (—) and modelled with XBG (—), LAM (—), NSO (—) and NGW (—) cross-shore profiles for CB2 . The top panel shows modelled and measured profiles at low tide after CB2 (d). The bottom three panels show from left to right: modelled and measured profiles at the first high tide of CB2 (a), low tide of CB2 (b) and the second high tide of CB2 (c). The non-erodible sea wall is shown in grey shading (▒). The tide level for each panel is represented by the dashed grey line.

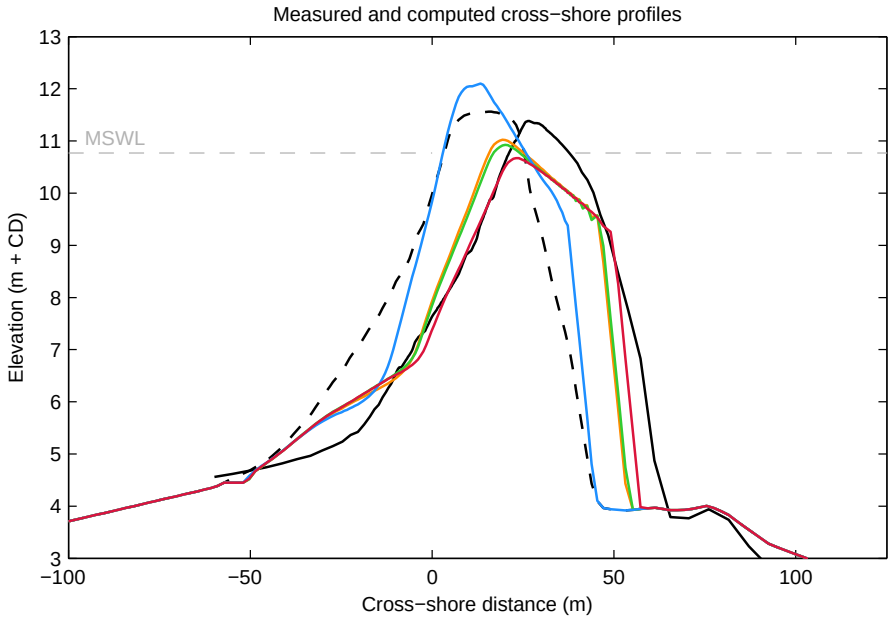

Figure E.11: Pre-storm (– –), measured post-storm (—) and modelled with XBG (—), LAM (—), NSO (—) and NGW (—) cross-shore profiles for ST1, and maximum still water level (– –).

E.2.5 Sillon de Talbert (Cobble barrier)

Figures E.11 shows the results of the XBG, LAM, NSO and NGW models for ST1. In this case, the differences between the XBG, NSO and NGW models are small, for reasons discussed in Chapter 5. However, the greatly increased infiltration and groundwater specific discharge rate of the LAM model allows the barrier to infiltrate more water during swash events (first-order process) and therefore also greater second-order effects on sediment mobility, which result in predicted crest build-up, rather than barrier rollover.

E.3 Conclusions

The results of the sensitivity simulations discussed in this appendix show that the morphodynamic effect of the inclusion of groundwater processes is primarily caused by the by modification of the surface water dynamics through the exchange of mass between the surface water and groundwater, leading to higher onshore-directed and lower offshore-directed bed shear stress and bed load transport rates in the swash (first-order groundwater processes). Ventilated boundary layer effects and the effect of through-bed flow on the submerged particle weight that affect sediment mobility (second-order groundwater processes) are generally of lesser importance in determining the overall cross-shore profile response. The use of a laminar groundwater model to compute infiltration on barriers with high hydraulic conductivity (e.g., BARDEX,

Chesil Beach and Sillon de Talbert in this study) can lead to an overestimation of the resilience of the barrier to storm events.

Appendix F

Sensitivity to the inertia parameter

Chapter 5 (Section 5.8) discusses the effect of variations of the inertia parameter c_i on cross-shore profile development in XBeach-G. The appendix elaborates upon the findings of Chapter 5 by presenting the effect of c_i on all five gravel barriers to the ten storm events discussed in Chapter 5 in sensitivity simulations in which c_i is varied between 0–2.

F.1 Inertia parameter and storm morphology

In this section, the effect of groundwater processes on modelled morphodynamics is investigated through sensitivity simulations of the ten storm events discussed in Chapter 5. In analogy with Appendix E, the results of this sensitivity analysis are grouped per barrier, thus highlighting the effect of differences in grain size.

F.1.1 Loe Bar (very fine gravel barrier)

Figure F.1 shows the results of the inertia parameter sensitivity models for LB5. In this case, the difference between the models is relatively minor due to the small grain size of the barrier, as discussed in Chapter 5.

F.1.2 Slapton Sands (fine gravel barrier)

Figures F.2 and F.3 show the results of the inertia parameter sensitivity models for SS2 and SS3, respectively. The figures show that in these cases, the effects of the inertia parameter is relatively minor, with a slight increase in the computed post-storm beach slope with increasing c_i.

F.1.3 BARDEX (medium gravel barrier)

Figures F.4, F.5, F.6 and F.7 show the results of the inertia parameter sensitivity models for BAB3, BABR, BAE9 and BAE10, respectively. The figures show that in the case of BAB3 and BABR, the model results are relatively insensitive to variations in the inertia parameter. In the case of BAE9 and BAE10 however, the value of the inertia parameter affects quite strongly the computed crest lowering and barrier retreat. As discussed in Section 5.7, the imposed wave and water level conditions during BAE9 and BAE10 were specifically designed to approach the threshold between crest build-up and crest lowering. Since minor changes in the inertia parameter change the amount of onshore and offshore sediment transport in the swash, these changes can lead to differences in the crest level at the start of the simulation. Further changes at the crest are then amplified by negative (through less wave overtopping) or positive (through more wave overtopping) processes, leading to substantial differences in the

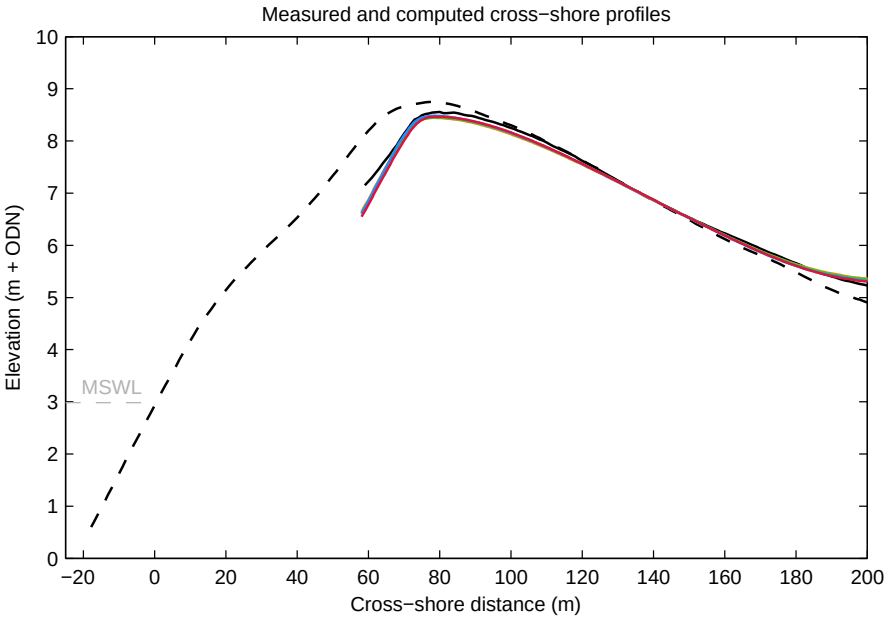

Figure F.1: Pre-storm (– –), measured post-storm (—) and modelled with $c_i = 0.0$ (—), $c_i = 0.5$ (—), $c_i = 1.0$ (—) and $c_i = 2.0$ (—) cross-shore profiles for LB5, and maximum still water level (– –).

final modelled profile.

F.1.4 Chesil Beach (very coarse gravel barrier)

Figures F.8 and F.9 show the results of the inertia parameter sensitivity models for CB13 and CB2, respectively. The figures show that in both cases, the inertia parameter affects the computed post-storm beach slope substantially, where higher values of c_i lead to more uniform beach slopes that are steeper on the lower beach profile and milder on the upper beach profile.

F.1.5 Sillon de Talbert (Cobble barrier)

Figures F.10 shows the results of the inertia parameter sensitivity models for ST1. In this case, the effect of the inertial parameter on the computed post-storm profile is very significant, as discussed in Chapter 5.

F.2 Conclusions

The results of the sensitivity simulations discussed in this appendix show that the sensitivity of the XBeach-G model to the inertia parameter c_i is in the first place strongly dependent on the barrier grain size, and secondly on the hydrodynamic forcing conditions and type of morphodynamic response. The model is relatively insensitive to the value of the inertia parameter c_i for very fine – fine gravel barriers (Loe Bar and Slapton Sands in this study). In the case of medium gravel barriers (BARDEX),

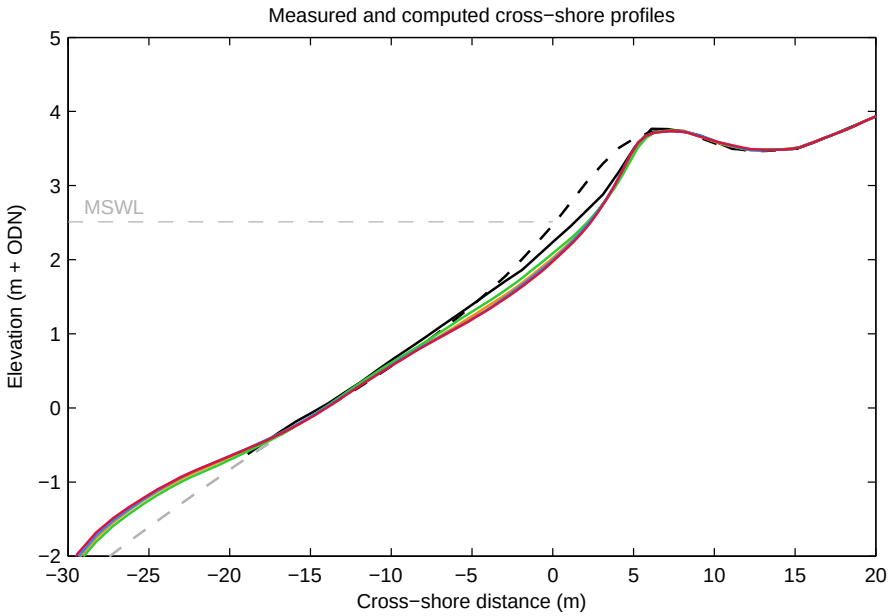

Figure F.2: Pre-storm (– –), measured post-storm (—) and modelled with $c_i = 0.0$ (—), $c_i = 0.5$ (—), $c_i = 1.0$ (—) and $c_i = 2.0$ (—) cross-shore profiles for SS2, and maximum still water level (– –). The estimated pre-storm profile below the elevation of measurements (– –) is given for comparative purposes.

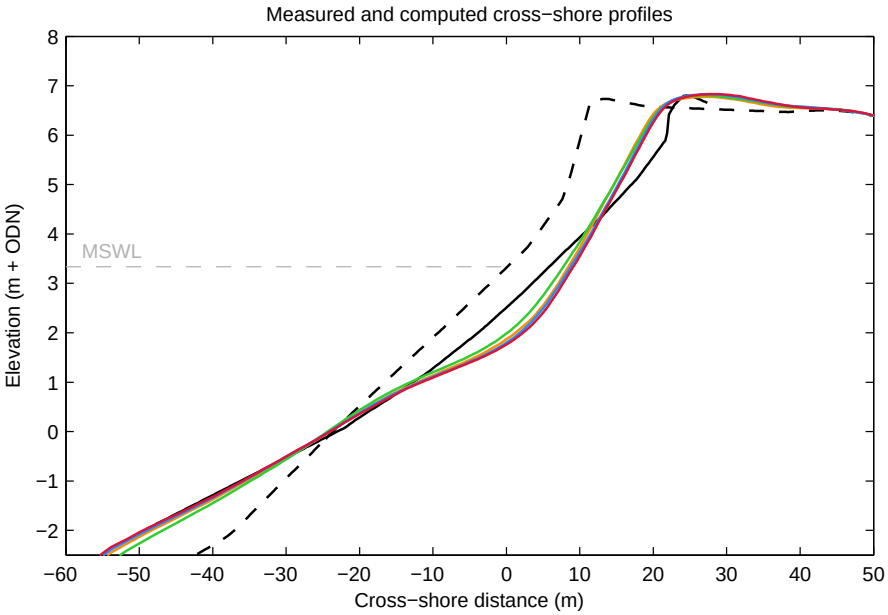

Figure F.3: Pre-storm (– –), measured post-storm (—) and modelled with $c_i = 0.0$ (—), $c_i = 0.5$ (—), $c_i = 1.0$ (—) and $c_i = 2.0$ (—) cross-shore profiles for SS3, and maximum still water level (– –).

the inertia parameter weakly affects the predicted morphodynamic response during less energetic (e.g., berm formation and crest build-up) events, but does affect the morphodynamic response of the barrier during more energetic (e.g., crest lowering and barrier rollover) events more strongly . The inertia parameter strongly affects the morphodynamic prediction on coarse gravel and cobble beaches (Chesil Beach and Sillon de Talbert).

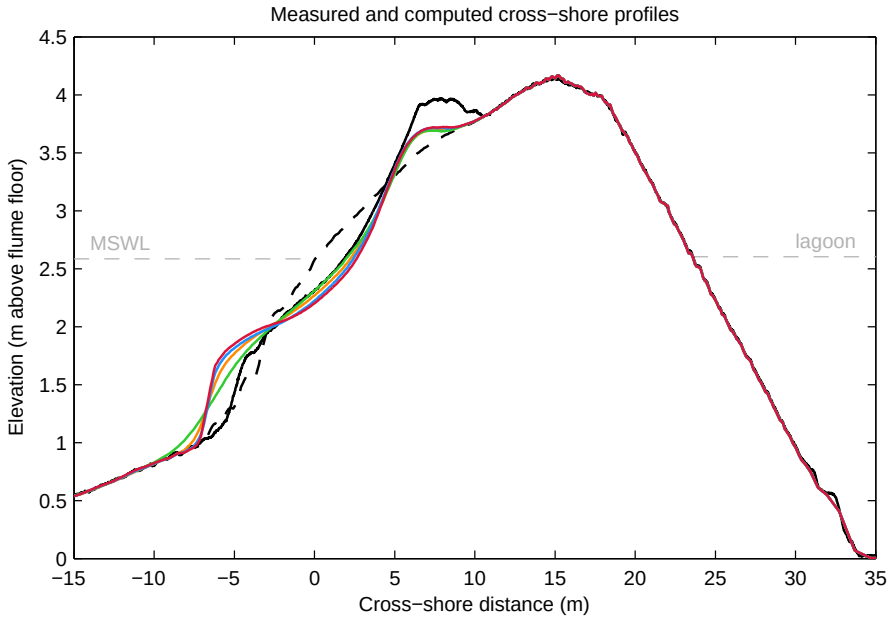

Figure F.4: Initial cross-shore profile (– –) and cross-shore profiles measured (—) and modelled with $c_i = 0.0$ (—), $c_i = 0.5$ (—), $c_i = 1.0$ (—) and $c_i = 2.0$ (—) at the end of wave series BAB3, and maximum still water level (– –).

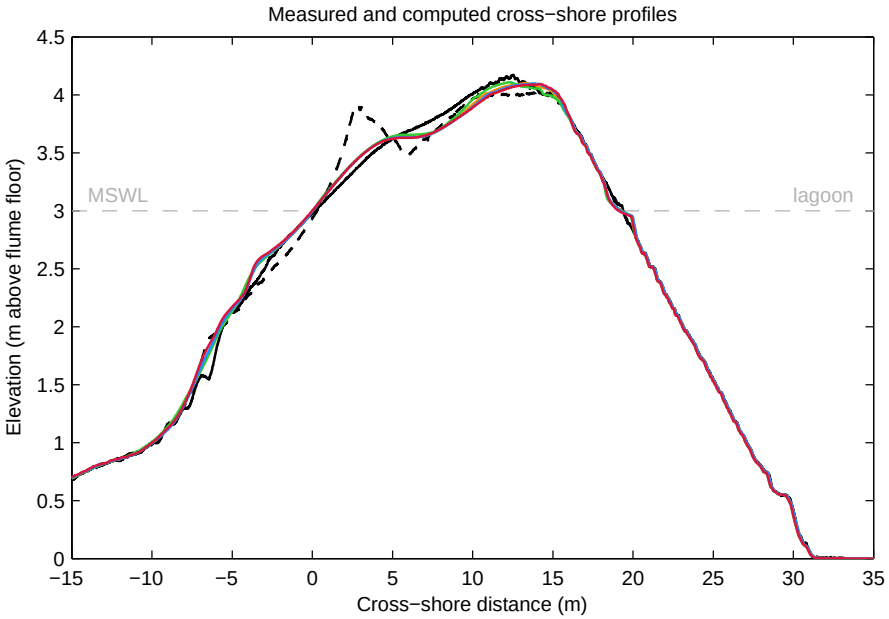

Figure F.5: Initial cross-shore profile (– –) and cross-shore profiles measured (—) and modelled with $c_i = 0.0$ (—), $c_i = 0.5$ (—), $c_i = 1.0$ (—) and $c_i = 2.0$ (—) at the end of wave series BABR, and maximum still water level (– –).

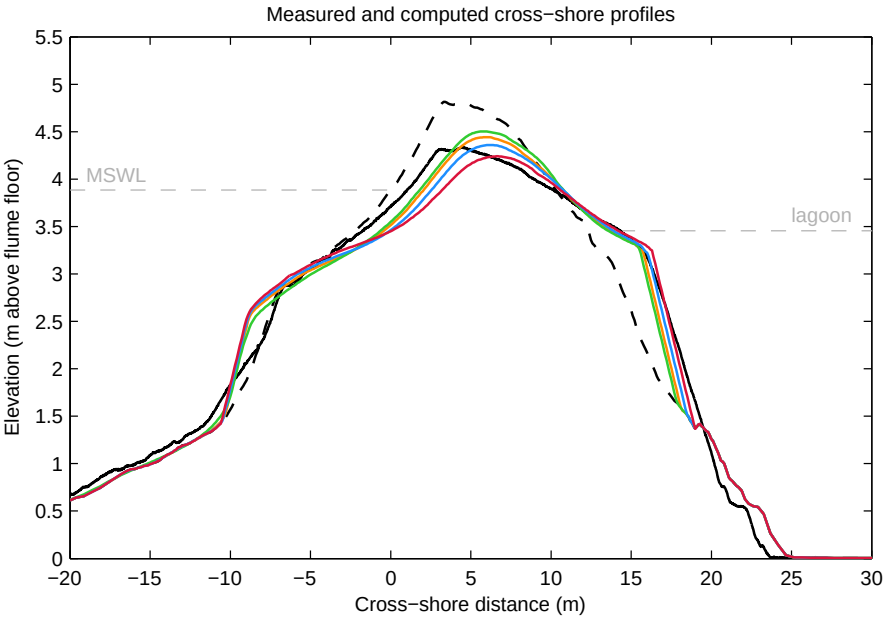

Figure F.6: Initial cross-shore profile (– –) and cross-shore profiles measured (—) and modelled with $c_i = 0.0$ (—), $c_i = 0.5$ (—), $c_i = 1.0$ (—) and $c_i = 2.0$ (—) at the end of wave series BAE9, and maximum still water level (– –).

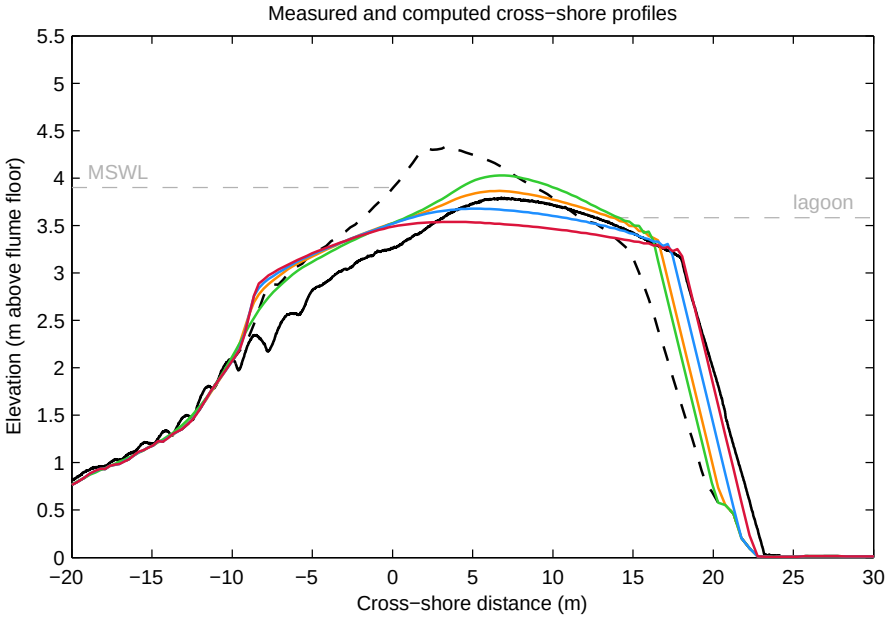

Figure F.7: Initial cross-shore profile (– –) and cross-shore profiles measured (—) and modelled with $c_i = 0.0$ (—), $c_i = 0.5$ (—), $c_i = 1.0$ (—) and $c_i = 2.0$ (—) at the end of wave series BAE10, and maximum still water level (– –).

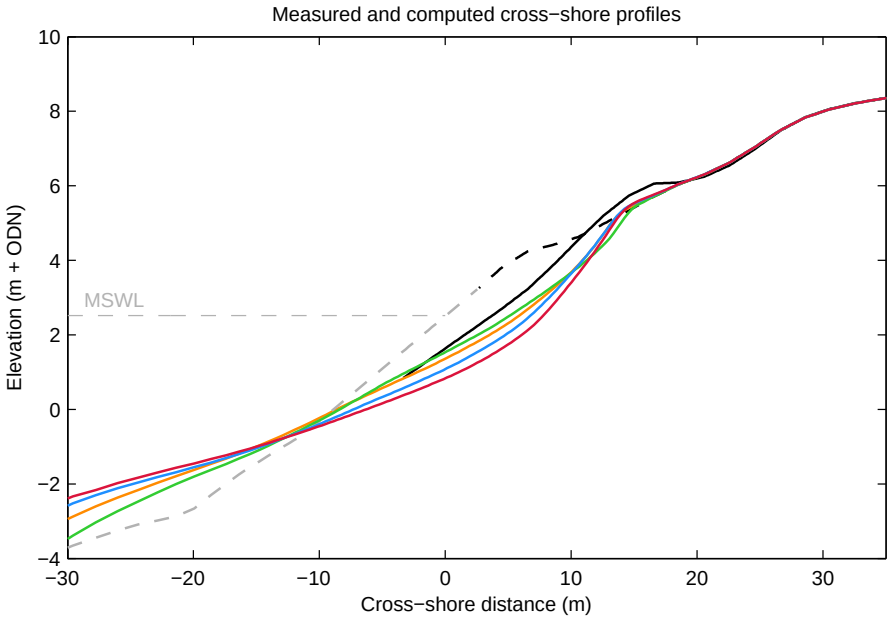

Figure F.8: Pre-storm (– –), measured post-storm (—) and modelled with $c_i = 0.0$ (—), $c_i = 0.5$ (—), $c_i = 1.0$ (—) and $c_i = 2.0$ (—) cross-shore profiles for CB1, and maximum still water level (– –).

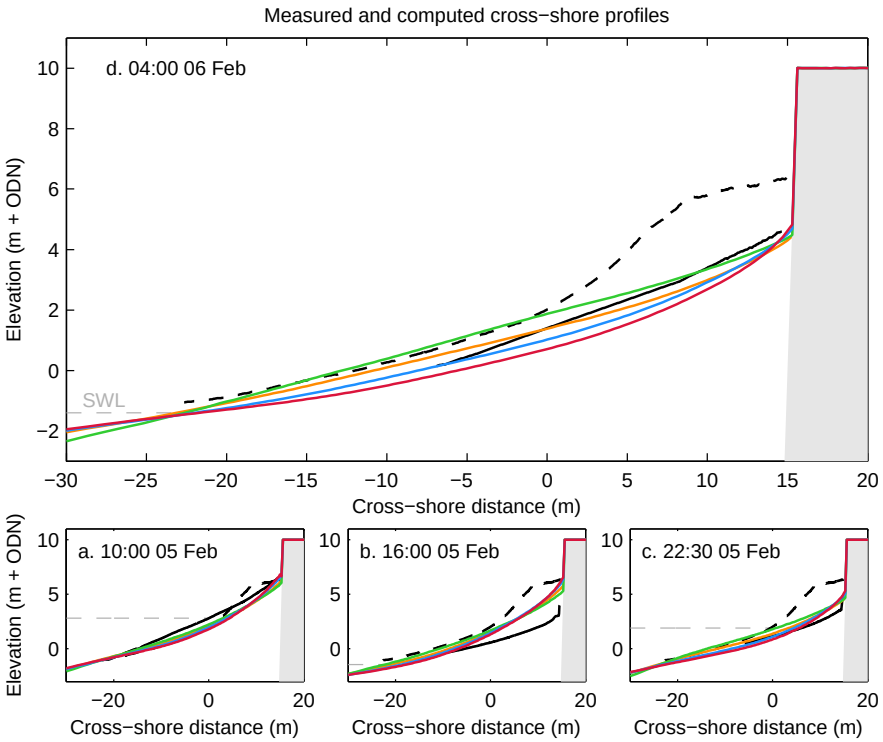

Figure F.9: Pre-storm (– –), measured post-storm (—) and modelled with $c_i = 0.0$ (—), $c_i = 0.5$ (—), $c_i = 1.0$ (—) and $c_i = 2.0$ (—) cross-shore profiles for CB2 . The top panel shows modelled and measured profiles at low tide after CB2 (d). The bottom three panels show from left to right: modelled and measured profiles at the first high tide of CB2 (a), low tide of CB2 (b) and the second high tide of CB2 (c). The non-erodible sea wall is shown in grey shading (▬). The tide level for each panel is represented by the dashed grey line.

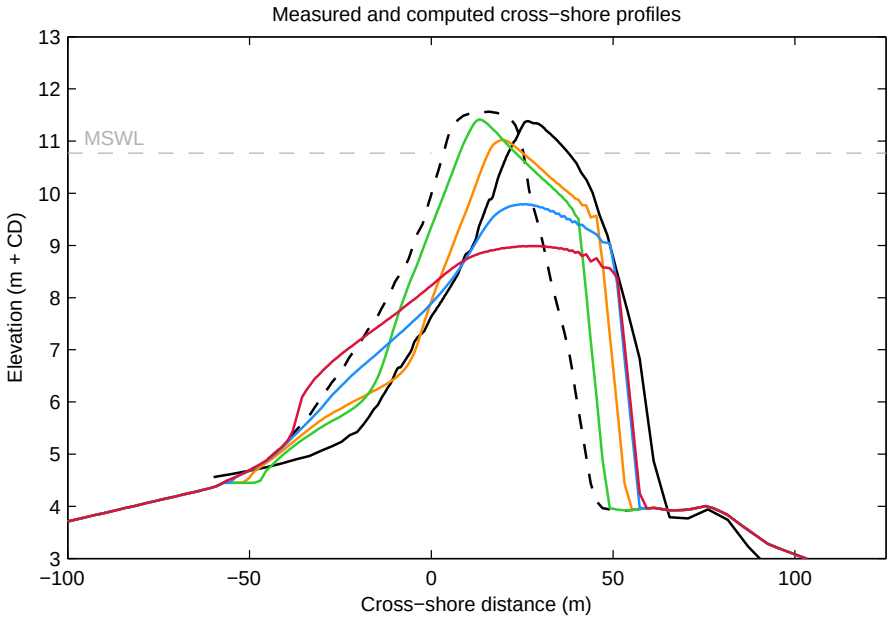

Figure F.10: Pre-storm (– –), measured post-storm (—) and modelled with $c_i = 0.0$ (—), $c_i = 0.5$ (—), $c_i = 1.0$ (—) and $c_i = 2.0$ (—) cross-shore profiles for ST1, and maximum still water level (– –).

Appendix G

Further sensitivity groundwater processes and overwash thresholds

As discussed in Section 6.4, groundwater processes play an important role in the determination of overwash thresholds on gravel barriers. The analysis in Section 6.4 was carried out using identical barrier crest heights and potential wave run-up values, and hence OP and RPRF values, in the XBeach-G and NGW model simulations in order to facilitate direct comparisons. However, since infiltration processes affect (lower) wave run-up levels, the OP in the NGW model simulations in Section 6.4 was in reality higher than the OP used in the analysis, which were based on the model results of the XBeach-G model, which includes groundwater processes. In this appendix, the analysis of Section 6.4 is repeated for the NGW model simulations for the academic case in which the crest level is modified (increased) to account for higher wave run-up levels in the NGW model. Crest levels applied in the current analysis for the NGW model were computed by re-simulating the potential wave run-up models of Section 6.3.1 using the NGW model.

The results of the analysis of the effect of groundwater processes on barrier crest morphology including the increased crest levels in the NGW model are shown in Figure G.1. The figure shows that due to the increased crest level in the NGW model simulations, the absolute differences between the XBeach-G and NGW model results are slightly smaller than those found in Section 6.4 (Figure 6.14 on page 143), although the general trend is very similar. Again, it is noted that if the results of this appendix are used in future analysis, users of the data should account for different methods in which the OP is computed in the XBeach-G and NGW model simulations, and that no one-to-one comparison can be made in terms of barrier crest elevation.

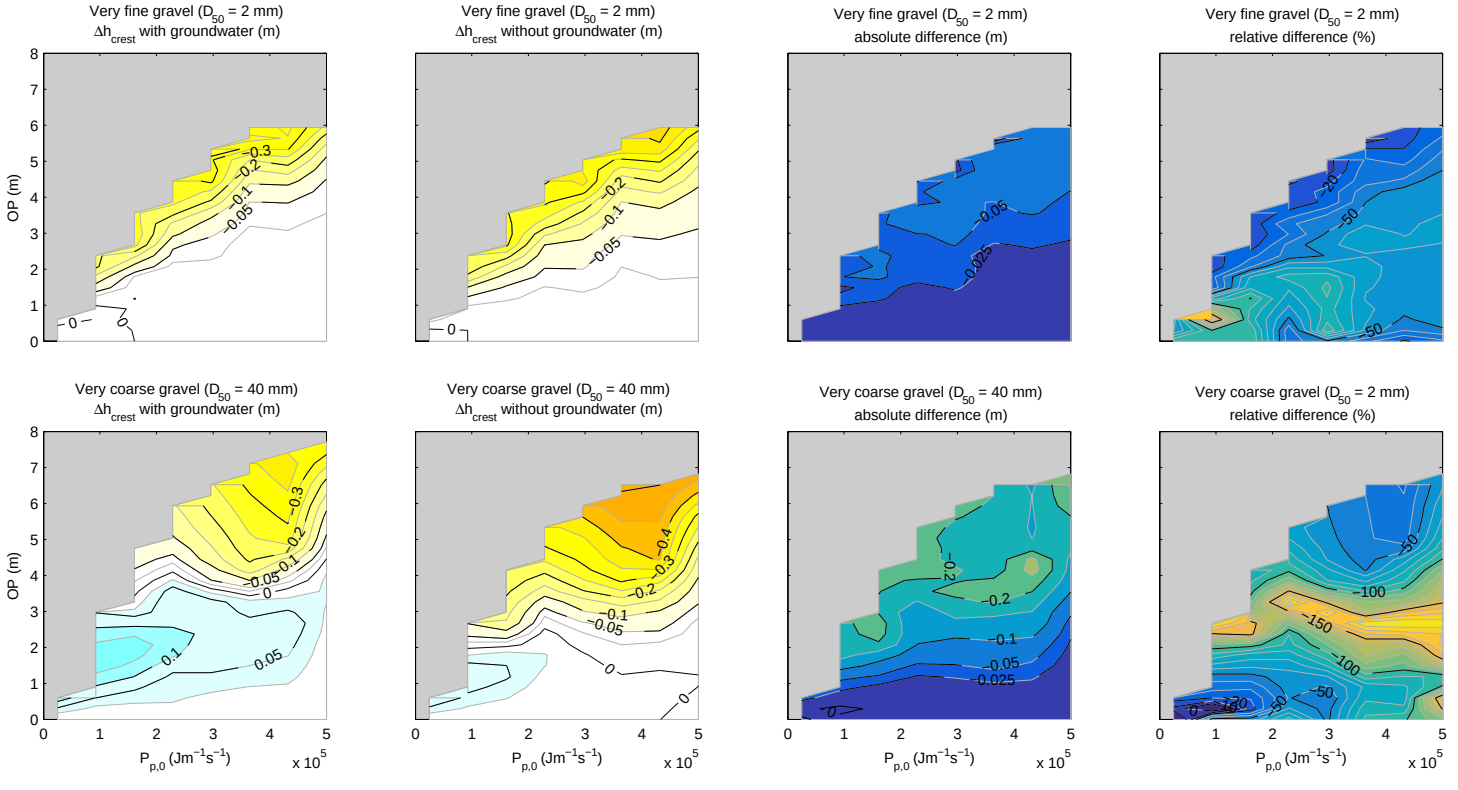

Figure G.1: Effect of including groundwater effects in the computed crest level change as a function of the OP (including groundwater effects on wave run-up levels), incident wave energy flux and grain size, shown for barriers with 10 m crest width. In the leftmost two columns, hot colours indicate crest lowering and cool colours indicate crest build-up. In the absolute and relative difference plots, negative values indicate that the crest of the model without groundwater is lower than the model with groundwater. Grey represents areas without data.

List of references

Adams, H., Williams, A., Xu, C., Rauscher, S., Jiang, X., McDowell, N., 2013. Empirical and process-based approaches to climate-induced forest mortality models. Frontiers in Plant Science 4 (438).

Ahrens, J., 1990. Dynamic revetments. In: Proceedings of 22nd Conference on Coastal Engineering, Delft, The Netherlands. pp. 1837–1850.

Almeida, L., Masselink, G., Russell, P., Davidson, M., 2015. Observations of gravel beach dynamics during high energy wave conditions using a laser scanner. Geomorphology 228 (0), 15 – 27.
URL http://www.sciencedirect.com/science/article/pii/S0169555X14004279

Almeida, L., Masselink, G., Russell, P., Davidson, M., Poate, T., McCall, R., Blenkinsopp, C., Turner, I., 2013. Observations of the swash zone on a gravel beach during a storm using a laser-scanner. Journal of Coastal Research Proceedings 12th International Coastal Symposium (Plymouth, England). Special Issue No. 65., 636–641.

Aminti, P., Cipriani, L. E., Pranzini, E., 2003. 'Back to the Beach': Converting Seawalls into Gravel Beaches. In: Goudas, C., Katsiaris, G., May, V., Karambas, T. (Eds.), Soft Shore Protection. Vol. 7 of Coastal Systems and Continental Margins. Springer Netherlands, pp. 261–274.

Anthony, E., 2008. Shore Processes and their Palaeoenvironmental Applications. Developments in Marine Geology. Elsevier Science, Ch. Gravel Beaches and Barriers, pp. 289–324.
URL https://books.google.nl/books?id=gwfbUoRztOYC

Ardhuin, F., Accensi, M., 2011. Etats de mer et agitation sur le fond dans la sous-région marine manche, mer du nord dcsmm/ei/mmn. ref. dcssm/ei/ee/mmn /1.1.7/2011. Tech. rep., Ministère de l'Ecologie du Développement Durable des Transports et du Logement.

Austin, M., 2005. Swash, groundwater and sediment transport processes on a gravel beach. Ph.D. thesis, Loughborough University.

Austin, M., Masselink, G., 2005. Infiltration and exfiltration on a steep gravel beach: Implications for sediment transport. In: Coastal Dynamics. No. 101.

Austin, M., Masselink, G., 2006a. Observations of morphological change and sediment transport on a steep gravel beach. Marine Geology 229, 59–77.

Austin, M., Masselink, G., 2006b. Swash-groundwater interaction on a steep gravel beach. Continental Shelf Research 26 (20), 2503 – 2519.

URL http://www.sciencedirect.com/science/article/pii/S0278434306002809

Austin, M. J., Buscombe, D., 2008. Morphological change and sediment dynamics of the beach step on a macrotidal gravel beach. Marine Geology 249 (3–4), 167–83.
URL http://www.sciencedirect.com/science/article/pii/S0025322707002940

Austin, M. J., Masselink, G., McCall, R. T., Poate, T. G., 2013. Groundwater dynamics in coastal gravel barriers backed by freshwater lagoons and the potential for saline intrusion: Two cases from the UK. Journal of Marine Systems 123-124 (0), 19 – 32.
URL http://www.sciencedirect.com/science/article/pii/S0924796313000870

Austin, M. J., Masselink, G., Russell, P. E., Turner, I. L., Blenkinsopp, C. E., 2011. Alongshore fluid motions in the swash zone of a sandy and gravel beach. Coastal Engineering 58 (8), 690–705.
URL http://www.sciencedirect.com/science/article/pii/S0378383911000391

Bagnold, R., 1940. Beach formation by waves; some model-experiments in a wave tank. Journal of the ICE 15, 27–52.

Bagnold, R., 1966. An approach to the sediment transport problem from general physics. Tech. Rep. Geological Survey Professional Paper 422-I, U.S. Geological Survey.

Baldock, T. E., Barnes, M., Hughes, M. G., 2005. Field observations of instantaneous cross-shore free surface profiles and flow depths in the swash zone.

Battjes, J. A., 1974. Surf similarity. In: 14th International Conference on Coastal Engineering. Vol. Volume I, Chapter 26. Copenhagen, pp. 467–479.

Battjes, J. A., Bakkenes, H. J., Janssen, T. T., van Dongeren, A. R., 2004. Shoaling of subharmonic gravity waves. Journal of Geophysical Research 109 (C02009), 1–15.

Bear, J., 1972. Dynamics of Fluids in Porous Media. Dover Civil and Mechanical Engineering Series. Dover.

Bluck, B. J., 1967. Sedimentation of beach gravels: examples from South Wales. Journal of Sedimentary Research 37 (1).

Boersma, S. M., Hoenderkamp, K., 2003. Tregor, final report. Tech. rep., IFREMER.

Bosboom, J., Reniers, A., Luijendijk, A., 2014. On the perception of morphodynamic model skill. Coastal Engineering 94, 112–125.
URL http://www.sciencedirect.com/science/article/pii/S0378383914001604

Bradbury, A., 1998. Response of shingle barrier beaches to extreme hydrodynamic conditions. Ph.D. thesis, University of Southampton.

Bradbury, A., Cope, S., Prouty, D., 2005. Predicting the response of shingle barrier beaches under extreme wave and water level conditions in southern england. In: Proc. 5th International Coastal Dynamics Conference, Barcelona, Spain.

Bradbury, A., Powell, K. A., 1992. The short-term profile response of shingle spits to storm wave action. In: Proc. 23rd International Conference on Coastal Engineering. pp. 2694–2707.

Bradbury, A., Stratton, M., Mason, T., 2011. Impacts of wave climate with bi-modal wave period on the profile response of gravel beaches. In: Proceedings of Coastal Sediments. Vol. 3. World Scientific, pp. 2004–2018.

Bradbury, A. P., 2000. Predicting breaching of shingle barrier beaches - recent advances to aid beach management. In: Papers and Proceedings 35th MAFF (DEFRA) Conference of River and Coastal Engineers. pp. 05.3.1 – 05.3.13.

Brocchini, M., Baldock, T. E., 2008. Recent advances in modeling swash zone dynamics: Influence of surf-swash interaction on nearshore hydrodynamics and morphodynamics. Reviews of Geophysics 46 (3).
URL http://dx.doi.org/10.1029/2006RG000215

Buscombe, D., Masselink, G., 2006. Concepts in gravel beach dynamics. Earth-Science Reviews 79, 33–52.
URL http://www.sciencedirect.com/science/article/pii/S0012825206000791

Butt, T., Russell, P., Turner, I., 2001. The influence of swash infiltration-exfiltration on beach face sediment transport: onshore or offshore? Coastal Engineering 42 (1), 35 – 52.
URL http://www.sciencedirect.com/science/article/pii/S0378383900000466

Calantoni, J., Holland, K. T., Drake, T. G., 2004. Modelling sheet-flow sediment transport in wave-bottom boundary layers using discrete-element modelling. Philosophical Transactions - Royal Society of London Series A Mathematical Physical and Engineering Sciences 362, 1987–2002.

Carr, A., 1974. Differential movement of coarse sediment particles. In: Proceedings of 14th Conference on Coastal Engineering, Copenhagen, Denmark. pp. 851–870.
URL https://icce-ojs-tamu.tdl.org/icce/index.php/icce/article/view/2944

Carrier, W., I., 2003. Goodbye, hazen; hello, kozeny-carman. Journal of Geotechnical and Geoenvironmental Engineering 129 (11), 1054–1056.
URL http://dx.doi.org/10.1061/(ASCE)1090-0241(2003)129:11(1054)

Carter, R., Orford, J., 1984. Coarse clastic barrier beaches: a discussion of the distinctive dynamic and morphosedimentary characteristics. Marine Geology 60, 377–389.

Carter, R., Orford, J., 1993. The morphodynamics of coarse clastic beaches and barriers: a short-and long-term perspective. Journal of Coastal Research, 158–179.

Chanson, H., 2006. The Sillon de Talbert, Cotes d'Armor, North Brittany, France. Shore & Beach 74 (3), 26–27.

Cienfuegos, R., Barthélemy, E., , Bonneton, P., 2010. Wave-breaking model for boussinesq-type equations including roller effects in the mass conservation equation. Journal of Waterway, Port, Coastal, and Ocean Engineering 136 (1), 10–26.
URL http://dx.doi.org/10.1061/(ASCE)WW.1943-5460.0000022

Clarke, S., Dodd, N., Damgaard, J., 2004. Modeling flow in and above a porous beach. Journal of Waterway, Port, Coastal, and Ocean Engineering 130 (5), 223–233.

Coduto, D., 1999. Geotechnical Engineering Principles and Practices. Prentice-Hall, Englewood Cliffs, NJ.
URL http://www.fhwa.dot.gov/engineering/geotech/pubs/05037/05d.cfm

Conley, D. C., Inman, D. L., 1994. Ventilated oscillatory boundary layers. Journal of Fluid Mechanics 273, 261–284.

Cope, S., 2005. Predicting overwashing and breaching of coarse-clastic barrier beaches and spits - application to medmerry, west sussex, southern england. In: Proc. 5th International Coastal Dynamics Conference, Barcelona, Spain.

Cowell, P. J., Stive, M. J., Niedoroda, A. W., de Vriend, H. J., Swift, D. J., Kaminsky, G. M., Capobianco, M., 2003. The coastal-tract (part 1): a conceptual approach to aggregated modeling of low-order coastal change. Journal of Coastal Research, 812–827.

Cowell, P. J., Thom, B., 1994. Morphodynamics of coastal evolution. In: Carter, R., Woodroffe, C. (Eds.), Coastal Evolution. Cambridge University Press, Cambridge, UK, pp. 33–86.

Dally, W., Dean, R., 1986. Transformation of random breaking waves on surf beat. In: Proceedings of 20th Conference on Coastal Engineering, Taipei, Taiwan. pp. 109–123.

Damgaard, J., Soulsby, R., 1996. Longshore bed-load transport. In: Proceedings of 25th Conference on Coastal Engineering, Orlando, Florida.

Darcy, H., 1856. Les fontaines publiques de la ville de Dijon. Tech. rep., Dalmont, Paris.

de Alegria-Arzaburu, A. R., Masselink, G., 2010. Storm response and beach rotation on a gravel beach, Slapton Sands, U.K. Marine Geology 278 (1–4), 77–99.
URL http://www.sciencedirect.com/science/article/pii/S0025322710002525

De Vet, P., 2014. Modelling sediment transport and morphology during overwash and breaching events. Master's thesis, Delft University of Technology and National University of Singapore.
URL http://resolver.tudelft.nl/uuid:d4e21d44-fcef-498b-b2e5-83df3b0e0c47

De Vriend, H. J., 1991. Mathematical modelling and large-scale coastal behaviour. Journal of Hydraulic Research 29 (6), 727–740.
URL http://dx.doi.org/10.1080/00221689109498955

De Vriend, H. J., 1998. On the predictability of coastal morphology. In: Proceedings 3rd Marine Science and Technology Conference, Luxemburg. pp. 289–300.

Dean, R., 1977. Equilibrium beach profiles: U.S. Atlantic and Gulf coasts. Dept. of Civil Engineering and College of Marine Studies, University of Delaware, Newark.

DEFRA, 2008. Understanding barrier beaches. R&D Technical Report FD1924/TR. Tech. rep., DEFRA.

DEFRA, 2010. Charting the progress 2: the state of UK seas. London.

Deltares, 2015. XBeach manual. Tech. rep., Deltares.

Den Heijer, C., 2013. The role of bathymetry, wave obliquity and coastal curvature in dune erosion prediction. Ph.D. thesis, Delft University of Technology.

Drake, T. G., Calantoni, J., 2001. Discrete particle model for sheet flow sediment transport in the nearshore. Journal of Geophysical Research: Oceans 106 (C9), 19859–19868. URL http://dx.doi.org/10.1029/2000JC000611

Duncan, J. R. J., 1964. The effects of water table and tide cycle on swash-backwash sediment distribution and beach profile development. Marine Geology 2 (3), 186–197. URL http://www.sciencedirect.com/science/article/pii/0025322764900398

Engelund, F., Fredsøe, J., 1976. A sediment transport model for straight alluvial channels. Nordic Hydrology 7 (5), 293–306.

Environment Agency, 2009. Investing for the future: Flood and coastal risk management in England: A long-term investment strategy.

Ergun, S., 1952. Fluid flow through packed columns. Chemical Engineering Progress 48, 88–94.

Etienne, S., Paris, R., 2010. Boulder accumulations related to storms on the south coast of the Reykjanes Peninsula (Iceland). Geomorphology 114, 55 – 70, rock Coast Geomorphology. URL http://www.sciencedirect.com/science/article/pii/S0169555X09000749

Fetter, C. W., 1988. Applied Hydrology. Merrill Publishing Company.

Forchheimer, P., 1901. Wasserbewegung durch boden. Zeitschrift des Vereines Deutscher Ingenieure 45 (1782), 1788.

Fredsøe, J., Deigaard, R., 1992. Mechanics of Coastal Sediment Transport. Advanced Series on Ocean Engineering, Vol.3. World Scientific, Singapore.

Frizell, K., Ruff, J., Mishra, S., 1998. Simplified design guidelines for riprap subjected to overtopping flow. In: Proceedings of the Annual Conference of the Association of State Dam Safety Officials, Las Vegas, Nevada, USA. pp. 301–312.

Fuller, R., Randall, R., 1988. The orford shingles, suffolk, uk - classic conflicts in coastline management. Biological Conservation 46 (2), 95 – 114.
URL http://www.sciencedirect.com/science/article/pii/0006320788900948

Galapatti, R., Vreugdenhil, C., 1985. A depth-integrated model for suspended sediment transport. Journal of Hydraulic Research 23 (4), 359–377.

Garcia, M., Parker, G., 1991. Entrainment of bed sediment into suspension. Journal of Hydraulic Engineering 117 (4), 414–435.
URL http://dx.doi.org/10.1061/(ASCE)0733-9429(1991)117:4(414)

Grant, U., 1948. Influence of the water table on beach aggradation and degradation. Journal of Marine Research 7, 655–660.

Gu, Z., Wang, H., 1991. Gravity waves over porous bottoms. Coastal Engineering 15, 497 – 524.
URL http://www.sciencedirect.com/science/article/pii/037838399190025C

Guza, R. T., Inman, D. L., 1975. Edge waves and beach cusps. Journal of Geophysical Research 80 (21), 2997–3012.
URL http://dx.doi.org/10.1029/JC080i021p02997

Halford, K., 2000. Simulation and interpretation of borehole flowmeter results under laminar and turbulent flow conditions. In: Proceedings of the Seventh International Symposium on Logging for Minerals and Geotechnical Applications, Golden, Colorado. The Minerals and Geotechnical Logging Society, pp. 157–168.

Harbaugh, A., 2005. Modflow-2005, the u.s. geological survey modular ground-water model - the ground-water flow process. In: U.S. Geological Survey Techniques and Methods. Vol. 6-A16. U.S. Geological Survey.

Hardisty, J., Collier, J., Hamilton, D., 1984. A calibration of the Bagnold beach equation. Marine Geology 61 (1), 95–101.
URL http://www.sciencedirect.com/science/article/pii/0025322784901105

Hattori, M., Kawamata, R., 1980. Onshore-offshore transport and beach profile change. In: Proceedings of 17th Conference on Coastal Engineering, Sydney, Australia. Vol. 1. pp. 1175–1193.

Hazen, A., 1892. Some physical properties of sands and gravels, with special reference to their use in filtration. Pub. Doc. 34, Massachusetts State Board of Health.

Heijne, I., West, G., 1991. Chesil sea defence scheme. paper 2: design of interceptor drain. Proceedings of the Institution of Civil Engineers 90, 799–817.

Hicks, B., Kobayashi, N., Puleo, J., Farhadzadeh, A., 2010. Cross-shore transport on gravel beaches. In: Proceedings of 32nd Conference on Coastal Engineering, Shanghai, China.

Holland, K. T., Puleo, J. A., 2001. Variable swash motions associated with foreshore profile change. Journal of Geophysical Research: Oceans 106 (C3), 4613–4623.
URL http://dx.doi.org/10.1029/1999JC000172

Holman, R., 1986. Extreme value statistics for wave run-up on a natural beach. Coastal Engineering 9 (6), 527–544.

Hook, B. J., Kemble, J. R., Heijne, I. S., Wes, G. M., 1994. Chesil sea defence scheme: Concept, design and construction, and design of interceptor drain. discussion of papers 9611 & 9657. Proceedings of the ICE - Water Maritime and Energy 106 (4), 385–391.

Horn, D., Li, L., 2006. Measurement and modelling of gravel beach groundwater response to wave run-up: Effects on beach profile changes. Journal of Coastal Research, 1241–1249.
URL http://dx.doi.org/10.2112/06A-0006.1

Hughes, M. G., Cowell, P. J., 1987. Adjustment of reflective beaches to waves. Journal of Coastal Research, 153–167.

Hunt, I., 1959. Design of seawalls and breakwaters. In: Proc. Am. Soc. Civ. Eng., J. Waterw. Harbors Div. Vol. 85. pp. 123–152.

Huntley, D., D. A., Bowen, A. J., 1975. Field observations of edge waves and their effect on beach material. Journal of the Geological Society 131 (1), 69–81.
URL http://jgs.lyellcollection.org/content/131/1/69.abstract

Isla, F., 1993. Overpassing and armouring phenomena on gravel beaches. Marine Geology 110 (3-4), 369–376.

Isla, F. I., Bujalesky, G. G., 1993. Saltation on gravel beaches, Tierra del Fuego, Argentina. Marine Geology 115 (3–4), 263–270.
URL http://www.sciencedirect.com/science/article/pii/002532279390055Z

Jamal, M. H., Simmonds, D., Magar, V., 2014. Modelling gravel beach dynamics with XBeach. Coastal Engineering 89, 20–29.

Jennings, R., Shulmeister, J., 2002. A field based classification scheme for gravel beaches. Marine Geology 186, 211–228.
URL http://www.sciencedirect.com/science/article/pii/S0025322702003146

Johnson, B., Grzegorzewski, A., 2011. Modeling nearshore morphologic evolution of Ship Island during Hurricane Katrina. In: Proceedings of Coastal Sediments. World Scientific, pp. 1797–1810.

Johnson, C. N., 1987. Rubble beaches versus rubble revetments. In: Proceedings ASCE Conference on Coastal Sediments 1987, New Orleans, Louisiana. pp. 1216–1231.

Kamphuis, J., 1991. Alongshore sediment transport rate. Journal of Waterway, Port, Coastal, and Ocean Engineering 117 (6), 624–640.
URL http://dx.doi.org/10.1061/(ASCE)0733-950X(1991)117:6(624)

Karambas, T., 2003. Modelling of infiltration-exfiltration effects of cross-shore sediment transport in the swash zone. Coastal Engineering Journal 45 (01), 63–82.
URL http://www.worldscientific.com/doi/abs/10.1142/S057856340300066X

Kemp, P., 1960. The relationship between wave action and beach profile characteristics. In: Proceedings of 7th International Conference on Coastal Engineering, The Hague, The Netherlands,.

Kirk, R., 1970. Swash zone processes: An examination of water motion and the relations between water motion and foreshore response on·some mixed sand-shingle beaches, kaikoura, new zealand. Ph.D. thesis, University of Canterbury, New Zealand.

Kobayashi, N., Agarwal, A., Johnson, B., 2007. Longshore current and sediment transport on beaches. Journal of Waterway, Port, Coastal, and Ocean Engineering 133 (4), 296–304.

Kobayashi, N., Hicks, B. S., Figlus, J., 2011. Evolution of gravel beach profiles. Journal of Waterway, Port, Coastal, and Ocean Engineering 137 (5), 258–262.

Kobayashi, N., Johnson, B., 1998. Computer program CSHORE for predicting cross-shore transformation of irregular breaking waves. Tech. Rep. CACR-98-04, Center for Applied Coastal Research, University of Delaware.

Kobayashi, N., Otta, A., Roy, I., 1987. Wave reflection and run-up on rough slopes. Journal of Waterway, Port, Coastal, and Ocean Engineering 113 (3), 282–298.

Kobayashi, N., Otta, A. K., 1987. Hydraulic stability analysis of armor units. Journal of Waterway, Port, Coastal, and Ocean Engineering 113(2), 171–186.

Komar, P. D., 1998. Beach Processes and Sedimentation. Prentice-Hall, Englewood Cliffs, New Jersey.

Kraus, N. C., Larson, M., Kriebel, D. L., 1991. Evaluation of beach erosion and accretion predictors. In: Coastal Sediments. ASCE, pp. 572–587.

Kriebel, D., Dean, R., 1993. Convolution method for time-dependent beach-profile response. Journal of Waterway, Port, Coastal, and Ocean Engineering 119(2), 204–226.

Krumbein, W. C., Sloss, L. L., 1963. Stratigraphy and sedimentation. Freeman San Francisco.

Kuniansky, E., Halford, K., Shoemaker, W., 2008. Permeameter data verify new turbulence process for modflow. Ground Water 46 (5), 768–771.

Kuo, J., 1998. Practical design calculations for groundwater and soil remediation. CRC Press, Ch. 2: Site characterization and remedial investigation, p. 21.

Lam, D., Simpson, R., 1976. Centered differencing and the box scheme for diffusion convection problems. Journal of Computational Physics 22 (4), 486 – 500.
URL http://www.sciencedirect.com/science/article/pii/0021999176900450

Lara, J. L., Ruju, A., Losada, I. J., 2010. Reynolds averaged navier–stokes modelling of long waves induced by a transient wave group on a beach. Proceedings of the Royal Society of London A: Mathematical, Physical and Engineering Sciences 467 (2129), 1215–1242.

Larson, M., Kraus, N., 1989. SBEACH: Numerical model for simulating storm-induced beach change, Report 1: Empirical foundation and model development, Technical Report. CERC-89-9. US Army Engineer Waterways Experiment Station, Vicksburg, MS.

Larson, M., Sunamura, T., 1993. Laboratory experiment on flow characteristics at a beach step. Journal of Sedimentary Research 63 (3), 495–500.

Lee, K.-H., Mizutani, N., Hur, D.-S., Kamiya, A., 2007. The effect of groundwater on topographic changes in a gravel beach. Ocean Engineering 34, 605 – 615.
URL http://www.sciencedirect.com/science/article/pii/S0029801806000965

Leont'yev, I., 1996. Numerical modelling of beach erosion during storm event. Coastal Engineering 29, 187–200.

Li, L., Barry, D., 2000. Wave-induced beach groundwater flow. Advances in Water Resources 23, 325–337.

Li, L., Barry, D., Pattiaratchi, C., Masselink, G., 2002. Beachwin: modelling groundwater effects on swash sediment transport and beach profile changes. Environmental Modelling & Software 17 (3), 313 – 320.
URL http://www.sciencedirect.com/science/article/pii/S1364815201000664

Longuet-Higgins, M., Stewart, R., 1962. Radiation stress and mass transport in gravity waves, with application to 'surf beats'. Journal of Fluid Mechanics 13, 481–504.

Longuet-Higgins, M., Stewart, R., 1964. Radiation stresses in water waves: A physical discussion, with applications. Deep Sea Research 11, 529–562.

López de San Román-Blanco, B., Coates, T. T., Holmes, P., Chadwick, A. J., Bradbury, A., Baldock, T. E., Pedrozo-Acuña, A., Lawrence, J., Grüne, J., 2006. Large scale experiments on gravel and mixed beaches: Experimental procedure, data documentation and initial results. Coastal Engineering 53 (4), 349 – 362.
URL http://www.sciencedirect.com/science/article/pii/S0378383905001456

Lynett, P. J., Wu, T.-R., Liu, P. L.-F., 2002. Modeling wave runup with depth-integrated equations. Coastal Engineering 46 (2), 89 – 107.
URL http://www.sciencedirect.com/science/article/pii/S0378383902000431

MacCormack, R. W., 1969. The effect of viscosity in hypervelocity impact cratering. In: AIAA Hyper Velocity Impact Conference. Paper 69-354.

Madsen, P., Sørensen, O., Schäffer, H., 1997. Surf zone dynamics simulated by a Boussinesq type model. part i. model description and cross-shore motion of regular waves. Coastal Engineering 32 (4), 255–287.
URL http://www.sciencedirect.com/science/article/pii/S0378383997000288

Martin, C., Aral, M., 1971. Seepage force on interfacial bed particles. Journal of the Hydraulics Division 7, 1081–1100.

Martin, C. S., 1970. Effect of a porous sand bed on incipient sediment motion. Water Resources Research 6 (4), 1162–1174.
URL http://dx.doi.org/10.1029/WR006i004p01162

Mase, H., 1989. Random wave runup height on gentle slope. Journal of Waterway, Port, Coastal and Ocean Engineering 115 (5), 649–661.

Mason, T., Coates, T. T., 2001. Sediment transport processes on mixed beaches: A review for shoreline management. Journal of Coastal Research 17 (3), 645–657.
URL http://www.jstor.org/stable/4300216

Masselink, G., Gehrels, R., 2014. Introduction to coastal environments and global change. In: Masselink, G., Gehrels, R. (Eds.), Coastal Environments and Global Change. John Wiley & Sons, Ltd, pp. 1–27.

Masselink, G., Li, L., 2001. The role of swash infiltration in determining the beachface gradient: a numerical study. Marine Geology 176, 139 – 156.
URL http://www.sciencedirect.com/science/article/pii/S002532270100161X

Masselink, G., McCall, R., Poate, T., van Geer, P., 2014. Modelling storm response on gravel beaches using xbeach-g. Proceedings of the ICE - Maritime Engineering 167, 173–191(18).
URL http://www.icevirtuallibrary.com/content/article/10.1680/maen.14.00020

Masselink, G., Russell, P., Blenkinsopp, C., Turner, I., 2010. Swash zone sediment transport, step dynamics and morphological response on a gravel beach. Marine Geology 274, 50–68.

Masselink, G., Turner, I., 2012. Large-scale laboratory investigation into the effect of varying back-barrier lagoon water levels on gravel beach morphology and swash zone sediment transport. Coastal Engineering 63, 23–38, BARDEX: a large-scale laboratory study of gravel barrier dynamics.
URL http://www.sciencedirect.com/science/article/pii/S0378383911001992

Matias, A., Williams, J., Masselink, G., Ferreira, O., 2012. Overwash threshold for gravel barriers. Coastal Engineering 63, 48 – 61, BARDEX: a large-scale laboratory study of gravel barrier dynamics.
URL http://www.sciencedirect.com/science/article/pii/S0378383911001980

McCall, R., Masselink, G., Poate, T., Bradbury, A., Russell, P., Davidson, M., 2013. Predicting overwash on gravel barriers. Journal of Coastal Research Special Issue No. 65 Proceedings 12th International Coastal Symposium, 1473–1478.

McCall, R., Masselink, G., Poate, T., Roelvink, J., 2015a. Modeling gravel barrier resilience during storms with XBeach-G: The role of infiltration. In: Wang, P., Rosati, J. D., Cheng, J. (Eds.), Proceedings of Coastal Sediments Conference, San Diego, USA. World Scientific.

McCall, R., Masselink, G., Poate, T., Roelvink, J., Almeida, L., 2015b. Modelling the morphodynamics of gravel beaches during storms with XBeach-G. Coastal Engineering 103, 52–66.
URL http://www.sciencedirect.com/science/article/pii/S0378383915001052

McCall, R., Masselink, G., Poate, T., Roelvink, J., Almeida, L., Davidson, M., Russell, P., 2014. Modelling storm hydrodynamics on gravel beaches with XBeach-G. Coastal Engineering 91, 231 – 250.
URL http://www.sciencedirect.com/science/article/pii/S0378383914001288

McCall, R., Masselink, G., Roelvink, J., Russell, P., Davidson, M., Poate, T., 2012. Modeling overwash and infiltration on gravel barriers. In: Proceedings of the 33rd International Conference on Coastal Engineering.

McCall, R., Van Thiel de Vries, J., 2010. Towards a process-based gravel model. Poster presented at NCK-days 2010, Westkapelle, the Netherlands.

McCall, R., Van Thiel de Vries, J. S. M., Plant, N., Van Dongeren, A. R., Roelvink, J. A., Thompson, D., Reniers, A., 2010. Two-dimensional time dependent hurricane overwash and erosion modeling at Santa Rosa Island. Coastal Engineering 57, 668–683. doi:10.1016/j.coastaleng.2010.02.006.

McLean, R. F., Kirk, R. M., 1969. Relationships between grain size, size-sorting, and foreshore slope on mixed sand - shingle beaches. New Zealand Journal of Geology and Geophysics 12 (1), 138–155.
URL http://dx.doi.org/10.1080/00288306.1969.10420231

Meyer-Peter, E., Müller, R., 1948. Formulas for bed-load transport. In: Proceedings of the 2nd Meeting of the International Association for Hydraulic Structures Research. pp. 39–64.

Miles, J., Russell, P., 2004. Dynamics of a reflective beach with a low tide terrace. Continental Shelf Research 24 (11), 1219–1247, sediment transport and morphodynamics on a complex coastline.
URL http://www.sciencedirect.com/science/article/pii/S0278434304000494

Morison, J., O'Brien, M., Johnson, R., Schaaf, S., 1950. The force exerted by surface waves on piles. Petroleum Transactions, American Institute of Mining and Metallurgical Engineers 189, 149–154.

Moses, C. A., Williams, R. B., 2008. Artificial beach recharge: the south east england experience. Zeitschrift für Geomorphologie, Supplementary Issues 52 (3), 107–124.
URL http://www.ingentaconnect.com/content/schweiz/zfgs/2008/00000052/00000003/art00008

Moss, A., 1962. The physical nature of common sandy and pebbly deposits, Part I. American Journal of Science 260 (5), 337–373.

Moss, A., 1963. The physical nature of common sandy and pebbly deposits; Part II. American Journal of Science 261 (4), 297–343.

Nicholls, R., 1990. Managing erosion problems on shingle beaches: examples from britain. In: Moutzouris, C. (Ed.), Proc. 3rd European Workshop on Coastal Zones, Paralimni, Cyprus.

Nielsen, P., 1986. Local approximations : A new way of dealing with irregular waves. Coastal Engineering Proceedings 1 (20).
URL http://journals.tdl.org/icce/index.php/icce/article/view/4049

Nielsen, P., 1992. Coastal bottom boundary layers and sediment transport. Vol. 4 of Advanced Series on Ocean Engineering. World Scientific, Singapore.

Nielsen, P., 1997. Coastal groundwater dynamics. In: Proceedings of Coastal Dynamics, Plymouth, UK. pp. 546–555.

Nielsen, P., 2002. Shear stress and sediment transport calculations for swash zone modelling. Coastal Engineering 45, 53–60.

Nielsen, P., Hanslow, D. J., 1991. Wave runup distributions on natural beaches. Journal of Coastal Research, 1139–1152.

Nott, J., 2003. Waves, coastal boulder deposits and the importance of the pre-transport setting. Earth and Planetary Science Letters 210, 269–276.
URL http://www.sciencedirect.com/science/article/pii/S0012821X03001043

Obhrai, C., Powell, K., Bradbury, A., 2008. A laboratory study of overtopping and breaching of shingle barrier beaches. In: Proceedings of 31st International Conference on Coastal Engineering, Hamburg, Germany.

O'Brien, M., Morison, J., 1952. The forces exerted by waves on objects. Transaction of the American Geophysical Union 33 (1), 32–38.

Oldenziel, D. M., Brink, W. E., 1974. Influence of suction and blowing on entrainment of sand particles. Journal of the Hydraulics Division 100 (7), 935–949.

Orford, J., Carter, R., Forbes, D., 1991. Gravel barrier migration and sea level rise: some observations from Story Head, Nova Scotia, Canada. Journal of Coastal Research, 477–489.

Orford, J., Carter, R., McKenna, J., Jennings, S., 1995. The relationship between the rate of mesoscale sea-level rise and the rate of retreat of swash-aligned gravel-dominated barriers. Marine Geology 124 (1–4), 177–186, coastal Evolution in the Quarternary: {IGCP} Project 274.
URL http://www.sciencedirect.com/science/article/pii/0025322795000392

Orford, J., Jennings, R., Pethick, J., 2003. Extreme storm effect on gravel-dominated barriers. In: Proceedings of the International Conference on Coastal Sediments.

Orford, J. D., 1977. A proposed mechanism for storm beach sedimentation. Earth Surface Processes 2 (4), 381–400.
URL http://dx.doi.org/10.1002/esp.3290020409

Orford, J. D., Anthony, E. J., 2011. Extreme events and the morphodynamics of gravel-dominated coastal barriers: Strengthening uncertain ground. Marine Geology 290, 41 – 45.
URL http://www.sciencedirect.com/science/article/pii/S0025322711002325

Packwood, A., 1983. The influence of beach porosity on wave uprush and backwash. Coastal Engineering 7 (1), 29 – 40.
URL http://www.sciencedirect.com/science/article/pii/037838398390025X

Parker, G., Klingeman, P. C., McLean, D. G., 1982. Bedload and size distribution in paved gravel-bed streams. Journal of the Hydraulics Division 108 (4), 544–571.

Pedrozo-Acuña, A., Simmonds, D., Otta, A., Chadwick, A., Mar 2006. On the cross-shore profile change of gravel beaches. Coastal Engineering 53 (4), 335–347.
URL http://dx.doi.org/10.1016/j.coastaleng.2005.10.019

Pedrozo-Acuña, A., Simmonds, D. J., Chadwick, A. J., Silva, R., 2007. A numerical-empirical approach for evaluating morphodynamic processes on gravel and mixed sand-gravel beaches. Marine Geology 241, 1 – 18.
URL http://www.sciencedirect.com/science/article/pii/S0025322707000606

Pedrozo-Acuña, A., Simmonds, D. J., Reeve, D. E., 2008. Wave-impact characteristics of plunging breakers acting on gravel beaches. Marine Geology 253, 26 – 35.
URL http://www.sciencedirect.com/science/article/pii/S0025322708001473

Pedrozo-Acuña, A., Torres-Freyermuth, A., Zou, Q., Hsu, T.-J., Reeve, D. E., 2010. Diagnostic investigation of impulsive pressures induced by plunging breakers impinging on gravel beaches. Coastal Engineering 57 (3), 252 – 266.
URL http://www.sciencedirect.com/science/article/pii/S0378383909001495

Petit, H., Tonjes, P., Van Gent, M., Van den Bosch, P., 1994. Numerical simulation and validation of plunging breakers using a 2d navier-stokes model. In: Proceedings of 24th Conference on Coastal Engineering, Kobe, Japan. pp. 511–524.

Pilarczyk, K., Den Boer, K., 1983. Stability and profile development of coarse material and their application in coastal engineering. Tech. rep., Delft Hydraulics.

Poate, T., Masselink, G., Davidson, M., McCall, R., Russell, P., Turner, I., 2013. High frequency in-situ field measurements of morphological response on a fine gravel beach during energetic wave conditions. Marine Geology 342 (0), 1 – 13.
URL http://www.sciencedirect.com/science/article/pii/S0025322713000959

Poate, T., Masselink, G., McCall, R., Russell, P., Davidson, M., 2014. Storm-driven cusp behaviour on a high energy gravel beach. Journal of Coastal Research Special Issue 70, Proceedings 13th International Coastal Symposium, Durban, South Africa, 645–650.

Poate, T., Masselink, G., McCall, R., Russell, P., Davidson, M., 2015. UK storms 2014: Gravel beach response. In: Proceedings of Coastal Sediments 2015, San Diego.

Poate, T., McCall, R., Masselink, G., Russell, P., in prep. Runup on gravel dominated beaches.

Poate, T., McCall, R., Masselink, G., Russell, P., Davidson, M., 2012. Contrasting storm impacts on gravel beaches - examples from South England. In: Proceedings of the 33rd International Conference on Coastal Engineering.

Polidoro, A., Dornbusch, U., Pullen, T., 2013. Improved maximum run-up formula for mixed beaches based on field data. In: ICE Coasts, Marine Structures and Breakwaters Conference, Edinburgh.

Polubarinova-Kochina, P. Y., 1962. Theory of ground water movement. Translated from the Russian by J. M. Roger De Wiest. Princeton University Press, Princeton, N.J.

Powell, K. A., 1990. Predicting short term profile response for shingle beaches. Tech. rep., HR Wallingford SR report 219.

Pranzini, E., Farrell, E., 2006. Shoreline evolution and protection strategies along the tuscany coastline, italy. Journal of Coastal Research, 842–847.

Puleo, J., Holland, K., Plant, N., Slinn, D., Hanes, D., 2003. Fluid acceleration effects on suspended sediment transport in the swash zone. Journal of Geophysical Research: Oceans (1978–2012) 108 (C11).

Raubenheimer, B., Elgar, S., Guza, R. T., 1998. Estimating wave heights from pressure measured in sand bed. Journal of Waterway, Port, Coastal and Ocean Engineering 124:3, 151–155.

Reniers, A. J. H. M., Gallagher, E. L., MacMahan, J. H., Brown, J. A., van Rooijen, A. A., van Thiel de Vries, J. S. M., van Prooijen, B. C., 2013. Observations and modeling of steep-beach grain-size variability. Journal of Geophysical Research: Oceans 118 (2),

577–591.
URL http://dx.doi.org/10.1029/2012JC008073

Ris, R., Holthuijsen, L., Booij, N., 1999. A third-generation wave model for coastal regions, part ii: Verification. Journal of Geophysical Research 104 (C4), 7667–7682.

Roberts, T. M., Wang, P., Puleo, J. A., 2013. Storm-driven cyclic beach morphodynamics of a mixed sand and gravel beach along the mid-atlantic coast, {USA}. Marine Geology 346, 403–421.
URL http://www.sciencedirect.com/science/article/pii/S0025322713001746

Roelvink, D., Stelling, G., Hoonhout, B., Risandi, J., Jacobs, W., Merli, D., 2012. Development and field validation of a 2DH curvilinear storm impact model. Coastal Engineering Proceedings 1 (33).
URL http://journals.tdl.org/icce/index.php/icce/article/view/6981

Roelvink, J. A., Reniers, A., van Dongeren, A. R., van Thiel de Vries, J. S. M., McCall, R., Lescinski, J., 2009. Modeling storm impacts on beaches, dunes and barrier islands. Coastal Engineering 56, 1133–1152.

Ruessink, B. G., Kleinhans, M. G., van den Beukel, P. G. L., 1998. Observations of swash under highly dissipative conditions. Journal of Geophysical Research: Oceans 103 (C2), 3111–3118.
URL http://dx.doi.org/10.1029/97JC02791

Ruggiero, P., Komar, P. D., McDougal, W. G., Marra, J. J., Beach, R. A., 2001. Wave runup, extreme water levels and the erosion of properties backing beaches. Journal of Coastal Research, 407–419.

Sallenger, A., 2000. Storm impact scale for barrier islands. Journal of Coastal Research 16 (3), 890–895.

Scott, T., Masselink, G., Davidson, M., Russell, P., Conley, D., Siggery, E., in prep. Impact of extreme Atlantic storms during 2013/1014 winter on the southwest coast of England.

Shepard, F., 1963. Submarine geology. Harper & Row, New York.

Sherman, D., 1991. Gravel beaches. National Geographic Research & Exploration 7 (4), 442–452.

Shoemaker, W., Kuniansky, E., Birk, S., Bauer, S., Swain, E., 2008. Documentation of a Conduit Flow Process (CFP) for MODFLOW-2005. U.S. Geological Survey Techniques and Methods, Ch. A24, p. 50.

Simm, J. (Ed.), 1991. Manual on the use of rock in coastal and shoreline engineering, special publication 83 Edition. Vol. CUR Report 154. CIRIA.

Smagorinsky, J., Mar. 1963. General circulation experiments with the primitive equations. Monthly Weather Review 91 (3), 99–164.
URL http://dx.doi.org/10.1175/1520-0493(1963)091<0099:GCEWTP>2.3.CO;2

Smit, P., Janssen, T., Holthuijsen, L., Smith, J., 2014. Non-hydrostatic modeling of surf zone wave dynamics. Coastal Engineering 83, 36 – 48.
URL http://www.sciencedirect.com/science/article/pii/S037838391300149X

Smit, P., Stelling, G., Roelvink, J., Van Thiel de Vries, J., McCall, R., Van Dongeren, A., Zwinkels, C., Jacobs, R., 2010. XBeach: Non-hydrostatic model: Validation, verification and model description. Tech. rep., Delft University of Technology.

Smit, P., Zijlema, M., Stelling, G., 2013. Depth-induced wave breaking in a non-hydrostatic, near-shore wave model. Coastal Engineering 76 (0), 1 – 16.
URL http://www.sciencedirect.com/science/article/pii/S0378383913000215

Soulsby, R. L., Damgaard, J. S., 2005. Bedload sediment transport in coastal waters. Coastal Engineering 52 (8), 673 – 689.
URL http://www.sciencedirect.com/science/article/pii/S0378383905000475

Soulsby, R. L., Whitehouse, R. J. S. W., 1997. Threshold of sediment motion in coastal environments. In: Pacific Coasts and Ports' 97 Conference. Univ. of Canterbury, Christchurch, New Zealand.

Sparrow, K., Pokrajac, D., Van der A, D., 2012. The effect of bed permeability on oscillatory boundary layer flow. In: Proceedings of 33rd Conference on Coastal Engineering, Santander, Spain.

Sparrow, K., Pokrajac, D., Van der A, D., 2013. Interaction between oscillatory boundary layer flow and a permeable bed. In: Coastal Dynamics. pp. 1527–1536.

Steetzel, H., 1990. Cross-shore transport during storm surges. In: Proceedings of 22nd Conference on Coastal Engineering, Delft, The Netherlands. pp. 1922–1934.

Stelling, G. S., Duinmeijer, S. P. A., 2003. A staggered conservative scheme for every froude number in rapidly varied shallow water flows. International Journal for Numerical Methods in Fluids 43 (12), 1329–1354.

Stelling, G. S., Zijlema, M., 2003. An accurate and efficient finite-difference algorithm for non-hydrostatic free-surface flow with application to wave propagation. International Journal for Numerical Methods in Fluids 43, 1–23.

Stive, M., Battjes, J., 1984. A model for offshore sediment transport. In: Proceedings of 19th Conference on Coastal Engineering, Houston, Texas. pp. 1420–1436.

Stockdon, H., Holman, R., Howd, P., Sallenger, Jr., A., 2006. Empirical parameterization of setup, swash, and runup. Coastal Engineering 53, 573–588.

Stone, H., 1968. Iterative solution of implicit approximations of multidimensional partial differential equations. SIAM Journal on Numerical Analysis 5 (3), 530–558.
URL http://epubs.siam.org/doi/abs/10.1137/0705044

Stéphan, P., Suanez, S., Fichaut, B., 2010. Franchissement et migration des cordons de galets par rollover. impact de la tempête du 10 mars 2008 dans l'évolution récente du sillon de talbert (côtes-d'armor, bretagne). Norois 215, 59–75.

Stéphan, P., Suanez, S., Fichaut, B., 2012. Long-term morphodynamic evolution of the sillon de talbert gravel barrier (brittany, france). Shore & Beach 80 (1), 19–36.

Symonds, G., Huntley, D. A., Bowen, A. J., 1982. Two-dimensional surf beat: Long wave generation by a time-varying breakpoint. Journal of Geophysical Research: Oceans 87 (C1), 492–498.
URL http://dx.doi.org/10.1029/JC087iC01p00492

Thieler, E. R., Pilkey Jr, O. H., Young, R. S., Bush, D. M., Chai, F., 2000. The use of mathematical models to predict beach behavior for US coastal engineering: a critical review. Journal of Coastal Research, 48–70.

Thomas, L., 1949. Elliptic problems in linear differential equations over a network. Tech. rep., Watson Sci. Comput. Lab Report, Columbia University, New York..

Tolman, H. L., Chalikov, D., 1996. Source terms in a third-generation wind wave model. Journal of Physical Oceanography 26, 2497–2518.

Tuan, T. Q., Verhagen, H. J., Visser, P., Stive, M. J. F., 2006. Numerical modelling of wave overwash on low-crested sand barriers. In: 30th Coastal Engineering Conference. World Scientific, San Diego.

Turner, I., Coates, B., Acworth, R., 1997. Tides, waves and the super-elevation of groundwater at the coast. Journal of Coastal Research 13(1), 46–60.

Turner, I., Masselink, G., 1998. Swash infiltration-exfiltration and sediment transport. Journal of Geophysical Research 103 (C13), 30,813–30,824.

Turner, I. L., Masselink, G., 2012. Coastal gravel barrier hydrology - observations from a prototype-scale laboratory experiment (BARDEX). Coastal Engineering 63, 13 – 22.
URL http://www.sciencedirect.com/science/article/pii/S0378383911002006

Turner, I. L., Russell, P. E., Butt, T., 2008. Measurement of wave-by-wave bed-levels in the swash zone. Coastal Engineering 55 (12), 1237 – 1242.
URL http://www.sciencedirect.com/science/article/pii/S0378383908001543

Van den Bos, J., Verhagen, H. J., Zijlema, M., Mellink, B., 2014. Towards a practical application of numerical models to predict wave-structure interaction: An initial validation. In: Proceedings of 34th Conference on Coastal Engineering, Seoul, Korea.

Van der Meer, J. W., 1988. Rock slopes and gravel beaches under wave attack. Ph.D. thesis, Delft University of Technology.

Van der Meer, J. W., 1989. Scale effects in stability of gravel and stone slopes under wave attack in Deltaflume (in dutch). Tech. Rep. M1983, Delft Hydraulics.

Van der Meer, J. W., Petit, H., Van den Bosch, P., Klopman, G., Broekens, R., 1992. Numerical simulation of wave motion on and in coastal structures. In: Proceedings of 23rd Conference on Coastal Engineering, Venice, Italy. pp. 1772–1784.

Van der Meer, J. W., Pilarczyk, K., 1986. Dynamic stability of rock slopes and gravel beaches. In: Proceedings of the 20th International Conference on Coastal Engineering, Taipei.

Van der Meer, J. W., Stam, C.-J. M., 1992. Wave runup on smooth and rock slopes of coastal structures. Journal of Waterway, Port, Coastal, and Ocean Engineering 118 (5), 534–550.

Van Dongeren, A., Bolle, A., Vousdoukas, M., Plomaritis, T., Etfimova, P., Williams, J., Armaroli, C., Idier, D., Van Geer, P., Van Thiel de Vries, J., Haerens, P., Taborda, R., Benavente, J., Trifonova, E., Ciavola, P., Balouin, Y., Roelvink, D., 2009. MICORE: Dune erosion and overwash model validation with data from nine European field sites. In: Proceedings of Coastal Dynamics, Tokyo, Japan.

Van Gent, M., 1995a. Wave interaction with berm breakwaters. Journal of waterway, port, coastal, and ocean engineering 121(5), 229–238.

Van Gent, M., 1995b. Wave interaction with permeable coastal structures. Ph.D. thesis, Delft University of Technology.

Van Gent, M., 1996. Numerical modelling of wave interaction with dynamically stable structures. In: Proceedings of 25th Conference on Coastal Engineering, Orlando, Florida. pp. 1930–1943.

Van Gent, M., 2001. Wave runup on dikes with shallow foreshores. Journal of Waterway, Port, Coastal and Ocean Engineering 127 (5), 254–262.

Van Hijum, E., 1974. Equilibrium profiles of coarse material under wave attack. In: Proceedings of 14th Conference on Coastal Engineering, Copenhagen, Denmark. pp. 939–957.

Van Hijum, E., 1976. Equilibrium profiles and longshore transport of coarse material under oblique wave attack. In: Proceedings of 15th Conference on Coastal Engineering, Honolulu, Hawaii. Vol. 1.
URL https://icce-ojs-tamu.tdl.org/icce/index.php/icce/article/view/3122

Van Hijum, E., Pilarczyk, K., 1982. Equilibrium profile and longshore transport of coarse material under regular and irregular wave attack. Tech. rep., Delft Hydraulics.

Van Rijn, L., 1982. Equivalent roughness of alluvial bed. Journal of the Hydraulics Division, ASCE 108 (HY 10), 1215–1218.

Van Rijn, L., June 2007a. Unified view of sediment transport by currents and waves. i: Initiation of motion, bed roughness, and bed-load transport. Journal of Hydraulic Engineering 133 (6), 649–667.

Van Rijn, L., 2007b. Unified view of sediment transport by currents and waves. ii: Suspended transport. Journal of Hydraulic Engineering 133 (6), 668–689.

Van Rijn, L., 2009. Prediction of dune erosion due to storms. Coastal Engineering 56 (4), 441–457.

Van Rijn, L., Sutherland, J., 2011. Erosion of gravel beaches and barriers. In: Proceedings of Coastal Sediments, Miami. World Scientific Publishing Co., Inc.

Van Rijn, L., Walstra, D., Grasmeijer, B., Sutherland, J., Pan, S., Sierra, J., 2003. The predictability of cross-shore bed evolution of sandy beaches at the time scale of storms and seasons using process-based Profile models. Coastal Engineering 47 (3), 295 – 327.
URL http://www.sciencedirect.com/science/article/pii/S0378383902001205

Van Rijn, L., Walstra, D., van Ormondt, M., 2007. Unified view of sediment transport by currents and waves. iv: Application of morphodynamic model. Journal of Hydraulic Engineering 133(7), 776–793.

Van Thiel de Vries, J. S. M., 2009. Dune erosion during storm surges. Phd, Delft University of Technology.

Van Wellen, E., 1999. Modelling of swash zone sediment transport on coarse grained beaches. Ph.D. thesis, University of Plymouth.

Van Wellen, E., Baldock, T. E., Chadwick, A., Simmonds, D., 2000a. Strand - a model for longshore sediment transport in the swash zone. In: Proceedings of 27th International Conference on Coastal Engineering.

Van Wellen, E., Chadwick, A., Mason, T., 2000b. A review and assessment of longshore sediment transport equations for coarse-grained beaches. Coastal Engineering 40, 243–275.

Vellinga, P., 1986. Beach and dune erosion during storm surges, phd thesis. Ph.D. thesis, Delft University of Technology.

Ward, J., 1964. Turbulent flow in porous media. Journal of Hydraulic Division (ASCE) 90, 1–12.

Watanabe, A., Maruyama, K., Shimizu, T., Sakakiyama, T., 1986. Numerical prediction model of three-dimensional beach deformation around a structure. Coastal Engineering in Japan 29, 179–194.

Williams, A., Caldwell, N., 1988. Particle size and shape in pebble-beach sedimentation. Marine Geology 82 (3–4), 199–215.
URL http://www.sciencedirect.com/science/article/pii/0025322788901417

Williams, J., Buscombe, D., Masselink, G., Turner, I., Swinkels, C., 2012a. Barrier dynamics experiment (BARDEX): Aims, design and procedures. Coastal Engineering 63 (0), 3 – 12.
URL http://www.sciencedirect.com/science/article/pii/S0378383911002018

Williams, J., de Alegría-Arzaburu, A. R., McCall, R. T., van Dongeren, A., 2012b. Modelling gravel barrier profile response to combined waves and tides using XBeach: Laboratory and field results. Coastal Engineering 63, 62 – 80, BARDEX: a large-scale laboratory study of gravel barrier dynamics.
URL http://www.sciencedirect.com/science/article/pii/S037838391100202X

Wong, M., Parker, G., 2006. Reanalysis and correction of bed-load relation of meyer-peter and müller using their own database. Journal of Hydraulic Engineering 132 (11), 1159–1168.

Wright, L., Chappell, J., Thom, B., Bradshaw, M., Cowell, P., 1979. Morphodynamics of reflective and dissipative beach and inshore systems: Southeastern Australia. Marine Geology 32 (1–2), 105–140.
URL http://www.sciencedirect.com/science/article/pii/002532277990149X

Wright, L., Short, A., 1984. Morphodynamic variability of surf zones and beaches: a synthesis. Marine Geology 56 (1–4), 93–118.

Wurjanto, A., Kobayashi, N., 1993. Irregular wave reflection and runup on permeable slopes. Journal of Waterway, Port, Coastal, and Ocean Engineering 119 (5), 537–557.

Zambreskey, L., 1988. A verification study of the global WAM model, December 1987 - November 1988. Tech. Rep. Report GKSS 89/E/37, GKSS Forschungzentrum Geesthacht GMBH.

Zenkovich, V., Schwartz, M., 1987. Protecting the Black Sea - Georgian S.S.R. gravel coast. Journal of Coastal Research 3 (2), 201–209.

Zijlema, M., Smit, P., Stelling, G., 2011a. Simulating nearshore wave transformation with non-hydrostatic wave-flow modelling. In: 12th International Workshop on Wave Hindcasting and Forecasting and 3rd Coastal Hazards Symposium, Kohala Coast (USA), 30 Oct.-4 Nov. 2011.

Zijlema, M., Stelling, G., Smit, P., 2011b. Swash: An operational public domain code for simulating wave fields and rapidly varied flows in coastal waters. Coastal Engineering 58 (10), 992 – 1012.
URL http://www.sciencedirect.com/science/article/pii/S0378383911000974

Gravel beaches and barriers occur on many high-latitude, wave-dominated coasts across the world. Due to their natural ability to dissipate large amounts of wave energy, gravel coasts are widely regarded as an effective and sustainable form of coastal defence. However, during extreme events waves may overtop, overwash, and even lower, the crest of the gravel beach, leading to flooding of the hinterland.

This thesis attempts to improve our current capacity to predict storm impacts on gravel coasts by presenting a process-based, morphodynamic numerical model, called XBeach-G. The model is extensively validated using detailed data collected in physical model experiments, as well as data collected in the field on four natural gravel beaches in the UK and one in France.